

Turbulence in Wendelstein 7-AS Plasmas Measured by Collective Light Scat- tering

Nils Plesner Basse

Abstract This Ph.D. thesis contains theoretical and experimental work on plasma turbulence measurements using collective light scattering.

The motivation for measuring turbulence in hot fusion plasmas is, along with the method used and results obtained, the subject of chapter 1.

The theoretical part is divided into three chapters. Chapter 2 contains a full analytical derivation of the expected dependency of the detected signal on plasma parameters. Thereafter, spatial resolution of the measurements using different methods is treated in chapter 3. Finally, the spectral analysis tools used later in the thesis are described and illustrated in chapter 4.

The experimental part is divided into four chapters. In chapter 5 transport concepts relevant to the thesis are outlined. Main parameters of the Wendelstein 7-AS (W7-AS) stellarator in which measurements were made are collected in chapter 6. The setup used to study fluctuations in the electron density of W7-AS plasmas is covered in chapter 7. This localised turbulence scattering (LOTUS) diagnostic is based on a CO₂ laser radiating at a wavelength of 10.59 μm . Fast, heterodyne, dual volume detection at variable wavenumbers between 14 and 62 cm^{-1} is performed. The central chapter of the thesis, chapter 8, contains an analysis of the measured density fluctuations before, during and after several confinement transition types. The aim was to achieve a better understanding of the connection between turbulence and the confinement quality of the plasma.

Conclusions and suggestions for further work are summarised in chapter 9.

This thesis has been submitted in partial fulfilment of the requirements for the Doctor of Philosophy (Ph.D.) degree of the Niels Bohr Institute for Astronomy, Physics and Geophysics, Copenhagen, Denmark.

ISBN 87-550-3092-0; 87-550-3093-9 (internet)
ISSN 0106-2840

Print: Pitney Bowes Management Services Denmark A/S · 2002

Contents

Preface	<i>5</i>
1 Introduction	<i>7</i>
1.1 Motivation	<i>7</i>
1.2 Method	<i>8</i>
1.3 Results	<i>8</i>
I Theory	<i>11</i>
2 Collective light scattering	<i>12</i>
2.1 Scattering classification	<i>12</i>
2.2 Scattering cross section	<i>13</i>
2.3 Scattering theory	<i>14</i>
2.4 The photocurrent	<i>15</i>
2.5 Demodulation	<i>18</i>
2.6 Phase separation	<i>19</i>
2.7 Density fluctuations	<i>20</i>
3 Spatial resolution	<i>23</i>
3.1 The measurement volume	<i>23</i>
3.2 Direct localisation	<i>26</i>
3.3 Indirect localisation	<i>27</i>
4 Spectral analysis	<i>38</i>
4.1 Event creation	<i>38</i>
4.2 Statistical quantities	<i>39</i>
4.3 The autopower spectrum	<i>40</i>
4.4 The crosspower spectrum	<i>40</i>
4.5 The autocorrelation function	<i>42</i>
4.6 The crosscorrelation function	<i>43</i>
4.7 Two phenomena	<i>43</i>
II Experiment	<i>47</i>
5 Transport in fusion plasmas	<i>48</i>
5.1 Energy confinement	<i>48</i>
5.2 Transport equations	<i>49</i>
5.3 Quasilinear fluxes	<i>50</i>
5.4 Drift waves	<i>51</i>
5.5 Turbulence	<i>54</i>
5.6 Brief review	<i>56</i>
5.7 Shear flow suppression of turbulence	<i>58</i>
6 The Wendelstein 7-AS stellarator	<i>60</i>
6.1 Engineering parameters	<i>60</i>
6.2 Plasma current	<i>62</i>
6.3 The magnetic field structure	<i>66</i>

7	Experimental setup	<i>69</i>
7.1	Optical buildup	<i>69</i>
7.2	Acquisition system	<i>75</i>
8	Investigated phenomena	<i>80</i>
8.1	Quasi steady-state	<i>82</i>
8.2	Fast confinement transitions	<i>92</i>
8.3	Confinement bifurcations	<i>110</i>
8.4	Slow confinement transitions	<i>119</i>
8.5	High density H-mode	<i>139</i>
9	Conclusions	<i>148</i>
9.1	Theoretical results	<i>148</i>
9.2	Experimental results	<i>148</i>
9.3	Roads not taken	<i>149</i>
A	LOTUS setups, 1999-2000	<i>160</i>
B	Dedicated experimental programs	<i>162</i>

Preface

Power is nothing without control

Pirelli

Although meant partly tongue-in-cheek, the above slogan from a famous tyre company does embody what fusion research is all about. The uncontrolled use of nuclear fusion - the Hydrogen bomb - was already demonstrated in 1952 by Edward Teller, Stanislaw Ulam and coworkers.

At that point, the 'power' was available, although the 'control' was missing. It was thought at the time that this issue would be solved rapidly. However, this was not to be the case. Now, 50 years later, the peaceful use of nuclear fusion energy seems finally to be within our reach. The design to demonstrate the use of controlled fusion on Earth is called the International Thermonuclear Experimental Reactor (ITER). Incidentally, *iter* means 'road' or 'journey' in Latin. In the conclusions of my 1998 M.Sc. thesis I stated that it was not certain this device would ever be built; regrettably, matters remain so. It is my personal hope that the decision to construct ITER will be made and my belief that such a machine would work.

The mixture between practical use and basic research inherent to this field of physics has always been my main source of motivation and inspiration. This, along with the truly international spirit of cooperation, is what makes working with fusion so exciting; it saddens me that the fusion community obviously fails to get this enthusiastic feeling properly across to the public and the politicians deciding the budget size.

* * *

I would like to thank my Ph.D. thesis supervisors Henrik Smith, Mark Saffman and Poul K. Michelsen wholeheartedly for excellent advice, assistance and cooperation during the course of my work.

Further, I wish to thank Sándor Zoletnik for constant support; without his help this thesis would not have come into existence.

I am beholden to Dominique Grésillon, Mogens Høgh Jensen and Jens Juul Rasmussen for all the work they did as members of the Ph.D. committee.

The dedicated effort of the technical staff at Risø (Henning E. Larsen, Bjarne O. Sass, Jess C. Thorsen) and at IPP-Garching (Michael Fusseder, Hans Scholz, Günter Zangl) was essential for the operation of the diagnostic.

The advice of Michael Endler, Matthias Hirsch and Eberhard Holzhauer was of great importance to me. The help from other colleagues at IPP-Garching, too numerous to mention, is greatly appreciated.

Fruitful discussions with the Risø plasma physics group are gratefully acknowledged.

The advice and help from the ALTAIR group measuring density fluctuations in the Tore Supra tokamak was important, in particular the assistance from Ghassan Antar.

I want to thank my Risø secretaries (Lone Astradsson, Heidi D. Carlsen, Bitten Skaarup) for all their kind help - and for ensuring the enhanced flow of money to my account during the long periods at IPP-Garching. Help from the IPP-Garching secretaries (Anne Eggeling, Anke Sopora, Heidrun Volkenandt, Doris Zimmermann) was indispensable.

Last but not least, a big thanks to my office mates, Francesco Volpe, Matthias Bruchhausen, Hugh Callaghan and other Ph.D. students at IPP-Garching for providing a pleasant and productive working environment (and quite a few good laughs!).

Stris 31/7-97

Kære Nils,

Her se din Fly-billet. Der er ikke
stet meget siden vi sidst talte. Vi har
endat pakket med hver party + champagne.

Det største i DK lige nu er en gammel
Bertel Harder bo, der starter i morgen 1/8.

Det er retskrivning.

Der er nu lovovertrædelse at stole forfærd!

EDS skal være med noget edb!

V-land skal være uend o.s.v.

He! det rigtig godt ry pas på dig selv
Mads at kunne hilsne & kunne se
"de gamle" i Stris

Mar & Fr.

1 Introduction

This thesis deals with measurements of fluctuations in the electron density of fusion plasmas. We will in the introduction outline the reasons these measurements are important for further progress (section 1.1) and sketch the measurement principles (section 1.2). A brief outline of the obtained results will be presented in section 1.3 along with an overview of the thesis structure.

1.1 Motivation

If one were to make a survey of where we are, what we know and what we do not know about fusion plasmas, turbulence would certainly be an area marked 'Here Be Monsters'. The cross-field transport (perpendicular to the main magnetic field) assuming that only binary particle collisions contribute is called the neoclassical transport. This transport level includes effects associated with toroidal geometry, see figure 1. However, in general the measured transport is several orders of magnitude larger than the neoclassical one, especially for the electrons. This phenomenon has been dubbed anomalous transport and is subject to intense studies on most experimental fusion devices. Anomalous transport is believed to be driven by turbulence in the plasma.

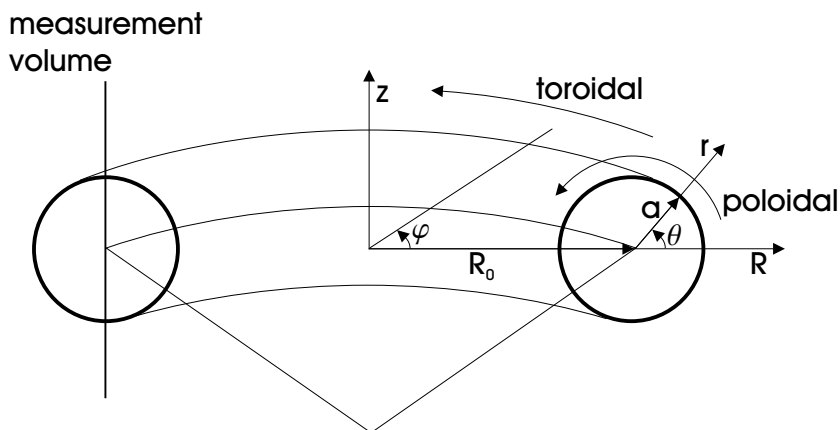


Figure 1. Geometry in a toroidal confinement device. The toroidal direction φ is the long way around the torus, the poloidal direction θ the short way. The major radius coordinate is R (R_0 being the center of the plasma column), the vertical coordinate z . The minor radius coordinate r is zero in the plasma center and a at the edge. The vertical line on the left-hand poloidal cross section indicates the approximate position of the volume where turbulence is measured.

It is generally thought that turbulence creates fluctuations visible in most plasma parameters. Therefore a concerted effort has been devoted to the study of fluctuations and their relation to the global (and local) plasma confinement quality.

The simplest *modus operandi* for the analysis of the importance of fluctuations with respect to confinement is to plot the amplitude of the fluctuations versus plasma confinement. But this approach often leads to more confusion than clarity, since it is frequently a fact that the fluctuation amplitude decreases while the confinement decreases or vice versa. However, comparing fluctuations at different spatial scales can lead to an improved understanding of anomalous transport. If

the measurements are frequency resolved, one can study the power in different frequency intervals to determine whether certain bands are linked to confinement.

A step up in sophistication is to cross correlate measurements of fluctuation amplitudes in different parameters, for example electron density and poloidal magnetic field. But even if a correlation exists, this does not mean that cross-field transport results; if the measurements are out of phase, the net transport will be zero.

Finally, one can calculate crosspower spectra (amplitude and phase) between different fluctuating quantities if they are sampled using a common clock. This method yields the 'true' transport level versus frequency.

1.2 Method

Most of the measurements presented in the thesis were made using a CO₂ laser having a wavelength of 10.59 μm . The laser light scatters off bunches of electrons and the technique is therefore called collective scattering.

In 1960 the first laser was demonstrated [100], which provided a stable source of monochromatic radiation.

The first observation of density fluctuations in a fusion device using laser scattering was made by C.M.Surko and R.E.Slusher in the Adiabatic Toroidal Compressor (ATC) tokamak [140].

Subsequently, detection of density fluctuations using lasers has been performed in numerous machines, both applying the technique used in the ATC tokamak [135] [154] [147] [19] [148] [28] and related methods, e.g. far-infrared (FIR) scattering [27] [77] [115] and phase-contrast imaging (PCI) [34] [90].

Scattering using infrared light has several advantages over alternative systems: The technique is non-intrusive, i.e. it does not perturb the investigated plasma in any way. Refraction effects can be neglected due to the high frequency of the laser radiation. Further, fluctuations can be measured at all densities, the lower density limit only depending on the signal-to-noise ratio (SNR) of the acquisition electronics.

The major drawback of collective scattering is spatial localisation: Direct localisation, where the measurement volume is limited in size by crossing beams is only possible for extremely large wavenumbers where the fluctuation amplitude is known to be minute. However, several methods of indirect localisation have been developed; one where two measurement volumes overlap in the plasma [141], one where the change of the magnetic field direction along the measurement volume is taken into account [148] and a third design which is an updated version of the crossed beam technique [132].

Summarising the state of collective scattering diagnostics on fusion machines in 2002: A large amount of measurements has been made in these devices. The massive database strongly suggests that the density fluctuations created by turbulence cause strong transport of energy and particles out of the plasma. However, a consistent detailed picture of how the various turbulent components are correlated with global transport has not yet emerged.

1.3 Results

The thesis is composed of two main parts:

The first part (containing chapters 2 through 4) deals with the theoretical aspects of collective light scattering (chapter 2), spatial localisation (chapter 3) and spectral analysis (chapter 4).

The second part (containing chapters 5 through 8) treats anomalous transport in fusion devices (chapter 5), the Wendelstein 7 Advanced Stellarator (W7-AS)

(chapter 6), the experimental setup (chapter 7) and experimental findings (chapter 8).

Finally, the main conclusions are put forth in chapter 9. A bibliography and two appendices complete the thesis.

In chapter 2 we derive an expression for the detected photocurrent from the basic principles involved. Thereafter, the issue of spatial localisation is treated in detail (chapter 3) to elucidate the components of the acquired signal. Finally, the first part is completed by chapter 4 where we give an overview of the spectral analysis tools necessary for subsequent analysis of simulations and measurements.

The second part of the thesis is opened by chapter 5 on transport in fusion plasmas. Here, we describe the terminology and the most important quantities associated with transport. Simple instabilities are described, along with relevant concepts from turbulence research. The penultimate section in the chapter consists of a brief review of fluctuation measurements in fusion plasmas. A possible turbulence suppression mechanism is sketched in the final section. Chapter 6 introduces the W7-AS stellarator; the density fluctuation measurements in this thesis are made in W7-AS plasmas. The actual realisation of the localised turbulence scattering (LOTUS) diagnostic is described in chapter 7. The diagnostic is very flexible, both in terms of the wavenumber range covered and because the measurement volume positions can be changed. Both of these quantities can be modified between each plasma discharge, and the wavenumbers measured are extremely large compared to other similar diagnostics. LOTUS has been operated both as a single and dual volume instrument, providing proof-of-principle of a novel dual volume localisation technique. Heterodyne detection enables the direction of fluctuations to be determined and fast data acquisition permits extraction of the full spectral information for up to one second. Since the LOTUS diagnostic is installed on a stellarator, it can partake in comparative studies on density fluctuations in tokamaks [160] and stellarators [153].

The overall theme of the measurements presented in this thesis is confinement transitions and their possible relation to fluctuations. The measurements are described in chapter 8 and are ordered according to the confinement transition type:

1. Quasi steady-state (no confinement transitions)
2. Fast confinement transitions (fast dithering, i.e. switching between two states)
3. Confinement bifurcations (switching from one quiescent state to another)
4. Slow confinement transitions (slow and reproducible transitions controlled by external means)
5. High density H-mode (steady-state plasmas of varying confinement quality)

For the plasmas studied in section 8.4 a specific strategy was adhered to: The same few plasma types were reproduced a considerable number of times, while the full flexibility of LOTUS was employed to arrive at a comprehensive picture of how the fluctuations evolved alongside the confinement development.

Part I
Theory

2 Collective light scattering

In this chapter we will investigate the theoretical aspects of scattering in detail. The main result will be the derivation of an expression for the observed photocurrent (section 2.4, equation 29).

The reader may wonder why such a large portion of the thesis has been used treating what is standard scattering theory. The reason is that we have read through all material covering this subject we could find; we found that none of the existing sources contains a clear derivation beginning with the basics and ending with the final results. The purpose of the present chapter is to provide such a derivation.

A classification of scattering is found in section 2.1, and the scattering cross section is briefly reviewed in section 2.2. Basic scattering theory is described in section 2.3, and a derivation of the detected photocurrent is the subject of section 2.4. Retrieval of the complex signal using demodulation is explained in section 2.5. The relationship between the observed phase and the direction of motion is explored in section 2.6. The final section (2.7) deals with spectral theory applied to the derived photocurrent.

2.1 Scattering classification

We would like to touch upon a few subjects relating to the type of scattering that is observed. First of all a classification of scattering is useful [82]:

- If one were to describe scattering of an electromagnetic field off a particle quantum mechanically, the description would be of photons bouncing off the particle.
 1. Thomson scattering: Negligible change in mean particle momentum during collision with the photon ($\hbar\omega \ll mc^2$).
 2. Compton scattering: The case where photons are so energetic that their momentum cannot be ignored.

As we work with a wavelength $\lambda_0 = 10.59 \mu\text{m}$ in the infrared range, the photon energy is much smaller than the rest mass of the electron. Therefore we will restrict ourselves to consider classical Thomson scattering.

- Since the ions are much heavier than the electrons, their acceleration and hence radiation is usually sufficiently small to be ignored. So the electrons do the scattering.
- The Salpeter parameter $\alpha_S = 1/k\lambda_D$ [133] determines whether the scattering observed is incoherent ($\alpha_S < 1$) or coherent ($\alpha_S > 1$). Here, k is the wavenumber observed and $\lambda_D = \sqrt{\epsilon_0 T / ne^2}$ is the Debye length. Note that temperature is written in eV in this thesis. Basically, incoherent scattering is due to scattering off single electrons, while coherent scattering is due to scattering off a bunch of electrons; this is also known as collective scattering and is the limit we are observing with the diagnostic.

To sum up, we are dealing with collective Thomson scattering. Four elements go into the process of scattering:

1. The incident radiation (the laser beam).
2. The set of scatterers (electrons).
3. The reference beam.

4. The detector.

In this chapter we describe the first 3 parts; a description of the detectors used is to be found in chapter 7 which also contains a detailed description of the practical implementation of the scattering diagnostic.

2.2 Scattering cross section

The power P per unit solid angle Ω_s scattered at an angle ζ by an electron is given by

$$\frac{dP}{d\Omega_s} = \sqrt{\frac{\varepsilon_0}{\mu_0}} |\mathcal{E}_0^2| r_e^2 \sin^2 \zeta, \quad (1)$$

where $\sqrt{\frac{\varepsilon_0}{\mu_0}} |\mathcal{E}_0^2|$ (see subsection 2.3.1 for the definition of \mathcal{E}_0) is the incident laser power per unit area,

$$r_e = \frac{\mu_0 e^2}{4\pi m_e} \quad (2)$$

is the classical electron radius and ζ is the angle between the incident and scattered power [82]. The scattering cross section σ per unit solid angle is then defined as

$$\frac{d\sigma}{d\Omega_s} = \frac{dP}{d\Omega_s} \frac{1}{\sqrt{\frac{\varepsilon_0}{\mu_0}} |\mathcal{E}_0^2|} = r_e^2 \sin^2 \zeta \quad (3)$$

Knowing that $d\Omega_s = 2\pi \sin \zeta d\zeta$ we get

$$\sigma = \int d\sigma = 2\pi r_e^2 \int_0^\pi \sin^3 \zeta d\zeta = 2\pi r_e^2 (4/3), \quad (4)$$

which one could interpret as an effective size of the electron for scattering.

We now wish to rewrite the classical electron radius using the polarisability α , defined by the equation for the dipole moment \mathbf{p} :

$$\mathbf{p} = \alpha \varepsilon_0 \mathbf{E}, \quad (5)$$

where \mathbf{E} is the incident electric field [46]. If this electric field possesses a harmonic time variation with frequency ω , the electron will execute an undamped, forced oscillation [91]. The equation of motion can be solved for the electron position, leading to a determination of the dipole moment. Using equation 5 we then calculate the static ($\omega = 0$) polarisability α_0 :

$$\alpha_0 = \frac{e^2}{\varepsilon_0 m_e \omega_0^2} = \frac{\mu_0 e^2 c^2}{m_e \omega_0^2} = \frac{\mu_0 e^2}{m_e k_0^2}, \quad (6)$$

where $\omega_0 = ck_0$ is the eigenfrequency of the electron [46]. Equation 6 enables us to express the classical electron radius in terms of α_0 :

$$r_e = \frac{k_0^2 \alpha_0}{4\pi} \quad (7)$$

2.3 Scattering theory

2.3.1 Radiation source

Our incident laser beam has a direction \mathbf{k}_0 , where $k_0 = \omega_0/c$, and a wavelength $\lambda_0 = 10.59 \mu\text{m}$. For a linearly polarized beam, the electric field is given as in equation 8, where $\mathcal{E}_0(\mathbf{r}) = \mathcal{E}_0 u_0(\mathbf{r}) e^{i(\mathbf{k}_0 \cdot \mathbf{r})}$. \mathcal{E}_0 is a vector whose direction and amplitude are those of the electric field at maximum.

$$\mathbf{E}_0(\mathbf{r}, t) = \text{Re}\{\mathcal{E}_0(\mathbf{r}) e^{-i\omega_0 t}\} \quad (8)$$

Assuming Gaussian beams, the radial profile near the waist w will be of the form $u_0(\mathbf{r}) = e^{-(r_\perp^2/w^2)}$, where r_\perp is the perpendicular distance from the beam axis.

The frequency of the laser radiation ω_0 is much higher than the plasma frequency $\omega_p = \sqrt{ne^2/\varepsilon_0 m_e}$. This means that the refractive index of the plasma

$$N = \sqrt{1 - \omega_p^2/\omega_0^2} \quad (9)$$

is close to one, or that refractive effects are negligible [130]. This is a significant advantage compared to microwave diagnostics, where raytracing calculations must assist interpretation of the measurements.

2.3.2 Single particle scattering

For a single scatterer having index j located at position \mathbf{r}_j (see figure 2), the scatterer radiates an electric field at \mathbf{r}' (the detector position) as a result of the incident beam field. This field is given in equation 10, where \mathbf{n}_j is along $\mathbf{r}' - \mathbf{r}_j$ and approximately perpendicular to \mathcal{E}_0 [79]:

$$\begin{aligned} \mathbf{E}_s(\mathbf{r}', t) &= \text{Re}\{\mathcal{E}_s(\mathbf{r}') e^{-i\omega_0 t}\} \\ \mathcal{E}_s(\mathbf{r}') &= \left\{ \frac{k_0^2 \alpha_0}{4\pi} \frac{e^{ik_0|\mathbf{r}' - \mathbf{r}_j|}}{|\mathbf{r}' - \mathbf{r}_j|} [\mathbf{n}_j \times \mathcal{E}_0(\mathbf{r}_j)] \times \mathbf{n}_j \right\} \end{aligned} \quad (10)$$

The scattered field is simply the radiation field from an oscillating dipole having a moment \mathbf{p} [84]:

$$\mathbf{E} = \frac{k^2}{4\pi\varepsilon_0} \frac{e^{ikr}}{r} [\mathbf{n} \times \mathbf{p}] \times \mathbf{n} \quad (11)$$

Therefore the above expression for the scattered electric field is often called the dipole approximation. It is an approximation because the equation is only valid in the nonrelativistic limit. For very energetic electrons the relativistic corrections become significant, see e.g. [82].

2.3.3 Far field approximation

Two assumptions are made:

1. The position where one measures (\mathbf{r}') is far from the scattering region
2. The opening angle of the detector is small,

leading to the validity of the far field approximation [79]. This means that we can consider the scattered field from all j particles in the scattering volume to have the same direction denoted \mathbf{n}' parallel to \mathbf{n}_j . Therefore the scattered wave

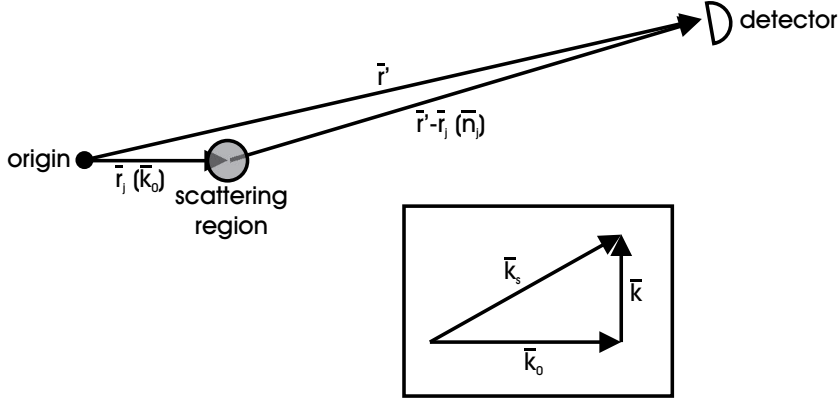


Figure 2. Scattering geometry. Main figure: The position of a scatterer is \mathbf{r}_j and \mathbf{r}' is the detector position. Inset: The incoming wave vector \mathbf{k}_0 and scattered wave vector \mathbf{k}_s determine the observed wave vector \mathbf{k} .

vector $\mathbf{k}_s = k_0 \mathbf{n}'$ and $\mathbf{k} = \mathbf{k}_s - \mathbf{k}_0$ is the wave vector selected by the optics, see figure 2.

The scattered field at the detector due to several particles can be written as a sum

$$\mathbf{E}_s(\mathbf{r}', t) = \text{Re}\{\mathcal{E}_s(\mathbf{r}')e^{-i\omega_0 t}\}$$

$$\mathcal{E}_s(\mathbf{r}') = \frac{k_0^2 \alpha_0}{4\pi} \sum_j \frac{e^{ik_0|\mathbf{r}' - \mathbf{r}_j|}}{|\mathbf{r}' - \mathbf{r}_j|} u_0(\mathbf{r}_j) [\mathbf{n}' \times \mathcal{E}_0] \times \mathbf{n}' e^{i\mathbf{k}_0 \cdot \mathbf{r}_j} \quad (12)$$

In going from a single particle scattering description to more particles, we will approximate the position of the individual scatterers \mathbf{r}_j by one common vector \mathbf{r} . The particles will have a density distribution $n(\mathbf{r}, t)$. We write the scattered field as an integral over the measurement volume V :

$$\mathcal{E}_s(\mathbf{r}', t) = \frac{k_0^2 \alpha_0}{4\pi} \int_V \frac{e^{ik_0|\mathbf{r}' - \mathbf{r}|}}{|\mathbf{r}' - \mathbf{r}|} u_0(\mathbf{r}) [\mathbf{n}' \times \mathcal{E}_0] \times \mathbf{n}' n(\mathbf{r}, t) e^{i\mathbf{k}_0 \cdot \mathbf{r}} d^3\mathbf{r} \quad (13)$$

2.4 The photocurrent

The electric field of the local oscillator (LO, see figure 3) beam along \mathbf{n}' at the detector is given as

$$\mathbf{E}_{\text{LO}}(\mathbf{r}', t) = \text{Re}\{\mathcal{E}_{\text{LO}}(\mathbf{r}')e^{-i(\omega_0 + \omega_\Delta)t}\}$$

$$\mathcal{E}_{\text{LO}}(\mathbf{r}') = \mathcal{E}_{\text{LO}} u_{\text{LO}}(\mathbf{r}') e^{i\mathbf{k}_0 \mathbf{n}' \cdot \mathbf{r}'}, \quad (14)$$

where ω_Δ is a frequency shift and $\mathbf{k}_{\text{LO}} = \mathbf{k}_s = k_0 \mathbf{n}'$.

The incident optical power reaching the detector can be found integrating the Poynting vector over the detector area A

$$S(t) = \frac{1}{\mu_0} \int_A (\mathbf{E} \times \mathbf{B}) \cdot d^2\mathbf{r}' =$$

$$\frac{1}{\mu_0 c} \int_A |\mathbf{E}_{\text{LO}}(\mathbf{r}', t) + \mathbf{E}_s(\mathbf{r}', t)|^2 d^2\mathbf{r}' =$$

$$\frac{1}{\mu_0 c} \int_A |\mathbf{E}_{\text{LO}}(\mathbf{r}', t)|^2 + |\mathbf{E}_s(\mathbf{r}', t)|^2 + 2 \times \text{Re}\{\mathbf{E}_{\text{LO}}^*(\mathbf{r}', t) \mathbf{E}_s(\mathbf{r}', t)\} d^2\mathbf{r}' \quad (15)$$

What we are interested in is the last term of the equation, namely the beating term

$$S_B(t) = \int_A \frac{2}{\mu_0 c} \text{Re}\{\mathbf{E}_{\text{LO}}^*(\mathbf{r}', t)\mathbf{E}_s(\mathbf{r}', t)\} d^2\mathbf{r}' \quad (16)$$

The term containing the LO power is constant, and the contribution to the power from the scattered field is very small because its field amplitude is much smaller than that of the LO [79].

Now we define the integrand of equation 16 to be $s_B(\mathbf{r}')$:

$$\begin{aligned} s_B(\mathbf{r}') &= \\ & \frac{2}{\mu_0 c} \text{Re}\{\mathbf{E}_{\text{LO}}^*(\mathbf{r}', t)\mathbf{E}_s(\mathbf{r}', t)\} = \\ & 2\sqrt{\frac{\varepsilon_0}{\mu_0}} \text{Re}\{\mathcal{E}_s(\mathbf{r}') \cdot \mathcal{E}_{\text{LO}}^*(\mathbf{r}') e^{i\omega_\Delta t}\} \end{aligned} \quad (17)$$

Assuming a detector quantum efficiency η leads to the photocurrent

$$i_B(t) = \frac{e\eta}{\hbar\omega_0} \int_A s_B(\mathbf{r}') d^2\mathbf{r}' \quad (18)$$

The photocurrent due to an ensemble of scatterers at the detector position \mathbf{r}' (replacing i_B by i_k , where the subscript k is the measured wavenumber) is

$$\begin{aligned} i_k(t) \frac{\hbar\omega_0}{e\eta} &= \int_A s_B(\mathbf{r}') d^2\mathbf{r}' = \\ & 2\text{Re} \left\{ \frac{1}{\mu_0 c} \int_A [\mathbf{E}_{\text{LO}}^*(\mathbf{r}', t)\mathbf{E}_s(\mathbf{r}', t)] d^2\mathbf{r}' \right\} = \\ & 2\text{Re} \left\{ \frac{1}{\mu_0 c} \int_A [\mathcal{E}_{\text{LO}}^* u_{\text{LO}}^*(\mathbf{r}') e^{-ik_0 \mathbf{n}' \cdot \mathbf{r}'} e^{it(\omega_0 + \omega_\Delta)} \right. \\ & \left. \frac{k_0^2 \alpha_0}{4\pi} \int_V \frac{e^{ik_0 |\mathbf{r}' - \mathbf{r}|}}{|\mathbf{r}' - \mathbf{r}|} u_0(\mathbf{r}) [\mathbf{n}' \times \mathcal{E}_0] \times \mathbf{n}' n(\mathbf{r}, t) e^{i\mathbf{k}_0 \cdot \mathbf{r}} e^{-i\omega_0 t} d^3\mathbf{r} \right\} d^2\mathbf{r}' \end{aligned} \quad (19)$$

where we have inserted equations 14 and 13 for the LO and scattered electric field, respectively. We now introduce the Fresnel-Kirchhoff diffraction formula

$$\frac{1}{i\lambda_0} \int_A \frac{e^{ik_0 |\mathbf{r}' - \mathbf{r}|}}{|\mathbf{r}' - \mathbf{r}|} u_{\text{LO}}^*(\mathbf{r}') \mathcal{E}_{\text{LO}}^* e^{-ik_0 \mathbf{n}' \cdot \mathbf{r}'} d^2\mathbf{r}' = u_{\text{LO}}^*(\mathbf{r}) \mathcal{E}_{\text{LO}}^* e^{-i\mathbf{k}_s \cdot \mathbf{r}}, \quad (20)$$

which is the radiated field for small angles of diffraction from a known monochromatic field distribution on a diaphragm A [20]. This radiated field (the antenna or virtual LO beam [63]) propagates from the detector to the scatterers [76]. The reciprocity theorem of Helmholtz states that a point source at \mathbf{r} will produce at \mathbf{r}' the same effect as a point source of equal intensity placed at \mathbf{r}' will produce at \mathbf{r} [20]. Therefore equation 20 describing the field in the measurement volume (position \mathbf{r}) due to a source at the detector (position \mathbf{r}') is equivalent to the reverse situation, where the measurement volume is the source.

In equation 21 we first reorganise equation 19 and then apply the Fresnel-Kirchhoff diffraction formula:

$$\begin{aligned}
& i_k(t) \frac{\hbar\omega_0}{e\eta} = \\
& 2Re \left\{ \frac{k_0^2 \alpha_0}{4\pi} \frac{1}{\mu_0 c} e^{it\omega_\Delta} \int_V \left[\frac{i\lambda_0}{i\lambda_0} \int_A \frac{e^{ik_0|\mathbf{r}'-\mathbf{r}|}}{|\mathbf{r}'-\mathbf{r}|} u_{LO}^*(\mathbf{r}') \mathcal{E}_{LO}^* e^{-i\mathbf{k}_s \cdot \mathbf{r}'} d^2 \mathbf{r}' \right] \right. \\
& \quad \left. [\mathbf{n}' \times \mathcal{E}_0] \times \mathbf{n}' e^{i\mathbf{k}_0 \cdot \mathbf{r}} u_0(\mathbf{r}) n(\mathbf{r}, t) d^3 \mathbf{r} \right\} = \\
& 2Re \left\{ i \frac{k_0^2 \alpha_0}{4\pi} \frac{\lambda_0}{\mu_0 c} e^{it\omega_\Delta} \int_V \mathcal{E}_{LO}^* u_{LO}^*(\mathbf{r}) e^{-i\mathbf{k}_s \cdot \mathbf{r}} \mathcal{E}_0 u_0(\mathbf{r}) e^{i\mathbf{k}_0 \cdot \mathbf{r}} n(\mathbf{r}, t) d^3 \mathbf{r} \right\} = \\
& 2Re \left\{ i \frac{\pi \alpha_0}{\lambda_0} \sqrt{\frac{\varepsilon_0}{\mu_0}} e^{it\omega_\Delta} \int_V \mathcal{E}_{LO}^* u_{LO}^*(\mathbf{r}) \mathcal{E}_0 u_0(\mathbf{r}) e^{-i\mathbf{k} \cdot \mathbf{r}} n(\mathbf{r}, t) d^3 \mathbf{r} \right\}, \quad (21)
\end{aligned}$$

since

$$\frac{k_0^2 \alpha_0}{4\pi} \frac{\lambda_0}{\mu_0 c} = \frac{\pi \alpha_0}{\lambda_0} \sqrt{\frac{\varepsilon_0}{\mu_0}} \quad (22)$$

and

$$[\mathbf{n}' \times \mathcal{E}_0] \times \mathbf{n}' = \mathcal{E}_0 \quad (23)$$

The expression for the current now becomes

$$\begin{aligned}
& i_k(t) = \\
& 2 \frac{e\eta}{\hbar\omega_0} \sqrt{\frac{\varepsilon_0}{\mu_0}} \lambda_0 Re \left\{ i r_e e^{i\omega_\Delta t} \mathcal{E}_0 \mathcal{E}_{LO}^* \int_V n(\mathbf{r}, t) u_0(\mathbf{r}) u_{LO}^*(\mathbf{r}) e^{-i\mathbf{k} \cdot \mathbf{r}} d^3 \mathbf{r} \right\}, \quad (24)
\end{aligned}$$

where \mathcal{E}_{LO}^* and \mathcal{E}_0 hereafter are to be considered as scalars since the laser field and the LO field are assumed to have identical polarisation.

We introduce a shorthand notation for the spatial Fourier transform

$$\begin{aligned}
(n(t)U)_k &= \int_V n(\mathbf{r}, t) U(\mathbf{r}) e^{-i\mathbf{k} \cdot \mathbf{r}} d^3 \mathbf{r} \\
U(\mathbf{r}) &= u_0(\mathbf{r}) u_{LO}^*(\mathbf{r}), \quad (25)
\end{aligned}$$

where U is called the beam profile [76] [63]. We note that

$$\begin{aligned}
\int_V n(\mathbf{r}, t) U(\mathbf{r}) e^{-i\mathbf{k} \cdot \mathbf{r}} d^3 \mathbf{r} &= \int n(\mathbf{k}', t) U(\mathbf{k} - \mathbf{k}') \frac{d^3 \mathbf{k}'}{(2\pi)^3} = n(\mathbf{k}, t) \star U(\mathbf{k}) \\
n(\mathbf{k}, t) &= \int_V n(\mathbf{r}, t) e^{-i\mathbf{k} \cdot \mathbf{r}} d^3 \mathbf{r} \\
U(\mathbf{k}) &= \int_V U(\mathbf{r}) e^{-i\mathbf{k} \cdot \mathbf{r}} d^3 \mathbf{r}, \quad (26)
\end{aligned}$$

where \star denotes convolution [137] [79]. We arrive at

$$i_k(t) = 2 \frac{e\eta}{\hbar\omega_0} \sqrt{\frac{\varepsilon_0}{\mu_0}} \lambda_0 Re [i r_e e^{i\omega_\Delta t} \mathcal{E}_0 \mathcal{E}_{LO}^* (n(t)U)_k] \quad (27)$$

Defining

$$\gamma = \frac{e\eta}{\hbar\omega_0} \sqrt{\frac{\varepsilon_0}{\mu_0}} \lambda_0 r_e \mathcal{E}_0 \mathcal{E}_{LO}^*, \quad (28)$$

equation 24 in its final guise is

$$i_k(t) = i[\gamma e^{i\omega_\Delta t}(n(t)U)_k - \gamma^* e^{-i\omega_\Delta t}(n(t)U)_k^*] \quad (29)$$

Note that the $e^{-i\mathbf{k}\cdot\mathbf{r}}$ term in $(n(t)U)_k$ constitutes a spatial band pass filter (\mathbf{k} is fixed). Three scales are involved [1]:

- Fluctuations occur at scales r much smaller than $\lambda = 2\pi/k \Rightarrow \mathbf{k}\cdot\mathbf{r} \ll 1 \Rightarrow e^{-i\mathbf{k}\cdot\mathbf{r}} \approx 1$. The Fourier transform becomes the mean value of the density fluctuations, which is zero.
- Fluctuations occur at scales r similar to $\lambda = 2\pi/k$; this leads to the main contribution to the signal.
- Fluctuations occur at scales r much larger than $\lambda = 2\pi/k \Rightarrow \mathbf{k}\cdot\mathbf{r} \gg 1 \Rightarrow e^{-i\mathbf{k}\cdot\mathbf{r}}$ is highly oscillatory. The mean value will be roughly equal to that of $e^{-i\mathbf{k}\cdot\mathbf{r}}$, which is zero.

The scattered power P_k resulting from the interference term can be written by defining a constant

$$\xi = \sqrt{\frac{\varepsilon_0}{\mu_0}} \lambda_0 r_e \mathcal{E}_0 \mathcal{E}_{LO}^* \quad (30)$$

and replacing γ with this in equation 29

$$\begin{aligned} P_k(t) &= \frac{\hbar\omega_0}{e\eta} i_k(t) = \\ & i[\xi e^{i\omega_\Delta t}(n(t)U)_k - \xi^* e^{-i\omega_\Delta t}(n(t)U)_k^*] = \\ & 2Re[i\xi e^{i\omega_\Delta t}(n(t)U)_k] \end{aligned} \quad (31)$$

If \mathcal{E}_0 and \mathcal{E}_{LO} are real numbers (meaning that ξ is real) we can go one step further and write

$$\begin{aligned} P_k(t) &= 2\xi Re[i e^{i\omega_\Delta t}(n(t)U)_k] = \\ & 8 \frac{\lambda_0 r_e}{\pi w^2} \sqrt{P_0 P_{LO}} Re[i e^{i\omega_\Delta t}(n(t)U)_k] \end{aligned} \quad (32)$$

assuming that $P_{0/LO} = \frac{\pi w^2}{4} \sqrt{\frac{\varepsilon_0}{\mu_0}} |\mathcal{E}_{0/LO}|^2$ (for a given U , see subsection 2.7.2).

2.5 Demodulation

The task now is to extract real and imaginary parts of $(n(t)U)_k$. We construct two signals that are shifted by $\pi/2$ [106]:

$$\begin{aligned} j_1(t) &= Re[e^{i\omega_\Delta t}] = \cos(\omega_\Delta t) \\ j_2(t) &= Re[e^{i(\omega_\Delta t + \pi/2)}] = \sin(\omega_\Delta t) \end{aligned} \quad (33)$$

Now two quantities are constructed using equations 29 (divided into two equal parts) and 33:

$$\begin{aligned}
i_{d,1} &= \frac{i_k(t)}{2} j_1(t) = \\
&\frac{i}{4} [\gamma e^{i2\omega_\Delta t} (n(t)U)_k + \gamma (n(t)U)_k - \\
&\gamma^* (n(t)U)_k^* - \gamma^* e^{-i2\omega_\Delta t} (n(t)U)_k^*] \\
i_{d,2} &= \frac{i_k(t)}{2} j_2(t) = \\
&\frac{i}{4} [\gamma e^{i2\omega_\Delta t} e^{i\pi/2} (n(t)U)_k + \gamma e^{-i\pi/2} (n(t)U)_k - \\
&\gamma^* e^{i\pi/2} (n(t)U)_k^* - \gamma^* e^{-i2\omega_\Delta t} e^{-i\pi/2} (n(t)U)_k^*] \tag{34}
\end{aligned}$$

Low pass filtering (LPF) of these quantities removes the terms containing the fast $2\omega_\Delta$ expression. The result is that

$$\begin{aligned}
i_{d,\text{complex}} &= [i_{d,2} - i i_{d,1}]_{\text{LPF}} = \\
&\frac{1}{2} (\text{Re}[\gamma (n(t)U)_k] - i(-\text{Im}[\gamma (n(t)U)_k])) = \\
&\frac{\gamma}{2} (n(t)U)_k \tag{35}
\end{aligned}$$

Now we have $(n(t)U)_k$ and can analyse this complex quantity using spectral tools. The alternative to heterodyne detection is called homodyne detection. There are two advantages that heterodyne detection has compared to homodyne detection:

1. The LO beam provides an amplification factor to the detected signal (see equation 32).
2. It leaves the complex $(n(t)U)_k$ intact multiplied by a wave having frequency ω_Δ ; in homodyne detection the electric field complex number is transformed into a real number and the phase information is lost. The frequency sign of the scattered power tells us in which direction the fluctuations are moving.

2.6 Phase separation

Since the theory behind phase separation is extensively described in section 2 of [3], we will here only give a brief recapitulation of the basics.

The observed signal is interpreted as being due to a large number of 'electron bunches', each moving in a given direction. An electron bunch is defined as a collection of electrons occupying a certain region of the measurement volume V . This definition is motivated by the fact that even though the measurement volume includes a large number of cells V/λ^3 [2] (typically ~ 3000 in W7-AS), the amplitude of the signal consists of both large and small values separated in time. The demodulated photocurrent $i_{d,\text{complex}}$ is a complex number; it can be written

$$i_{d,\text{complex}}(t) = \sum_{j=1}^{N_b} a_j e^{i\phi_j} = A e^{i\Phi}, \tag{36}$$

where N_b is the number of bunches, while a_j and ϕ_j is the amplitude and phase of bunch number j , respectively. The criterion for determination of direction is

$$\begin{aligned}
\partial_t \Phi > 0 &\Rightarrow \mathbf{k} \cdot \mathbf{U} > 0 \Rightarrow \text{fluctuations} \parallel \mathbf{k} \\
\partial_t \Phi < 0 &\Rightarrow \mathbf{k} \cdot \mathbf{U} < 0 \Rightarrow \text{fluctuations} \parallel -\mathbf{k}, \tag{37}
\end{aligned}$$

where $\Phi = \mathbf{k} \cdot \mathbf{U}t$ and \mathbf{U} is the average bunch velocity. The phase derivative sign reflects the bunches with highest intensities occurring most frequently.

2.7 Density fluctuations

2.7.1 Derivation

The current frequency spectral density measured is

$$I_k(\omega) = \frac{|i_k(\omega)|^2}{T}$$

$$i_k(\omega) = \int_{t_1}^{t_2} e^{i\omega t} i_k(t) dt = \int_{t_1}^{t_2} e^{i\omega t} i_k(t) dt, \quad (38)$$

where $T = t_2 - t_1$ is a time interval. Using 29 this can be written

$$I_k(\omega) = \frac{|\gamma|^2}{T} \{ |(n(\omega)U)_k|^2 + |(n(-\omega)U)_k|^2 \}$$

$$(n(\omega)U)_k = \int d^3\mathbf{r} \int_{t_1}^{t_2} n(\mathbf{r}, t) U(\mathbf{r}) e^{i(\omega t - \mathbf{k} \cdot \mathbf{r})} dt$$

$$n(\mathbf{k}, \omega) = \int_{t_1}^{t_2} n(\mathbf{k}, t) e^{i\omega t} dt, \quad (39)$$

assuming that $n(\mathbf{k}, \omega)$ and $n(\mathbf{k}, -\omega)$ are independent (i.e. no mixed terms) [63]. Note that we have dropped the ω_Δ terms; it has previously been explained how we filter these high frequencies away. Now we are approaching an analytical expression for the weighted mean square density fluctuation. The time fluctuating part of $n(\mathbf{r}, t)$ is

$$\delta n(\mathbf{r}, t) = n(\mathbf{r}, t) - \frac{1}{T} \int_{t_1}^{t_2} n(\mathbf{r}, t) dt \quad (40)$$

When δn is written without a subscript, it is taken to refer to the electron density fluctuations. Equation 40 enables us to express the weighted mean square density fluctuation as

$$\langle \delta n^2 \rangle_{UT} = \frac{\int_{t_1}^{t_2} dt \int d^3\mathbf{r} \delta n^2(\mathbf{r}, t) |U(\mathbf{r})|^2 d^3\mathbf{r}}{T \int |U(\mathbf{r})|^2 d^3\mathbf{r}} \quad (41)$$

The subscript means averaging over the beam profile $U(\mathbf{r})$ and a time interval T . We can transform this via Parseval's theorem

$$\int_{t_1}^{t_2} dt \int d^3\mathbf{r} |\delta n(\mathbf{r}, t) U(\mathbf{r})|^2 d^3\mathbf{r} = \int \frac{d\omega}{2\pi} \int \frac{d^3\mathbf{k}}{(2\pi)^3} |(\delta n(\omega)U)_k|^2 \quad (42)$$

to the wave vector-frequency domain

$$\langle \delta n^2 \rangle_{UT} = n_0 \int \frac{d\omega}{2\pi} \int \frac{d^3\mathbf{k}}{(2\pi)^3} S_U(\mathbf{k}, \omega)$$

$$S_U(\mathbf{k}, \omega) = \frac{|(\delta n(\omega)U)_k|^2}{n_0 T \int |U(\mathbf{r})|^2 d^3\mathbf{r}}, \quad (43)$$

where n_0 is the mean density in the scattering volume. $S_U(\mathbf{k}, \omega)$ is the measured spectral density also known as the form factor. Conventionally, this is given as

$$S(\mathbf{k}, \omega) = \frac{|\delta n(\mathbf{k}, \omega)|^2}{n_0 VT}$$

$$\delta n(\mathbf{r}, t) = \int \frac{d\omega}{2\pi} \int \frac{d^3\mathbf{k}}{(2\pi)^3} \delta n(\mathbf{k}, \omega) e^{-i(\omega t - \mathbf{k} \cdot \mathbf{r})} \quad (44)$$

Combining equations 43 and 39 (replacing n by δn) we get

$$S_U(\mathbf{k}, \omega, -\omega) = S_U(\mathbf{k}, \omega) + S_U(\mathbf{k}, -\omega) = \frac{I_k(\omega)}{n_0 |\gamma^2| \int |U(\mathbf{r})|^2 d^3\mathbf{r}} \quad (45)$$

The term with positive frequency corresponds to density fluctuations propagating in the \mathbf{k} -direction, while negative frequency means propagation in the opposite direction [148].

The wavenumber resolution width is

$$\Delta k^3 = \left[\int |U(\mathbf{r})|^2 d^3\mathbf{r} \right]^{-1} \quad (46)$$

We have now arrived at the goal; replacing $S_U(\mathbf{k}, \omega)$ by $S_U(\mathbf{k}, \omega, -\omega)$ in the first line of equation 43, our final expression for the mean square density fluctuations is

$$\langle \delta n^2 \rangle_{UT} = \int \frac{d^3\mathbf{k}}{(2\pi)^3} \frac{\langle \delta n^2 \rangle_k}{\Delta k^3}$$

$$\langle \delta n^2 \rangle_k = \frac{1}{|\gamma^2| \left[\int |U(\mathbf{r})|^2 d^3\mathbf{r} \right]^2} \int_{-\infty}^{\infty} \frac{d\omega}{2\pi} I_k(\omega) \quad (47)$$

The frequency integration is done numerically, while a wavenumber integration can be done by measuring I_k for different wavenumber values.

2.7.2 An example

When the beam profile $U(\mathbf{r})$ is known, quantitative expressions for the density fluctuations can be calculated [63]. The following assumptions are made:

- Antenna beam corresponds to LO beam.
- Beams have Gaussian profiles.
- Beams are focused in the measurement region with identical waists w .
- Forward scattering.

Furthermore, the beam profile $U(\mathbf{r})$ is assumed to be

$$U(\mathbf{r}) = u_0(\mathbf{r}) u_{LO}^*(\mathbf{r}) = e^{-2(x^2+y^2)/w^2} \text{ for } |z| < L/2$$

$$U(\mathbf{r}) = 0 \text{ for } |z| > L/2, \quad (48)$$

where L is the measurement volume length and the beams are along z .

The wavenumber resolution width Δk^3 becomes $4/(\pi w^2 L)$ and we find the wavenumber resolution itself by calculating

$$\begin{aligned}
U(\mathbf{k}) &= \\
&= \int_V U(\mathbf{r}) e^{-i\mathbf{k}\cdot\mathbf{r}} d^3\mathbf{r} = \\
&= \int_{-L/2}^{L/2} e^{-ik_z z} dz \left[\int_{-\infty}^{\infty} e^{-\left(\frac{2}{w^2}x^2 + ik_x x\right)} dx \right] \left[\int_{-\infty}^{\infty} e^{-\left(\frac{2}{w^2}y^2 + ik_y y\right)} dy \right] = \\
&= \frac{2}{k_z} \sin\left(\frac{k_z L}{2}\right) \left[\sqrt{\frac{\pi}{2}} w e^{-\frac{k_x^2 w^2}{8}} \right] \left[\sqrt{\frac{\pi}{2}} w e^{-\frac{k_y^2 w^2}{8}} \right], \quad (49)
\end{aligned}$$

allowing us to define the transverse wavenumber resolutions $\Delta k_{x,y} = 2/w$ (e^{-1} value [76]) and a longitudinal wavenumber resolution $\Delta k_z = 2\pi/L$ (sine term zero) [148]. We further obtain an expression for the main (and LO) beam power

$$\begin{aligned}
P_0 &= \sqrt{\frac{\varepsilon_0}{\mu_0}} \int_{-\infty}^{\infty} |\mathcal{E}_0^2| e^{-\frac{4(x^2+y^2)}{w^2}} dx dy = \\
&= \frac{\pi w^2}{4} \sqrt{\frac{\varepsilon_0}{\mu_0}} |\mathcal{E}_0^2|, \quad (50)
\end{aligned}$$

$$I_n = \frac{e^2 \eta P_{\text{LO}}}{\hbar \omega_0} \text{ and } P_{\text{LO}} = \frac{\pi w^2}{4} \sqrt{\frac{\varepsilon_0}{\mu_0}} |\mathcal{E}_{\text{LO}}^2|.$$

Using equation 47 for this example we get

$$\begin{aligned}
\langle \delta n^2 \rangle_k &= \frac{1}{(2\pi)^3} \left(\frac{\hbar \omega_0}{e \eta} \right)^2 \frac{1}{\lambda_0^2 r_e^2 L^2} \frac{1}{P_0 P_{\text{LO}}} \int_{-\infty}^{\infty} \frac{d\omega}{2\pi} I_k(\omega) = \\
&= \frac{1}{(2\pi)^3} \frac{\hbar \omega_0}{\eta} \frac{1}{\lambda_0^2 r_e^2 L^2} \frac{1}{P_0} \int_{-\infty}^{\infty} \frac{d\omega}{2\pi} \frac{I_k(\omega)}{I_n} \quad (51)
\end{aligned}$$

This example concludes our chapter on the theory of collective light scattering. In section 2.4 we derived the analytical expression for the photocurrent, enabling us to interpret the signal as a spatial Fourier transform of density multiplied by the beam profile. In the present section this result was used to deduce an equation for δn^2 (equation 47).

3 Spatial resolution

In this chapter we first investigate the geometry of the measurement volume (section 3.1). Thereafter we explore the possibilities of obtaining localised measurements; first using a simple method directly limiting the volume length (section 3.2) and then by assuming that the density fluctuations have certain properties (section 3.3).

3.1 The measurement volume

3.1.1 Geometrical estimate

A measurement volume is created by interference between the incoming main (M) beam (wave vector \mathbf{k}_0) and the local oscillator (LO) beam (wave vector \mathbf{k}_s), see figure 3.

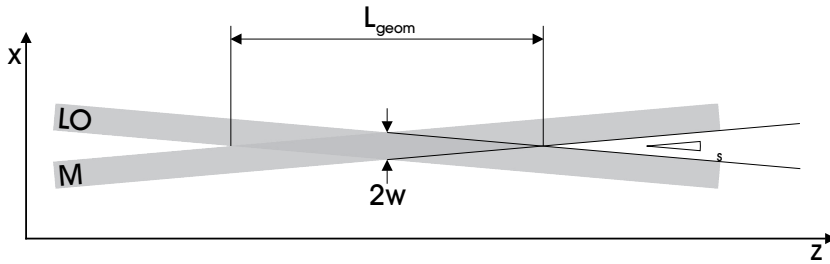


Figure 3. Scattering geometry. The main (M) and local oscillator (LO) beams cross at an angle thereby creating an interference pattern.

The angle between the LO and M beams is called the scattering angle θ_s . The distance between the interference fringes [66] is

$$\lambda_{\text{geom}} = \frac{\lambda_0}{2 \sin\left(\frac{\theta_s}{2}\right)} \approx \frac{\lambda_0}{\theta_s} \quad (52)$$

The scattering angle determines the measured wavenumber

$$\begin{aligned} k &= 2k_0 \sin\left(\frac{\theta_s}{2}\right) \approx k_0 \theta_s \\ \lambda &= \frac{2\pi}{k} \\ k &\ll k_0 \end{aligned} \quad (53)$$

The approximations above are valid for small scattering angles. Assuming that the beams have identical diameters $2w$, the volume length can be estimated as

$$L_{\text{geom}} = \frac{2w}{\tan\left(\frac{\theta_s}{2}\right)} \approx \frac{4w}{\theta_s} \quad (54)$$

The fringe number, i.e. the number of wavelengths that can be fitted into the measurement volume, is

$$N = \frac{2w}{\lambda} = \frac{wk}{\pi} \quad (55)$$

3.1.2 Exact result

The time-independent field from each of the two Gaussian beams creating a measurement volume can be written

$$u(\mathbf{r}) = u(x, y, z) = \sqrt{\frac{2P}{\pi w^2(z)}} e^{-\frac{x^2+y^2}{w^2(z)} + ik_0 z \left(1 + \frac{x^2+y^2}{2(z_R^2+z^2)}\right) + i\phi(z)} \quad (56)$$

Here, P is the beam power,

$$w(z) = w_0 \sqrt{1 + \left(\frac{z}{z_R}\right)^2} \quad (57)$$

is the beam radius at z and z_R is the Rayleigh range

$$z_R = \frac{\pi w_0^2}{\lambda_0}, \quad (58)$$

which is the distance from the waist w_0 to where the beam radius has grown by a factor $\sqrt{2}$. Note that we have introduced the beam waist w_0 and the Rayleigh range explicitly for the following calculations. The phase is given by

$$\phi(z) = \arctan\left(\frac{z}{z_R}\right) \quad (59)$$

We use the complete Gaussian description here instead of the simple form used in chapter 2.

An excellent treatment of the measurement volume has been given in [66]; therefore we will here restrict ourselves to simply quoting the important results and approximations in the remainder of this section.

Intensity We now want to find an expression for the interference power in the measurement volume. Since the full angle between the LO and M beams is θ_s , we will construct two new coordinate systems, rotated $\pm \theta_s/2$ around the y -axis. We define the constants

$$\begin{aligned} c &= \cos\left(\frac{\theta_s}{2}\right) \\ s &= \sin\left(\frac{\theta_s}{2}\right) \end{aligned} \quad (60)$$

and use them to construct the two transformations from the original system:

$$\begin{aligned} x_0 &= cx - sz \\ y_0 &= y \\ z_0 &= sx + cz \end{aligned} \quad (61)$$

and

$$\begin{aligned} x_{\text{LO}} &= cx + sz \\ y_{\text{LO}} &= y \\ z_{\text{LO}} &= -sx + cz \end{aligned} \quad (62)$$

This enables us to use expression 56 for each beam in the rotated systems. The intensity distribution in rotated coordinates can be written

$$|u_0 u_{\text{LO}}^*| = \frac{2\sqrt{P_0 P_{\text{LO}}}}{\pi w(z_0) w(z_{\text{LO}})} e^{-\frac{w^2(z_{\text{LO}})[x_0^2 + y_0^2] + w^2(z_0)[x_{\text{LO}}^2 + y_{\text{LO}}^2]}{w^2(z_0)w^2(z_{\text{LO}})}} \quad (63)$$

The intensity distribution in the original coordinate system can now be found by inserting the transformations 61 and 62 into equation 63. A few approximations lead to the following expression:

$$|u_0 u_{\text{LO}}^*| = \frac{2\sqrt{P_0 P_{\text{LO}}}}{\pi w_0^2} \left(1 + \frac{c^2 z^2}{z_R^2}\right)^{-1} \times e^{-\frac{2(1+c^2 z^2/z_R^2)(c^2 x^2 + y^2 + s^2 z^2) + 8(csxz/z_R)^2}{w_0^2(1+c^2 z^2/z_R^2)^2}} \quad (64)$$

Here, the terms including z_R are due to beam divergence effects. Equation 64 can be integrated over the (x, y) -plane to obtain the variation of the interference power as a function of z :

$$P(z) = \int \int dx dy |u_0 u_{\text{LO}}^*| = \frac{\sqrt{P_0 P_{\text{LO}}}}{c} \left(\frac{1 + c^2 z^2/z_R^2}{1 + (1 + 3s^2)z^2/z_R^2}\right)^{1/2} e^{-\frac{2s^2 z^2}{w_0^2(1+c^2 z^2/z_R^2)}} \quad (65)$$

For small scattering angles,

$$\begin{aligned} c &\approx 1 \\ s &\approx \frac{\theta_s}{2}, \end{aligned} \quad (66)$$

meaning that the z -dependent pre-factor in equation 65 is close to unity for $z \leq z_R$. Therefore the behaviour of $P(z)$ can be gauged from the exponential function. We define the position z_a where the power has fallen to a times its maximum value:

$$P(z_a) = aP(0) \quad (67)$$

The z_a -position is now inserted into the exponential function of equation 65

$$\begin{aligned} a &= e^{-\frac{2s^2 z_a^2}{w_0^2(1+c^2 z_a^2/z_R^2)}} \\ z_a &= \pm \sqrt{\frac{\ln(1/a)}{2}} \frac{w_0}{s} \left(1 + \frac{\ln a}{2} \left(\frac{cw_0}{sz_R}\right)^2\right)^{-1/2} \end{aligned} \quad (68)$$

The measurement volume length can now be defined as

$$\begin{aligned} L_{\text{exact}} &= 2|z_{e^{-2}}| = \frac{2w_0}{s} \left(1 - \left(\frac{cw_0}{sz_R}\right)^2\right)^{-1/2} \approx \frac{4w_0}{\theta_s} \left(1 - \left(\frac{4}{\pi N}\right)^2\right)^{-1/2} \end{aligned} \quad (69)$$

The correction from the geometrical estimate 54 can be estimated by assuming that $N \geq 2$; this means that the correction factor

$$\left(\frac{4}{\pi N}\right)^2 \leq \frac{4}{\pi^2} \quad (70)$$

The increase of the measurement volume length from the geometrical estimate is due to the divergence of the Gaussian beams.

As a final point, we can compare the beam divergence angle θ_d to the scattering angle θ_s :

$$\theta_d = \frac{\lambda_0}{\pi w_0} = \frac{w_0}{z_R} = \frac{2\theta_s}{\pi N} \quad (71)$$

A large N means that $\theta_d \ll \theta_s$, so that the beams will separate as one moves away from $z = 0$.

Phase The phase of the interference in rotated coordinates is given by

$$e^{\left[ik_0 \left(z_0 - z_{LO} + \frac{z_0 [x_0^2 + y_0^2]}{2[z_R^2 + z_0^2]} - \frac{z_{LO} [x_{LO}^2 + y_{LO}^2]}{2[z_R^2 + z_{LO}^2]} \right) + i(\phi(z_0) - \phi(z_{LO})) \right]} \quad (72)$$

Neglecting the $(\phi(z_0) - \phi(z_{LO}))$ -term and inserting the original coordinates, the fringe distance is

$$\lambda_{\text{exact}} = \frac{\lambda_0}{2s[1 + \delta(z)]} \approx \frac{\lambda_0}{\theta_s[1 + \delta(z)]}$$

$$\delta(z) = \frac{(1 - 3c^2)z_R^2 z^2 - (1 + c^2)c^2 z^4}{2(z_R^2 + c^2 z^2)^2} \approx -\frac{z^2}{z_R^2 + z^2} \quad (73)$$

The exact expression for the fringe distance has a correction term $\delta(z)$ compared to the geometrical estimate in equation 52. For example, if $z = z_R/2$, δ is equal to -0.2, meaning a 25% increase of the fringe distance. But of course the power in the interference pattern $P(z)$ decreases rapidly as well.

3.2 Direct localisation

From equation 54 we immediately see that spatial localisation along the measurement volume can be achieved by having a large scattering angle (large k). We will call this method direct localisation, since the measurement volume is small in the z direction.

To localise along the beams, the measurement volume length L_{geom} must be much smaller than the plasma diameter $2a$, where a is the minor radius of the plasma.

Assuming that $a = 0.3$ m, $w = 0.01$ m and that we want L_{geom} to be 0.2 m, the scattering angle θ_s is 11° (or 199 mrad). This corresponds to a wavenumber k of 1180 cm^{-1} .

However, measurements show that the scattered power decreases very fast with increasing wavenumber, either as a power-law or even exponentially (see chapter 8). This means that with our detection system, we have investigated a wavenumber range of $[14,62] \text{ cm}^{-1}$. For this interval, the measurement volume is much longer than the plasma diameter, meaning that the measurements are integrals over the entire plasma cross section.

3.3 Indirect localisation

We stated above that the measured fluctuations are line integrated along the entire plasma column because the scattering angle is quite small (of order 0.3° or 5 mrad). However, the possibility to obtain localised measurements still exists, albeit indirect localisation. For this method to work, we use the fact that the density fluctuation wavenumber κ is anisotropic in the directions parallel and perpendicular to the local magnetic field in the plasma. This method was experimentally demonstrated in the Tore Supra tokamak [148].

We owe a great deal to the work presented in [106] and [42] regarding the derivations presented in this section.

The section is organised as follows: In subsection 3.3.1 we introduce the dual volume geometry and the definition of the magnetic pitch angle. Thereafter we derive an analytical expression for the crosspower between the volumes and finally describe issues concerning the correlation between spatially separated measurement volumes. In subsection 3.3.2 we describe the single volume geometry and present a simplified formula for the autopower. A few assumptions are introduced, allowing us to simulate the expression for the autopower. In subsection 3.3.3 we compare the dual and single volume localisation criteria found in the two initial subsections.

3.3.1 Dual volume

Dual volume geometry The geometry belonging to the dual volume setup is shown in figure 4. The left-hand plot shows a simplified version of the optical setup and the right-hand plot shows the two volumes as seen from above. The size of the vector \mathbf{d} connecting the two volumes is constant for a given setup, whereas the angle $\theta_R = \arcsin(d_R/d)$ can be varied. The length d_R is the distance between the volumes along the major radius R . The wave vectors selected by the diagnostic (\mathbf{k}_1 and \mathbf{k}_2) and their angles with respect to R (α_1 and α_2) have indices corresponding to the volume number, but are identical for our diagnostic.

The magnetic pitch angle The main component of the magnetic field is the toroidal magnetic field, B_φ . The small size of the magnetic field along R , B_R , implies that a magnetic field line is not completely in the toroidal direction, but also has a poloidal part. The resulting angle is called the pitch angle θ_p , see figure 5.

The pitch angle is defined to be

$$\theta_p^{\text{def}} = \arctan\left(\frac{B_\theta}{B_\varphi}\right), \quad (74)$$

which for fixed z (as in figure 5) becomes

$$\theta_p = \arctan\left(\frac{B_R}{B_\varphi}\right) \quad (75)$$

As one moves along a measurement volume from the bottom to the top of the plasma (thereby changing z), the ratio B_R/B_φ changes, resulting in a variation of the pitch angle θ_p . The central point now is that we assume that the fluctuation wavenumber parallel to the magnetic field line (κ_{\parallel}) is much smaller than the wavenumber perpendicular to the field line (κ_{\perp}):

$$\kappa_{\parallel} \ll \kappa_{\perp} \quad (76)$$

This case is illustrated in figure 5, where only the κ_{\perp} part of the fluctuation wave vector $\boldsymbol{\kappa}$ is shown. It is clear that when θ_p changes, the direction of κ_{\perp} will vary as well.

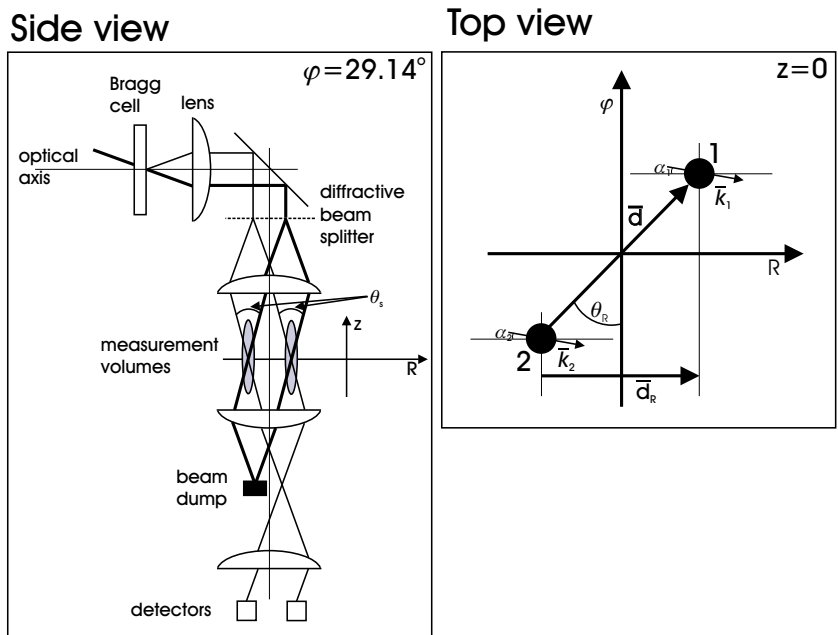


Figure 4. Left: Schematic representation of the dual volume setup (side view). Thick lines are the M beams, thin lines the LO beams, right: The dual volume setup seen from above. The black dots are the measurement volumes.

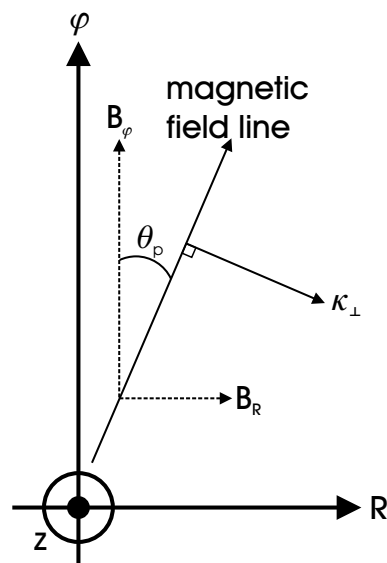


Figure 5. Geometry of a magnetic field line for fixed z .

Localised crosspower Below we will derive an expression for the scattered crosspower between two measurement volumes (equation 95). We will ignore constant factors and thus only do proportionality calculations to arrive at the integral. This equation will prove to be crucial for the understanding of the observed signal and the limits imposed on localisation by the optical setup.

The wave vectors used for the derivation are shown in figure 6. The size and direction of the wave vectors \mathbf{k}_1 and \mathbf{k}_2 are allowed to differ. The positions of the measurement volumes are \mathbf{r} (volume 1) and \mathbf{r}' (volume 2). We assume that d is

zero (see figure 4); effects associated with a spatial separation of the volumes are discussed after the derivation.

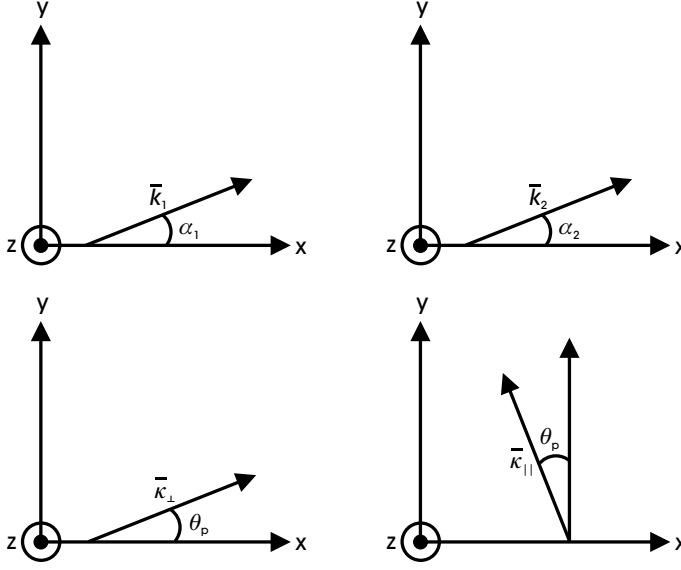


Figure 6. Wave vectors in rectangular coordinates. Top left: $\mathbf{k}_1 = (k_1 \cos \alpha_1, k_1 \sin \alpha_1, 0)$, top right: $\mathbf{k}_2 = (k_2 \cos \alpha_2, k_2 \sin \alpha_2, 0)$, bottom: $\boldsymbol{\kappa} = (\kappa_{\perp} \cos \theta_p - \kappa_{\parallel} \sin \theta_p, \kappa_{\perp} \sin \theta_p + \kappa_{\parallel} \cos \theta_p, \kappa_{\perp z})$.

We introduce a few additional definitions that will prove to be useful; the difference between the two measured wave vectors \mathbf{k}_d , the vector \mathbf{R} and the difference in volume position $\boldsymbol{\rho}$:

$$\begin{aligned} \mathbf{k}_d &= \mathbf{k}_1 - \mathbf{k}_2 = (k_d \cos \beta, k_d \sin \beta, 0) \\ \mathbf{R} &= \mathbf{r} = (X, Y, Z) \\ \boldsymbol{\rho} &= \mathbf{r} - \mathbf{r}' = (x, y, z) \end{aligned} \quad (77)$$

Our starting point is the current spectral density (equation 39)

$$I_{12}(\mathbf{k}_1, \mathbf{k}_2, \omega) \propto \int d\mathbf{r} \int d\mathbf{r}' \langle n(\mathbf{r}, \omega) n^*(\mathbf{r}', \omega) \rangle U_1(\mathbf{r}) U_2^*(\mathbf{r}') e^{i\mathbf{k}_1 \cdot \mathbf{r}} e^{-i\mathbf{k}_2 \cdot \mathbf{r}'}, \quad (78)$$

where $\langle \cdot \rangle$ is a temporal average. Since

$$\mathbf{k}_1 \cdot \mathbf{r} - \mathbf{k}_2 \cdot \mathbf{r}' = \mathbf{k}_d \cdot \mathbf{R} + \mathbf{k}_2 \cdot \boldsymbol{\rho} \quad (79)$$

we can rewrite equation 78 using the substitution $\boldsymbol{\rho} = \mathbf{r} - \mathbf{r}'$ to become:

$$I_{12}(\mathbf{k}_1, \mathbf{k}_2, \omega) \propto \int d\mathbf{R} \int d\boldsymbol{\rho} \langle n(\mathbf{R}, \omega) n^*(\mathbf{R} - \boldsymbol{\rho}, \omega) \rangle U_1(\mathbf{R}) U_2^*(\mathbf{R} - \boldsymbol{\rho}) e^{i\mathbf{k}_d \cdot \mathbf{R}} e^{i\mathbf{k}_2 \cdot \boldsymbol{\rho}} \quad (80)$$

We define the local spectral density of the density fluctuations to be

$$S(\mathbf{k}_2, \mathbf{R}, \omega) = \int d\boldsymbol{\rho} \langle n(\mathbf{R}, \omega) n^*(\mathbf{R} - \boldsymbol{\rho}, \omega) \rangle e^{i\mathbf{k}_2 \cdot \boldsymbol{\rho}}, \quad (81)$$

where the inverse Fourier transform yields

$$\langle n(\mathbf{R}, \omega) n^*(\mathbf{R} - \boldsymbol{\rho}, \omega) \rangle \propto \int d\boldsymbol{\kappa} e^{-i\boldsymbol{\kappa} \cdot \boldsymbol{\rho}} S(\boldsymbol{\kappa}, \mathbf{R}, \omega) \quad (82)$$

This allows us to simplify equation 80

$$I_{12}(\mathbf{k}_1, \mathbf{k}_2, \omega) \propto \int d\mathbf{R} \int d\boldsymbol{\rho} \int d\boldsymbol{\kappa} S(\boldsymbol{\kappa}, \mathbf{R}, \omega) U(\mathbf{R}) U(\mathbf{R} - \boldsymbol{\rho}) e^{i(\mathbf{k}_2 - \boldsymbol{\kappa}) \cdot \boldsymbol{\rho}} e^{i\mathbf{k}_1 \cdot \mathbf{R}}, \quad (83)$$

where we have assumed that the two beam profiles U_1 and U_2^* are identical and equal to U . Further, we assume that they have the functional form that was used in chapter 2, so that

$$U(\mathbf{R}) U(\mathbf{R} - \boldsymbol{\rho}) = e^{-\frac{2}{w^2}(2X^2 + 2Y^2 + x^2 + y^2 - 2xX - 2yY)} \quad (84)$$

We note that

$$\mathbf{k}_d \cdot \mathbf{R} = X k_d \cos \beta + Y k_d \sin \beta \quad (85)$$

and we assume that the local spectral density only varies along (and not across) the measurement volumes:

$$S(\boldsymbol{\kappa}, \mathbf{R}, \omega) = S(\boldsymbol{\kappa}, Z, \omega) \quad (86)$$

Inserting equations 84 - 86 into equation 83 we arrive at

$$\begin{aligned} I_{12}(\mathbf{k}_1, \mathbf{k}_2, \omega) &\propto \int dZ \int d\boldsymbol{\kappa} S(\boldsymbol{\kappa}, Z, \omega) \int dx dy dz e^{i(\mathbf{k}_2 - \boldsymbol{\kappa}) \cdot \boldsymbol{\rho}} \\ &\int dXdYe^{-\frac{2}{w^2}(2X^2 + 2Y^2 + x^2 + y^2 - 2xX - 2yY)} e^{i(Xk_d \cos \beta + Yk_d \sin \beta)} \propto \\ &\int dZ \int d\boldsymbol{\kappa} S(\boldsymbol{\kappa}, Z, \omega) \int dx dy dz e^{i(\mathbf{k}_2 - \boldsymbol{\kappa}) \cdot \boldsymbol{\rho}} \\ &e^{-\frac{x^2}{w^2} + \frac{ik_d x \cos \beta}{2}} e^{-\frac{y^2}{w^2} + \frac{ik_d y \sin \beta}{2}} e^{-\frac{k_d^2 w^2}{16}}, \end{aligned} \quad (87)$$

where we have used that

$$\begin{aligned} \int_{-\infty}^{\infty} e^{-(ax^2 + bx + c)} dx &= \sqrt{\frac{\pi}{a}} e^{(b^2 - 4ac)/4a} \\ \int dXe^{-\left(\frac{4}{w^2}X^2 + \left(-\frac{4}{w^2}x - ik_d \cos \beta\right)X + \frac{2}{w^2}x^2\right)} &= \sqrt{\pi} \frac{w}{2} e^{-\frac{x^2}{w^2} + \frac{ik_d x \cos \beta}{2} - \frac{k_d^2 w^2 \cos^2 \beta}{16}} \\ \int dYe^{-\left(\frac{4}{w^2}Y^2 + \left(-\frac{4}{w^2}y - ik_d \sin \beta\right)Y + \frac{2}{w^2}y^2\right)} &= \sqrt{\pi} \frac{w}{2} e^{-\frac{y^2}{w^2} + \frac{ik_d y \sin \beta}{2} - \frac{k_d^2 w^2 \sin^2 \beta}{16}} \end{aligned} \quad (88)$$

From geometrical considerations (see figure 6) we find that

$$\begin{aligned} i(\mathbf{k}_2 - \boldsymbol{\kappa}) \cdot \boldsymbol{\rho} &= i(k_2 \cos \alpha_2 - (\kappa_{\perp} \cos \theta_p - \kappa_{\parallel} \sin \theta_p))x \\ &+ i(k_2 \sin \alpha_2 - (\kappa_{\perp} \sin \theta_p + \kappa_{\parallel} \cos \theta_p))y \\ &- i\kappa_{\perp z} z \end{aligned} \quad (89)$$

Since the measurement volume length L is much longer than the plasma minor radius a we find that

$$\int_{-L/2}^{L/2} dz e^{-i\kappa_{\perp z} z} \approx \delta(\kappa_{\perp z}) \quad (90)$$

Inserting equations 89 and 90 into equation 87 and performing the integrations over x , y and z we arrive at

$$\begin{aligned} I_{12}(\mathbf{k}_1, \mathbf{k}_2, \omega) &\propto \int dZ \int d\boldsymbol{\kappa} S(\boldsymbol{\kappa}, Z, \omega) e^{-\frac{k_d^2 w^2}{16}} e^{-\frac{w^2}{4}(c_1^2 + c_2^2)} \\ c_1 &= \frac{k_d}{2} \cos \beta + k_2 \cos \alpha_2 - \kappa_{\perp} \cos \theta_p + \kappa_{\parallel} \sin \theta_p \\ c_2 &= \frac{k_d}{2} \sin \beta + k_2 \sin \alpha_2 - \kappa_{\perp} \sin \theta_p - \kappa_{\parallel} \cos \theta_p, \end{aligned} \quad (91)$$

where we have used that

$$\begin{aligned} \int_{-\infty}^{\infty} e^{-(ax^2 + bx)} dx &= \sqrt{\frac{\pi}{a}} e^{(b^2)/4a} \\ \int_{-\infty}^{\infty} e^{-\left(\frac{1}{w^2}x^2 - ic_1 x\right)} dx &= \sqrt{\pi} w e^{-\frac{c_1^2 w^2}{4}} \\ \int_{-\infty}^{\infty} e^{-\left(\frac{1}{w^2}y^2 - ic_2 y\right)} dy &= \sqrt{\pi} w e^{-\frac{c_2^2 w^2}{4}} \end{aligned} \quad (92)$$

To perform the integration over $\boldsymbol{\kappa}$ we assume that $\kappa_{\parallel} \ll \kappa_{\perp}$:

$$\begin{aligned} S(\boldsymbol{\kappa}, Z, \omega) &= S(\boldsymbol{\kappa}_{\perp}, Z, \omega) \delta(\kappa_{\parallel}) \\ d\boldsymbol{\kappa} &= d\boldsymbol{\kappa}_{\perp} d\kappa_{\parallel}, \end{aligned} \quad (93)$$

so that

$$\begin{aligned} I_{12}(\mathbf{k}_1, \mathbf{k}_2, \omega) &\propto \int dZ S(\mathbf{k}_1, \mathbf{k}_2, Z, \omega) e^{-\frac{k_d^2 w^2}{16}} e^{-\frac{w^2}{4}(c_1^2 + c_2^2)} \\ c_1 &= \frac{k_d}{2} \cos \beta + k_2 (\cos \alpha_2 - \cos \theta_p) \\ c_2 &= \frac{k_d}{2} \sin \beta + k_2 (\sin \alpha_2 - \sin \theta_p) \\ c_1^2 + c_2^2 &= \frac{k_d^2}{4} + 2k_2^2 (1 - \cos(\alpha_2 - \theta_p)) \\ &\quad + k_2 k_d [\cos(\beta - \alpha_2) - \cos(\beta - \theta_p)] \end{aligned} \quad (94)$$

We can reorganise the above equation to

$$\begin{aligned} I_{12}(\mathbf{k}_1, \mathbf{k}_2, \omega) &\propto \int dZ S(\mathbf{k}_1, \mathbf{k}_2, Z, \omega) \\ &\quad e^{-\frac{w^2 k_2^2}{2} (1 - \cos(\alpha_2 - \theta_p))} e^{-\frac{w^2}{4} \left(\frac{k_d^2}{2} + k_2 k_d [\cos(\beta - \alpha_2) - \cos(\beta - \theta_p)] \right)} \end{aligned} \quad (95)$$

The following relations exist

$$\begin{aligned} k_d &= \sqrt{k_1^2 + k_2^2 - 2k_1 k_2 \cos(\alpha_2 - \alpha_1)} \\ \beta &= \arccos \left(\frac{k_1 \cos \alpha_1 - k_2 \cos \alpha_2}{k_d} \right), \end{aligned} \quad (96)$$

meaning that equation 95 is fully determined by \mathbf{k}_1 , \mathbf{k}_2 and ω .

Spatially separated measurement volumes Equation 76 means that turbulence in real space consists of elongated structures extended along the magnetic field lines. Since κ_{\perp} is large, the structure size perpendicular to the magnetic field (i.e. cross-field) is modest. This in turn indicates that the cross-field correlation length \mathcal{L}_{\perp} is small, experimentally found to be typically of order 1 cm [172]. The angle θ_R of the vector connecting the two measurement volumes is fixed, whereas θ_p varies with z . Letting \mathbf{d} and \mathbf{B} coincide at one volume, the difference between the two angles leads to the volumes being either connected or unconnected at the other volume, see figure 7. An approximate threshold criterion for the fluctuations in the volumes being correlated is

$$\sin(|\theta_R - \theta_p(z)|) = \frac{w + \mathcal{L}_{\perp}/2}{d}, \quad (97)$$

or

$$\theta_{\perp}(z) = |\theta_R - \theta_p(z)| \approx \frac{w + \mathcal{L}_{\perp}/2}{d} \quad (98)$$

for small angles. This last formula allows us to distinguish between three cases:

1. $\theta_{\perp}(z) < \frac{w + \mathcal{L}_{\perp}/2}{d}$ for all z : The fluctuations in the volumes are correlated along the entire path.
2. $\frac{w + \mathcal{L}_{\perp}/2}{d} < \theta_{\perp}(z)$ for some z and $\theta_{\perp}(z) < \frac{w + \mathcal{L}_{\perp}/2}{d}$ for other z : The fluctuations are correlated for a section of the path.
3. $\theta_{\perp}(z) > \frac{w + \mathcal{L}_{\perp}/2}{d}$ for all z : The fluctuations in the volumes are uncorrelated along the entire path.

For experimental settings where case 2 is true, some localisation can be obtained by calculating the crosspower spectrum between the volumes. In chapter 8 we demonstrate this technique for a situation where $w = 4$ mm and $d = 29$ mm. This along with $\mathcal{L}_{\perp} = 1$ cm means that $\frac{w + \mathcal{L}_{\perp}/2}{d} \times \frac{180}{\pi} = 18^{\circ}$.

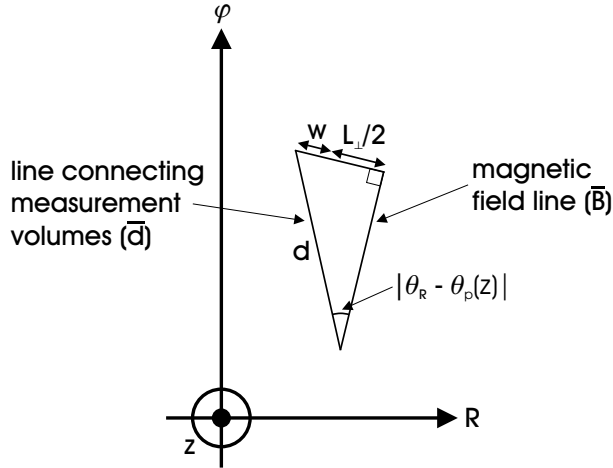


Figure 7. Geometry concerning dual volume localisation. Assuming that one of the measurement volumes is situated at the nadir of the triangle, \mathbf{d} and \mathbf{B} will diverge towards the second measurement volume. The threshold condition is shown (equation 97), where the two volumes are borderline connected.

The final issue is how to incorporate the measurement volume separation into the local spectral density $S(\mathbf{k}_1, \mathbf{k}_2, Z, \omega)$ from equation 95. Assuming that we work

with frequency integrated measurements we can drop ω ; further, we assume that S is independent of the wave vector. The remaining dependency is that of Z , the vertical coordinate along the measurement volumes. For the single volume case below, S is simply assumed to be proportional to δn^2 , see equation 105. In the present case, however, we need to treat the correlation between the volumes. A plausible expression for the correlation function is

$$C_{\perp}(z) = \exp \left[- \left(\frac{|\theta_R - \theta_p(z)|d}{w + \mathcal{L}_{\perp}/2} \right)^2 \right], \quad (99)$$

which is a Gaussian-type function. All quantities are known and independent of z except $\theta_p(z)$; but we would like to note that \mathcal{L}_{\perp} could depend on z . The correlation function $C_{\perp}(z)$ possesses the correct limits:

- $C_{\perp}(z) = 1$ for $|\theta_R - \theta_p(z)| = 0$
- $C_{\perp}(z) = 1$ for $d = 0$
- $\lim_{w \rightarrow \infty} C_{\perp}(z) = 1$
- $\lim_{\mathcal{L}_{\perp} \rightarrow \infty} C_{\perp}(z) = 1$

For actual calculations we would replace S by $C_{\perp}(z) \times \delta n^2$ in equation 95 and use equation 107 for the density fluctuation profile. For the single volume simulations below we do not need to include $C_{\perp}(z)$.

One could argue that the pitch angle θ_p in the two spatially separated measurement volumes is different, so that the exponential functions in equation 95 would have to be modified. However, the actual distance between the volumes is small and therefore the pitch angles are almost identical.

3.3.2 Single volume

Single volume geometry Figure 8 shows the geometry associated with the single volume setup. The definitions are completely analogous to the ones in figure 4.

Localised autopower The current spectral density (or autopower) for a single volume can be found from equation 95 by assuming that $k_d = 0$ and that we only have a single wave vector \mathbf{k} :

$$I_{11}(\mathbf{k}, \omega) \propto \int dZ S(\mathbf{k}, Z, \omega) e^{-\frac{w^2 k^2}{2}(1 - \cos(\alpha - \theta_p))} \quad (100)$$

Assuming that the angles α and θ_p are small, we can expand the function in the exponent of equation 100 as

$$2k^2[1 - \cos(\alpha - \theta_p)] \approx 2k^2[(\alpha - \theta_p)^2]/2 = k^2(\alpha - \theta_p)^2 \quad (101)$$

We introduce the instrumental selectivity function

$$\chi = e^{-\left(\frac{\alpha - \theta_p}{\Delta\alpha}\right)^2}, \quad (102)$$

where $\Delta\alpha = \frac{\Delta k}{k} = \frac{2}{kw}$ is the transverse relative wavenumber resolution. Using this instrumental function, the scattered power can be written

$$I_{11}(\mathbf{k}, \omega) \propto \int dZ S(\mathbf{k}, Z, \omega) e^{-\left(\frac{\alpha - \theta_p}{\Delta\alpha}\right)^2} = \int dZ S(\mathbf{k}, Z, \omega) \chi \quad (103)$$

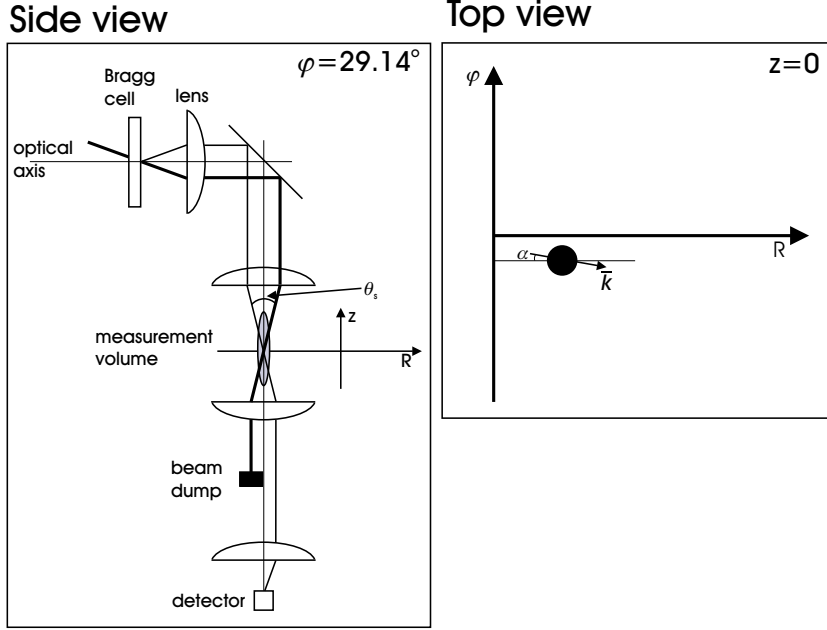


Figure 8. Left: Schematic representation of the single volume setup (side view). Thick lines are the M beam, thin lines the LO beam, right: The single volume setup seen from above. The black dot is the measurement volume.

We will use this simplified equation to study how spatial resolution can be obtained indirectly. To make simulations for this purpose we need to assume a pitch angle profile and an expression for the frequency integrated local spectral density $S(\mathbf{k}, Z)$.

Modelled magnetic pitch angle For our simulations we will take the pitch angle to be described by

$$\theta_p(r) = \arctan\left(\frac{B_\theta}{B_\varphi}\right) = \frac{r}{q_a R_0} (2 - 2\rho^2 + \rho^4) (2 - \rho^2), \quad (104)$$

an analytical profile constructed by J.H.Misguich [42], see figure 9. Here, $\rho = r/a$ is the normalised minor radius coordinate, $q_a = 1/t_a$ is the magnetic field winding number at $r = a$ (see chapter 6) and R_0 is the major radius of the plasma. The total pitch angle variation $\Delta\theta_{p,\text{tot}}$ is seen to be about 15° .

Fluctuation profiles The frequency integrated local spectral density is assumed to be independent of the selected wave vector:

$$S(\mathbf{k}, r) = S(r) = \delta n^2, \quad (105)$$

where we have replaced the beam coordinate Z by the radial coordinate r . The normalised density profile is assumed to be

$$\frac{n(r)}{n_0} = 0.1 + 0.9\sqrt{(1 - \rho^2)}, \quad (106)$$

see figure 10.

Further, the relative density fluctuation profile is assumed to have the following structure:

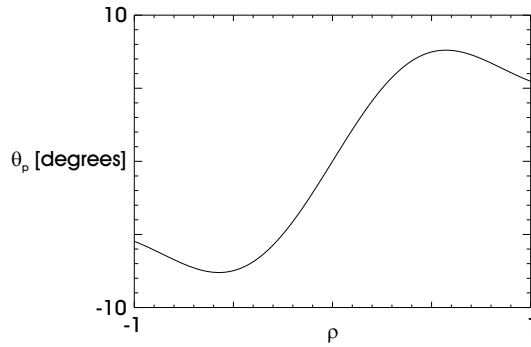


Figure 9. Modelled pitch angle in degrees versus ρ . We have used $q_a = 3.3$, $R_0 = 2.38$ m and $a = 0.75$ m (Tore Supra parameters, see [42]).

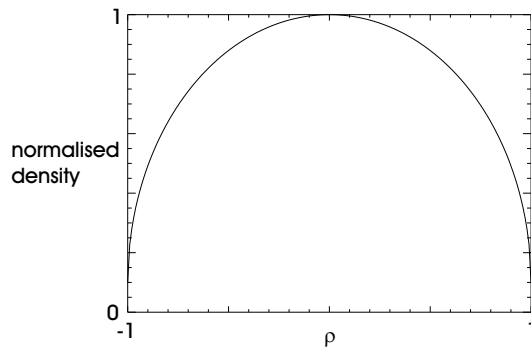


Figure 10. Modelled normalised density versus ρ .

$$\frac{\delta n(r)}{n(r)} = b + c|\rho|^p, \quad (107)$$

where b , c and p are fit parameters. At present we will assume the following fit parameters: $b = 0.01$, $c = 0.1$ and $p = 3$, see the left-hand plot of figure 11.

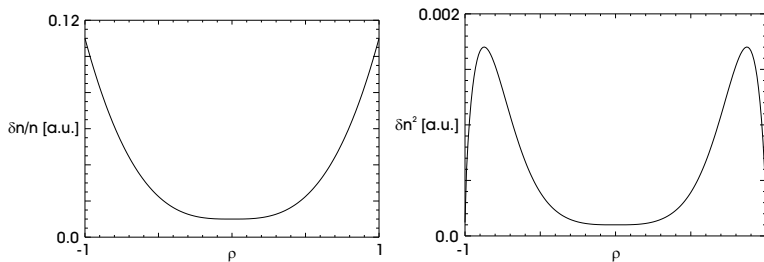


Figure 11. Left: $\delta n/n$ versus ρ , right: δn^2 versus ρ .

Simulations Above we have introduced spatially localised expressions for all external quantities entering equation 103. We set the wavenumber k to 15 cm^{-1} and the beam waist w to 2.7 cm. This means that the transverse relative wavenumber resolution $\Delta\alpha$ is equal to 2.8° . Figure 12 shows χ for $\alpha = 0^\circ$ (left) and 5° (right).

We observe that by changing the diagnostic angle α , χ changes position in the plasma.

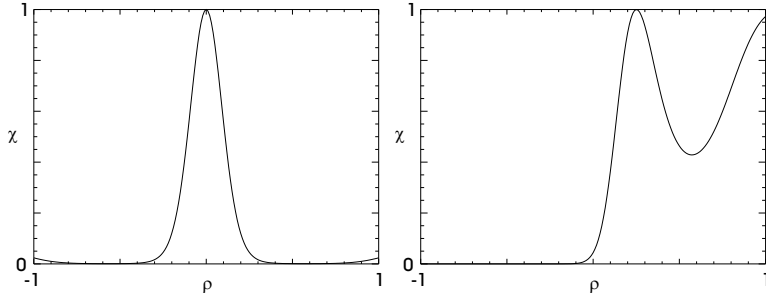


Figure 12. Left: χ versus ρ for $\alpha = 0^\circ$, right: χ versus ρ for $\alpha = 5^\circ$ ($k = 15 \text{ cm}^{-1}$, $w = 2.7 \text{ cm}$).

Figure 13 shows the integrand of equation 103 for the two cases shown in figure 12. We see that the 0° case corresponds to a signal originating in the central part of the plasma, while the 5° case detects edge fluctuations.

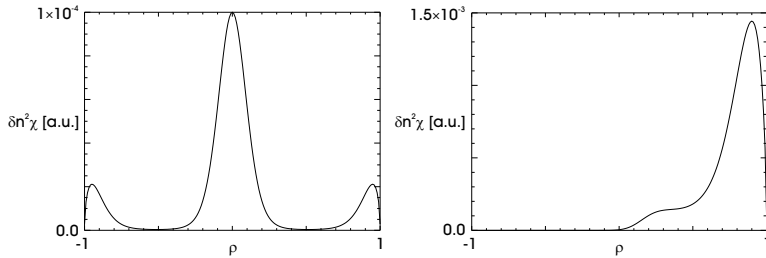


Figure 13. Left: Integrand for $\alpha = 0^\circ$, right: Integrand for $\alpha = 5^\circ$ ($k = 15 \text{ cm}^{-1}$, $w = 2.7 \text{ cm}$).

Figure 14 shows figures corresponding to figures 12 and 13, but now for a mini α -scan: $[-5^\circ, -2.5^\circ, 0^\circ, 2.5^\circ, 5^\circ]$.

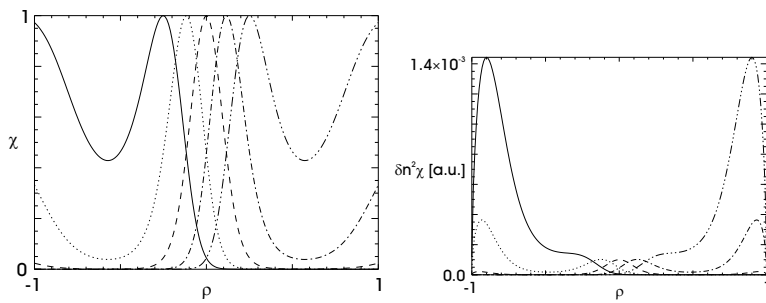


Figure 14. Left: χ for five α values, right: Corresponding integrands ($k = 15 \text{ cm}^{-1}$, $w = 2.7 \text{ cm}$).

Figure 15 shows the integrands in figure 14 integrated along ρ ($= I_{11}$).

Finally, figure 16 shows the effect of increasing the transverse relative wavenumber resolution $\Delta\alpha$ from 2.8° to 28.0° . The instrumental selectivity function (left) becomes extremely broad, leading to the total scattered power having no significant variation with α .

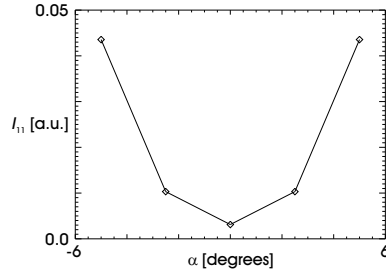


Figure 15. Total scattered power (I_{11}) versus α ($k = 15 \text{ cm}^{-1}$, $w = 2.7 \text{ cm}$).

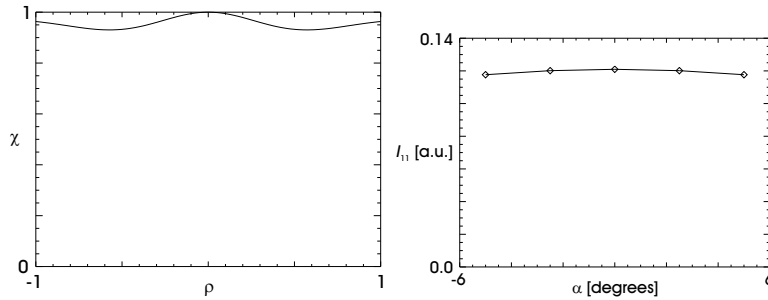


Figure 16. Left: χ for $\alpha = 0$ degrees versus ρ , right: Total scattered power (I_{11}) versus α ($k = 15 \text{ cm}^{-1}$, $w = 0.27 \text{ cm}$).

What we have demonstrated with the above simulations is that for localisation to be possible, the following has to be true:

$$\Delta\theta_{p,\text{tot}}[\text{degrees}] \gg \Delta\alpha[\text{degrees}] = \frac{2}{kw} \times \frac{180}{\pi} \quad (108)$$

3.3.3 Discussion

We end the chapter with a brief discussion on the dual and single volume localisation criteria. The single volume criterion has already been written in equation 108. To discuss the dual volume criterion in more detail, we introduce $\Delta\theta_{\perp,\text{tot}}$, which is the maximum absolute difference between θ_R and $\theta_p(z)$ assuming that they are equal at some z (case 2 in subsection 3.3.1). The dual volume localisation condition for this situation is

$$\Delta\theta_{p,\text{tot}}[\text{degrees}] \geq \Delta\theta_{\perp,\text{tot}}[\text{degrees}] \gg \frac{w + \mathcal{L}_{\perp}/2}{d} \times \frac{180}{\pi} \quad (109)$$

Alternatively, even if this criterion is not fulfilled (case 1), some localisation can be obtained using case 3: If θ_R is set so that it is outside the plasma (does not coincide with $\theta_p(z)$ for any z), measurements weighted towards the top and bottom of the plasma can be made.

4 Spectral analysis

In this chapter we will describe the main spectral quantities used for our examination in the thesis. The analysis procedure is very similar to the one we made in [132], and a large part of the programs has been written by S.Zoletnik.

In section 4.1 we describe the creation of simulated data and describe eight cases used in this chapter. We briefly summarise the necessary statistical definitions in section 4.2. In sections 4.3 and 4.4 we review the autopower and crosspower spectrum, respectively. We define and illustrate the autocorrelation and crosscorrelation function in sections 4.5 and 4.6, respectively. Finally, section 4.7 contains an analysis of simulated data including several distinguishable phenomena.

4.1 Event creation

Measured frequency and wavenumber spectra have no distinct peaks at certain frequencies or wavenumbers, see chapter 8. This fact indicates that the fluctuations are not composed of waves, but rather random 'bumps' in space and time. To assist in the interpretation of our spectral analysis, we therefore create simulated data using finite lifetime 'events'. An event is a finite length piece of complex signal S . The time evolution of the event amplitude A is Gaussian; the phase is either fixed or linearly proportional to $v_\phi t$ (note here that the phase velocity v_ϕ is defined to be in units s^{-1}). The total simulated signal can be written

$$\sum_{j=1}^{n_{ev}} S(t) = \sum_{j=1}^{n_{ev}} X(t) + iY(t) = \sum_{j=1}^{n_{ev}} A(t) \times e^{i(v_\phi t + \phi_0)} \quad (110)$$

The initial time point and phase (ϕ_0) of an event is random; the amplitude of events is fixed. Figure 17 shows an event versus time. We will analyse simulated signals having a length of $N = 2 \times 10^5$ time points. Since our diagnostic samples with a rate of 20 MHz (see chapter 7), this corresponds to 10 ms of data. We will superimpose $n_{ev} = 2 \times 10^3$ events onto this array, at random times and with a random initial phase. These events have a lifetime of $2 \mu s$, where the lifetime is defined to be four standard deviations of the Gaussian amplitude.

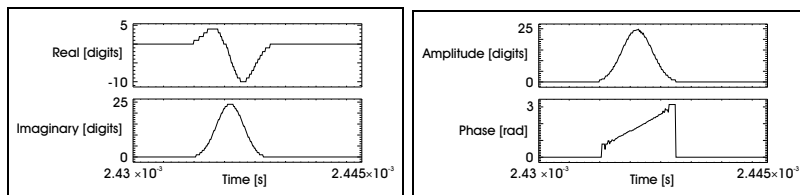


Figure 17. Left: Real and imaginary part of a simulated event versus time, right: Amplitude and phase of the same event. In this example, the event lifetime is $4 \mu s$, the amplitude is 25 and it has a phase velocity of $5 \times 10^5 s^{-1}$. The total length of the time window is $15 \mu s$.

The additional effect of more than one type of event is also simulated in the signals by generating events with different parameters in the same signal.

Furthermore, normally distributed white noise is added to the simulated signals. The relative amplitude of the average event signal and the noise is chosen to resemble the relative amplitude of noise and the density fluctuation signal in the experiments. The noise signal is generated separately for the two measurement volumes.

Since we have two measurement volumes, we would like to perform cross spectral analysis. The simulated signal in one volume is created as described above, while the signal in the second volume can be shifted Δ_t in time and Δ_ϕ in phase.

Below, we will treat eight cases:

1. $(\Delta_t, \Delta_\phi, v_\phi) = (0, 0, 0)$
2. $(\Delta_t, \Delta_\phi, v_\phi) = (1.5 \mu\text{s}, 0, 0)$
3. $(\Delta_t, \Delta_\phi, v_\phi) = (0, 1, 0)$
4. $(\Delta_t, \Delta_\phi, v_\phi) = (0, 0, 6 \times 10^6 \text{ s}^{-1})$
5. $(\Delta_t, \Delta_\phi, v_\phi) = ([0.5, 0.5] \mu\text{s}, [0, 0], [6 \times 10^6, -6 \times 10^6] \text{ s}^{-1})$ and $n_{\text{ev}} = [2 \times 10^3, 5 \times 10^2]$
6. $(\Delta_t, \Delta_\phi, v_\phi) = ([-1.5, 1.5] \mu\text{s}, [0, 0], [6 \times 10^6, 6 \times 10^6] \text{ s}^{-1})$ and $n_{\text{ev}} = [2 \times 10^3, 5 \times 10^2]$
7. $(\Delta_t, \Delta_\phi, v_\phi) = (0, 0, 0)$ and $n_{\text{ev}} = 0$
8. $(\Delta_t, \Delta_\phi, v_\phi) = ([0, 0] \mu\text{s}, [0, 0], [5 \times 10^5, -5 \times 10^5] \text{ s}^{-1})$, $n_{\text{ev}} = [2 \times 10^2, 2 \times 10^1]$, $A_{\text{ev}} = [25, 25]$, lifetime $4 \mu\text{s}$ and a noise level A_{noise} of 2.5

Case 1 is the baseline case, events having zero phase velocity and no time or phase delay. The noise level A_{noise} is set to 1.5, while the event amplitude A_{ev} is 1.

In cases 2-4 we set Δ_t , Δ_ϕ and v_ϕ to non-zero values in turn to observe the effects in cross spectral analysis.

Cases 5 and 6 include two phenomena, see section 4.7:

- In case 5 the time delays Δ_t are identical, while the phase velocities v_ϕ are equal in size but counter propagating
- In case 6 the time delays are equal in size but of opposite sign, while the phase velocities are identical

Case 7 is as the baseline case 1, except for the fact that no events are present (pure noise signal).

Finally, case 8 is used for the phase separation procedure.

In the remaining sections of this chapter, we will refer to these simulation numbers and what can be learned from their behaviour.

4.2 Statistical quantities

If the signal probability distribution is $p(d)$, d being a digit, we can define the following statistical quantities:

$$\begin{aligned}
 \text{Average :} \quad \bar{d} &= \frac{\sum dp(d)}{\sum p(d)} \\
 \text{Variance :} \quad V &= \frac{\sum (d - \bar{d})^2 p(d)}{\sum p(d)} \\
 \text{Skewness :} \quad S &= \frac{\sum (d - \bar{d})^3 p(d)}{\sum p(d)} \frac{1}{V^{3/2}} \\
 \text{Flatness :} \quad F &= \frac{\sum (d - \bar{d})^4 p(d)}{\sum p(d)} \frac{1}{V^2}
 \end{aligned} \tag{111}$$

For a Gaussian distribution, $S = 0$ and $F = 3$. Figure 18 shows the probability distribution function (PDF) of the real and imaginary parts of the signal from case 7 (left-hand) and case 4 (right-hand).

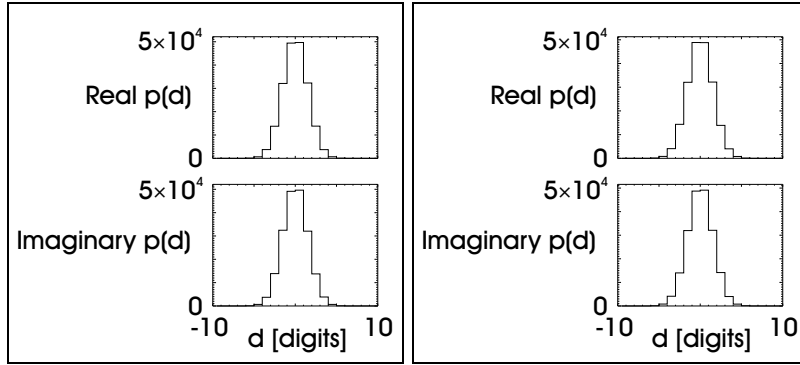


Figure 18. Left: PDF of case 7, right: PDF of case 4.

4.3 The autopower spectrum

The autopower spectrum (I_{11} in chapter 3) is defined to be

$$\begin{aligned}
 P_{jj}(\nu) &= \\
 F_j^*(\nu)F_j(\nu) &= \\
 \left(\int_{t_1}^{t_2} S_j(t)e^{i2\pi\nu t} dt \right)^* \left(\int_{t_1}^{t_2} S_j(t)e^{i2\pi\nu t} dt \right) &= \\
 \left| \int_{t_1}^{t_2} S_j(t)e^{i2\pi\nu t} dt \right|^2, & \quad (112)
 \end{aligned}$$

for a time interval $T = t_2 - t_1$ and volume number j (1 or 2). An example of the autopower for case 4 is shown in figure 19.

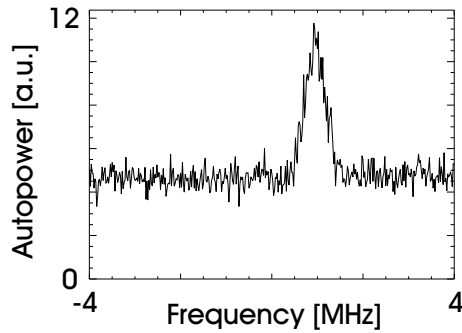


Figure 19. Autopower spectrum of case 4.

4.4 The crosspower spectrum

The crosspower spectrum is defined to be

$$\begin{aligned}
P_{12}(\nu) &= \\
F_1^*(\nu)F_2(\nu) &= \\
\left(\int_{t_1}^{t_2} S_1(t)e^{i2\pi\nu t} dt \right)^* &\left(\int_{t_1}^{t_2} S_2(t)e^{i2\pi\nu t} dt \right), \tag{113}
\end{aligned}$$

for a time interval $T = t_2 - t_1$. The crosspower spectrum is a complex number; the amplitude (I_{12} in chapter 3) and phase are called the crosspower amplitude and phase, respectively.

Usually one averages in frequency from the original $\delta\nu = 1/T_s$ of the fast Fourier transform (FFT) (T_s is the original sample length, 50 ns), to some $\Delta\nu$ value, typically of order 10-100 kHz. If the actual sample length is 10 ms, this means that we average over $N = \Delta\nu/\delta\nu = 100$ -1000 points in the spectrum. The power in uncorrelated parts of the spectrum is reduced due to phase mixing by a factor $\sqrt{N} = 10 - 30$ [16]. Contributions to the remaining spectrum are due to correlated signals, the power being proportional to the power of the correlated fluctuations.

To understand the significance of the crosspower phase, we will assume that the signal in one volume is delayed by Δ_t relative to the signal in the other volume:

$$S_2(t) = S_1(t - \Delta_t) \tag{114}$$

This means that

$$\begin{aligned}
F_2(\nu) &= \\
\int_{t_1}^{t_2} S_2(t)e^{i2\pi\nu t} dt &= \\
\int_{t_1}^{t_2} S_1(t - \Delta_t)e^{i2\pi\nu t} dt &= \\
e^{i2\pi\nu\Delta_t} \int_{t_1}^{t_2} S_1(t - \Delta_t)e^{i2\pi\nu(t-\Delta_t)} dt &= \\
e^{i2\pi\nu\Delta_t} \int_{t_1-\Delta_t}^{t_2-\Delta_t} S_1(u)e^{i2\pi\nu u} du &\approx \\
e^{i2\pi\nu\Delta_t} F_1(\nu) & \tag{115}
\end{aligned}$$

The crosspower spectrum then becomes

$$P_{12}(\nu) = F_1^*(\nu)F_2(\nu) \approx F_1^*(\nu)e^{i2\pi\nu\Delta_t}F_1(\nu) = e^{i2\pi\nu\Delta_t}P_{11}(\nu) \tag{116}$$

The crosspower phase is here

$$\phi_{12} = 2\pi\nu\Delta_t + \phi_0, \tag{117}$$

where we have added a constant ϕ_0 ; due to the optical setup, the crosspower phase is not zero at 0 Hz. The slope of the crosspower phase is equal to the time delay:

$$\frac{\partial\phi_{12}}{\partial\omega} = \Delta_t \tag{118}$$

If there is no crosspower phase delay ($\Delta_t = 0$) but still a crosspower amplitude above noise level, this means that the structure overlaps both volumes [63].

If there is a time delay, the group velocity of the fluctuations is $v_g = d/\Delta_t$, d being the distance between the two measurement volumes along the group velocity vector.

The crosspower spectrum for cases 1-4 is shown in figure 20. The baseline (case 1, top left) shows a crosspower amplitude centered at 0 Hz and a constant crosspower phase (no time delay). A non-zero time delay (case 2, top right) leads to a slope of the crosspower phase, while a constant non-zero phase difference (case 3, bottom left) introduces a constant non-zero crosspower phase. Finally, a non-zero phase velocity (case 4, bottom right) centers the crosspower amplitude maximum at a non-zero frequency.

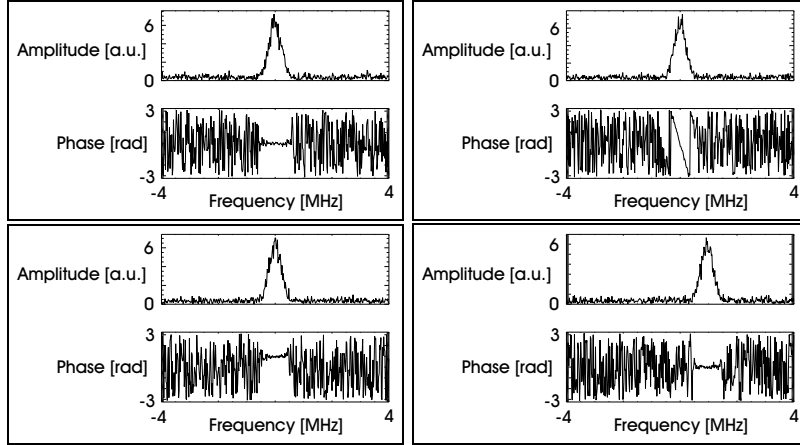


Figure 20. Crosspower spectrum for cases 1-4. Top left: Case 1, top right: Case 2, bottom left: Case 3 and bottom right: Case 4.

4.5 The autocorrelation function

The autocorrelation function is defined to be

$$C_{jj}(\tau) = \frac{1}{T} \int_{t_1}^{t_2} S_j^*(t) S_j(t + \tau) dt \quad (119)$$

for volume number j (1 or 2); τ is called the time lag. In figure 21 we show $C_{11}(\tau)$ for case 7 (left-hand column) and case 4 (right-hand column). Case 7 corresponds to noise only, giving rise to a peak at $\tau = 0$. If events are added to the noise (as in case 4), a signal away from $\tau = 0$ is observed along with the $\tau = 0$ noise peak.

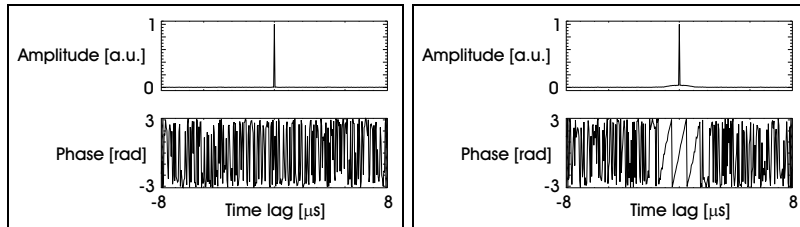


Figure 21. Left/right column: Autocorrelation function $C_{11}(\tau)$ for $\tau = [-8, 8]$ μs , case 7/4.

The width of the noise peak is inversely proportional to the bandwidth of the signal amplifier. In the simulations the noise signal was not band pass limited,

therefore the peak is limited to $\tau = 0$.

4.6 The crosscorrelation function

The crosscorrelation function is defined to be

$$C_{12}(\tau) = \frac{1}{T} \int_{t_1}^{t_2} S_1^*(t) S_2(t + \tau) dt \quad (120)$$

If the signal in one volume is delayed with respect to the other volume (equation 114), the crosscorrelation function can be expressed using the shifted autocorrelation function:

$$C_{12}(\tau) = C_{11}(\tau - \Delta_t) \quad (121)$$

The normalised crosscorrelation function is

$$\overline{C_{12}(\tau)} = \frac{C_{12}(\tau)}{\sqrt{C_{11}(0)C_{22}(0)}} \quad (122)$$

Since the peak at $\tau = 0$ for the autocorrelation function is not related to the actual fluctuation events, the autocorrelations are corrected for this peak before being used for normalisation, see [132].

The normalised crosscorrelation function for cases 1-4 is shown in figure 22. This figure corresponds to the crosspower spectra shown in figure 20.

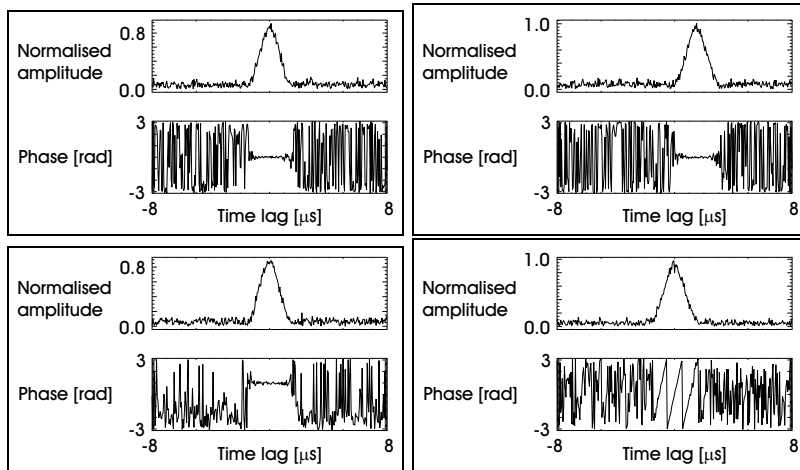


Figure 22. Normalised crosscorrelation function for cases 1-4. Top left: Case 1, top right: Case 2, bottom left: Case 3 and bottom right: Case 4.

4.7 Two phenomena

In this section we will use cross spectral analysis to study case 5 and 6 events. These signals contain events from two distinct phenomena: In case 5, the phenomena have different phase velocities, and in case 6 different time delays.

4.7.1 Crosspower and crosscorrelation

Figure 23 shows the crosspower spectrum (left-hand plot) and normalised crosscorrelation function (right-hand plot) for case 5. In this case, where two phenom-

ena have distinguishable phase velocities, the separation is best done using the crosspower spectrum representation.

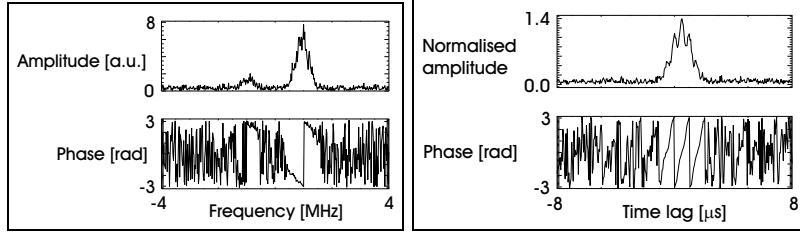


Figure 23. Left: Crosspower spectrum, right: Normalised crosscorrelation function for case 5.

The situation is reversed for phenomena having different time delays, see figure 24. Here, the separation is best using the normalised crosscorrelation function.

The reason for the differences in separating two phenomena is due to the fact that they add as complex numbers.

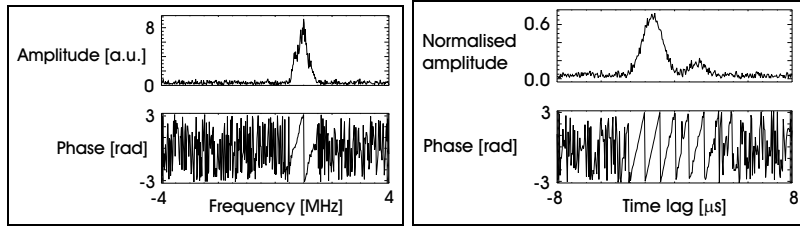


Figure 24. Left: Crosspower spectrum, right: Normalised crosscorrelation function for case 6.

4.7.2 Phase separation

Having two counter propagating phenomena present in the measured signal (phase velocities of opposite signs), these phenomena can be separated using the time derivative of the phase as explained in chapter 2. Figure 25 shows the autopower spectrum of a signal constructed using counter propagating events (case 8); the solid line is the total signal including noise, the dotted/dashed line is the signal due to events having a positive/negative phase velocity, respectively.

Once the events are created and noise is added, we are ready to use the phase separation technique on the simulated data. Before the phase derivative of

$$S_{\text{sim}} = S_{\text{sim}}^- + S_{\text{sim}}^+, \quad (123)$$

where

$$\begin{aligned} S_{\text{sim}}^+ &= X_{\text{sim}}^+ + iY_{\text{sim}}^+ = A_{\text{sim}}^+ e^{i\Phi_{\text{sim}}^+} \\ S_{\text{sim}}^- &= X_{\text{sim}}^- + iY_{\text{sim}}^- = A_{\text{sim}}^- e^{i\Phi_{\text{sim}}^-} \end{aligned} \quad (124)$$

is constructed, the data is band pass filtered to the [1 kHz, 1 MHz] frequency range. Thereafter the separation is done using the sign of $\partial_t \Phi_{\text{sim}}$:

$$\partial_t \Phi_{\text{sim}} < 0 : \begin{cases} S_{\text{sep}}^- = S_{\text{sim}}^- \\ S_{\text{sep}}^+ = 0 \end{cases} \quad \partial_t \Phi_{\text{sim}} > 0 : \begin{cases} S_{\text{sep}}^- = 0 \\ S_{\text{sep}}^+ = S_{\text{sim}}^+ \end{cases} \quad (125)$$

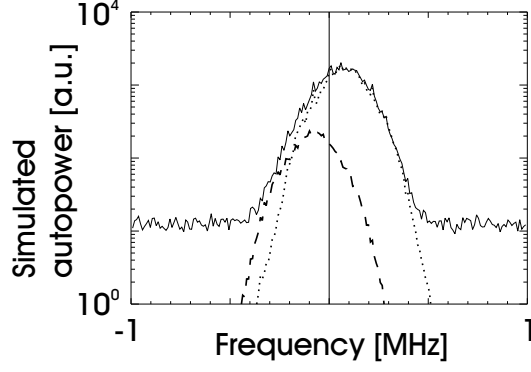


Figure 25. Autopower spectrum for a simulated signal composed of two counter propagating features (case 8). The solid line is the total signal (including noise), the dotted/dashed line is due to events having a positive/negative phase velocity, respectively.

and the result is

$$S_{\text{sep}} = S_{\text{sep}}^- + S_{\text{sep}}^+, \quad (126)$$

where

$$\begin{aligned} S_{\text{sep}}^+ &= X_{\text{sep}}^+ + iY_{\text{sep}}^+ = A_{\text{sep}}^+ e^{i\Phi_{\text{sep}}^+} \\ S_{\text{sep}}^- &= X_{\text{sep}}^- + iY_{\text{sep}}^- = A_{\text{sep}}^- e^{i\Phi_{\text{sep}}^-} \end{aligned} \quad (127)$$

Since we have used the phase to separate the signals, we will use the amplitude to gauge the quality of the phase separation. The tool we have chosen is the zero time lag crosscorrelation function

$$C(B, C) = \frac{\sum_{k=1}^N (B_k - \bar{B})(C_k - \bar{C})}{\sqrt{\left[\sum_{k=1}^N (B_k - \bar{B})^2\right] \left[\sum_{k=1}^N (C_k - \bar{C})^2\right]}} \quad (128)$$

and the correlations we calculate are $C(A_{\text{sim}}^+, A_{\text{sep}}^+)$, $C(A_{\text{sim}}^+, A_{\text{sep}}^-)$, $C(A_{\text{sim}}^-, A_{\text{sep}}^+)$ and $C(A_{\text{sim}}^-, A_{\text{sep}}^-)$. It is important to note that we calculate the correlations using the *noise-free* (i.e. 'real') simulated signals. The correlations supply us with a quantitative measure of the phase separation; for a successful separation, we expect the '+' '+'/'-' '-' correlations to be significant and the '+' '-'/'-' '-' correlations to be small. This is indeed the case for the separated autopower spectrum shown in figure 26, where the '+' '+'/'-' '-' correlations are of order 80 %, whereas the '+' '-'/'-' '-' correlations are about 2 %.

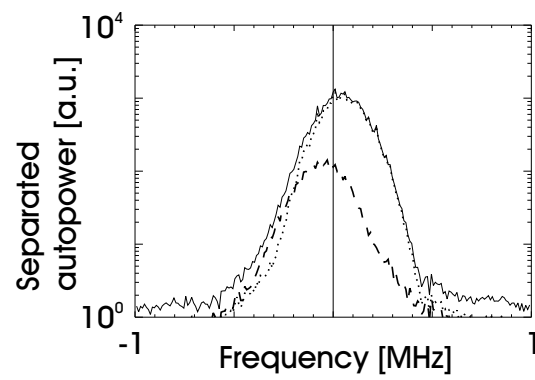


Figure 26. Autopower spectrum for a phase separated signal composed of two counter propagating features. The solid line is the total signal, the dotted/dashed line is due to events having a positive/negative phase velocity, respectively.

Part II
Experiment

5 Transport in fusion plasmas

In this chapter we summarise the transport concepts used in the thesis; the sections will necessarily be short. In section 5.1 we introduce the energy confinement time and scaling laws relating this to machine parameters. Thereafter, in section 5.2, we describe the major transport equations and discuss the concept of anomalous transport. Sections 5.3 and 5.4 deal with two different approaches to the calculation of fluxes due to fluctuations. In section 5.5 definitions connected to turbulence theories are presented and section 5.6 contains an extremely short review on the measured properties of fluctuations in fusion plasmas. In section 5.7 we describe one of the candidate theories concerning turbulence suppression at the transition to improved confinement regimes.

5.1 Energy confinement

In this first section we describe a central quantity in transport analysis, the energy confinement time τ_E . The total energy in the plasma is

$$W = \int 3nT d^3x = 3\langle nT \rangle V, \quad (129)$$

where $\langle \cdot \rangle$ is a spatial average and V is the plasma volume [160]. The energy loss rate P_L is characterised by an energy confinement time defined by the relation

$$P_L = \frac{W}{\tau_E} \quad (130)$$

In machines currently operating, the energy loss is balanced by the externally supplied heating power, P_H ($P_H = P_L$). Using this fact along with equation 130, we arrive at the following expression for the energy confinement time in terms of measurable quantities:

$$\tau_E = \frac{W}{P_H} \quad (131)$$

The theory dealing with transport of energy and particles due to binary collisions across the confining magnetic field of a toroidal device is called the neoclassical transport theory [69]. Fusion plasmas do not behave as predicted by neoclassical transport theory, in the sense that the neoclassical transport level is orders of magnitude smaller than what is experimentally observed. This also has consequences for the neoclassical energy confinement time, which is found to be very large compared to measurements.

Since no detailed understanding of the reason for this discrepancy has emerged, we have to make empirical expressions for τ_E . This is usually done by scaling laws, where τ_E is set equal to a product of powers of various parameters involved. For the most basic approach, one uses engineering parameters, such as the toroidal magnetic field strength and the major radius of the machine in question. The scaling studies have been made using a multi-machine database consisting of hundreds or thousands of plasma discharges. An example for stellarators is the International Stellarator Scaling (ISS) from 1995:

$$\tau_E^{\text{ISS95}} = 0.079 \times a^{2.21} R_0^{0.65} P_{\text{tot}}^{-0.59} \bar{n}_e^{-0.51} B_\varphi^{0.83} t_{2/3}^{0.4}, \quad (132)$$

where a is the plasma minor radius, R_0 the machine major radius, P_{tot} the total absorbed heating power, \bar{n}_e the line density, B_φ the toroidal magnetic field and

$t_{2/3}$ the rotational transform at two-thirds of the plasma minor radius (see chapter 6) [139]. The units of equation 132 from left to right are: s, m, m, MW, 10^{19} m^{-3} and T.

A slightly more sophisticated procedure is to make use of the invariance of the governing equations under scale transformations [39]. We will not describe the technique here, but just mention an application, the so-called ρ^* -scaling, ρ^* being the normalised ion Larmor radius ρ_i/a . Different models lead to different scaling behaviours of τ_E , see table 1.

gyro-Bohm	$\chi \propto a^2 B \rho^{*3}$	$\tau_E \propto \rho^{*-3} / B \propto a^{5/2} B$
Bohm	$\chi \propto a^2 B \rho^{*2}$	$\tau_E \propto \rho^{*-2} / B \propto a^{5/3} B^{1/3}$
Stochastic	$\chi \propto a^2 B \rho^*$	$\tau_E \propto \rho^{*-1} / B \propto a^{5/6} B^{-1/3}$

Table 1. Energy confinement time for three theories; χ is the thermal diffusivity.

The terms gyro-Bohm, Bohm and stochastic in table 1 refer to different plasma transport theories. In ρ^* -experiments, other dimensionless parameters are kept constant, while ρ^* is varied. Due to the different scaling of τ_E with B , such a procedure can help distinguish between different types of transport. For example, we note that the ISS95 scaling law is close to gyro-Bohm, where the turbulence correlation width is ρ_i , the ion Larmor radius.

5.2 Transport equations

The radial particle flux Γ_j and the radial heat flux q_j for particle species j are the central quantities that define cross-field transport of particles and energy. Our treatment in this section is taken from [160]. The fluxes can be represented as

$$\begin{aligned}\Gamma_j &= -\alpha_{11} \frac{dn_j}{dr} - \alpha_{12} \frac{dT_j}{dr} \\ q_j &= -\alpha_{21} \frac{dn_j}{dr} - \alpha_{22} \frac{dT_j}{dr},\end{aligned}\tag{133}$$

where α is a transport matrix, the diagonal elements being the particle diffusivity $\alpha_{11} = D_j$ and the thermal diffusivity $\alpha_{22} = n\chi_j$. This can be simplified further by expressing the fluxes as the sum of a diffusive and a convective term, for example

$$\Gamma_e = -D \frac{dn_e}{dr} - V n_e\tag{134}$$

for the electron particle flux, where D is the diffusivity and V is an inward pinch velocity (represents the off-diagonal terms of the transport matrix).

The typical measured heat diffusivities are

$$\chi_i, \chi_e \sim 1 \text{ m}^2 \text{ s}^{-1},\tag{135}$$

while the measured particle diffusivities are

$$D \sim \frac{1}{4} \chi_e\tag{136}$$

The pinch velocity is typically

$$V \sim 10 \text{ m/s}\tag{137}$$

The above measured values should be compared with neoclassical (superscript nc) values

$$\begin{aligned}\chi_i^{\text{nc}} &\sim 0.3 \text{ m}^2\text{s}^{-1} \\ \chi_e^{\text{nc}} \sim D^{\text{nc}} &\sim \sqrt{\frac{m_e}{m_i}} \chi_i^{\text{nc}}\end{aligned}\quad (138)$$

Equations 135 through 138 imply that $\chi_i \sim 1$ to $10 \chi_i^{\text{nc}}$ and $\chi_e \sim 10^2 \chi_e^{\text{nc}}$. This illustrates the main problem facing us: The neoclassical transport coefficients are too small to account for the observed transport. The missing transport - called the anomalous transport - is thought to be due to fluctuations created by turbulence in the plasma parameters. Two approaches are possible here:

1. Take the underlying instability as given and calculate the turbulent fluxes due to magnetic and electric fluctuations, see section 5.3.
2. Calculate the saturated state of the instability and the resulting transport. We will discuss one of the most prominent instability candidates (drift waves) in section 5.4.

5.3 Quasilinear fluxes

Fluctuations are traditionally divided into three categories:

- Electrostatic fluctuations: Here, the fluctuations in the magnetic field $\delta\mathbf{B}$ are assumed to be non-existent, while the fluctuations in the electric field $\delta\mathbf{E}$ have some non-zero value.
- Magnetic fluctuations: Here, the fluctuations in the magnetic field $\delta\mathbf{B}$ are assumed to have a non-zero value, while no fluctuations in the electric field $\delta\mathbf{E}$ occur.
- Electromagnetic fluctuations: Here, both fluctuations in $\delta\mathbf{E}$ and $\delta\mathbf{B}$ exist.

A fluctuating quantity, for example the electron density n_e , can be written as a sum of an average value and a fluctuating part:

$$n_e = \langle n_e \rangle + \delta n_e, \quad (139)$$

where brackets denote a time average, so that $\langle \delta n_e \rangle = 0$. This representation allows us to calculate the radial particle (equation 140) and energy (equation 141) flux due to fluctuations [126] [163].

$$\begin{aligned}\Gamma_j &= \Gamma_j^E + \Gamma_j^B \\ \Gamma_j^E &= \frac{\langle \delta E_\theta \delta n_j \rangle}{B_\varphi} \\ \Gamma_j^B &= -\frac{\langle \delta j_{\parallel j} \delta B_r \rangle}{e B_\varphi}\end{aligned}\quad (140)$$

$$\begin{aligned}Q_j &= Q_j^E + Q_j^B \\ Q_j^E &= \frac{3}{2} \frac{\langle \delta E_\theta \delta p_j \rangle}{B_\varphi} = \frac{3}{2} n_j \frac{\langle \delta E_\theta \delta T_j \rangle}{B_\varphi} + \frac{3}{2} T_j \frac{\langle \delta E_\theta \delta n_j \rangle}{B_\varphi} \\ Q_j^B &= g_j \left(\frac{\delta B_r}{B_\varphi} \right) \frac{dT_j}{dr}\end{aligned}\quad (141)$$

In equation 141, the function g_j is usually proportional to $(\delta B_r/B_\varphi)^2$ [98]. Equations 140 and 141 for the anomalous fluxes are usually called quasilinear, since they are bilinear correlations of perturbed quantities.

Usually, the energy flux Q_j is split up in two parts, a conducted heat flux q_j and a convected flux $\frac{5}{2}T_j\Gamma_j$:

$$Q_j = q_j + \frac{5}{2}T_j\Gamma_j \quad (142)$$

There is some controversy whether the factor 5/2 in equation 142 should in fact be 3/2, see e.g. [127].

It is clear that measurements of density fluctuations as presented in this thesis are very important ingredients in the determination of anomalous fluxes. However, it is crucial to note that not only the amplitude of the fluctuations is important for transport, but also the phase between the fluctuating fields. For example, the particle transport due to the correlated δE_θ and δn_e can be written [117]

$$\begin{aligned} \Gamma_e^E(\omega) &= \\ \frac{\langle \delta E_\theta(\omega)\delta n_e(\omega) \rangle}{B_\varphi} &= \\ \delta n_e^{\text{RMS}}(\omega)\delta\phi^{\text{RMS}}(\omega)|\gamma_{n_e\phi}(\omega)|\frac{k_\theta(\omega)}{B_\varphi} \sin \alpha_{n_e\phi}(\omega) & \quad (143) \end{aligned}$$

Here, k_θ is the measured wavenumber, $\delta\phi = -\delta E_\theta/k_\theta$ is the plasma potential, $\gamma_{n_e\phi}$ is the normalised crosspower spectrum and $\alpha_{n_e\phi}$ is the phase between δn_e and $\delta\phi$. Even if the fluctuating root-mean-square (RMS) amplitudes δn_e^{RMS} and $\delta\phi^{\text{RMS}}$ are large, the net transport could be negligible if the normalised crosspower is small or the phase is close to integer multiples of π .

5.4 Drift waves

A major candidate for an instability causing fluctuations is the so-called drift wave. This instability feeds on the energy associated with a gradient in the plasma density (and/or temperature). In this section we will initially describe the basic features of this wave, and thereafter sketch a derivation of the dispersion relation in the cold ion limit ($T_i \ll T_e$). Finally, a primitive estimate for the fluctuation level will be presented.

It is important to note that we here treat collisionless drift waves, where kinetic effects provide the dissipation needed to release the energy required to make drift waves unstable.

Another class of drift waves is resistive drift waves, where resistivity is responsible for the dissipation [113] [155]. We will not treat this type of drift waves.

5.4.1 Basic mechanism

The geometry we use is called the plane plasma slab. We assume that the magnetic field is shearless and uniform in the z -direction: $\mathbf{B} = B\hat{\mathbf{z}}$. The equilibrium density $n_0(x)$ is non-uniform in the x -direction; that is, it has a non-zero gradient ∇n_0 . The equilibrium temperature $T_0(x)$ is constant, $\nabla T_0 = 0$.

The parallel equation of motion of electrons in the electrostatic approximation can be written [155]

$$\frac{\partial v_{e\parallel}}{\partial t} + (\mathbf{v}_e \cdot \nabla)v_{e\parallel} = \frac{e}{m} \frac{\partial \phi}{\partial z} - \frac{1}{mn_e} \frac{\partial p_e}{\partial z} \quad (144)$$

The left-hand side of equation 144 (electron inertia terms) can be neglected for low frequencies, i.e. for $\omega \ll \omega_{ci} = eB/m_i$. Assuming that the electrons are isothermal ($\frac{\partial p_e}{\partial z} = T_e \frac{\partial n_e}{\partial z}$) the equation of motion reduces to

$$e \frac{\partial \phi}{\partial z} = \frac{T_e}{n_e} \frac{\partial n_e}{\partial z} \quad (145)$$

Solving this for n_e and introducing the equilibrium electron density n_{e0} we arrive at

$$n_e = n_{e0} e^{\frac{e\phi}{T_e}} \quad (146)$$

Writing the density as $n_e = \langle n_e \rangle + \delta n_e = n_{e0} + \delta n_e$ and expanding the exponential function we end up having the Boltzmann distribution

$$\frac{\delta n_e}{n_{e0}} = \frac{e\phi}{T_{e0}}, \quad (147)$$

where we have assumed that $T_e = T_{e0}$. The electrostatic potential implies a perturbed electric field in the y -direction, directed from regions of increased density ($\delta n_e > 0$) to those of decreased density ($\delta n_e < 0$). The electric field (in the y -direction) is associated with an $\mathbf{E} \times \mathbf{B}$ drift in the x -direction, which leads to an increasing density in the $\delta n_e < 0$ regions and a decreasing density in the $\delta n_e > 0$ regions. The resulting wave propagating in the y -direction is the drift wave [160].

5.4.2 Dispersion relation

We wish to find the dispersion relation $\omega(\mathbf{k})$ of drift waves to investigate whether these frequencies are comparable to those measured. We will use a kinetic approach and base our procedure on the one given in [58]. What this subsection contains is not a derivation, but rather an overview of the ingredients in making the derivation.

Instead of using the particle distribution function $f(\mathbf{x}, \mathbf{v}, t)$ we will make use of the guiding center distribution function $f_{gc}(\mathbf{x}_{gc}, v_{\perp}, v_{\parallel}, t)$, where \mathbf{x}_{gc} is the position of the guiding center [160]. We again work in the plane plasma slab geometry as used in subsection 5.4.1. We from now on omit the 'gc' subscript, and so write the electron guiding center distribution as $f_e(\mathbf{x}, v_{\perp}, v_z, t)$, where $v_{\parallel} = v_z$ for our geometry. The distribution is assumed to be a Gaussian

$$f_0(\mathbf{x}, v) = n_0(x) \left(\frac{m}{2\pi T_0(x)} \right)^{3/2} e^{-\frac{mv^2}{2T_0(x)}}, \quad (148)$$

where $v = \sqrt{v_{\perp}^2 + v_z^2}$. A perturbed quantity ψ can be written

$$\psi(\mathbf{x}, t) = \hat{\psi}(x) e^{-i\omega t + ik_y y + ik_z z}, \quad (149)$$

an assumption to be used when we linearise equations. The basic equation for the electrons is the drift-kinetic equation

$$\frac{\partial f_e}{\partial t} + \frac{\mathbf{E} \times \mathbf{B}}{B^2} \cdot \nabla_{\perp} f_e + v_z \frac{\partial f_e}{\partial z} - \frac{e}{m} E_z \frac{\partial f_e}{\partial v_z} = 0 \quad (150)$$

If this equation is solved, the electron density can be found by integrating over all velocities, $n_e = \int f_e d^3v = 2\pi \int f_e v_{\perp} dv_{\perp} dv_z$. Treating the ions as cold, the governing ion equations are:

1. The continuity equation $\partial n_i / \partial t + \nabla \cdot (n_i \mathbf{u}) = 0$, \mathbf{u} being the velocity.

2. The perpendicular velocity $\mathbf{u}_\perp = \frac{\mathbf{E} \times \mathbf{B}}{B^2} + \frac{M \partial_t \mathbf{E}_\perp}{e B^2}$, where the second term on the right-hand side is the polarisation drift.
3. The parallel equation of motion $M \frac{du_z}{dt} = e E_z$.

Linearising the electron drift equation one arrives at the expression

$$\delta n_e = \frac{n_{e0} e \phi}{T_{e0}} \left[1 + i \sqrt{\frac{\pi}{2}} \frac{\omega - k_y v_{de}}{|k_z| v_{t,e}} \right], \quad (151)$$

for the electron density perturbation. Here, $v_{t,e} = \sqrt{T_{e0}/m}$ is the electron thermal velocity and $v_{de} = -\frac{T_{e0}}{n_{e0} e B_{z0}} \frac{dn_{e0}}{dx}$ is the electron diamagnetic drift (DD) velocity. Linearising the ion equations we obtain an expression for the ion density perturbation

$$\delta n_i = \frac{n_{i0} e \phi}{T_{e0}} \left(\frac{k_y v_{de}}{\omega} + \frac{k_z^2 C_s^2}{\omega^2} - k_\perp^2 \rho_s^2 \right), \quad (152)$$

where the sound speed $C_s = \sqrt{T_{e0}/M}$ and the ion Larmor radius at the electron temperature $\rho_s = \sqrt{M T_{e0}}/e B_{z0}$. Finally, using the quasi-neutrality approximation $\delta n_e = \delta n_i$ to equate equations 151 and 152, we reach the expression for the cold ion dispersion relation

$$\omega(1 + k_\perp^2 \rho_s^2) - k_y v_{de} - \frac{k_z^2 C_s^2}{\omega} = -i \sqrt{\frac{\pi}{2}} \frac{\omega(\omega - k_y v_{de})}{|k_z| v_{t,e}} \quad (153)$$

Setting the imaginary right-hand side equal to zero we see that the equation has two solutions, the electron branch (ω and $k_y v_{de}$ have the same sign) and the ion branch (ω and $k_y v_{de}$ have the opposite sign). If $k_\perp \rho_s \ll 1$ and $k_z C_s \ll k_y v_{de}$, the electron branch can be written

$$\omega \approx k_y v_{de}, \quad (154)$$

which is the electron drift wave linear dispersion relation. Keeping the two terms on the left-hand side of equation 153 as small corrections, we obtain a slightly more complicated dispersion relation, namely

$$\omega = \frac{k_y v_{de}}{1 + k_\perp^2 \rho_s^2} + \frac{k_z^2 C_s^2}{k_y v_{de}} \quad (155)$$

Usually, since $k_z = k_\parallel$ is very small, we neglect the second term on the right-hand side and use

$$\omega = \frac{k_y v_{de}}{1 + k_\perp^2 \rho_s^2} \quad (156)$$

as our final dispersion relation.

To obtain an expression for the growth rate γ , we let $\omega \rightarrow \omega + i\gamma$ (ω and γ are assumed to be real, $\gamma/\omega \ll 1$) in equation 153 and equate the imaginary parts

$$\gamma = \sqrt{\frac{\pi}{2}} \frac{k_y^2 v_{de}^2}{|k_z| v_{t,e}} \left(k_\perp^2 \rho_s^2 - \frac{k_z^2 C_s^2}{k_y^2 v_{de}^2} \right) \quad (157)$$

A negative γ means damping, positive γ growth. The physical process enabling an instability to develop is inverse Landau damping by electrons [58]. The growth rate can be used to obtain a diffusion coefficient [40]

$$D = L_n^2 \sum_k \gamma(\mathbf{k}) \left[\frac{\delta n_e(\mathbf{k})}{n_{e0}} \right]^2, \quad (158)$$

where $L_n = 1/|\partial_r \ln(n_{e0})|$ is the density gradient scale length and the sum is to be taken over all existing modes. Results akin to this motivate experimentalists to relate the energy confinement time τ_E to $\delta n_e/n_{e0}$. In some cases it has been found that they are related for core turbulence (τ_E decreases for an increased density fluctuation level) but not related for edge turbulence [45].

Since it is unlikely that the density perturbation should grow beyond the amplitude at which it reverses the local density gradient, we get the upper bound $k_\perp \delta n_e \leq dn_{e0}/dr$, or

$$\frac{\delta n_e}{n_{e0}} \leq \frac{1}{k_\perp L_n}, \quad (159)$$

known as the mixing length estimate. Inserting this into equation 158, we get an upper limit on the diffusion coefficient, $D \leq \sum_k \gamma(\mathbf{k})/k_\perp^2$.

The warm ion dispersion relation ($T_e \sim T_i$) for small scales ($k_\perp \rho_s \geq 1$) is quite complex (see e.g. [113] or [138]), but for $k_\perp \rho_s \leq 1$ one can include an additional factor in the numerator of equation 156 [164].

5.5 Turbulence

This section on turbulence theory is motivated by the fact that measuring turbulence on different spatial scales (i.e. wavenumbers) allows us to test whether these theories apply to fusion plasmas. The governing equation of turbulence in an incompressible fluid is the Navier-Stokes equation

$$\begin{aligned} \frac{\partial \mathbf{v}}{\partial t} + \mathbf{v} \cdot \nabla \mathbf{v} &= -\nabla p + \nu \nabla^2 \mathbf{v} \\ \nabla \cdot \mathbf{v} &= 0, \end{aligned} \quad (160)$$

where \mathbf{v} is the fluid velocity, p is the pressure and ν the kinematic viscosity [54]. We can introduce a dimensionless quantity, the Reynolds number, given by

$$R = \frac{LV}{\nu}, \quad (161)$$

where L is a characteristic scale and V a characteristic velocity of the flow. The Reynolds number can be used to re-write the Navier-Stokes equation in a dimensionless form

$$\frac{\partial \mathbf{v}'}{\partial t'} + \mathbf{v}' \cdot \nabla' \mathbf{v}' = -\nabla' p' + \frac{1}{R} \nabla'^2 \mathbf{v}', \quad (162)$$

where we have made use of the substitutions $\mathbf{r} = L\mathbf{r}'$, $t = Tt'$ and $\mathbf{v} = V\mathbf{v}'$, with $T = L/V$ and $p' = p/V^2$. The Reynolds number R is the 'knob' controlling whether a system is turbulent; a small R means that the turbulence level is small, a large R that the system is turbulent.

The Kolmogorov 1941 (K41) theory [54] implies that the energy spectrum has a power-law dependency on the wavenumber k :

$$E(k) \sim \varepsilon^{2/3} k^{-5/3}, \quad (163)$$

where ε is the mean energy dissipation per unit mass. This law is valid in the inertial range, i.e. far away from the integral scale l_0 or the dissipation scale $\eta = (\nu^3/\varepsilon)^{1/4}$. The physical picture of turbulence in this framework is the following:

- The integral scale l_0 : At the largest scale l_0 , energy is injected.
- The inertial range l ($k \sim l^{-1}$): Here, the structure scale l is intermediate, $\eta < l < l_0$. Successive smaller scale structures ('eddies') of size $l_n = l_0 r^n$, where $0 < r < 1$ and $n = 0, 1, 2, \dots$ transfer energy; this is called the energy cascade. The inertial range is where equation 163 is valid.
- The dissipation scale η : Energy is dissipated on this small scale.

The above results are for three-dimensional (3D) turbulence, while turbulence in fusion plasmas can be regarded as 2D, perpendicular to the toroidal magnetic field B_φ . In the 2D case, the Kolmogorov-Kraichnan theory ([2] and references therein) states:

1. At an initial time, all energy and enstrophy is concentrated at a forcing wavenumber k_0 . Enstrophy is the integrated square of the vorticity $\boldsymbol{\omega} = \nabla \times \mathbf{v}$.
2.
 - Fluctuations are transferred from the forcing scale to larger scales, i.e. what is known as the inverse energy cascade. Fluctuations are damped at about k_L .
 - Fluctuations are transferred from the forcing scale to smaller scales by an enstrophy cascade. Fluctuations are dissipated at about k_η .

Away from these three wavenumbers, we have two distinct transfer ranges, the energy range for $k_L < k < k_0$ and the enstrophy range for $k_\eta > k > k_0$. For each of these intervals, different dependencies on the wavenumber k is found:

$$\begin{aligned} E_{\text{energy}}(k) &= C\varepsilon^{2/3}k^{-5/3} \\ E_{\text{enstrophy}}(k) &= C'\varkappa^{2/3}k^{-3}, \end{aligned} \quad (164)$$

where C and C' are dimensionless constants and \varkappa is the average rate of enstrophy [94]. Our measured spectrum is equivalent to the d -dimensional energy spectrum $F_d(k)$ [1] [54] [146]

$$\begin{aligned} F_d(k) &= \frac{E(k)}{A_d} \\ A_2 &= 2\pi k \\ A_3 &= 4\pi k^2, \end{aligned} \quad (165)$$

where A_d is the surface area of a sphere having radius k and dimension d . Assuming that $d = 2$ (2D turbulence), the relations in equation 164 become

$$\begin{aligned} F_{\text{energy}}^{2D}(k) &= \frac{1}{2\pi}C\varepsilon^{2/3}k^{-8/3} \\ F_{\text{enstrophy}}^{2D}(k) &= \frac{1}{2\pi}C'\varkappa^{2/3}k^{-4} \end{aligned} \quad (166)$$

Assuming that our measurement wavenumber k is within the outer limits ($k_L \ll k \ll k_\eta$), measurements of the frequency integrated spectrum versus k and fitting these to a power-law should tell us if we are observing one or the other range.

For extremely small scales ($k \gtrsim k_\eta$) one enters the dissipation range; here, it has been argued that the energy spectrum could have one of the following dependencies

$$\begin{aligned} E_{\text{Neumann}}(k) &\propto e^{-ak} \\ E_{\text{Heisenberg}}(k) &\propto k^{-7}, \end{aligned} \quad (167)$$

where $a > 0$ is a constant (see [110] and references therein).

5.6 Brief review

In this section we use review papers on anomalous transport in fusion plasmas ([98], [163] and [32]) to summarise what has been accomplished so far. We will focus on the observations of density fluctuations and mention their relationship to fluctuations in the poloidal electric field (see e.g. equations 140 and 143).

We will generally deal with what has been named microturbulence; that is, fluctuations on a scale much smaller than the plasma minor radius a ($k_{\perp}a \gg 1$). These microscopic modes are also called high- m modes, m being the poloidal mode number (see chapter 6). This is because assuming that $k_{\theta} = m/r$ and $k_{\theta}a \gg 1$, one has $m \gg 1$ (for $r = a$). Macroscopic low- m modes also exist, where $k_{\perp}a \sim 1$; they are magnetohydrodynamic (MHD) modes.

5.6.1 Broadband spectra

In general, autopower spectra of low frequency fluctuations have a broadband spectrum, the frequencies $\nu = \omega/2\pi$ extending from 10 kHz to about 1 MHz. As a rule, no coherent modes with a width $\Delta\nu \ll \nu$ exist, except MHD modes which appear to be superimposed onto the broadband spectrum. A review on MHD instabilities in W7-AS can be found in [157].

In the last paragraph we discussed spectra for a fixed wavenumber k . If one varies k and plots the frequency integrated autopower versus k , significant fluctuations over a broad range of wavenumbers is observed. However, most of the energy is in the region where $k_{\perp}\rho_s < 1$, and usually a maximum is observed at about 1 cm^{-1} .

5.6.2 Radial variation of fluctuation level

Generally, the relative fluctuation level $\delta n_e/n_{e0}(r)$ is observed to increase with radius. The relative level is below 1 % in the core and reaches 10 to 100 % at the edge. Some examples of the measured fluctuation level versus minor radius can be found in [125] [53] [172]. An example of how the relative fluctuation profile can be modelled has been introduced in chapter 3.

5.6.3 Wavenumber components

It has been shown that the parallel component of the fluctuations κ_{\parallel} is much smaller than the perpendicular component κ_{\perp} : $\kappa_{\parallel} \ll \kappa_{\perp}$. This has already been assumed in the derivations concerning spatial localisation in chapter 3. Basically, this means that turbulence is confined to a 2D-space perpendicular to the main magnetic field component B_{φ} .

5.6.4 Direction of rotation

Definitions When speaking about rotation of the turbulence, we mean the direction of the poloidal propagation. This is being defined in terms of the diamagnetic drift (DD) velocity

$$\mathbf{v}_{\text{dia,q}} = \frac{\mathbf{B} \times \nabla p}{nqB^2}$$

$$[v_{\text{dia,q}}]_{\theta} = \frac{T_q}{qB_{\varphi}L_n}, \quad (168)$$

where q is the charge (see subsection 5.4.2). The direction of the velocity (the DD direction) is opposite for ions and electrons, see figure 27.



Figure 27. Definition of the diamagnetic drift (DD) directions. Left: The electron DD direction, right: The ion DD direction.

Rotation of the plasma bulk can also be caused by $\mathbf{E} \times \mathbf{B}$ rotation with a velocity

$$\mathbf{v}_{\mathbf{E} \times \mathbf{B}} = \frac{\mathbf{E} \times \mathbf{B}}{B^2}$$

$$[v_{\mathbf{E} \times \mathbf{B}}]_{\theta} = \frac{E_r}{B_{\varphi}}, \quad (169)$$

where E_r is the radial electric field. A negative E_r is inward pointing, a positive E_r outward pointing, see figure 28. We observe that rotation due to a negative/positive radial electric field is in the electron/ion DD direction, respectively.

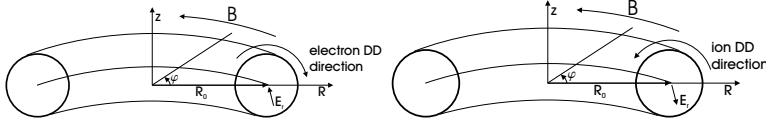


Figure 28. Definition of the $\mathbf{E} \times \mathbf{B}$ directions. Left: The direction for a negative radial electric field, $E_r < 0$, right: The direction for $E_r > 0$.

Usually, the observed frequencies in the laboratory frame ω_{lab} are due to the cumulative effect of a mode frequency ω_{turb} and an $\mathbf{E} \times \mathbf{B}$ Doppler shift $\omega_{\mathbf{E} \times \mathbf{B}}$:

$$\omega_{\text{lab}} = \omega_{\text{turb}} + \omega_{\mathbf{E} \times \mathbf{B}}, \quad (170)$$

where the mode frequency could be the linear mode frequency of electron drift waves [164]. It is often the case that the Doppler shift dominates the observed frequencies, so that the mode frequency is a minor correction [120].

Measurements It is frequently seen that fluctuations (in the laboratory frame) travel in the electron DD direction. Sometimes fluctuations in the core travel in the electron DD direction, while edge fluctuations travel in the ion DD direction [55]. This is attributed to a sign reversal of E_r in the edge plasma, where $E_r < 0$ in the core and $E_r > 0$ at the edge.

A reversal of the rotation direction with a change in density (electron/ion DD direction for low/high density) has also been reported [154].

5.6.5 Correlations of fluctuations

Simultaneous measurements of δE_{θ} and δn_e can be made in the edge of fusion plasmas using Langmuir probes. These measurements enable the calculation of the radial particle transport according to equation 140. We briefly describe results of this kind of analysis:

Probe measurements in Caltech Research Tokamak plasmas made it possible to determine the measured radial particle transport [178]. The following conclusions were drawn:

- The flux was outward
- The flux was concentrated at low frequencies (< 200 kHz)
- The phase $\alpha_{n_e E_\theta}$ was between 0° and 60°
- The particle flux enabled one to estimate a particle confinement time τ_p similar to the energy confinement time τ_E

More recent probe measurements in the ASDEX tokamak and W7-AS [47] [48] included comparable findings, e.g. that the flux is mostly outward and that a large part of the transport is due to a small number of large events.

5.6.6 Confinement regimes

Until 1982 fusion devices operated in what has since become known as the low (L) confinement mode. That year, a new confinement regime was found in the ASDEX tokamak, dubbed the high (H) confinement mode [149] [160]. In the H-mode, the energy confinement time is typically double that of the L-mode. The L-H transition has a bifurcation-like character and plasmas can make a spontaneous switch between the two regimes.

The L-H (or H-L) transition is observable in most plasma parameters; the measured light from the plasma edge is used to define the transitions (see chapter 8 for measurements). The most important changes from L- to H-mode are:

- A rapid increase of the edge pressure gradient, primarily due to a steepening of the edge density profile. This leads to an increase of the plasma energy.
- The poloidal rotation increases.
- The improved confinement also applies to impurities, leading to an accumulation and subsequent radiation collapse of the plasma.
- Turbulence is reduced, both magnetic and density fluctuations.

Often, plasmas close to the H-mode will have edge localised mode (ELM) activity [37]. ELMs are edge instabilities causing a transient reduction of the edge pressure gradient and loss of a few percent of the stored energy. These ELMs can be benign in that an ELMy H-mode can keep the impurity level constant.

The drop in turbulence activity combined with the improved plasma performance are thought to be connected but the responsible mechanism(s) has not been found. For a comprehensive review of present candidate theories see [38]. In the next section we will briefly describe one of the main contenders, suppression of turbulence due to a shear in E_r .

In W7-AS, the H-mode occurs below a certain heating power threshold and above a density determined by the applied power [72]. Further, the occurrence of the H-mode is linked to the magnetic field configuration; the H-mode exists in operational windows where the viscous damping has a local minimum [162].

5.7 Shear flow suppression of turbulence

The theory we describe here is connected to the $\mathbf{E} \times \mathbf{B}$ rotation explained in subsection 5.6.4. Since E_r can depend on the minor radius r , we define the shear in the radial electric field to be

$$E_r' = \frac{dE_r}{dr} \quad (171)$$

A certain value of E_r corresponds to a given poloidal velocity; therefore a non-zero E_r' would mean that the poloidal rotation is differential, i.e. varies with r . If

we imagine a turbulent cell extending in the radial direction, the varying $\mathbf{E} \times \mathbf{B}$ velocity (sheared flow) means that the cell is torn apart due to the difference in velocity. That is the basic idea of turbulence suppression (or decorrelation) by a sheared flow, see [38] (additional references in chapter 8). In actual comparisons between theory and experiment, one calculates the $\mathbf{E} \times \mathbf{B}$ shearing rate [65]

$$\omega_s = \frac{(RB_\theta)^2}{B} \frac{\partial}{\partial \psi} \left(\frac{E_r}{RB_\theta} \right), \quad (172)$$

where ψ is the normalised radial flux coordinate. The shearing rate formula is written using a number of approximations, see [30]. For shear flow decorrelation of turbulence to occur, the shearing rate ω_s must exceed the maximum growth rate γ_{MAX} of the instability dominating the plasma [30]. Note that ω_s is not constant on a flux surface and that it depends on radius. This is where the shear in the radial electric field enters: If E'_r is large, ω_s is large and more likely to dominate over the instability growth rates.

Shear flow decorrelation is currently being investigated as a possible explanation for the L-H transition and the transition to other improved confinement regimes. The first experimental evidence that E'_r changes before the turbulence suppression at the L-H transition was presented in [109]. The measured E_r in W7-AS and its possible connection to turbulence will be discussed in chapter 8.

6 The Wendelstein 7-AS stellarator

The electron density fluctuation measurements in this thesis were made in the Wendelstein 7 Advanced Stellarator (W7-AS) [119]. W7-AS is named after the Wendelstein mountain in the Bavarian Alps. It is a continuation of the stellarator program at the Max-Planck-Institut für Plasmaphysik (IPP) in Garching, Germany, and came into operation in 1988.

In section 6.1 we describe the main hardware parameters of the W7-AS machine. Section 6.2 deals with the plasma current and associated quantities, while we discuss the magnetic field structure in section 6.3.

6.1 Engineering parameters

6.1.1 The magnetic field

W7-AS is a pentagon-shaped (viewed from above) stellarator, where the main magnetic field is created by a set of 45 modular (i.e. non-planar) copper coils, see figure 29. Modular coils create both the poloidal and toroidal component of the confining magnetic field, in contrast to tokamaks where external coils only produce the toroidal magnetic field [160]. The machine can be viewed as five linked mirrors, where larger coils are positioned at the corners. These large coils can be used to change the magnetic mirror ratio; that is, the toroidal variation of the magnetic field [21] [75]. The maximum toroidal magnetic field on axis B_0 is 2.5 T.



Figure 29. (Colour) The modular coil system of W7-AS. Each of the five modules consists of eight coils, with additional larger coils connecting the straight sections. The central red ring inside the coils symbolises the plasma.

Additional planar coils are positioned outside the modular coils to allow for experimental flexibility, see figure 30 and section 6.2. The flux surface shape varies as a function of the toroidal angle φ , meaning that W7-AS is a non-axisymmetric device (tokamaks are axisymmetric). Flux surfaces vary from being triangular in the straight sections (centered at $\varphi = 0^\circ$) to elliptical in the corners (centered at $\varphi = \pm 36^\circ$). The final set of coils around the plasma is poloidal field coils creating a vertical magnetic field B_z . This field controls the position of the plasma along R .

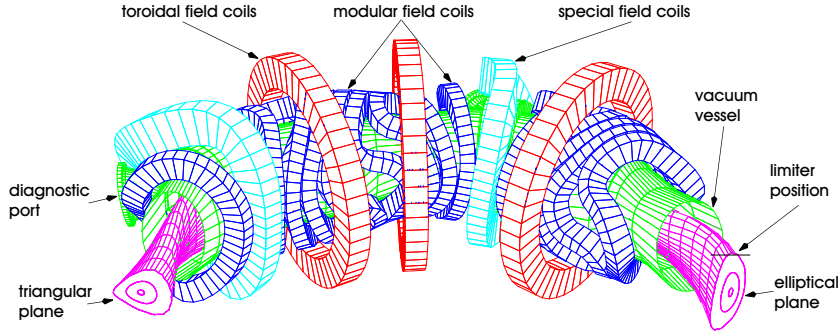


Figure 30. (Colour) The coil system of W7-AS along with a flux surface contour; the flux surface varies from being triangular (straight sections) to elliptical (corner sections).

6.1.2 Dimensions

The major radius R_0 (averaged over the toroidal angle φ) is 2 m, while the minor radius $a \leq 18$ cm. This means that the aspect ratio $1/\varepsilon = R_0/a \geq 11$. One often uses the effective minor radius r_{eff} to enable mapping between diagnostics situated at different φ . This is the radius corresponding to a circular torus enclosing the same volume as that of an actual W7-AS flux surface:

$$2\pi^2 R_0 r_{\text{eff}}^2 = \int_{\text{flux surface}} d\mathbf{r} \quad (173)$$

The total volume of a W7-AS plasma is about 1 m^3 . When we from now on write r for the minor radius, it is to be understood as r_{eff} . The vacuum vessel is made of stainless steel, with a base pressure of about 10^{-8} mbar. Cleaning of the vessel during operational campaigns is done using He glow discharges (daily) or by applying Boronisation (occasionally), where a Boron layer of a few hundred Å is deposited on the walls [156].

6.1.3 Plasma-wall interaction

Impurities entering the plasma from the vessel walls are detrimental for a plasma discharge because they lead to a large amount of radiation and dilute the fuel [160]. To restrict impurities from entering the plasma, one needs to separate the plasma from the vacuum vessel. This can be done using two techniques:

- An outer boundary of the plasma can be defined by material limiters extending from the vessel into the machine.
- The magnetic field can be modified to create a magnetic divertor.

Each of the two methods creates a last closed flux surface (LCFS), meaning well-defined flux surfaces. Outside the LCFS radius, field lines are open, meaning that they hit the vessel wall after a certain number of toroidal revolutions.

The plasma-wall interaction in W7-AS has undergone several changes during the years of operation:

1. Two vertically moveable limiters (TiC-coated graphite), 80×40 cm (toroidal \times poloidal) were placed in neighbouring field periods at the top and bottom of the elliptical cross section [156] [68].
2. Ten inner limiters (carbon-fiber-composite (CFC)), 12×23 cm (toroidal \times poloidal), two in each module [102].

3. Ten divertor modules (CFC), 70×15 cm (toroidal \times poloidal) and graphite baffles, two in each module at the top and bottom of the elliptical cross section [64].

6.1.4 Heating and fuelling

Heating of the plasma is done using either electron cyclotron resonance heating (ECRH), ion cyclotron resonance heating (ICRH) or neutral beam injection (NBI) [160]:

- ECRH: The localisation of the power deposition can be varied by changing the magnetic field, from being on-axis to about 10 cm off-axis.
 1. 0.5 MW heating power from one 70 GHz gyrotron [86]. The heating is restricted to densities $n \leq 3 \times 10^{19} \text{ m}^{-3}$ for 1.25 T and $n \leq 6 \times 10^{19} \text{ m}^{-3}$ for 2.5 T.
 2. 2.1 MW heating power from four 140 GHz gyrotrons delivering 3×600 kW and 1×300 kW [50]. The heating is restricted to densities $n \leq 1.2 \times 10^{20} \text{ m}^{-3}$ for 2.5 T. However, heating can be accomplished at higher densities using a mode conversion scheme [96].
- ICRH: An antenna system with frequencies between 35 and 110 MHz yielding up to 1.2 MW of power is installed [119].
- NBI: Two beam boxes each with four neutral beams are installed on W7-AS [86]. Each of the eight beam lines delivers 500 kW of heating power at 45/55 keV (H/D), totalling 4 MW. Initially, the beams in one box fired in the co-direction, whereas the beams in the other box fired in the counter-direction. Here, the co-direction is the direction opposite to the toroidal magnetic field, increasing the rotational transform. Now, both boxes fire in the co-direction, leading to an improved heating efficiency at low magnetic fields and at high densities [87].

A W7-AS plasma discharge has a typical duration of 0.5 to 1 s and is also called a pulse or a shot.

The plasma is fuelled by gas puffing from valves in the vessel and/or by NBI particles deposited in the plasma.

6.2 Plasma current

6.2.1 The rotational transform

The rotational transform ι is a quantity related to the winding of the magnetic field lines on a flux surface. This helical winding occurs because the magnetic field has both a toroidal and poloidal component. The rotational transform is defined as

$$\iota = \frac{2\pi}{\Delta\varphi}, \tag{174}$$

where $\Delta\varphi$ is the toroidal angle interval for a field line to return to the initial poloidal angle [160]. If ι has an irrational value, the field line covers a flux surface ergodically. However, if ι is a rational number (n/m) it returns to the exact poloidal position after n poloidal and m toroidal rotations round the torus. These rationals play an important role in plasma stability; we will return to this subject in section 6.3.

The rotational transform of W7-AS created by the modular coils is about 0.4, and can be varied between 0.25 and 0.67 using the planar coils [85]. Since ι varies with minor radius r , we can define a quantity called the magnetic shear [24]

$$\iota' = \frac{d\iota}{dr} \quad (175)$$

The shear in W7-AS in the basic configuration is quite small for the vacuum field of W7-AS, $|\Delta\iota/\iota_0| = |t_a - t_0|/\iota_0 < 0.04$, where t_0 is the rotational transform on axis and t_a is the boundary value (at $r = a$) [21].

The rotational transform profile is determined by two components: The external transform and a contribution due to internal plasma currents

$$\iota(r) = \iota_{\text{ex}}(r) + \frac{\mu_0 R_0}{B_\varphi r^2} \int_0^r (J_{\text{BS}} + J_{\text{PS}} + J_{\text{OH}}) r' dr', \quad (176)$$

where ι_{ex} is the external rotational transform and the current densities J in the integrand are bootstrap (BS), Pfirsch-Schlüter (PS) and Ohmic (OH) [24] [160]. Each of these currents are treated in subsections 6.2.2, 6.2.3 and 6.2.4, respectively.

6.2.2 The bootstrap current

The bootstrap current has its name from Baron von Münchhausen's claim to be able to lift himself by tugging on his own bootstraps. In the same sense, it is hoped that the large toroidal plasma current creating the poloidal magnetic field in tokamaks can be created by the plasma itself.

The bootstrap current is related to the variation of the magnetic field strength with major radius: $B_\varphi \propto 1/R$. The two adiabatic invariants of motion - the total particle energy ($E = m(v_{\parallel}^2 + v_{\perp}^2)/2$) and magnetic moment ($\mu = mv_{\perp}^2/2B_\varphi$) - are conserved. The variation of the toroidal field strength can be written

$$B_\varphi = B_0 \frac{R_0}{R} = \frac{B_0 R_0}{R_0 + r \cos \theta} \approx B_0 (1 - \varepsilon \cos \theta), \quad (177)$$

where the inverse aspect ratio ε is assumed to be small. A particle follows a field line with $r = \text{constant}$, and the variation in its parallel velocity is

$$v_{\parallel}^2 = \frac{2E}{m} - v_{\perp}^2 = \frac{2E}{m} - v_{\perp 0}^2 (1 - \varepsilon \cos \theta), \quad (178)$$

where the subscript 0 is for a poloidal angle θ of 0° . If $2E/m - v_{\perp 0}^2 < \varepsilon v_{\perp 0}^2$ (or $v_{\parallel 0}^2 < 2\varepsilon v_{\perp 0}^2$), v_{\parallel}^2 becomes negative when $\theta > \theta_r = \arccos(1 - v_{\parallel 0}^2/\varepsilon v_{\perp 0}^2)$ which has no physical meaning. What actually happens is that the parallel velocity changes sign, and bounces between the reflection points $\pm \theta_r$. This is called the magnetic mirror effect and leads to trapping of particles with a sufficiently small parallel velocity at $\theta = 0^\circ$ [40].

The trapped orbits reside on the outboard (low field) side of the machine and follow a banana shaped orbit if one represents the motion in a poloidal cross section. The particles have a drift due to the inhomogeneity of the magnetic field, leading to a finite width w of the banana orbits [160]:

$$w = \frac{mv_{\parallel 0}}{eB_\theta} \quad (179)$$

If we consider two trapped ions starting with the same energy and moment from the same point with parallel velocities having equal sizes but opposite signs, their averaged radii will differ due to the banana width. If a radial density gradient

exists, an asymmetry will develop in the velocity distribution [114]. This asymmetry will also occur for electrons, but in the opposite direction. The resulting parallel current is called the banana current J_B . The magnitude of this current can be found as follows: The surplus of particles in the direction of the current is $n_i = wd n_t/dr$, where $n_t \approx \sqrt{\varepsilon}n$ is the trapped particle density. Their average velocity is $u_{\parallel i, \text{trapped}} \approx \sqrt{\varepsilon}v_{\text{th}}$, where $v_{\text{th}}^2 = T/m$ is the thermal velocity. These equations lead to a current due to the trapped ions of

$$J_B = en_i u_{\parallel i, \text{trapped}} = \frac{\varepsilon^{3/2}}{B_\theta} T \frac{dn}{dr} \quad (180)$$

The major part of the bootstrap current is carried by passing particles and is caused by collisional coupling of trapped and passing particles. This scattering can either lead to trapped particles becoming passing or vice versa. The equation for the parallel velocity of passing particles is

$$n \frac{du_{\parallel p}}{dt} = \frac{\nu_{ii}}{\varepsilon} n_i u_{\parallel i} [t \rightarrow p] - \sqrt{\varepsilon} \nu_{ii} n u_{\parallel p} [p \rightarrow t] = \frac{\nu_{ii}}{\varepsilon} \frac{\varepsilon^{3/2} T}{e B_\theta} \frac{dn}{dr} - \sqrt{\varepsilon} \nu_{ii} n u_{\parallel p}, \quad (181)$$

where ν_{ii} is the ion-ion collision frequency. Defining the ion viscosity coefficient $\mu_i = mn\sqrt{\varepsilon}\nu_{ii}$, the electron viscosity coefficient $\mu_e \approx m_e n_e \sqrt{\varepsilon}\nu_{ei}$ and the electron-ion friction coefficient $l_{ei} = m_e n_e \nu_{ei}$, the steady-state equations for the parallel velocity of the ions and electrons are

$$\begin{aligned} \mu_i \left[\frac{T}{en_i B_\theta} \frac{dn_i}{dr} - u_{\parallel i} \right] &= 0 \\ \mu_e \left[\frac{T}{en_e B_\theta} \frac{dn_e}{dr} - u_{\parallel e} \right] &= l_{ei} (u_{\parallel e} - u_{\parallel i}) \end{aligned} \quad (182)$$

These equations can be solved for the parallel velocities, and the bootstrap current can be calculated from the velocity difference:

$$J_{\text{BS}} = \frac{T}{B_\theta} \frac{\mu_e}{\mu_e + l_{ei}} \left[\frac{dn_i}{dr} + \frac{dn_e}{dr} \right] \approx \sqrt{\varepsilon} \frac{T}{B_\theta} \left[\frac{dn_i}{dr} + \frac{dn_e}{dr} \right], \quad (183)$$

where the last approximation is valid for small ε , so that $\mu_e \ll l_{ei}$. We see that this current is a factor $1/\varepsilon$ larger than the banana current. In general the bootstrap current is a function of the pressure gradient instead of the density gradient; therefore it is a pressure-driven current. We refer to [114] and references therein for a more thorough description of the bootstrap current and useful illustrations.

It is usually sufficient for W7-AS to use an expression of the bootstrap current derived for a circular tokamak times a factor:

$$J_{\text{BS}} = f_{\text{BS}} J_{\text{BS}}^{\text{HH}}, \quad (184)$$

where the factor f_{BS} accounts for the elongation of W7-AS flux surfaces and is between 0.5 and 0.7 [24]. The current density $J_{\text{BS}}^{\text{HH}}$ is taken from [69].

6.2.3 The Pfirsch-Schlüter current

As the bootstrap current, the Pfirsch-Schlüter current is pressure-driven. For a small plasma β ,

$$\beta = \frac{p_{\text{particle}}}{p_{\text{magnetic field}}} = \frac{nT}{B^2/2\mu_0}, \quad (185)$$

which is the particle pressure divided by the magnetic field pressure, the Pfirsch-Schlüter current is small compared to the bootstrap current. We will here limit ourselves to a description of the current and simply state the result.

The fact that the magnetic field has a $B_\varphi \propto 1/R$ dependency gives rise to a vertical drift of the charged particles. This would lead to an accumulation of oppositely charged particles at the top and bottom of the torus. The resulting vertical electric field would cause the plasma to drift to the outboard side of the torus. To prevent this situation from materialising, a poloidal magnetic field must be created by a plasma current in the toroidal direction. Thereby magnetic field lines spiral and the surplus of electrons and ions neutralise each other by flowing along the magnetic field. This current is known as the Pfirsch-Schlüter current [40]. A derivation of the Pfirsch-Schlüter current is given in [160] and the result is

$$J_{\text{PS}} = -2 \frac{1}{B_\theta} \frac{r}{R} \frac{dp}{dr} \cos \theta \quad (186)$$

6.2.4 Ohmic current

To drive a toroidal current, an external transformer is installed; this can be viewed as a primary winding, while the plasma is the secondary winding [46]. A change of flux through the torus induces a toroidal electric field, driving the toroidal current [160]. The resulting current is called the Ohmic current. The loop voltage V_{loop} in W7-AS is given by

$$V_{\text{loop}} = -L_p \frac{dI_p}{dt} - \frac{L_{\text{OH}}}{N} \frac{dI_{\text{OH}}}{dt}, \quad (187)$$

where $L_{\text{OH}} = 12.7$ mH is the inductance of the transformer, $N = 162$ is the number of windings in the transformer, L_p is the inductance of the plasma ring, I_p is the plasma current and I_{OH} is the current in the transformer [25].

To clarify the effect of the Ohmic current, we write equation 176 for the boundary value of the total rotational transform:

$$t_a = t_{\text{ex}}(a) + \Delta t_I, \quad (188)$$

where $\Delta t_I = \mu_0 R_0 I_p / 2\pi a^2 B_0$ for a total plasma current I_p [21]. For typical parameters $a = 0.15$ m, $R_0 = 2$ m and $B_0 = 2.5$ T, so that $\Delta t_I = 0.007$ kA⁻¹ I_p . Since the Ohmic current is part of the total current, it can be chosen so that the desired t_a is realised. Plasma currents up to ± 30 kA can be inductively driven, where a positive/negative current increases/decreases t , respectively.

6.2.5 Stellarator optimisation

By stellarator optimisation we mean a reduction of the parallel current density J_{\parallel} [152]. For a classical stellarator such as W7-A (with $l = 2$ pairs of conductors), the ratio of parallel to perpendicular current is

$$\frac{\langle J_{\parallel}^2 \rangle}{\langle J_{\perp}^2 \rangle} = \frac{2}{t^2}, \quad (189)$$

while the factor 2 in the numerator is reduced in W7-AS and further decreased in W7-X [152]. A reduction of the parallel current reduces the outward Shafranov shift Δ_0 of the plasma axis and the neoclassical fluxes in the long-mean-free-path (LMFP) regime [75]. A reduction of the Shafranov shift in W7-AS compared to the classical stellarator has been verified using soft X-ray measurements to localise

the magnetic axis. The Shafranov shift is related to the average beta $\langle\beta\rangle$ through the equation

$$\frac{\Delta_0}{a} \approx \frac{R}{a} \left(\frac{C_{01}}{r/R} \right)^2 \frac{\langle\beta\rangle}{2t^2}, \quad (190)$$

where $C_{01}/(r/R)$ is the normalised toroidal curvature (0.7 for W7-AS) [75].

6.3 The magnetic field structure

The magnetic field structure in W7-AS is rather complex and often composed of two separate components, a central main plasma and an intricate superimposed structure. These two phenomena will be described in subsections 6.3.1 and 6.3.2.

6.3.1 Nested flux surfaces

A set of nested flux surfaces always inhabits the central portion of the plasma. An example is shown for three toroidal angles in figure 31 at $t_a = 0.344$. The intact flux surfaces extend all the way to the limiters in this case, resulting in a limiter configuration. The main plasma decreases in size with increasing t_a , so that for $0.25 \leq t_a < 0.5$ the plasma is limiter bound, whereas for $0.5 \leq t_a \leq 0.67$ it is separatrix bound [85] [102]. This means that the LCFS is not defined by limiters, but by a natural island chain surrounding the main plasma.

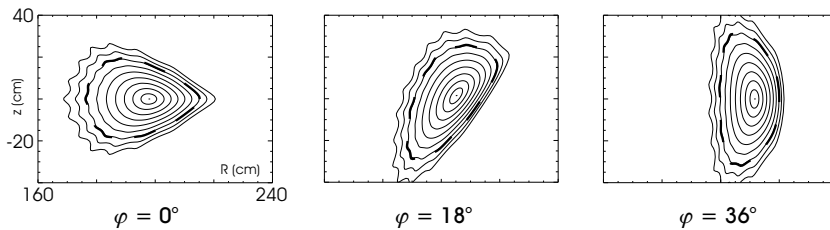


Figure 31. Flux surfaces of a plasma having a boundary rotational transform of 0.344. Left to right: Toroidal angle $\varphi = 0^\circ$, 18° and 36° . The dashed line shows the LCFS due to limiter action.

6.3.2 Magnetic island formation

Magnetic islands - closed flux surfaces separated from the main set of nested flux surfaces - exist in W7-AS plasmas for three different situations:

1. Natural islands: Due to the pentagon shape of W7-AS.
2. Field errors: Due to imperfections in the confining magnetic field.
3. MHD activity: Due to instabilities.

Each of these cases will now be described in turn.

Natural islands Natural islands in W7-AS are related to the five-fold symmetry of the magnetic field and occur if the t -value is equal to $5/m$, m being the poloidal mode number. The t -profile can be adjusted so that the boundary rotational transform t_a is resonant with the intrinsic $B_{5,m}$ perturbation field component [64]. Note that the number of poloidal windings n is 5. The poloidal mode numbers can be $8 \leq m \leq 12$ [75]. Three examples of magnetic islands are shown

in figure 32, for an increasing m -number from left to right ($m = 10, 11$ and 12). The m -number is equal to the number of islands in a poloidal cross section. The toroidal angle is 30° and the flux surfaces are calculated for a vacuum magnetic field configuration, meaning $\beta = 0$. The center of an island is called the O-point, the separation between two islands is called the X-point (see right-hand plot in figure 32). The size of the islands can be varied using control coils mounted inside the vessel [102].

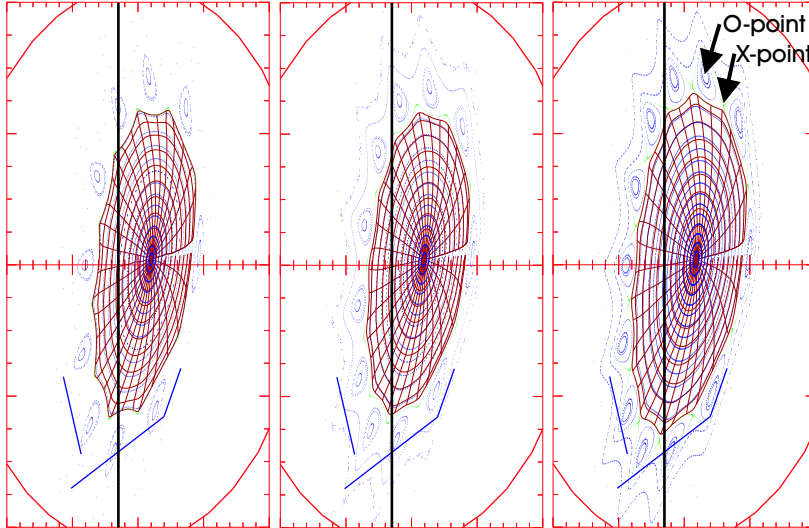


Figure 32. (Colour) Magnetic island formation for the vacuum case. Left to right: Poloidal mode number $m = 10, 11$ and 12 . The vertical line marks the measurement volume and the bottom lines show the position of the divertor and enclosing baffles [159].

Field errors An ideal torus confining a plasma can be viewed as an integrable system with a Hamiltonian $H_0(\mathbf{p}, \mathbf{q})$, where \mathbf{p} is momentum and \mathbf{q} is position. One can here add a non-integrable part $\varepsilon H_1(\mathbf{p}, \mathbf{q})$

$$H(\mathbf{p}, \mathbf{q}) = H_0(\mathbf{p}, \mathbf{q}) + \varepsilon H_1(\mathbf{p}, \mathbf{q}), \quad (191)$$

where ε determines the strength of the non-integrable part of the total Hamiltonian $H(\mathbf{p}, \mathbf{q})$ [111]. This symmetry-breaking can occur in fusion machines due to e.g. errors in the external field coils (manufacturing/positioning), asymmetries of the vessel wall or because of a plasma current. The effect of the perturbations has been described by the Kolmogorov-Arnold-Moser (KAM) theorem; the result can be the formation of island structures.

The effect of field errors in W7-AS has been thoroughly investigated [85]. It was found that the presence of rational ι -values in the plasma has a significant influence on the magnetic field topology, both due to the natural islands and field errors. Especially the low-order (small m and n values) rationals $\iota = 1/2$ and $1/3$ have a large effect on the main plasma size and energy confinement, while higher order (larger m and n values) rationals are of minor importance. We will return to the relationship between ι and confinement in chapter 8.

MHD activity MHD instabilities arise for example due to current or pressure gradients [160]. These instabilities have an infinite spectrum of possible modes

which can be written in the form $e^{i(m\theta - n\varphi)}$, where m and n are the poloidal and toroidal mode numbers, respectively.

In W7-AS, an important MHD instability is driven by the interaction with fast particles injected by neutral beams [157]. This is called the global Alfvén eigenmode (GAE) and leads to low frequency (20 to 300 kHz) fluctuations. The mode numbers (m,n) can be determined by tomographic inversion of soft X-ray measurements, see figure 33. The mode propagates in the ion DD direction.

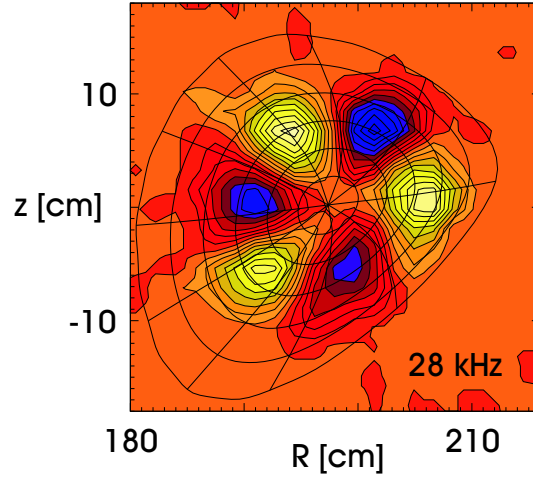


Figure 33. (Colour) Tomographic inversion of soft X-ray measurements of a $(m,n) = (3,1)$ GAE mode. The figure is adapted from [157].

7 Experimental setup

In this chapter the practical realisation of the density fluctuation diagnostic is described [128] [129] [130]. Our abbreviation for the system is the localised turbulence scattering (LOTUS) diagnostic. The three main parts of the optical system - transmitting bench, measurement plane and receiving bench - are described in section 7.1 along with details of uncertainties, stepper motors and the diagnostic position. In section 7.2 we then proceed to describe the detectors, their SNR and the acquisition electronics in detail.

7.1 Optical buildup

The three following subsections containing the detailed description of the optical setup are organised as a step-by-step explanation of the optical components. Please consult figure 34 for the optical components on the transmitting and receiving tables.

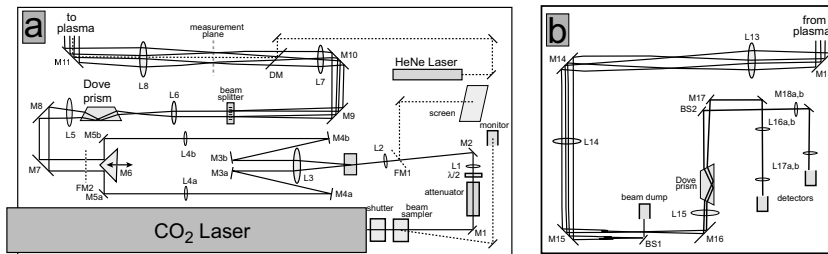


Figure 34. Optical layout of transmitting (a) and receiving (b) tables. The figure is adapted from [132].

One can calculate the beam waist between the lenses of the system by assuming that the lenses have a confocal spacing. This means that two lenses L and L' having focal lengths f (first lens) and f' (last lens) should be placed with a distance of $f + f'$ between them. If this is the case, the two lenses create a Newtonian telescope, with a magnification factor $M = f'/f$ [134]. This means that the beam is expanded if $f < f'$ and condensed if $f > f'$. Two lenses with identical focal lengths will simply relay the beam. When quoting actual focal lengths, we will do so in mm. All lenses in the setup are Zinc Selenide (ZnSe) anti-reflection (AR) coated. Assuming that the beam is Gaussian, one obtains that the relationship between the beam waist before (w_0^{before}) and after (w_0^{after}) a lens with focal length f is given by equation 192:

$$w_0^{\text{after}} = \frac{\lambda_0 f}{\pi w_0^{\text{before}}} \quad (192)$$

One then steps through the optical system and calculates the waist between each pair of lenses at their focal lengths. The most important waist sizes are those in the plasma and at the detectors.

We need an additional simple formula to proceed with the optical layout:

$$\theta = d/f, \quad (193)$$

where d is the distance between two parallel beams before the lens and θ is their crossing angle at the focal point after the lens. The angle θ is assumed to be small.

7.1.1 Transmitting bench

1. When describing the transmitting system, we initially encounter the radiation source, which is a CO₂ laser, built by Ultra Lasertech and modified by Risø. The laser delivers roughly 20 W continual wave (CW) and is operated in the fundamental TEM₀₀ mode. The laser wavelength λ_0 is 10.59(1043458) μm . Mode suppression calculations have been made [130], resulting in the insertion of an aperture of adjustable size into the laser cavity just before the output mirror. The standard diameter used is 7.8 mm. The typical values of the exciter voltage and current are 25 kV and 9.5 mA, respectively.

The cavity length is 1380 mm, the radius of curvature of the end mirror (or diffraction grating) 3000 mm with a flat output mirror connected to a piezo electric transducer (PZT). The gain medium is contained in a glass tube with Brewster windows mounted on each end.

Several modifications to the laser system had to be made in the course of my project, including replacement of high voltage resistors in the exciter and the installation of a new laser stabilisation scheme due to inadequacies of the built-in system [132]. In this scheme the PZT is dithered at 700 Hz, resulting in a modulation of the intracavity intensity. A PDI-10.6 photovoltaic detector from Vigo-System Ltd. collects the light reflected from one of the Brewster windows and an error signal is constructed.

The beam waist w_0^{laser} at the output mirror has a nominal value of 2.25 mm.

2. Shutter: Enables one to block the beam. The shutter is connected to an interlock system preventing operation if personnel are present in the torus hall.
3. ZnSe beam sampler: Diffracts 0.1 % power from the main beam. The diffracted beam is focused using a mirror and a 200 mm lens into a PCI-L-1 photoconductive detector from Vigo-System Ltd. to monitor the laser stability.
4. Mirror *M1*
5. Variable attenuator: Six ZnSe Brewster plates reduce the power during alignment. As a side effect, the attenuator rotates the optical polarisation.
6. Cadmium Selenide (CdSe) half wave plate: Makes the beam horizontally polarised. This is required by the Bragg cell for maximum deflection of power into the frequency shifted LO beam (see below).
7. Lens *L1*
8. Mirror *M2*
9. Flip mirror *FM1*: If this mirror is used, the beam is expanded using a 85 mm lens and sent to a thermal image plate for visual beam quality inspection.
10. Lens *L2*
11. The Bragg cell is a Germanium (Ge) device; the diffracted beam is frequency shifted 40 MHz and used as the LO beam.
12. Lens *L3*
13. Mirrors *M3a* and *M3b*
14. Mirrors *M4a* and *M4b*
15. Lenses *L4a* and *L4b*
16. Mirrors *M5a* and *M5b*

17. Scattering angle adjuster: A 90° mirror ($M6$) is mounted on a translation stage. Moving the mirror changes the beam separation d_1 , thereby altering the scattering angle θ_s in the plasma.
18. Flip mirror $FM2$: If this mirror is used, the two beams are sent from the transmitting table to a thermal image plate several meters away. This checks if the beams are parallel.
19. Mirror $M7$
20. Mirror $M8$
21. Lens $L5$
22. ZnSe Dove prism [134]: Changes the angle α at which the wave vector is measured, see chapter 3. Usually set so that we measure mainly perpendicular to the toroidal magnetic field. The parallel LO and M beams (before the lens $L5$ having a focal length f_5) overlap after the lens with a crossing angle $\theta_1 = \frac{d_1}{f_5}$. The focal plane after $L5$ is called a measurement plane, since the LO and M beams here define a measurement volume. Each lens hereafter Fourier transforms the beams [59], meaning that we have alternating Fourier and measurement planes.
23. Lens $L6$
24. ZnSe diffractive beam splitter: The beam waists are centered on this 50 mm diameter splitter. The distance between the incoming parallel LO and M beams is here $d_2 = f_6\theta_1$. The angular separation of the beams after the beam splitter is 10 or 25 mrad ($\theta_2 = 0.010$ or 0.025 rad). The splitter means that we have two measurement volumes instead of one. Further, by rotating the splitter, the relative position of the measurement volumes θ_R is changed, see chapter 3. 20 % of the incident power is contained in higher order spots.
25. Mirror $M9$
26. Mirror $M10$
27. Lens $L7$
28. Dichroic mirror DM : Combines the CO_2 beams with a Helium-Neon (HeNe) laser beam. First, the HeNe beam is used to obtain the proper torus alignment, then the CO_2 beams are adjusted to be parallel with and symmetric about the HeNe beam.
29. Pinhole: Stops the higher order spots (originating at the beam splitter) from passing. The distance between the measurement volumes is $d_3 = f_7\theta_2$ and the angle between the LO/M beams $\theta_3 = \frac{d_2}{f_7}$.
30. Lens $L8$
31. Mirror $M11$
32. In this Fourier plane the LO/LO and M/M beams overlap, with a distance $d_4 = f_8\theta_3$. The angle between the beams $\theta_4 = \frac{d_3}{f_8}$.
33. Lens $L9$
34. From here onwards we simply state the formulas for the calculation of volume separation and angle: $d_5 = f_9\theta_4$ and $\theta_5 = \frac{d_4}{f_9}$.
35. Lens $L10$
36. $d_6 = f_{10}\theta_5$ and $\theta_6 = \frac{d_5}{f_{10}}$.
37. Mirror $M12$
38. Lens $L11$

7.1.2 Measurement plane

1. Window $W1$
2. Plasma measurement volume. $d_7 = f_{11}\theta_6$ and $\theta_7 = \frac{d_6}{f_{11}}$. For clarity we here write

$$d_7 = d_{\text{vol}} = \frac{f_{11}f_9f_7}{f_{10}f_8}\theta_2, \quad (194)$$

θ_2 being the beam splitter angle. From this formula we see that the separation of the measurement volumes is fixed for a given set of lenses. We can express the scattering angle as

$$\theta_7 = \theta_s = \frac{f_{10}f_8f_6}{f_{11}f_9f_7f_5}d_1, \quad (195)$$

d_1 being the LO and M beam separation at the 90° mirror. This shows that the scattering angle can be varied by changing d_1 . We note that the measured wavenumber $k = k_0\theta_s$. Finally, equation 192 enables us to write the beam waist in the plasma as

$$w_p = \frac{\lambda_0}{\pi} \frac{f_{11}f_9f_7f_5f_3f_1}{f_{10}f_8f_6f_4f_2} \frac{1}{w_0^{\text{laser}}} \quad (196)$$

3. Window $W2$

7.1.3 Receiving bench

1. Lens $L12$
2. $d_8 = f_{12}\theta_7$ and $\theta_8 = \frac{d_7}{f_{12}}$.
3. Mirror $M13$
4. Lens $L13$
5. $d_9 = f_{13}\theta_8$ and $\theta_9 = \frac{d_8}{f_{13}}$.
6. Mirror $M14$
7. Lens $L14$
8. Mirror $M15$
9. The M beams are sent to a beam dump with a beam scraper (i.e. a mirror with a straight edge) $BS1$. $d_{10} = f_{14}\theta_9$ and $\theta_{10} = \frac{d_9}{f_{14}}$. To ensure a sufficient separation of the LO and M beams, the volume separation

$$d_{10} = d_{BS1} = \frac{f_{14}f_{12}}{f_{13}}\theta_s \quad (197)$$

must be much larger than the beam waist

$$w_{BS1} = \frac{f_{14}f_{12}f_{10}f_8f_6f_4f_2}{f_{13}f_{11}f_9f_7f_5f_3f_1}w_0^{\text{laser}} \quad (198)$$

10. Mirror $M16$
11. Lens $L15$
12. ZnSe Dove prism: Aligns the two LO beams so that they have equal height over the table. $d_{11} = f_{15}\theta_{10}$ and $\theta_{11} = \frac{d_{10}}{f_{15}}$.
13. A mirror $M17$ and a beam scraper $BS2$ pick up the two LO beams and send them to the two separate detectors.
14. Mirrors $M18a$ and $M18b$

15. Lenses *L16a* and *L16b*

16. $d_{12} = f_{16}\theta_{11}$ and $\theta_{12} = \frac{d_{11}}{f_{16}}$.

17. Lenses *L17a* and *L17b*

18. Detectors: Detect the mixed (LO + scattered) signal. $d_{13} = f_{17}\theta_{12}$ and $\theta_{13} = \frac{d_{12}}{f_{17}}$. The beam waist on the detectors is

$$w_d = \frac{\lambda_0}{\pi} \frac{f_{17}f_{15}f_{13}f_{11}f_9f_7f_5f_3f_1}{f_{16}f_{14}f_{12}f_{10}f_8f_6f_4f_2} \frac{1}{w_0^{\text{laser}}} \quad (199)$$

Note that mirror *M12*, lenses *L9–L11* (below torus) and lens *L12* (above torus) are not visible in figure 34. Various configurations have been used during the years of operation, see appendix A for details.

7.1.4 Uncertainties

We will estimate the uncertainty (the precision, not the accuracy [17]) on the following four quantities: The volume separation d_{vol} (equation 194), the measured wavenumber k (equation 195), the beam waist in the plasma w_p (equation 196) and the beam waist on the detectors w_d (equation 199). Note that uncertainties due to the positioning of the lenses (non-confocal spacing) are not treated; they could be accounted for using ray matrices [134]. The following relative uncertainties are assumed:

- $\frac{\sigma_{\theta_2}}{\theta_2} = \frac{0.01 \text{ mrad}}{10 \text{ mrad}} = 0.001 = 0.1 \%$. The same relative uncertainty is assumed for the 25 mrad diffractive beam splitter.
- $\frac{\sigma_f}{f} = 0.005 = 0.5 \%$
- $\frac{\sigma_{d_1}}{d_1} = \frac{1 \text{ mm}}{d_1}$
- $\frac{\sigma_{\lambda_0}}{\lambda_0} = \frac{1.9 \times 10^{-5} \text{ } \mu\text{m}}{10.59 \text{ } \mu\text{m}} = 1.8 \times 10^{-6} = 1.8 \times 10^{-4} \%$
- $\frac{\sigma_{w_0^{\text{laser}}}}{w_0^{\text{laser}}} = \frac{0.1125 \text{ mm}}{2.25 \text{ mm}} = 0.05 = 5 \%$

We are now equipped to write the equations for the total relative uncertainties. We make use of the error propagation equation [17]:

$$\begin{aligned} \frac{\sigma_{d_{\text{vol}}}^2}{d_{\text{vol}}^2} &= \frac{\sigma_{\theta_2}^2}{\theta_2^2} + \frac{\sigma_{f_7}^2}{f_7^2} + \frac{\sigma_{f_8}^2}{f_8^2} + \frac{\sigma_{f_9}^2}{f_9^2} + \frac{\sigma_{f_{10}}^2}{f_{10}^2} + \frac{\sigma_{f_{11}}^2}{f_{11}^2} = \frac{\sigma_{\theta_2}^2}{\theta_2^2} + \frac{\sigma_{f_{7,8,9,10,11}}^2}{f_{7,8,9,10,11}^2} \\ \frac{\sigma_k^2}{k^2} &= \frac{\sigma_{d_1}^2}{d_1^2} + \frac{\sigma_{\lambda_0}^2}{\lambda_0^2} + \frac{\sigma_{f_{5,6,7,8,9,10,11}}^2}{f_{5,6,7,8,9,10,11}^2} \\ \frac{\sigma_{w_p}^2}{w_p^2} &= \frac{\sigma_{\lambda_0}^2}{\lambda_0^2} + \left(\frac{\sigma_{w_0^{\text{laser}}}}{w_0^{\text{laser}}} \right)^2 + \frac{\sigma_{f_{1,2,3,4,5,6,7,8,9,10,11}}^2}{f_{1,2,3,4,5,6,7,8,9,10,11}^2} \\ \frac{\sigma_{w_d}^2}{w_d^2} &= \frac{\sigma_{\lambda_0}^2}{\lambda_0^2} + \left(\frac{\sigma_{w_0^{\text{laser}}}}{w_0^{\text{laser}}} \right)^2 + \frac{\sigma_{f_{1,2,3,4,5,6,7,8,9,10,11,12,13,14,15,16,17}}^2}{f_{1,2,3,4,5,6,7,8,9,10,11,12,13,14,15,16,17}^2} \end{aligned} \quad (200)$$

Inserting the actual relative uncertainties, the equations are

$$\begin{aligned}
\frac{\sigma_{d_{\text{vol}}}^2}{d_{\text{vol}}^2} &= 0.000126 \\
\frac{\sigma_k^2}{k^2} &= \frac{\sigma_{d_1}^2}{d_1^2} + 0.000175 \\
\frac{\sigma_{w_p}^2}{w_p^2} &= 0.00278 \\
\frac{\sigma_{w_d}^2}{w_d^2} &= 0.00293
\end{aligned} \tag{201}$$

An example We would like to calculate the relative and absolute uncertainties of the setup completed 28/7/99, see appendix A. This was the single volume case, so we will not treat the uncertainty on d_{vol} (which has a relative uncertainty of 1.1 %). We assume that $k = 15 \text{ cm}^{-1}$, so that the beam separation d_1 at $M6$ was 27.93 mm. The relative uncertainties are therefore already given by equations 201:

$$\begin{aligned}
\frac{\sigma_k}{k} &= 0.038 = 3.8 \% \\
\frac{\sigma_{w_p}}{w_p} &= 0.053 = 5.3 \% \\
\frac{\sigma_{w_d}}{w_d} &= 0.054 = 5.4 \%
\end{aligned} \tag{202}$$

Using the values $(k, w_p, w_d) = (15 \text{ cm}^{-1}, 33.1 \text{ mm}, 0.45 \text{ mm})$, we arrive at the absolute uncertainties:

$$\begin{aligned}
\sigma_k &= 0.6 \text{ cm}^{-1} \\
\sigma_{w_p} &= 1.8 \text{ mm} \\
\sigma_{w_d} &= 0.02 \text{ mm}
\end{aligned} \tag{203}$$

The results above can be used to estimate errorbars on I_{11} , see subsection 3.3.2. For the simulations described in that subsection, we varied k and w_p using the relative uncertainties found above. The corresponding modification of I_{11} was of order 10 %, which is the errorbar we will use in chapter 8.

7.1.5 Stepper motors

The mirror $M6$, the beam splitter and the Dove prisms are all controlled electronically. The stepper motors are manufactured by Physik Instrumente and controlled using Berger Lahr cards. Usually, the Dove prism on the transmitting table is left fixed, while the other three components are controlled independently by stepper motors. This enables us to change the relative measurement volume position and measured wavenumber between shots.

7.1.6 Diagnostic position

The diagnostic position is determined by the location of the access ports allocated to the system. These ports are at the top and bottom of the vacuum vessel; they are circular and have a diameter of 200 mm. The ends are closed off by ZnSe AR coated windows. The ports are located in module 4 (5 modules in total) on the south side of the machine. The toroidal angle φ of the diagnostic position was

29.14° in 1999 but was changed to 30.09° in 2000 due to the divertor installation. The windows are centered at major radius $R = 2089.57$ mm. Figure 35 shows the flux surfaces for a $t_a = 0.344$ discharge. The center of the single volume setup/center of rotation for the dual volume setup is indicated by a vertical line. The insets show the pitch angle and the conversion between r_{eff} and z coordinates.

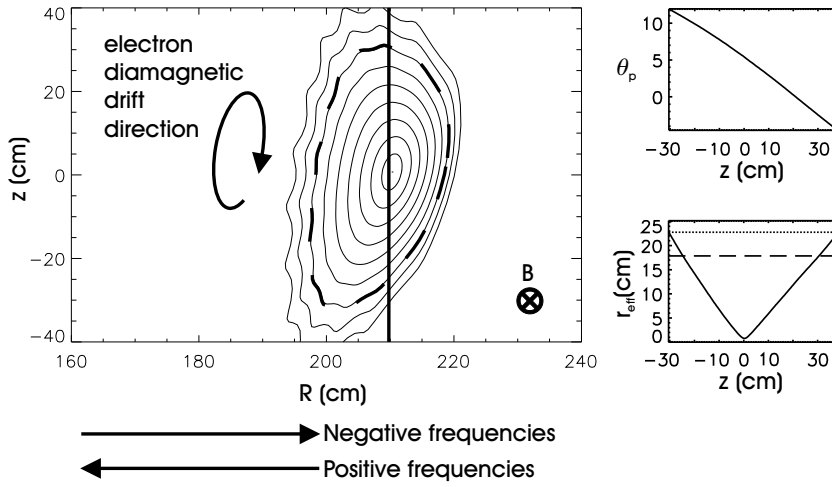


Figure 35. Main figure: Flux surfaces and measurement volume position (vertical line) for the 1999 diagnostic position, upper small inset: Pitch angle along the measurement volume, lower small inset: Conversion between r_{eff} and z coordinates. In this lower plot the dashed line shows the LCFS and the dotted line marks the largest r_{eff} value treated.

7.2 Acquisition system

7.2.1 Detectors

We have used photoconductive Mercury Cadmium Telluride (HgCdTe, sometimes called MCT) detectors operated at room temperature. They are of type PCI-L-3 from Vigo-System Ltd.. The active area is 1 mm^2 and the damage level is 100 W/cm^2 , so that the power into the detectors should be below 1 W . For more details on the detectors and their measured parameters see [130] [132]. The detector electronics is shown in figure 36.

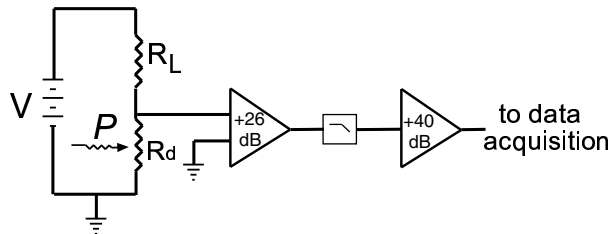


Figure 36. Detector electronics. The load resistance is R_L , the detector resistance R_d and the detector output is amplified in two stages sandwiching a low pass filter. The figure is taken from [132].

The detectors are biased with a constant current (usually 7 mA) using a load resistor of $R_L = 950 \text{ } \Omega$. The detector resistance $R_d \approx 50 \text{ } \Omega$. The voltage across

the detector resistance is first amplified 26 dB by a Boston Electronics amplifier model 490. It is a 50 Ω device with a bandwidth of 1 kHz to 100 MHz. The noise figure (NF) [89] of the amplifier is 2.8 dB. Following this amplifier there is a 48 MHz low pass filter (Mini-Circuits BLP-50) and then a second amplifier with 40 dB gain (Boston Electronics 493A/40) with a bandwidth of 1 kHz to 500 MHz. Finally, there is a Boston Electronics 491 video line driver with unity gain. The line driver is used due to the distance (~ 10 m) between the detectors and the acquisition system.

7.2.2 Signal-to-noise ratio

The dominant noise source in our room temperature system is thermal noise (also called Johnson or Nyquist noise) [130]. This noise is the fluctuation caused by thermal motion of the charge carriers in a resistive element [41]. Since the thermal noise is created in both the photoconductor and the load resistor we can write the thermal noise current as

$$I_{\text{th}} = \sqrt{\frac{4T_d B}{R_d} + \frac{4T_L B}{R_L}} = \sqrt{\frac{4TB}{R_{\text{eq}}}}, \quad (204)$$

assuming that $T_d = T_L = T$ and defining $R_{\text{eq}} = R_d R_L / (R_d + R_L)$ which is the equivalent resistance of the detector and load resistor in parallel. We can proceed to calculate the SNR

$$SNR = \frac{I_{\text{hd}}^2}{I_{\text{th}}^2}, \quad (205)$$

where $I_{\text{hd}} = \frac{\eta e}{h\nu_0} \eta_{\text{hd}} \sqrt{P_0 P_{\text{LO}}} G$ is the current due to the heterodyne detection. The quantities have the following meaning and size:

- $\eta = 0.5$ is the quantum efficiency, the efficiency of converting a photon to an electron (a typical value for MCT, not measured).
- $h = 6.67 \times 10^{-34}$ Js is Planck's constant.
- $\nu_0 = c/\lambda_0 = 28$ THz is the optical frequency of the laser.
- $\eta_{\text{hd}} = 0.9$ is the heterodyning efficiency, the efficiency of heterodyne mixing at the detector surface (an estimate, not measured).
- $G = \tau/\tau_t = 5 \times 10^{-3}$ is the photoconductive gain, the ratio of the carrier lifetime τ to the transit time τ_t (from manufacturers data sheet).

Combining equations 204 and 205 we arrive at the following expression:

$$SNR = \frac{R_{\text{eff}}}{4TB} \left(\frac{\eta \eta_{\text{hd}} e G}{h\nu_0} \right)^2 P_0 P_{\text{LO}}, \quad (206)$$

where we have replaced R_{eq} with $R_{\text{eff}} = R_{\text{eq}} R_{\text{eff,pa}} / (R_{\text{eq}} + R_{\text{eff,pa}})$, which is the combined noise effective impedance of the detector, the load resistor and the amplifier. We note that $R_{\text{eff,pa}} = R_{\text{pa}} 10^{-\text{NF}/10}$, where $R_{\text{pa}} = 50 \Omega$ is the amplifier resistance.

To complete the SNR expression, we need an approximate equation for the scattered power P_0 [82]:

$$P_0 = P_{\text{inc}} \pi \frac{L^2}{k^2} (\pi r_e^2) (n_{e0} \delta n_e)^2, \quad (207)$$

where P_{inc} is the incident laser power, L is the measurement volume length and r_e is the classical electron radius. In equation 207, δn_e^2 includes the contribution from all wavenumbers present in the plasma. To account for this we can write

$$\delta n_e^2 = \int_{k_{\text{min}}}^{\infty} \delta n_e^2(k) dk, \quad (208)$$

where k_{min} is around 1 cm^{-1} . Further, the wavenumber spectrum typically decays as

$$\delta n_e^2(k) = \frac{a}{k^m}, \quad (209)$$

where a is a constant and m is the decay exponent, often found to be close to 3. The expression for the wavenumber spectrum can be inserted into equation 208

$$\begin{aligned} \delta n_e^2 &= a \int_{k_{\text{min}}}^{\infty} k^{-3} dk = \frac{a}{2k_{\text{min}}^2} \\ a &= 2\delta n_e^2 k_{\text{min}}^2, \end{aligned} \quad (210)$$

leading to a determination of the constant a assuming that $m = 3$. Modifying equation 208 to include an instrumental filter function $f(k)$ which is unity for $k_{\text{meas}} - 1/w < k < k_{\text{meas}} + 1/w$ and zero elsewhere, we can proceed and write

$$\begin{aligned} \delta n_e^2 &= \int_{k_{\text{min}}}^{\infty} \delta n_e^2(k) dk \rightarrow \int_{k_{\text{min}}}^{\infty} f(k) \delta n_e^2(k) dk = \int_{k_{\text{meas}} - 1/w}^{k_{\text{meas}} + 1/w} \delta n_e^2(k) dk \sim \\ &\delta n_e^2(k_{\text{meas}}) \int_{k_{\text{meas}} - 1/w}^{k_{\text{meas}} + 1/w} dk = \delta n_e^2(k_{\text{meas}}) \left(\frac{2}{w} \right) = \\ &\delta n_e^2 \frac{4k_{\text{min}}^2}{wk_{\text{meas}}^3}, \end{aligned} \quad (211)$$

which we insert into equation 207 to arrive at the final expression

$$P_0 = P_{\text{inc}} \pi \frac{L^2}{k^2} (\pi r_e^2) (n_{e0} \delta n_e)^2 \frac{4k_{\text{min}}^2}{wk_{\text{meas}}^3} \quad (212)$$

This equation along with equation 206 provides us with a realistic SNR. Plots of the SNR versus δn_e for three wavenumbers can be found in [132].

7.2.3 Acquisition and demodulation

In the following we describe the actual implementation of the data acquisition and demodulation. We have seen in chapter 2 that demodulation is done by splitting the acquired signal in two and multiplying one part with a sine, the other with a cosine of $\omega_{\Delta} t$ followed by low pass filtering. Figure 37 shows the implemented layout of the peripheral component interconnect (PCI) bus card [95]. The steps can schematically be written (for ONE channel):

1. 8 bit analogue to digital (A/D) conversion (160 MHz). This means 160 MB data per second.
2. Signal $i_k(t)$ split in two parts (called quadrature channels).
3. One part is multiplied by $c(n) = \text{Re}[e^{i(\omega_{\Delta} t - n\pi/2)}] = \cos(\omega_{\Delta} t - n\pi/2)$, the other part by $c(n+1) = \sin(\omega_{\Delta} t - n\pi/2)$, where $n = 0,1,2,3$ because the multiplication is done four times per period. The step in n corresponds to a phase shift of $\pi/2$. The multiplication factors are written in table 2.

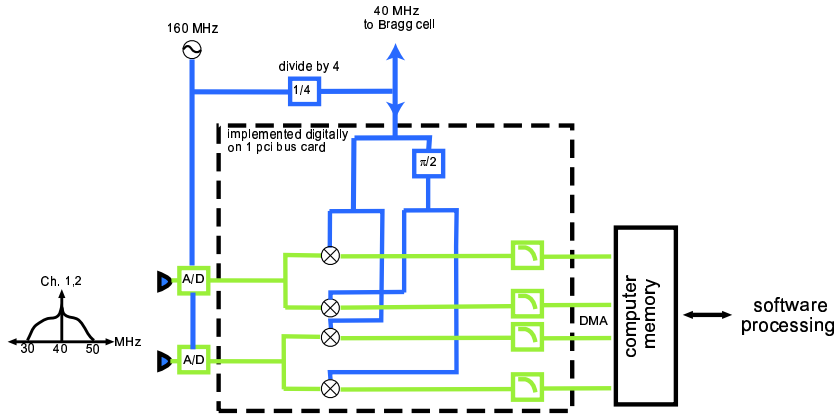


Figure 37. (Colour) Acquisition electronics. The figure is taken from [132].

4. We have four samples per quadrature channel per period. If quadrature channel 1 is to be our cosine channel, the $c(n)$'s become $[1,0,-1,0]$ and the sine quadrature channel 2 $c(n+1)$'s are $[0,-1,0,1]$. These values are obtained by setting $t = 0$ in table 2 (phase locking). This means that every second sample is zero and can be thrown away without loss of information, leaving two samples per quadrature channel per period. So in total this means that 160 MB of data is transferred through the two quadrature channels per second.
5. Low pass filtering removes the $2\omega_{\Delta}$ terms.
6. The data rate is reduced (decimated) by 4 resulting in 40 MB of data per second of acquisition.
7. The data is transferred to a computer by direct memory access (DMA) transfer.
8. The data is analysed off-line with software. The programming language used both for data acquisition and analysis is the interactive data language (IDL) [166] [167] [168] [170] [171] [173] [174] [175].

n	$e^{-in\pi/2}$	$c(n)$, quadrature channel 1	$c(n+1)$, quadrature channel 2
0	1	$\cos(\omega_{\Delta}t)$	$\sin(\omega_{\Delta}t)$
1	-i	$\cos(\omega_{\Delta}t - \pi/2) = \sin(\omega_{\Delta}t)$	$\sin(\omega_{\Delta}t - \pi/2) = -\cos(\omega_{\Delta}t)$
2	-1	$\cos(\omega_{\Delta}t - \pi) = -\cos(\omega_{\Delta}t)$	$\sin(\omega_{\Delta}t - \pi) = -\sin(\omega_{\Delta}t)$
3	i	$\cos(\omega_{\Delta}t - 3\pi/2) = -\sin(\omega_{\Delta}t)$	$\sin(\omega_{\Delta}t - 3\pi/2) = \cos(\omega_{\Delta}t)$

Table 2. Demodulation multiplication factors.

In conclusion, one quadrature channel contains samples of the measurements multiplied by cosine, the other channel contains samples multiplied by sine, leading to real and imaginary parts of the signal after low pass filtering.

Fractional phase shifting Due to the practical implementation of the acquisition card, the two quadrature channel signals are phase shifted by $1/160 \mu\text{s}$. The technical reason for this is that the card was constructed using two instead of four A/D converters. That is to say, each of the two channels is sampled by a separate A/D converter. The phase shift can be understood as follows: The raw data out of the card (for TWO channels) has the sequence

1. $Re[i_{k,1}(n = 0)] = c(n = 0)i_{k,1}(n = 0)$
2. $Im[i_{k,1}(1)] = c(1)i_{k,1}(1)$
3. $Re[i_{k,2}(2)] = c(2)i_{k,2}(2)$
4. $Im[i_{k,2}(3)] = c(3)i_{k,2}(3)$

The second subscript on the photocurrent $i_k(n)$ refers to the channel number. If we now consider one channel, say number 1, the quadrature data is used to reconstruct the complex signal according to

$$i_{k,1}^{\text{shifted}} = Re[i_{k,1}(0)] + iIm[i_{k,1}(1)] \quad (213)$$

We have now identified the problem; the real and imaginary parts of the complex signal are recorded by two successive A/D clock cycles. This means they are shifted by the sampling period $1/160 \mu\text{s}$. The correction for this time delay is done off-line and is explained in detail in [132].

8 Investigated phenomena

This chapter contains analysis results of measurements obtained using the LOTUS diagnostic. Each section describes different discharges (except sections 8.1 and 8.2 treating the same series); the unifying theme of the chapter is confinement transitions.

Section 8.1 describes comparable discharges that can be viewed as quasi stationary when averaged over several ms [14].

Analysing the discharges introduced in section 8.1 on sub ms time scales, it is found that the plasmas dither spontaneously between two confinement states, the low (L) confinement and high (H) confinement mode (see chapter 5). The relationship between the fast switching of confinement modes and the density fluctuations is the subject of section 8.2 [11] [14].

In section 8.3 we treat a single shot evolving through several confinement states: Initially it is in stationary L-mode, thereafter it exhibits pronounced dithering and finally enters the edge localised mode (ELM)-free H-mode (H^{*}). ELMs are burst-like phenomena occurring in the outer parts of the confined plasma; they are associated with a flattening of the edge pressure gradient and lead to a loss of plasma energy [37]. The goal of this section is to compare the analysis to that of section 8.2. The purpose of this comparison is to determine whether the hills and troughs of the dithering phase have the same properties as stationary L- and H-modes.

Having studied fast L-H confinement transitions, we turn to slow confinement transitions in section 8.4. The confinement quality of the discharges can be controlled by changing the rotational transform of the magnetic field, either using the external coils or by inducing a plasma current. The confinement transition can be made as slow or fast as desired, meaning that a detailed study can be made of the mechanisms causing the transition. In this section we present spatially localised measurements of density fluctuations using two different methods, one being a novel concept [169] [9] [10] [175] [12] [15] [177].

Our final section on measurements, section 8.5, contains an analysis of a new high density H-mode (HDH) regime found in W7-AS in 2001. This mode exists above a certain density threshold and has a fluctuation level significantly larger than that of the standard H-mode. LOTUS is very well suited to monitor this discharge type, since it is the only fluctuation diagnostic on W7-AS able to measure core fluctuations in high density plasmas.

* * *

Although we described spectral analysis in chapter 4, we briefly recapitulate the results here and add a few definitions.

The real signals acquired from each detector are centered at the heterodyne carrier frequency of 40 MHz. These are quadrature demodulated to obtain complex signals centered at zero frequency. The resulting signals are denoted

$$S_j(t) = X_j(t) + iY_j(t), \quad (214)$$

where j is the volume number (1 or 2). We can proceed and calculate

$$P_{jj}(\nu) = \left| \int_{t_1}^{t_2} S_j(t) e^{i2\pi\nu t} dt \right|^2, \quad (215)$$

the autopower spectrum of volume j for a time interval $\Delta t = t_2 - t_1$. The autopower in a certain frequency band $\Delta\nu = \nu_2 - \nu_1$

$$P_{jj}^b = \int_{\nu_1}^{\nu_2} P_{jj}(\nu) d\nu \quad (216)$$

is called the band autopower, as indicated by the lowercase superscript, b , in equation 216. The mean frequency is

$$\langle \nu \rangle_j = \frac{\int_{\nu_1}^{\nu_2} \nu P_{jj}(\nu) d\nu}{\int_{\nu_1}^{\nu_2} P_{jj}(\nu) d\nu} \quad (217)$$

Finally, the power of the density fluctuations integrated over all frequencies where turbulence is observed is given by

$$P_{jj} = \int_{-\nu_2}^{-\nu_1} P_{jj}(\nu) d\nu + \int_{\nu_1}^{\nu_2} P_{jj}(\nu) d\nu \quad (218)$$

Note that the frequency interval $[-\nu_1, \nu_1]$ is excluded from the integrals; this is because the signal is dominated by the carrier frequency at low frequencies [93]. In the following we use $\nu_1 = 50$ kHz (except in section 8.5 where $\nu_1 = 100$ kHz).

8.1 Quasi steady-state

In this first section describing the analysis of measured density fluctuations, we treat a wavenumber scan. That is, a series of plasmas where the probed wavenumber of the density fluctuations was varied in steps from 14 to 62 cm^{-1} in eight similar discharges. Table 3 summarises the corresponding shot/wavenumbers.

Shot	47133	47135	47136	47137	47138	47141	47142	47143
[cm^{-1}]	14	21	28	34	41	48	55	62

Table 3. Measured wavenumber for a given shot.

The section is organised as follows: Subsection 8.1.1 describes the discharges analysed in this section and the next, and subsection 8.1.2 includes an overview of auxiliary diagnostics. Subsection 8.1.3 deals with the raw data from LOTUS and subsection 8.1.4 collects statistical analysis results of the density fluctuation data. Subsection 8.1.5 presents autopower spectra of the density fluctuations for the wavenumber scan and we discuss the results in subsection 8.1.6.

8.1.1 Discharge description

The discharges were separatrix limited with an edge rotational transform t_a of 0.56 (the '5/9 boundary island' configuration, where the main plasma is bounded by nine magnetic islands [64]) and had a duration of 400 ms [102]. The Deuterium plasmas were heated by Hydrogen neutral beam injection (NBI) of up to 2.5 MW, where the absorbed power is about 75 %. The discharges exhibited pronounced dithering; high NBI power was used to suppress the ELM-free H-mode [72] (see section 8.2). The effective plasma minor radius a was 15 cm, with a toroidal magnetic field B_φ of 2.5 T and zero net current.

Figure 38 displays five time traces from 100 to 450 ms - from top to bottom: Diamagnetic stored energy, line density, H_α -trace for shot 47133, NBI power and density fluctuations integrated over frequency for the eight discharges; top trace is the smallest wavenumber (length of time windows is 1 ms). The fluctuations are normalised to the 50 ms time interval chosen for our main analysis, namely from 200 to 250 ms. The analysis time interval is represented by a gray semi-transparent rectangle in all figures containing quantities shown versus time (for additional time traces covering the analysis time window see figure 52). Each trace is displaced for clarity, with horizontal lines marking the average values. The discharges had three phases: A startup phase to 150 ms, a quasi steady-state period from 150 to 300 ms and dynamical development from 300 to 400 ms where the discharges were terminated. The change of parameters at 300 ms is due to heavy gas puffing initiated at this point. Before this, the plasmas were exclusively fuelled by the beams (total fuelling $\sim 2.5 \times 10^{20} \text{ s}^{-1}$). It can be seen from the traces that the global plasma parameters in the analysis time window were roughly stationary. Note that one discharge (largest wavenumber) was heated by only 2 MW NBI.

8.1.2 Complementary diagnostics

The two main diagnostics we use for direct comparisons to the density fluctuations are H_α -light signals and magnetic fluctuations measured by Mirnov coils:

H_α and magnetic fluctuations A diode measuring the H_α -emission at an inner limiter is used in this section, see figure 38. The signal was sampled at 10

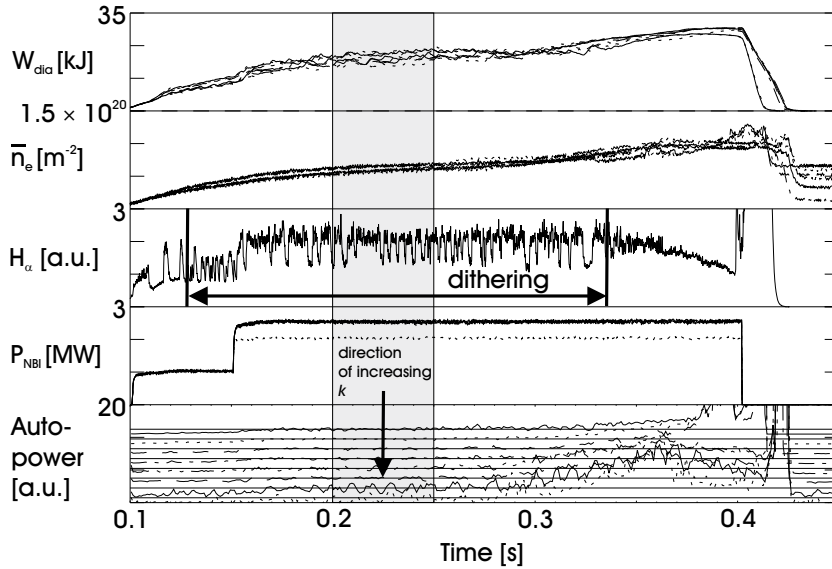


Figure 38. Discharge overview - time traces from 100 to 450 ms. Linestyles in order of ascending wavenumber is: Solid, dotted, dashed, dash dot, dash dot dot and long dashes (cyclic usage). From top to bottom: Diamagnetic energy [kJ], line density, H_α -light for shot 47133 (the dithering period is marked), NBI power [MW] and frequency integrated density fluctuations (1 ms time windows) in volume 1 normalised to the analysis time window (grey semi-transparent rectangle). The arrow on the density fluctuation data points in the direction of increasing wavenumber.

kHz (100 μ s). The emission comes from neutral Hydrogen entering the plasma, so the H_α -signal is a measure of recycling between the plasma and vessel surfaces [160]. Therefore, the abrupt drop in the H_α -signal at the L-H transition is due to a fast reduction of recycling. This is interpreted as being connected to an edge transport barrier associated with improved confinement [150].

The Mirnov coil system used consists of 16 coils (called 'MIR-1') around the plasma [5] and measures fluctuations in the poloidal magnetic field B_θ . Simulations show that the signal in a single coil primarily originates from a 5 cm region in front of the coil [5]. Figure 39 (top) shows the calibrated signal from a monitor coil ('MIRTIM') in T/s, while the bottom plot shows a spectrogram for this trace. The time resolution was 4 μ s. The dithering manifests itself as switching in the magnetic fluctuations and consists of broadband bursts [157]. As the sampling rate was 250 kHz (Nyquist frequency 125 kHz), aliasing problems are to be expected since bursts are observed up to 125 kHz. These bursts have for our discharges been determined to have an inversion point just inside the LCFS by the use of soft X-ray cameras [158]. For a detailed explanation of how to find the pivot point, see figure 18 in [157]. Mode analysis shows that the poloidal mode numbers $m = 2,3$ dominate during the bursts, while most of the mode activity disappears in the quiescent phases. A crude estimate of the perpendicular wavenumber of the perturbations is $k_{\text{MHD}} \sim m/r_{\text{MHD}} \sim 0.2 \text{ cm}^{-1}$, where r_{MHD} ($\sim 14 \text{ cm}$) is the minor radius location of the bursts. For the correlation calculations we use the RMS signal of a coil situated at the midplane on the high field side of the plasma; the correlation calculations show that the coil selection is not important.

Spectroscopic measurements of the radial electric field Measurements of the edge radial electric field E_r from shot 47133 were obtained by passive

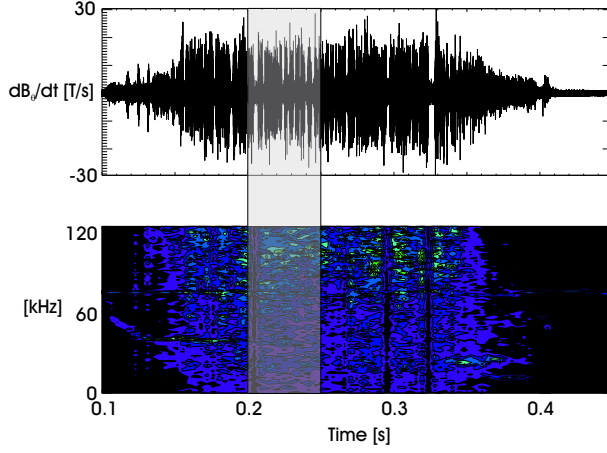


Figure 39. (Colour) Magnetic field derivative in T/s from the 'MIRTIM' monitor coil (top) and a spectrogram (bottom) covering 350 ms. Dithering is observed as switching between a small and a large derivative.

spectroscopy using the 2824 Å Boron IV line [7]. The electric field (using the lowest-order force balance equation) is given by

$$E_r = (v_\varphi B_\theta - v_\theta B_\varphi) + \frac{1}{eZ_I n_I} \nabla P_I, \quad (219)$$

where I is the common atomic species (see [7] for more elaborate formulae, equations 9 and 10). Typically, the major contribution to E_r in W7-AS comes from poloidal rotation v_θ [7].

Figure 40 shows the edge E_r measured at five radial positions z in the edge plasma. The diagnostic coordinate z is about two times r ; the measurement at $z = 25$ cm is at the LCFS. The time resolution was 4 ms, which is not sufficient to resolve the fast switching between L- and H-mode. Therefore the figure shows data averaged over the 50 ms analysis time window.

We can convert E_r to $\mathbf{E} \times \mathbf{B}$ frequencies according to the relation

$$\omega_{E \times B} = 2\pi\nu_{E \times B} = k_\theta \frac{E_r}{B_\varphi}, \quad (220)$$

where we use $k_\theta \sim k$ [92]. A negative/positive E_r means flow in the electron/ion diamagnetic drift (DD) direction, respectively. It is seen that E_r towards the plasma edge is small and negative (zero within errorbars), whereas it is large and negative inside the confined plasma. This would indicate that low frequencies rotate in the electron DD direction at the edge, high frequencies in the electron DD direction in the outer core. Using $E_r \sim -800/-4100$ V/m for edge/outer core, we arrive at

$$\begin{aligned} \nu_{E \times B}^{\text{edge}}(14 \text{ cm}^{-1}) &= -71 \text{ kHz} & \nu_{E \times B}^{\text{outer core}}(14 \text{ cm}^{-1}) &= -365 \text{ kHz} \\ \nu_{E \times B}^{\text{edge}}(62 \text{ cm}^{-1}) &= -316 \text{ kHz} & \nu_{E \times B}^{\text{outer core}}(62 \text{ cm}^{-1}) &= -1.6 \text{ MHz} \end{aligned} \quad (221)$$

An important point with regards to E_r in the type of discharge we analyse is that it usually is quite small in the inner regions of the confined plasma, has a deep well (negative E_r) inside but close to the LCFS and a small hill (positive E_r) outside the LCFS. The measurements shown in figure 40 only display the outside slope of the well; the radial electric field at the bottom of the well is about -20

kV/m. An E_r -profile for a discharge with profiles comparable to ours is shown as figure 6 in [7]. In similar discharges having a lower dithering frequency (due to smaller NBI power), clear switching is established inside the LCFS, corresponding to a deepening of the E_r -well in H-mode phases (see section 8.3). The E_r inversion radius is, within errorbars, situated at the LCFS. The E_r is similar for the other discharges analysed, resulting in a linear increase of the frequencies with k . In the following paragraphs dealing with profile measurements we will estimate the electron drift wave mode frequency to determine whether rotation or drift waves dominate our spectra.

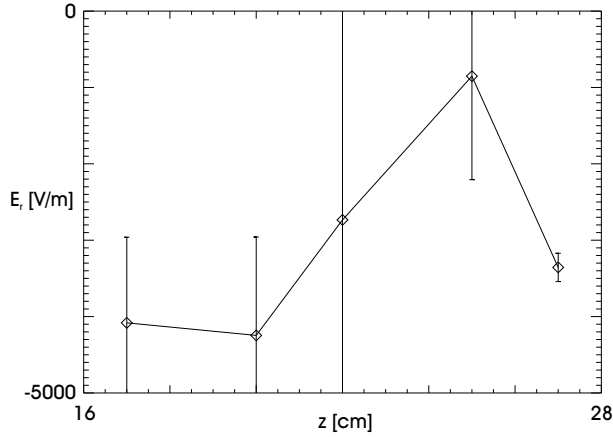


Figure 40. Edge radial electric field E_r as determined by Boron IV spectroscopy versus z . The diagnostic coordinate z is roughly double the minor radius value.

Thomson scattering measurements of electron density and temperature

The final auxiliary measurements presented are electron density and temperature profiles, see figure 41. The measurements are made using a Ruby laser Thomson scattering system that provides one density/temperature profile per discharge. We show profiles from three of our discharges, where the measurement time point was shifted between each discharge so as to provide the profile evolution. The red solid dots are taken at 200 ms, green open dots at 330 ms and blue solid squares at 380 ms. Our analysis interval begins at the 200 ms time point, where the central density was slightly above $1 \times 10^{20} \text{ m}^{-3}$, while the density rose to $2.5 \times 10^{20} \text{ m}^{-3}$ in the final stages. The central electron temperature was 0.6 keV.

Assuming a pure H plasma in our analysis time window (mass number $A = 1$) and an electron temperature of 0.3 keV (at $r = 12$ cm), the ion Larmor radius at the electron temperature ρ_s is equal to 1 mm. This means that the product $k\rho_s$ varies between 1.4 and 6.2 at the edge for the wavenumbers we are measuring, and is somewhat larger in the core. The profile information allows us to calculate estimates of the linear mode frequency of electron drift waves, given by

$$\begin{aligned} \omega_e(k_\theta) &= \omega_e^* \frac{1}{1 + k_\theta^2 \rho_s^2} \\ \omega_e^* &= -\frac{k_\theta T_e}{B_\varphi L_n}, \end{aligned} \quad (222)$$

where $L_n^{-1} = |\partial_r \ln(n_e)|$ is the inverse electron density scale length (see chapter 5 and [164]). We again assume that $k_\theta \sim k$ and we know that $L_n \sim 6$ cm from the density profile measurements. Thus, we conclude that

$$\begin{aligned}
\nu_e^*(14 \text{ cm}^{-1}) &= -446 \text{ kHz} & \nu_e(14 \text{ cm}^{-1}) &= -151 \text{ kHz} \\
\nu_e^*(62 \text{ cm}^{-1}) &= -2.0 \text{ MHz} & \nu_e(62 \text{ cm}^{-1}) &= -50 \text{ kHz}
\end{aligned}
\tag{223}$$

In subsection 8.1.5 we show that the measured density fluctuation frequencies extend up to 2 MHz. Comparing the drift wave electron DD frequencies to the ones due to $\mathbf{E} \times \mathbf{B}$ rotation, we conclude that rotation and not drift wave modes is responsible for the major part of the observed frequency shift for large wavenumbers. But since the observed frequency is the sum

$$\nu_{E \times B} + \nu_e = \frac{k_\theta}{B_\varphi} \left(\frac{E_r}{2\pi} - \frac{T_e}{L_n(1 + k_\theta^2 \rho_s^2)} \right),
\tag{224}$$

it is possible that low frequency drift wave turbulence is rotating at the $\mathbf{E} \times \mathbf{B}$ velocity.

Although rotation is dominating the measured spectra for large wavenumbers, the situation at small wavenumbers is ambiguous. This is because $\lim_{k_\theta \rightarrow 0} \nu_e = \lim_{k_\theta \rightarrow \infty} \nu_e = 0$ whereas $\nu_{E \times B}$ increases linearly with k_θ .

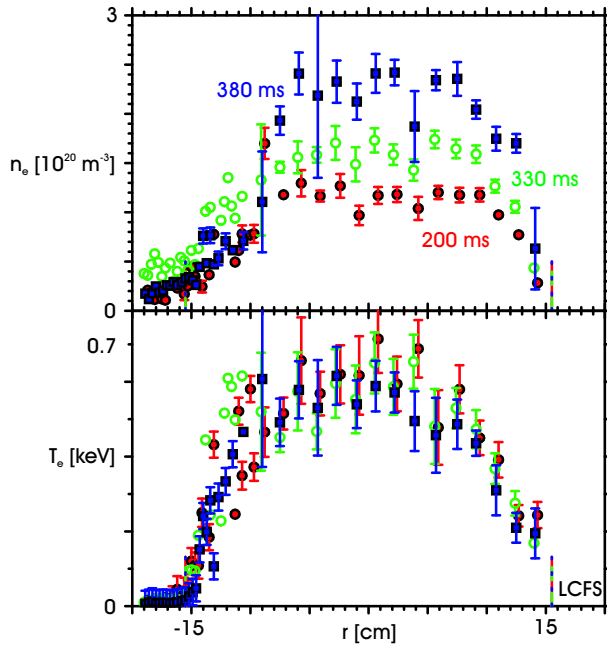


Figure 41. (Colour) Electron density (top) and temperature (bottom) profiles obtained using Ruby laser Thomson scattering. Solid red dots are measured in shot 47141 at 200 ms, open green dots in shot 47138 at 330 ms and solid blue squares in shot 47133 at 380 ms.

8.1.3 Raw data

We will now briefly describe the raw complex data acquired by the LOTUS diagnostic. Figure 42 shows the real/imaginary (left) and amplitude/phase (right) representations of the background signal from one volume. We note that a quasi-periodic oscillation having a period of about 10 ms exists, corresponding to 100 Hz. This oscillation is due to mechanical vibrations and is superimposed onto a faster variation.

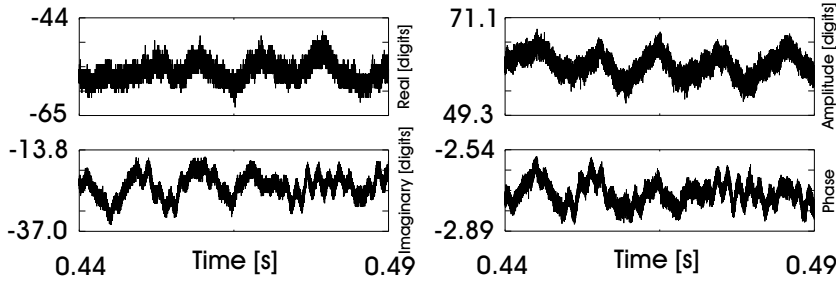


Figure 42. 50 ms time windows of background data, displayed with a 1 μ s time resolution. The left-hand plots show the real/imaginary numbers, the right-hand plots the amplitude/phase numbers.

Figure 43 shows the same quantities as figure 42, but now for measurement data where a plasma was present. The slow variation of the signal almost vanishes in the stronger signal due to scattering. Note the 2π jumps in the phase.

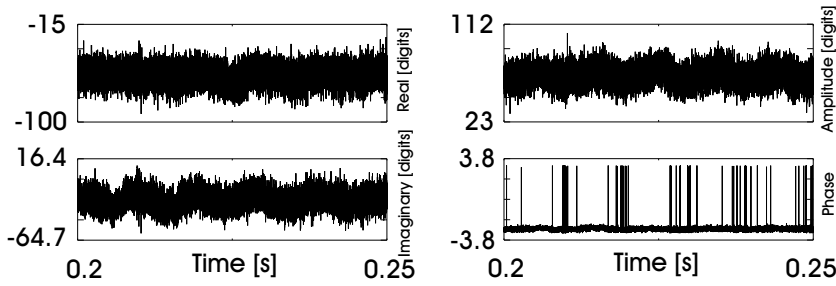


Figure 43. 50 ms time windows of measurement data, displayed with a 1 μ s time resolution. The left-hand plots show the real/imaginary numbers, the right-hand plots the amplitude/phase numbers.

Finally, we compare 1 ms time intervals of background and measurement data in figure 44. It is immediately obvious that the background signal only varies a few digits, whereas the measurement data inhabits a larger dynamical range.

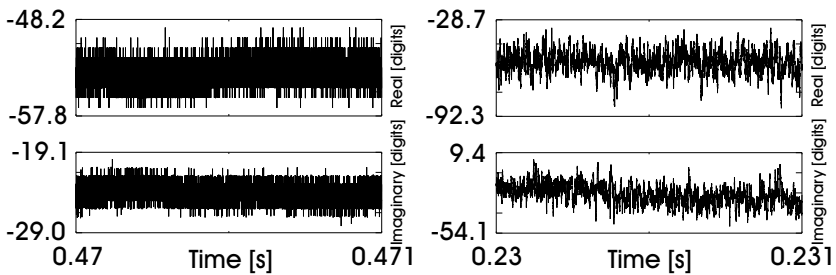


Figure 44. 1 ms time windows of background (left) and measurement (right) data. The time resolution here is the maximum attainable, 50 ns.

8.1.4 Statistical analysis

It is rather difficult to gain insight by observing raw data directly as we did in the last subsection. Therefore we now continue with a brief statistical analysis of the

plasmas. Figure 45 shows the PDF's of the raw data in figure 44. The left-/right-hand plots correspond to the left-/right-hand plots of figure 44, respectively. It is clear that the PDF's of the background data are narrow, and wider for the measurement data.

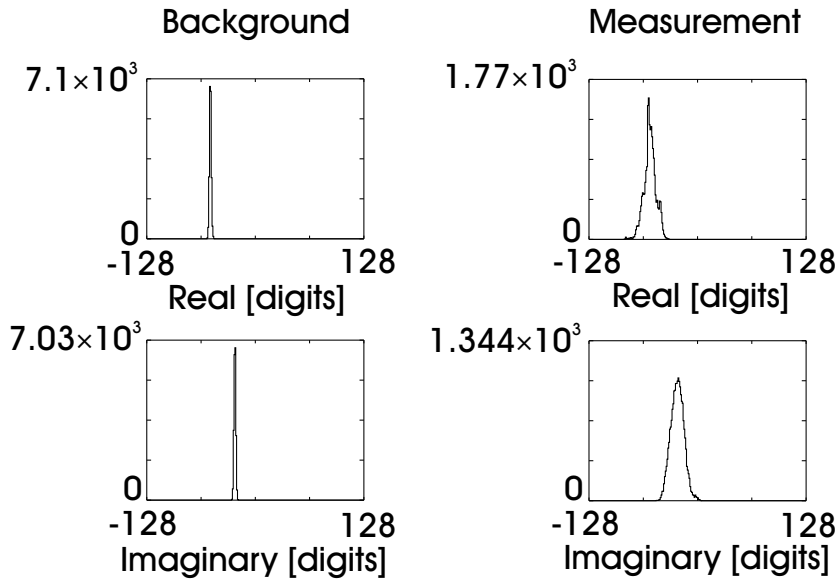


Figure 45. PDF's of background (left) and measurement (right) data for the raw signals shown in figure 44.

This implies that the variance of the measurement data is larger than that of the background data. This can be verified by comparing the variance of the background to that of the measurement, see figure 46. The measurement variance increases with decreasing wavenumber, meaning that more and/or larger events occur away from the average.

To complete our characterization of the statistical properties of our signal, we calculate the skewness and flatness of the background and measurement data. These quantities have previously been analysed for data similar to ours [2]; it was found that the skewness was 0 and the flatness 3 within experimental errorbars, meaning that the signal was Gaussian.

Figure 47 shows the background skewness and flatness versus wavenumber. Although a significant scatter is present, our background data is close to being Gaussian.

A similar situation is found for measurement data, see figure 48.

8.1.5 Autopower spectra

We begin our description of the density fluctuation autopower spectra by showing a spectrogram of shot 47133 (volume 1) in figure 49. Density fluctuations are shown up to ± 2 MHz on a logarithmic colourscale; the DC signal is our carrier frequency. The plot demonstrates our ability to obtain full spectral information over the entire discharge length. The L-H dithering shows as vertical lines and an increase in the autopower is observed as gas puffing commences around 300 ms.

To display the decrease of scattered power with increasing wavenumber, we overplot autopower spectra for the 8 wavenumbers in figure 50. The ± 50 kHz interval has been left out. We observe that the density fluctuation amplitude decreases rapidly with wavenumber and that the spectra decrease monotonically

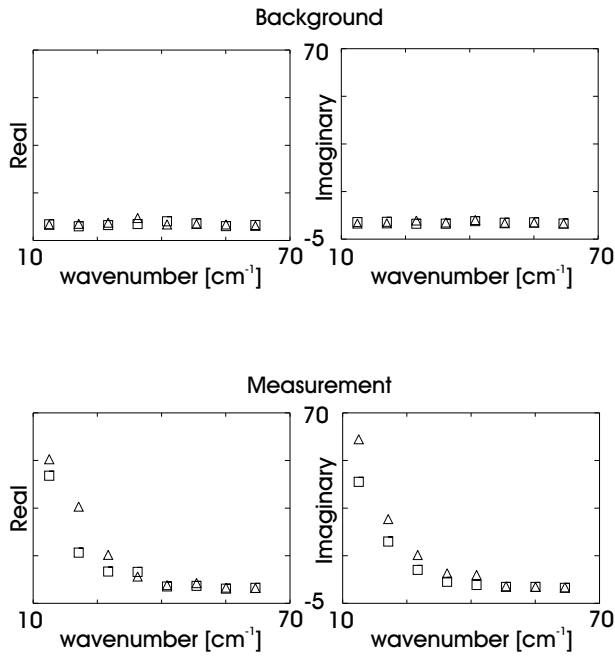


Figure 46. Top: Variance of background data as a function of observed wavenumber, bottom: Variance of measurement data versus wavenumber. Triangles are volume 1, squares volume 2 and all vertical scales are identical.

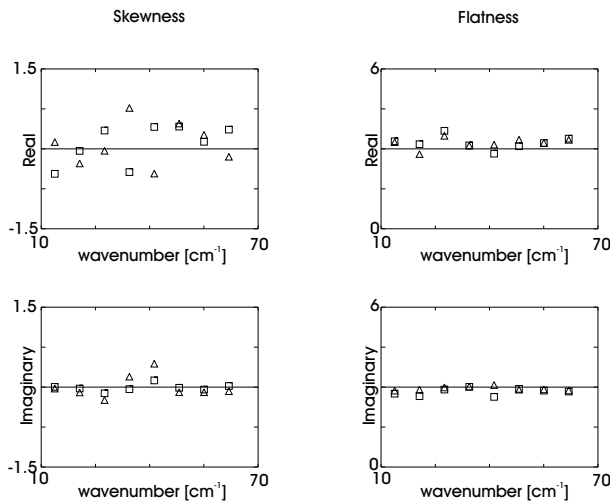


Figure 47. Background data. Left: Skewness versus wavenumber, right: Flatness versus wavenumber. Triangles are volume 1, squares volume 2.

with frequency.

The decrease of fluctuations with increasing wavenumber can also be represented as a wavenumber spectrum. Here, the fluctuations are integrated over frequency and plotted versus wavenumber, see figure 51. Two power-law fits ($P \propto k^{-m}$) and an exponential fit ($P \propto e^{-nk}$) are plotted along with the datapoints. The power-law fit to the 3 smallest wavenumbers gives $m \sim 2.9$ and the power-law fit to the 5 largest wavenumbers gives $m \sim 6.9$. The exponential fit to all 8 wavenumbers gives $n \sim 0.16$ cm.

The small wavenumber fit is close to $8/3$ as would be expected for turbulence

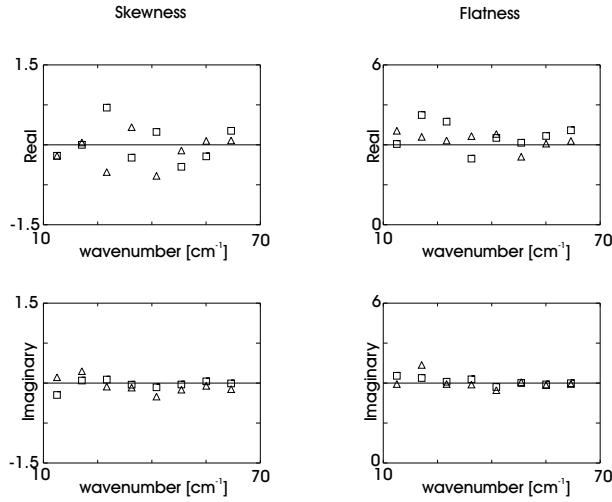


Figure 48. Measurement data. Left: Skewness versus wavenumber, right: Flatness versus wavenumber. Triangles are volume 1, squares volume 2.

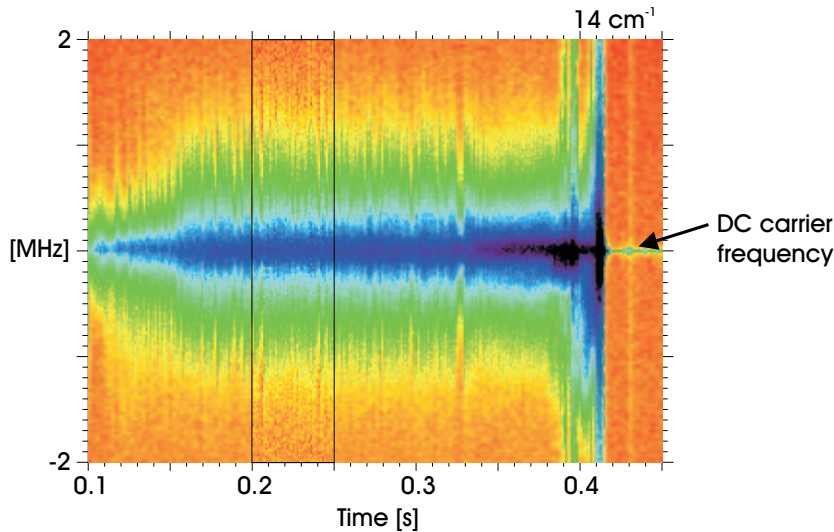


Figure 49. (Colour) Autopower versus time and frequency for discharge 47133, volume 1. The time resolution of the spectra is 1 ms and the colour scale is logarithmic. The measured spectra in volume 2 are quantitatively similar to those in volume 1.

in the energy range (see chapter 5), while the large wavenumber fit is close to the Heisenberg scaling for the dissipation range. However, the exponential falloff as proposed by von Neumann for the dissipation range fits all measurements.

8.1.6 Summary

We close the section with a few words on what has been found. We concluded that the fluctuations observed have frequencies compatible with $\mathbf{E} \times \mathbf{B}$ rotation due to a radial electric field, up to 2-3 MHz. Our statistical treatment made it clear that the data is roughly Gaussian, and that the variance decreases with increasing measured wavenumber. The autopower spectra decrease monotonically with frequency, and the frequency integrated scattered power decreases rapidly

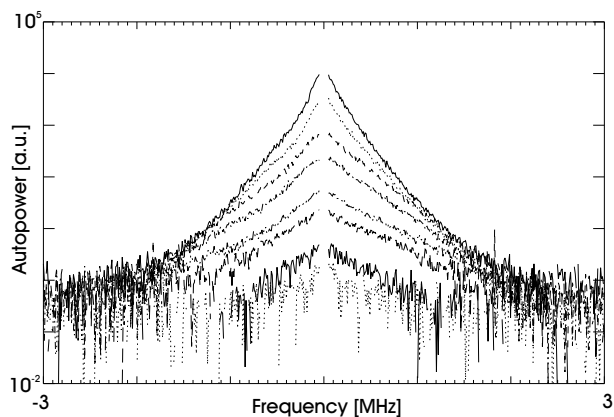


Figure 50. Autopower spectra versus frequency for the 8 wavenumber scan discharges, volume 1. Linestyles in order of ascending wavenumber is: Solid, dotted, dashed, dash dot, dash dot dot dot and long dashes (cyclic usage).

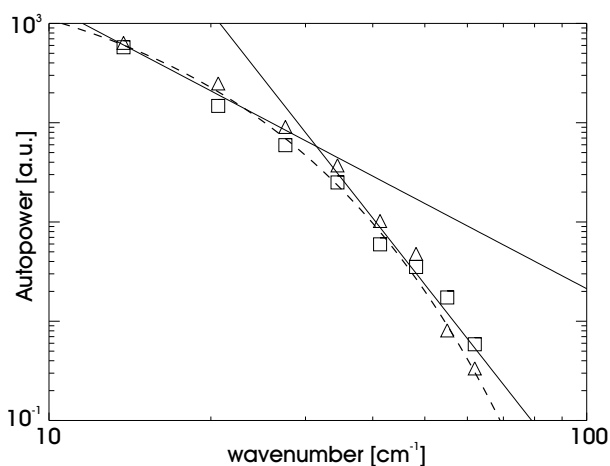


Figure 51. Wavenumber spectrum. The solid lines are power-law fits to the 3 smallest and 5 largest wavenumbers, the dashed line is a fit to an exponential function. The power-law fit grouping of points used is the only one where convergence is obtained. Triangles are volume 1, squares volume 2.

with wavenumber, either as power-laws or as an exponential function.

8.2 Fast confinement transitions

In the present section we continue the analysis of the shots treated in section 8.1. However, we now put emphasis on the dithering behaviour between L- and H-mode instead of the steady-state properties.

The section is organised as follows: In subsection 8.2.1 we motivate the need for an increased understanding of turbulence in improved confinement regimes and explain how this can be obtained. In subsection 8.2.2 we reveal the quasi-periodic dithering of the discharges and in subsection 8.2.3 we separate the autopower spectra into L- and H-mode parts. Correlations between the density fluctuations, H_α -light and magnetic fluctuations on different time scales are dealt with in subsection 8.2.4 and the results of the section are discussed in subsection 8.2.5 and compared to similar tokamak investigations. Finally, conclusions are put forth in subsection 8.2.6.

8.2.1 Introduction

Understanding the mechanism controlling access to improved confinement regimes such as the H-mode [149] [49] [151] in fusion plasmas remains a puzzle only partially solved. The literature dealing with the possible connection between turbulence suppression and the L-H transition is extensive - a present candidate being $\mathbf{E} \times \mathbf{B}$ shear flow decorrelation [18] [29] [109] [143] [30] [144] [38] - but several important questions remain unanswered. This statement is also valid for the so-called 'advanced tokamak scenarios', such as internal transport barriers (ITBs) [97] [142] during reversed magnetic shear (RS) operation, the radiatively improved (RI) mode [107] and quiescent double barrier (QDB) [61] discharges.

Transport in fusion plasmas appears to possess an intermittent nature with associated bursts [101] [99] of fluctuations in several plasma parameters. Observing the details of these bursts might shed light on the underlying phenomena. It would be especially interesting to examine the temporal and spatial scales of the turbulent structures involved: (i) The correlation and time delay between bursts in various quantities, (ii) the behaviour of bursts on different spatial scales and (iii) the lifetime of the bursts. Concerning this last point, the paramount question is whether the fluctuations display a 'Chinese boxes' [33] type of correlation or if we can resolve the temporal scale with the available sampling rates. That is, the time resolution has to be sufficient to determine the correlation time of the bursts. We define the correlation time to be the full-width at half-maximum (FWHM) of the crosscorrelation function.

Apart from LOTUS, the other main diagnostic is a Mirnov coil system which provides information on magnetic fluctuations. For previous work done correlating magnetic and density fluctuations in W7-AS, we refer the reader to [172]. The results therein show that the quantities are correlated in a region extending from 70 % of the normalised minor radius out to the LCFS.

In the previous paragraphs and throughout this chapter, we use the expression 'correlation of fluctuations'. To prevent confusion, we wish to make it clear that we mean the correlation of fluctuation power or its RMS amplitude averaged over certain time windows, typically 10-100 μs . The measurements we correlate were not sampled using a common clock (the different A/D converters were not synchronised), therefore we will not analyse crosspower spectra.

To the best of our knowledge, density fluctuations in dithering plasmas have never previously been investigated at the large wavenumbers we measure [36]. However, measurements at these wavenumbers have recently become of interest due to nonlinear numerical simulations treating electron temperature gradient (ETG) driven turbulence [88]. For certain conditions, these simulations show that

transport due to ETG modes can constitute a significant part of the total transport.

We will show that there is indeed a very fast correlation between magnetic and density fluctuations in L-mode, the crosscorrelation having a FWHM of order 100 μs . Further, we prove that these correlations are strongest for the smallest wavenumbers measured and that the frequency of the density fluctuations, where a maximum correlation is observed with respect to other fluctuating quantities, increases with wavenumber.

A secondary aim is the thorough characterization of L- and H-mode separated density fluctuation autopower spectra. Although spectral shapes varied appreciably between L- and H-mode, the frequency integrated autopower change was quite modest. The differences found between L- and H-mode behaviour in W7-AS and comparable scattering measurements in tokamaks warrants a comparative analysis.

It is of central importance to realise that when we in this section mention L- and H-modes, these are occurring under dithering conditions. No statements are made concerning either stationary L-mode or edge localised mode (ELM)-free H-mode (H^* -mode). Our work presented is first part of an effort to clarify if dithering can be viewed as collections of closely spaced ELMs. Whether the two are manifestations of a single mechanism could be determined by the following two steps:

1. We elaborate certain properties of the fluctuations by picking out only the H-mode part of a dithering phase, and show that these are clearly different from properties found by picking out only the L-mode part of a dithering phase.
2. We compare the results from the first step to an analysis of fluctuation properties in H^* -mode and during steady-state L-mode.

Below we will address the first step; in section 8.3 we deal with the tasks belonging to the second step.

8.2.2 Quasi-periodic dithering

To facilitate an immediate 'correlation-by-eye', the top four time traces of figure 52 show correlations between density fluctuations for a wavenumber of 14 cm^{-1} at 700 kHz, H_α -light and magnetic fluctuations. The stored energy is shown for reference at the bottom. The dithering observed is clearly long-time (ms) correlated, see subsection 8.2.4. That magnetic and density fluctuations are highly correlated is well known, see e.g. [78] for a comparison between far-infrared (FIR) scattering and magnetic fluctuations. The separated bottom plot of figure 52 displays how we construct a series of L- and H-mode time windows from a time interval of 50 ms. A horizontal line delineates L-mode (plusses) and H-mode (asterisks) time points.

8.2.3 L- and H-mode separated autopower spectra

Autopower spectra Constructing a series of L- and H-mode time windows as shown in figure 52 enables us to calculate autopower spectra of the density fluctuations for L- and H-mode plasmas separately: The autopower spectra are integrated over all L- or H-mode time intervals. This is illustrated in figure 53, where the spectra are plotted for a single volume (1). Our initial observation is that the spectra all have a tent-like profile, which indicates that they might obey a

$$P(k, \nu) = c_1(k) \times e^{c_2(k)\nu} \quad (225)$$

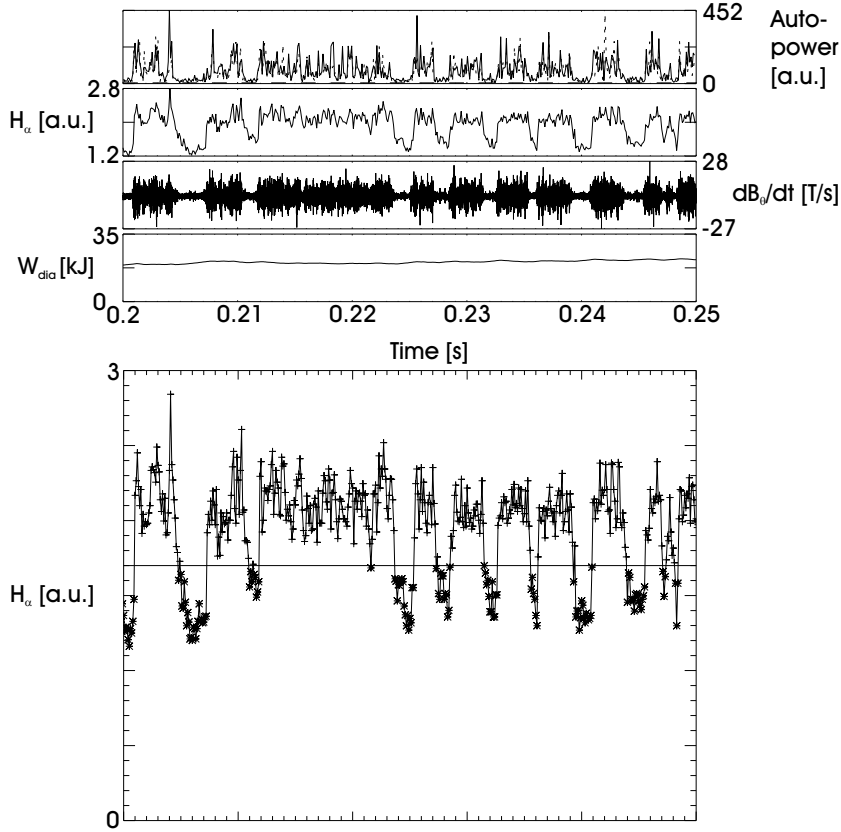


Figure 52. Top to bottom: Density fluctuations at 700 kHz, $k = 14 \text{ cm}^{-1}$ in volume 1 (solid) and 2 (dotted), H_α -light, magnetic fluctuations and the stored energy, separate bottom plot: H_α -trace for the same 50 ms time window. The horizontal threshold line selects L-mode (plusses) and H-mode (asterisks) time windows.

type scaling [154], where P is autopower. This scaling is applied separately for positive and negative frequencies. Further, the H-mode spectra (dotted) are limited to lower frequencies than the L-mode spectra (solid) and are steeper as a function of frequency.

To get a better impression of the differences between the spectral shapes, figure 54 shows c_1 and $1/c_2$ along with the fits

$$c_1(k) = d_1 \times e^{-d_2 k} \quad (226)$$

and

$$c_2(k) = \frac{1}{d_3 \left[1 + \frac{d_4}{d_3} k^2 \right]} \quad (227)$$

to negative (three top rows) and positive (three bottom rows) frequencies of the measured spectra shown in figure 53. The d 's are constants. The solid lines in the left-hand columns are exponential fits to c_1 , where the smallest wavenumber is excluded from the fit (to ensure convergence). The solid curves in the right-hand columns are fits to the data (excluding the two largest wavenumbers where the measurements are dominated by noise) assuming the dependency of equation 227, while the dotted curves (all identical) are results presented in [154] shown for reference. These reference fits were made to measurements of density fluctuations in the Alcator C tokamak.

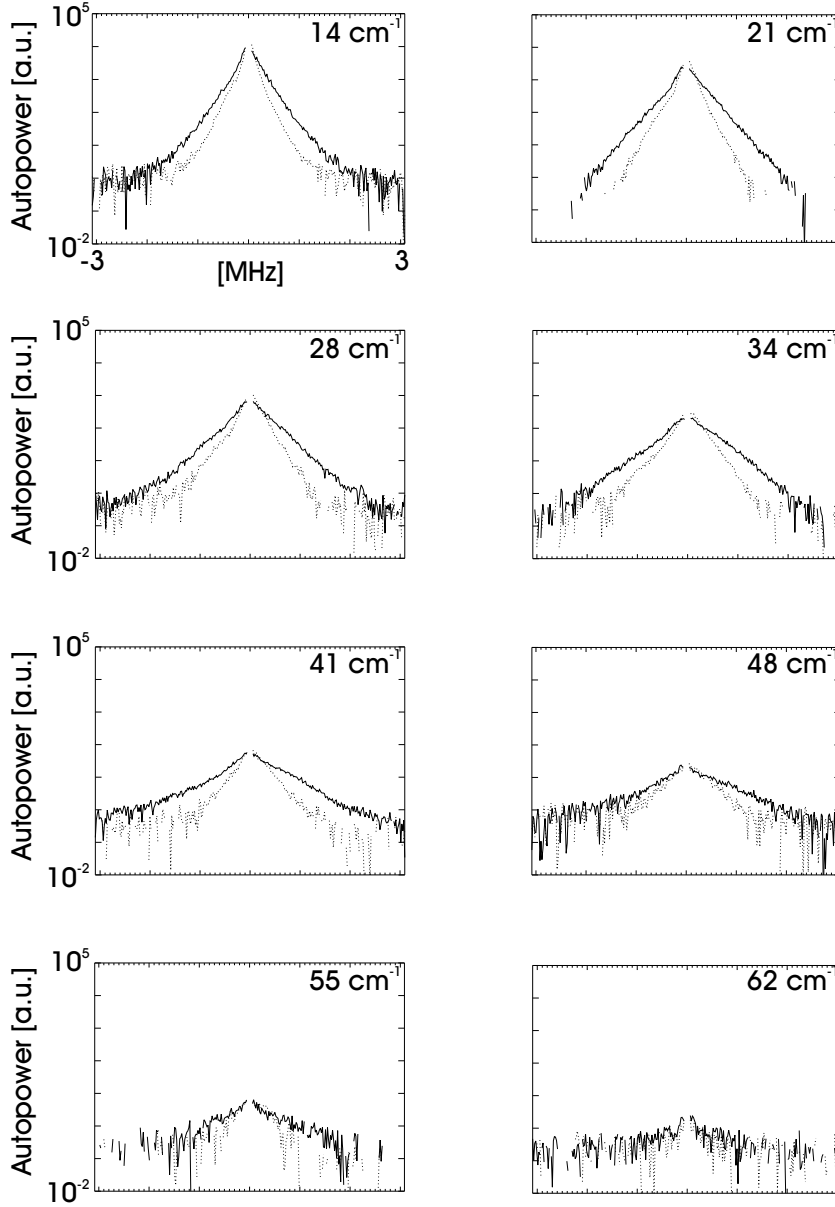


Figure 53. Averaged autopower spectra for L-mode (solid) and H-mode (dotted) time windows.

The fit coefficients are shown in table 4. Since d_3 and d_4 represent the slopes of the autopower spectra, we have directly shown that the H-mode slopes are much steeper than the corresponding L-mode ones. The average of the ratios

$$\left(\frac{d_3^L}{d_3^H} \right) \quad \left(\frac{d_4^L}{d_4^H} \right) \quad (228)$$

for negative and positive frequencies is 1.8 ± 0.3 .

This implies that if we 'stretch' the H-mode frequency scale by this amount, the L- and H-mode slopes should be comparable. That this is indeed the case is shown in figure 55, where the H-mode frequencies are multiplied by 1.8. Or stated in another fashion, the velocity of H-mode fluctuations is only about half the L-mode velocity.

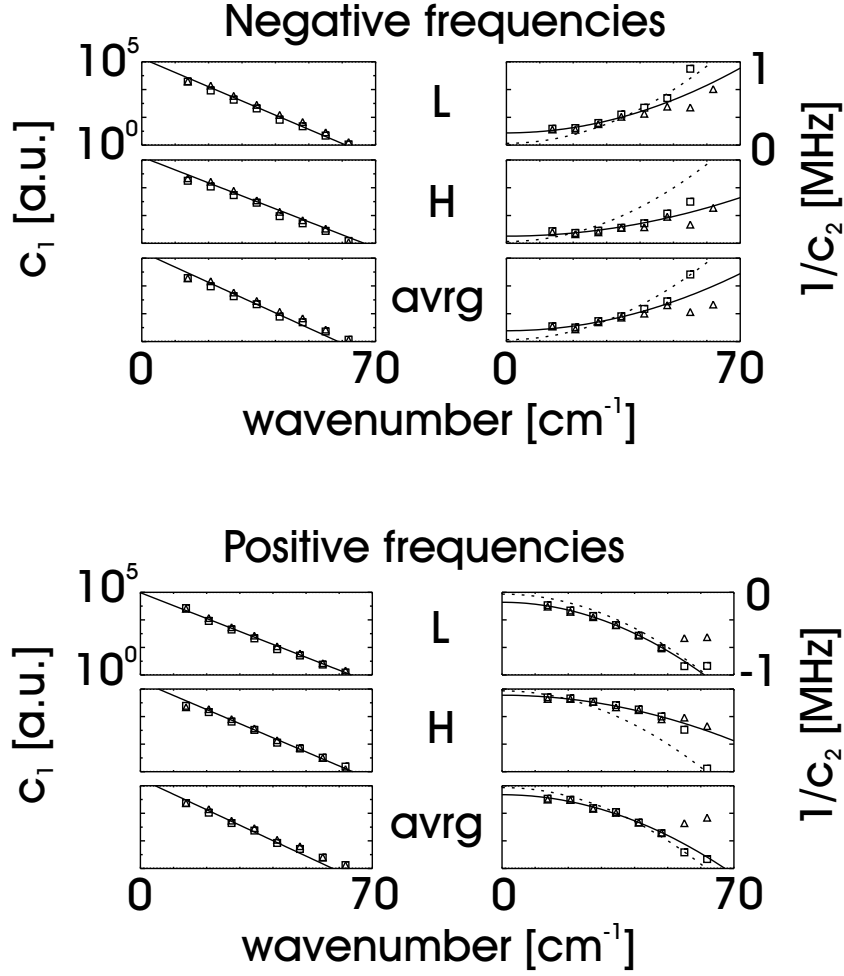


Figure 54. Autopower fit coefficients for negative (three top rows) and positive (three bottom rows) frequencies. For each frequency sign: Left, top to bottom: c_1 versus k for L-mode, H-mode and average spectra. Right, top to bottom: $1/c_2$ versus k for L-mode, H-mode and average spectra. The solid lines on the left-hand sides are exponential fits to c_1 , while the right-hand solid lines are fits according to equation 227 (see text). The dotted lines are reference values from measurements in Alcator C (see text). Triangles are volume 1, squares volume 2.

Parameter	L_{neg}	H_{neg}	$\text{Average}_{\text{neg}}$	L_{pos}	H_{pos}	$\text{Average}_{\text{pos}}$	Reference
$d_1/10^5$ [a.u.]	1.6	1.5	2.4	0.9	2.9	2.6	-
d_2 [mm]	2.0	1.8	2.1	1.8	2.0	2.2	-
d_3 [kHz]	147	86	129	-121	-75	-108	22
d_4 [cm ² kHz]	0.159	0.094	0.140	-0.235	-0.113	-0.197	0.257
$\sqrt{d_4/d_3}$ [mm]	0.3	0.3	0.3	0.4	0.4	0.4	1.1

Table 4. The d fit coefficients. The subscripts refer to the frequency sign. Last column shows the result from [154].

Mean frequencies The velocity differences between L- and H-mode fluctuations can also be evaluated using mean frequencies. We show mean frequencies calculated separately for L- and H-mode time windows in figure 56. The results are shown for both negative and positive frequencies; the solid lines are fits to the datapoints assuming that the mean frequency scales linearly with wavenumber.

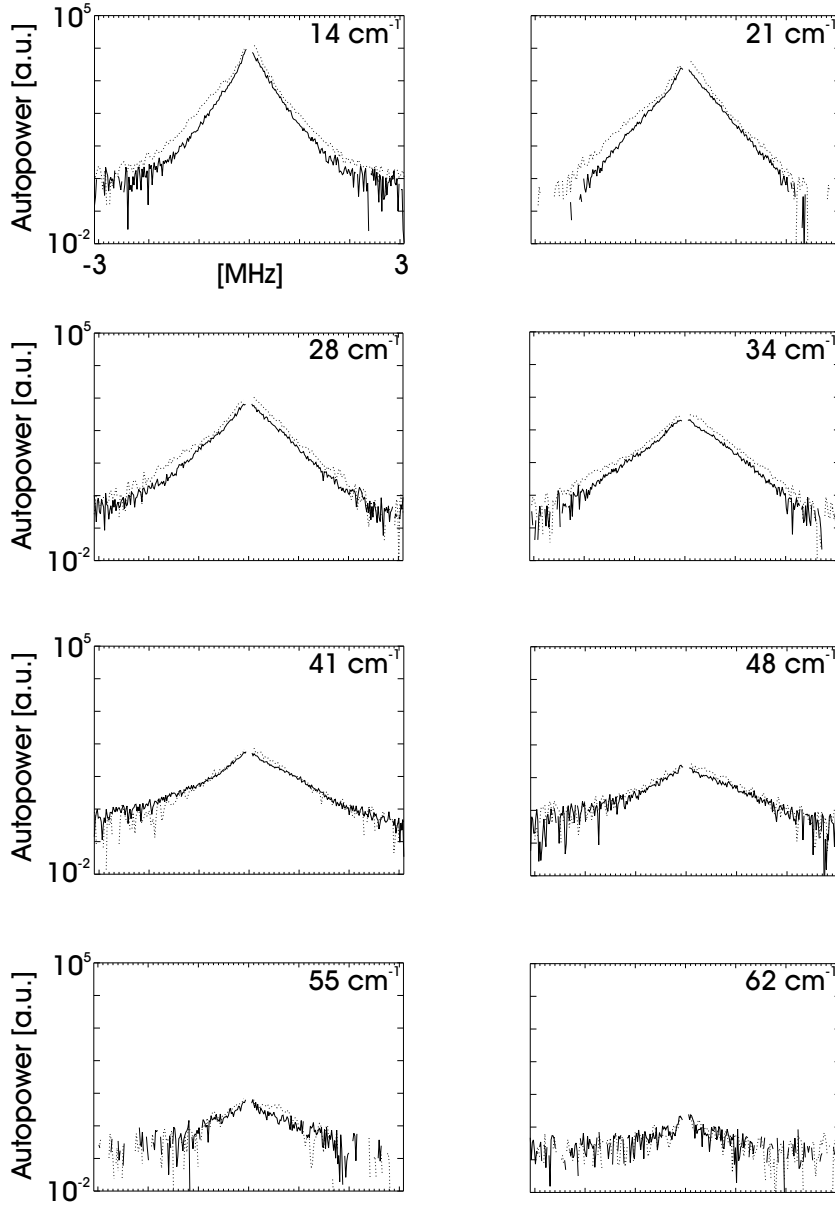


Figure 55. Averaged autopower spectra for L-mode (solid) and H-mode (dotted) time windows. *NOTE:* The H-mode frequencies have been scaled by a factor 1.8 (see text).

The slope of the fits gives us mean velocities

$$\begin{aligned} \langle v \rangle_L &= 658 \pm 29 \text{ m/s} \\ \langle v \rangle_H &= 405 \pm 12 \text{ m/s}, \end{aligned} \quad (229)$$

where the uncertainty estimate is constructed using frequencies of both signs. The ratio between the velocities is 1.6, slightly smaller than the value found previously. If the mean velocities are exclusively due to a radial electric field, the size of this field would be

$$\begin{aligned}
\langle E_r \rangle &= B_\varphi \times \langle v \rangle \\
\langle E_r \rangle_L &= 1.6 \text{ kV/m} \\
\langle E_r \rangle_H &= 1.0 \text{ kV/m},
\end{aligned} \tag{230}$$

which is the typical E_r size at the plasma edge.

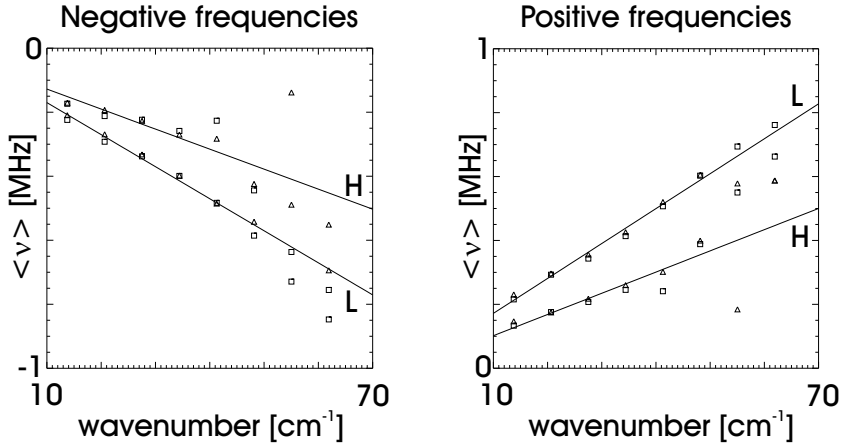


Figure 56. Left: Mean frequency versus wavenumber for negative frequencies, right: For positive frequencies. The solid lines are fits assuming that the mean frequency scales linearly with wavenumber. Note that the L-mode slopes are larger than the H-mode slopes, and that the datapoints have a larger scatter above 50 cm^{-1} . Triangles are volume 1, squares volume 2.

Wavenumber spectra We now discuss separated L- and H-mode wavenumber spectra, see figure 57. The left-hand plot shows the frequency integrated L-mode power versus wavenumber, two power-law fits (solid lines) and an exponential function fit (dashed line). The right-hand side shows the H-mode frequency integrated power versus wavenumber, again fitted using power-laws or an exponential function. Two features are especially interesting here: (i) The L- and H-mode wavenumber spectra are similar, both in amplitude and as a function of wavenumber and (ii) either spectrum can be fitted using two power-laws or a single exponential function. Fits to power-laws $P \propto k^{-m}$ give $m \sim 2.7$ at small wavenumbers and $m \sim 7$ at large wavenumbers (see also [80] and [28]), whereas fits to exponential functions $P \propto e^{-nk}$ give $n \sim 0.15 \text{ cm}$ (fitting to the entire wavenumber range). Similar conclusions were reached in Tore Supra for Ohmic and L-mode plasmas [67]. We again emphasise that these numbers are valid for both L- and H-mode.

8.2.4 Correlations

The temporal evolution of the autopower spectra indicated that: (i) The amplitude of density fluctuations, magnetic field fluctuations and the H_α -signal changes in a correlated way at the L-H-L transitions. (ii) The time evolution of density and magnetic field fluctuations shows an intermittent nature (see figure 52). These phenomena will be analysed in detail in the following.

In this subsection we will focus on results obtained from density fluctuations in volume 1. The results from volume 2 have also been analysed and were found to be qualitatively in agreement with the volume 1 results. Further, we only describe

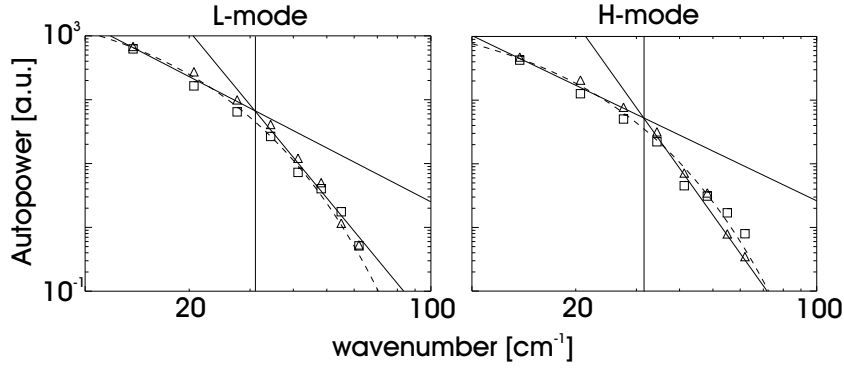


Figure 57. Left: Wavenumber spectrum of L-mode density fluctuations, right: H-mode wavenumber spectrum. Solid lines are power-law fits to the 3 smallest and 5 largest wavenumbers, dashed lines are fits to exponential functions. The vertical lines indicate the transition wavenumber for the power-law fits. The power-law fit grouping of points used is the only one where convergence is obtained. Triangles are volume 1, squares volume 2.

analysis made using positive frequencies from LOTUS; again, the results obtained from negative frequencies are analogous to the positive frequency results.

The quantities that are correlated below are density fluctuations from volume 1 having different frequencies, the RMS power of Mirnov coil measurements and an H_α -signal. The Mirnov coil samples are $4 \mu\text{s}$ apart, so that 25 samples are used to construct the RMS Mirnov power in the first subsection ($100 \mu\text{s}$ time lag steps) and 5 samples are used in the last subsection to arrive at the $20 \mu\text{s}$ time lag resolution.

Correlated changes in density fluctuations, limiter H_α -emission and magnetic fluctuation power We wish to quantitatively analyse the correlation between the limiter H_α -emission, density and magnetic field fluctuation amplitude by calculating crosscorrelations between these signals. The time lag resolution is limited by the H_α -signal, which is $100 \mu\text{s}$. We will correlate time windows of 50 ms length, including several L- and H-mode phases. The objective is to establish that all the fluctuating fields are strongly correlated on this time scale. We begin by recalling the basic definitions: Usually, the crosscovariance between two time series x and y is given as

$$R_{xy}(\tau) = \frac{1}{N} \sum_{k=0}^{N-\tau-1} (x_{k+|\tau|} - \bar{x})(y_k - \bar{y}) \text{ for } \tau < 0$$

$$R_{xy}(\tau) = \frac{1}{N} \sum_{k=0}^{N-\tau-1} (x_k - \bar{x})(y_{k+\tau} - \bar{y}) \text{ for } \tau \geq 0, \quad (231)$$

where τ is time lag and N is the size of the two series [16]. Similarly, the cross-correlation is conventionally defined in terms of crosscovariances as

$$C_{xy}(\tau) = \frac{R_{xy}(\tau)}{\sqrt{R_{xx}(0) \times R_{yy}(0)}} \quad (232)$$

We use this standard definition of the crosscorrelation in the present subsection, where the L- and H-mode separation is not done. We will in the next subsection describe modified versions of the correlations, designed to treat a series of time windows in order to calculate separate L- and H-mode correlations.

We will let the band autopower of the density fluctuations be the x series, and y be either the H_α -signal or the power of the Mirnov signal. This means that for positive lags, density fluctuations occur first, while for negative lags, they are delayed with respect to the other series. We will denote the lag where the correlation has a maximum the 'toplag', τ_0 [165]. The crosscorrelation will be calculated for several density fluctuation frequency bands and represented in contour plots; in these plots we define a global maximum correlation position in (τ, ν) -space: $\tau_0^{\max} = \text{MAX}(\tau_0)^b$.

We show two series of plots in figures 58 and 59. The contour plots show $C_{xy}(\tau)$ versus frequency of the density fluctuations and time lag in units of $100 \mu\text{s}$ (covering ± 1 ms time lag in total).

Figure 58 shows the crosscorrelation between the density fluctuations and H_α for the discharge series analysed. Our first observation is that τ_0^{\max} is close to zero time lag and displaced away from low frequency density fluctuations. For 21 cm^{-1} the correlation is largest, about 75 %; it is clear that τ_0^{\max} shifts towards higher frequencies as the wavenumber is increased. The decay of the correlation is slower for positive lags, where H_α is delayed relative to the density fluctuations. This delay is due to the fact that the decay time of H_α in the L-H transition is hundreds of μs , whereas the density fluctuations drop on a very fast time scale. So we have established that these two signals are highly correlated for small wavenumbers, that the correlation is lost for the largest wavenumbers and that there is a shift of τ_0^{\max} to higher frequencies with increasing wavenumber. On the $100 \mu\text{s}$ time scale it is not possible to establish a time delay between the signals.

Figure 59 displays the crosscorrelation between the density fluctuations and the RMS value of the magnetic fluctuations. Qualitatively, these plots are in agreement with what was found for the H_α -correlations, but now there is a small systematic shift of the toplag to negative values; this indicates that the density fluctuations are somewhat delayed relative to the magnetic fluctuations. The time lag resolution is too coarse to conclude anything quantitative at this point - a rough estimate is a $100 \mu\text{s}$ time delay. In the next subsection the analysis will be done using a faster time resolution. Finally, the shift of τ_0^{\max} towards higher frequencies for larger wavenumbers is also observed. The decay of the correlations is quite similar for lags of both signs.

Correlation between δn_e and $\partial_t B_\theta$ bursts We saw that the dithering itself is highly correlated, especially for small wavenumbers. To discover if the single spikes are correlated on an even faster time scale, we will separate the calculations to deal with either L- or H-mode time intervals. Since we treat a number of L- and H-mode time windows, an averaging procedure must be made. In our notation, the number of L-mode time windows is N_L , where the length of L-mode window number n_L is equal to l_{n_L} (and equivalently N_H , n_H and l_{n_H} for H-mode). Two initial corrections to the crosscovariance were made: (i) The normalisation of the sum ($1/N$) was dropped and (ii) the averages used (\bar{x}_{tot} , \bar{y}_{tot}) were not simply averages of each time window, but averages over all time windows, L or H. This does not make a large difference since the overall time window is selected with care to be quasi stationary. We denote the resulting crosscovariances $R_{xy}^{\text{mod}}(\tau)_{j,m,n_m}$, where j is volume number (1 or 2) and m is mode designation (L or H):

$$R_{xy}^{\text{mod}}(\tau)_{j,m,n_m} = \sum_{k=0}^{l_{n_m}-\tau-1} (x_{k+|\tau|} - \bar{x}_{\text{tot}})(y_k - \bar{y}_{\text{tot}}) \text{ for } \tau < 0$$

$$R_{xy}^{\text{mod}}(\tau)_{j,m,n_m} = \sum_{k=0}^{l_{n_m}-\tau-1} (x_k - \bar{x}_{\text{tot}})(y_{k+\tau} - \bar{y}_{\text{tot}}) \text{ for } \tau \geq 0, \quad (233)$$

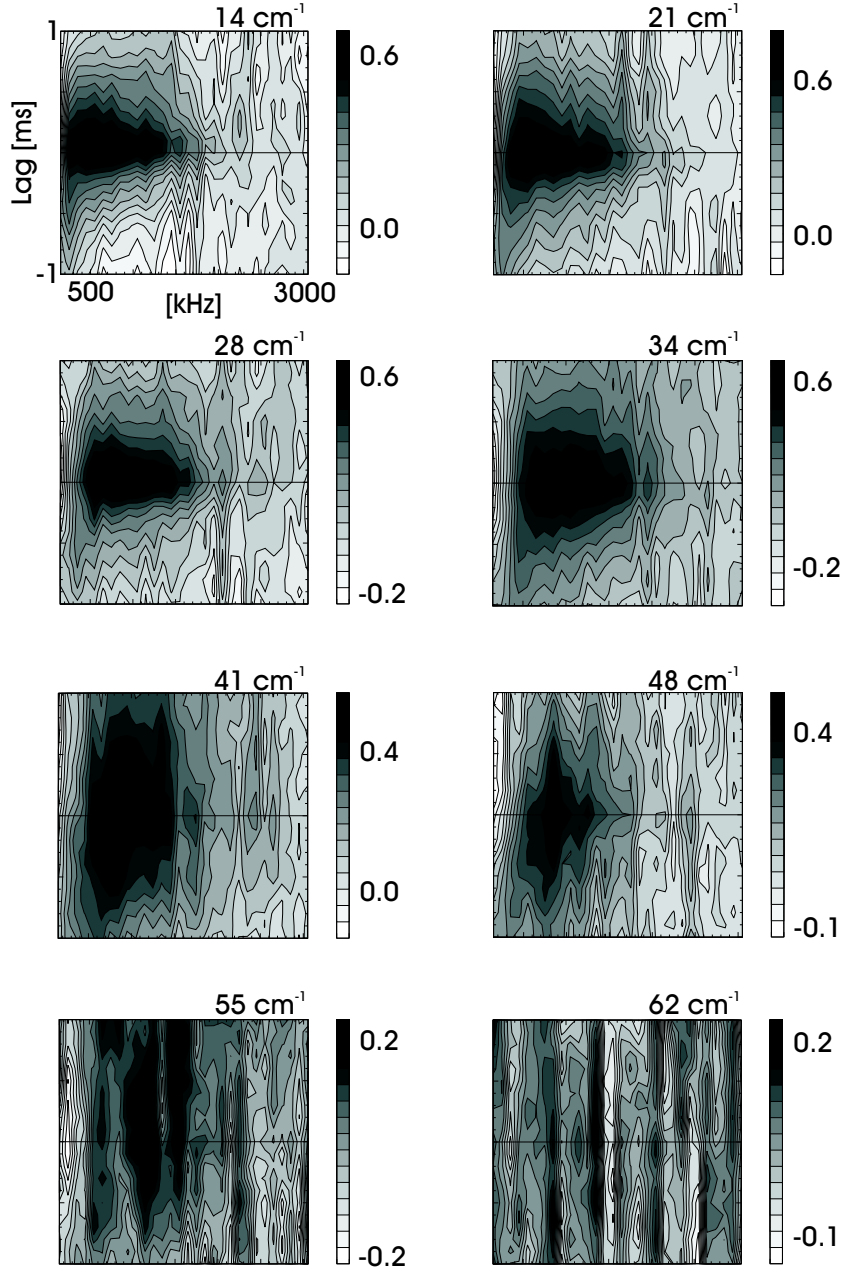


Figure 58. Crosscorrelation between H_α and density fluctuation band autopower from collective scattering versus band central frequency and time lag (units of 100 μ s). Note that the greyscale is different for each discharge.

where we have dropped the (j, m, n_m) subscripts on the right-hand sides for simplicity.

From the series of time windows we can construct an estimate of the mean crosscovariance

$$\langle R_{xy}^{\text{mod}}(\tau)_{j,m} \rangle = \frac{\sum_{n_m=1}^{N_m} l_{n_m} R_{xy}^{\text{mod}}(\tau)_{j,m,n_m}}{\sum_{n_m=1}^{N_m} l_{n_m}}, \quad (234)$$

weighted by the length of the different time windows [17]. In analogy with this definition, we can construct a mean standard deviation

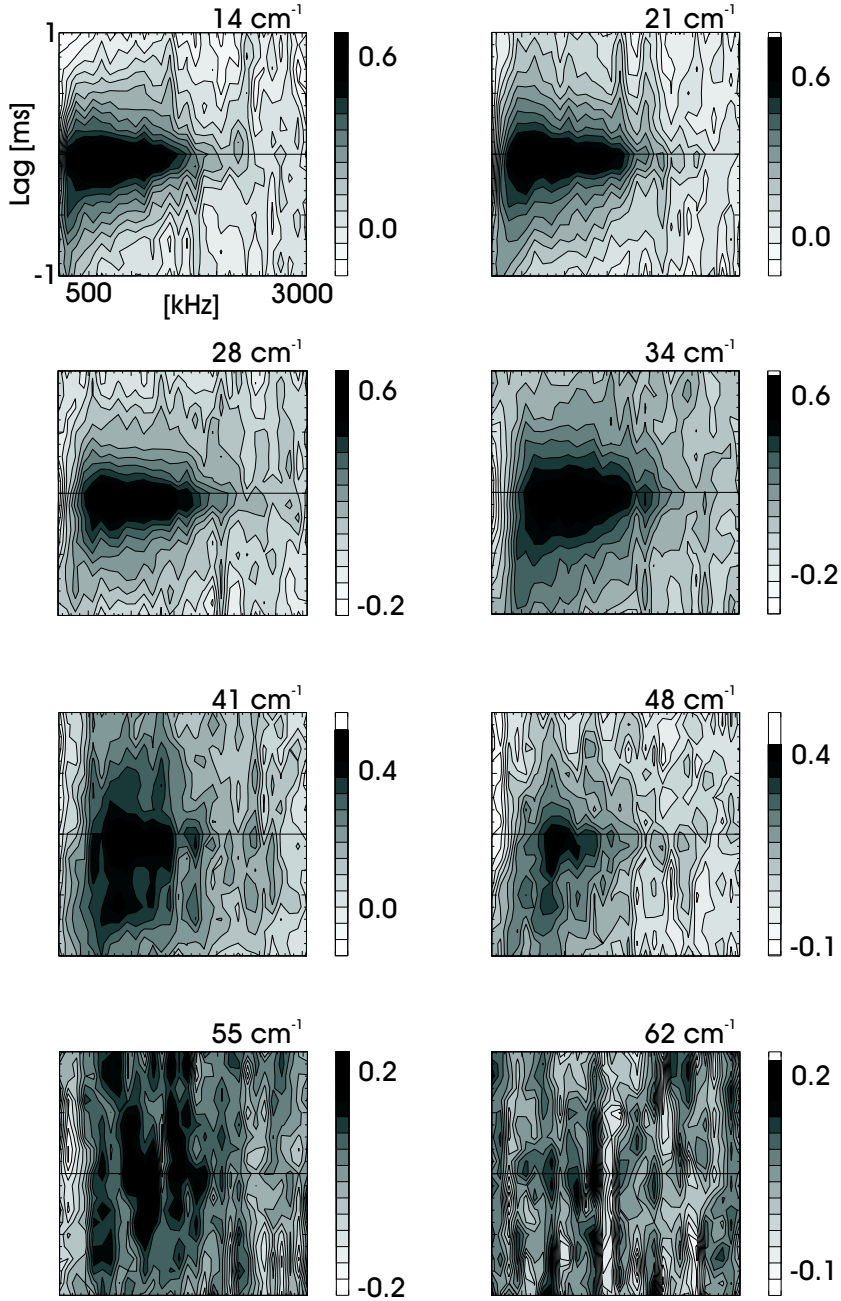


Figure 59. Crosscorrelation between RMS Mirnov signal and density fluctuation band autopower from collective scattering versus band central frequency and time lag (units of $100 \mu\text{s}$). Note that the greyscale is different for each discharge.

$$\langle \sigma(\tau)_{j,m} \rangle = \sqrt{\left(\frac{\sum_{n_m=1}^{N_m} l_{n_m} R_{xy}^{\text{mod}}(\tau)_{j,m,n_m}^2}{\sum_{n_m=1}^{N_m} l_{n_m}} - \langle R_{xy}^{\text{mod}}(\tau)_{j,m} \rangle^2 \right) \times \frac{1}{N_m - 1}}, \quad (235)$$

to calculate approximate errorbars on the correlations.

A corresponding procedure can be used for the crosscorrelation: We modify the crosscorrelation to arrive at $C_{xy}^{\text{mod}}(\tau)_{j,m,n_m}$ and take all time windows into account when averaging. The mean and mean standard deviation of the crosscorrelation is then found as was done for the crosscovariance.

Having explained our procedure to calculate separated crosscovariances, cross-correlations and errorbars on these, we can proceed to the results. Figure 60 shows crosscorrelations between magnetic and density fluctuations for two frequencies, 150 kHz (left column) and 750 kHz (right column). The top plots show L-mode results, bottom H-mode. It is immediately apparent that neither L- nor H-mode fluctuations are correlated at low frequencies, whereas L-mode fluctuations are clearly correlated at higher frequencies. However, H-mode fluctuations remain uncorrelated. The L-mode high frequency toplag is slightly shifted towards negative lags (but at the limit of the lag resolution), indicating that the magnetic fluctuations occur about $20 \mu\text{s}$ before the density fluctuations. We must note that since the A/D converters are not synchronised, systematic time delays could be due to electronic artifacts instead of actual time delays. The crosscorrelation in L-mode for high frequencies is seen to be 30 %. This reduction in the crosscorrelation is due to the reduced SNR arising from the binning of fewer measurement points. The FWHM of the correlation is of order $100 \mu\text{s}$, which means that we have found the fastest time scales that are correlated. If the fluctuations had been correlated on even faster scales, we would only see a sharp peak of the correlation at one given lag.

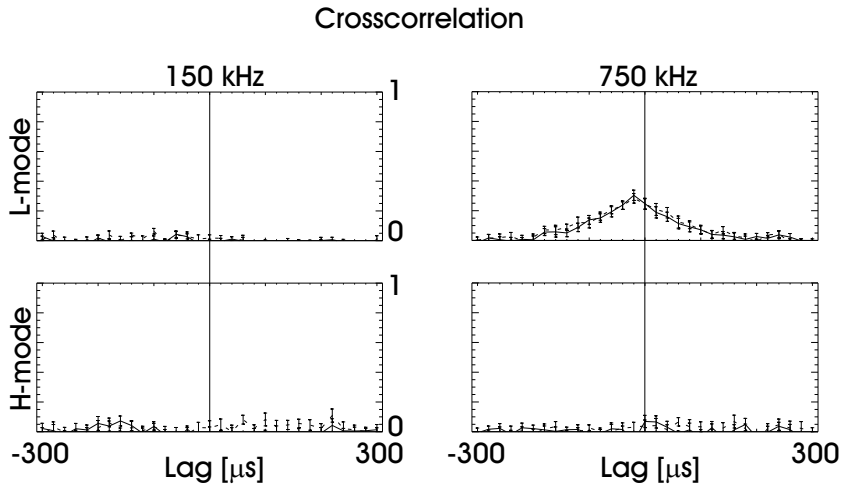


Figure 60. Crosscorrelation between magnetic and density fluctuations for L- and H-mode time windows versus time lag (units of $20 \mu\text{s}$), 14 cm^{-1} . Left, crosscorrelation for 150 kHz density fluctuations, right for 750 kHz. Solid line is volume 1, dotted line volume 2.

Cross correlating a series of L- or H-mode time windows can also be applied to calculate the crosscorrelation between the density fluctuations measured in volume 1 and 2 of LOTUS. An example for the same frequencies as those treated in the previous paragraph is shown in figure 61. At low frequencies, the fluctuations are correlated at zero time lag and have disappeared at $\tau = \pm 20 \mu\text{s}$. Our time resolution is in this case not sufficient to resolve the shape of the crosscorrelation. At higher frequencies, this feature disappears in H-mode, but remains in the L-mode crosscorrelation. Further, an additional broad shape emerges in the L-mode correlation and seems to be superimposed onto the narrow feature. This behaviour persists for the discharges having larger wavenumbers.

We have now shown 2D plots of the results from one shot at two frequencies (figure 60 left/right column). It is of course interesting to get the full picture, which can be accomplished by making 3D plots showing the L- and H-mode cross-correlations versus density fluctuation frequency and time lag. These are shown

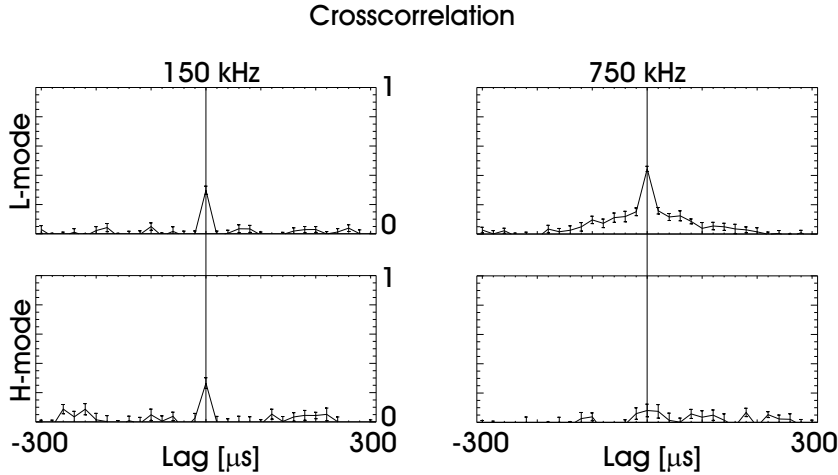


Figure 61. Crosscorrelation between the density fluctuations in volumes 1 and 2 for L- and H-mode time windows versus time lag (units of $20 \mu\text{s}$), 14 cm^{-1} . Left, crosscorrelation for 150 kHz density fluctuations, right for 750 kHz.

for L-mode in figure 62 and H-mode in figure 63. Looking at the plots in figure 62, we see the same structure as was observed for the unseparated crosscorrelations: τ_0^{max} is slightly shifted to negative lags, and towards higher frequencies. The global maximum correlation shifts to higher frequencies with increasing wavenumber, and disappears at the highest values. In contrast to these clear correlations, the H-mode case shown in figure 63 exhibits no systematic correlation.

8.2.5 Discussion

We have divided the discussion into two parts: The analysis results pertaining to W7-AS are discussed first, thereafter we describe measurements from the Doublet III-D (DIII-D) tokamak and compare them to our findings.

W7-AS measurements Discussing the W7-AS results, we treat measurements in the order they appear in the main text.

Our autopower spectra are all decreasing monotonically with frequency. We note that this spectral shape has been observed in the FT-2 tokamak as well [28] (for $k \geq 14 \text{ cm}^{-1}$), whereas pronounced 'double hump' spectra peaking away from DC as observed in Tore Supra (see e.g. [112]) have not been observed in W7-AS, even with good spatial resolution [132]. The frequency range of the fluctuations does not increase substantially with wavenumber. This means that the phase velocity

$$v_{\text{ph}} = \frac{\omega}{k} \quad (236)$$

decreases with increasing wavenumber, i.e. smaller structures have a smaller phase velocity. Again, the same conclusion was reached in [28] and is thought to indicate that 'the character of motion is different for fluctuations with different scale lengths'.

We found that the autopower slope versus frequency was steepest for H-mode phases, and that the L- and H-mode spectral shapes were close to identical if the H-mode frequencies were scaled by a factor 1.8. The trend of this observation was confirmed by the calculation of mean frequencies/velocities showing that the L-mode mean velocity was 1.6 times larger than the H-mode one. This velocity decrease at the L-H transition could be caused by a decrease of $|E_r|$ at the

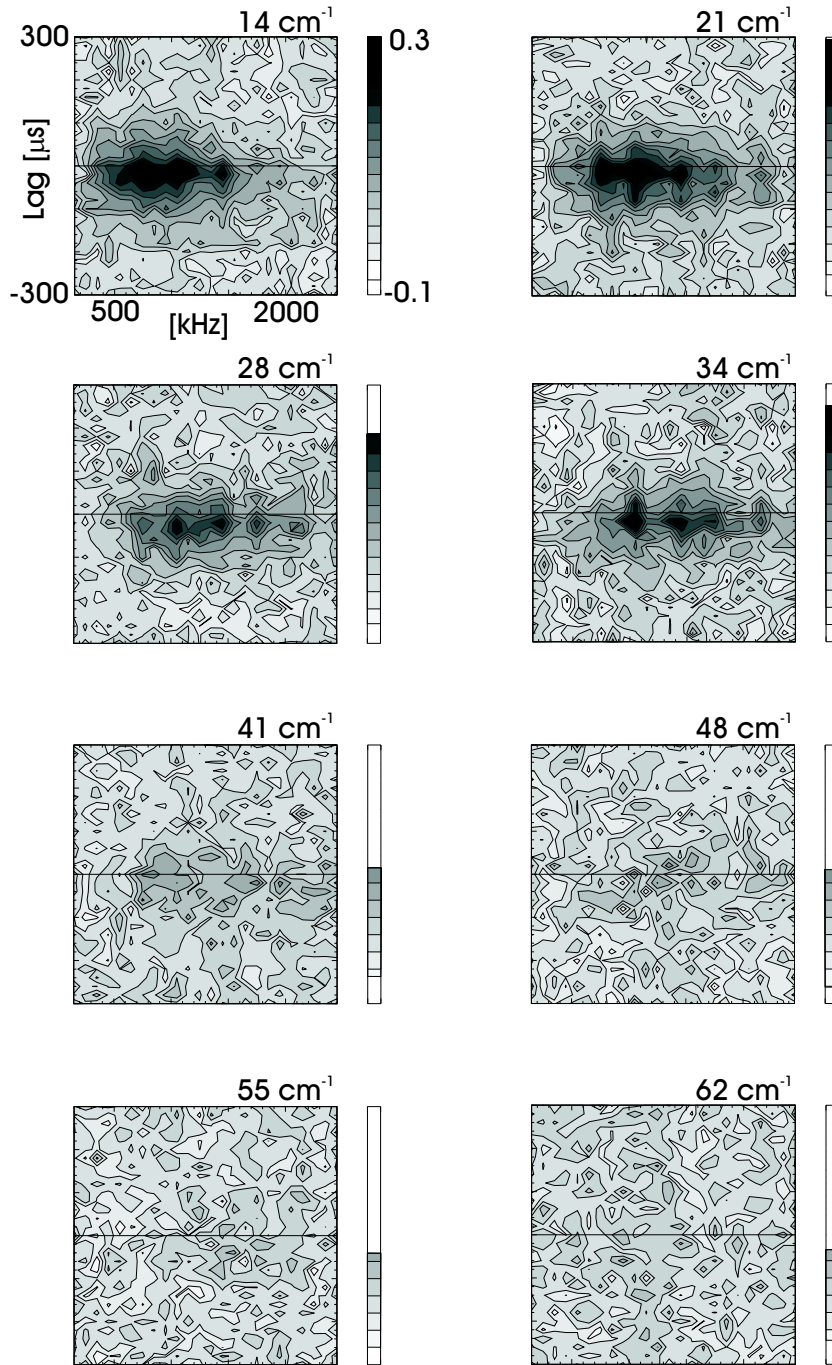


Figure 62. Crosscorrelation between Mirnov RMS signal and density fluctuation band autopower from collective scattering versus band central frequency and time lag for L-mode time windows (units of $20 \mu\text{s}$). The greyscale on the right-hand sides of the plots shows what range of the total scale is relevant for the particular wavenumber.

radial position of the fluctuations. Usually the L-H transition is associated with a velocity increase at the plasma edge; these contradictory observations can be brought into agreement if the velocity decrease we observe is located deep inside the plasma. Alternatively, fluctuations could possess different characteristics than have previously been studied at the large wavenumbers we measure.

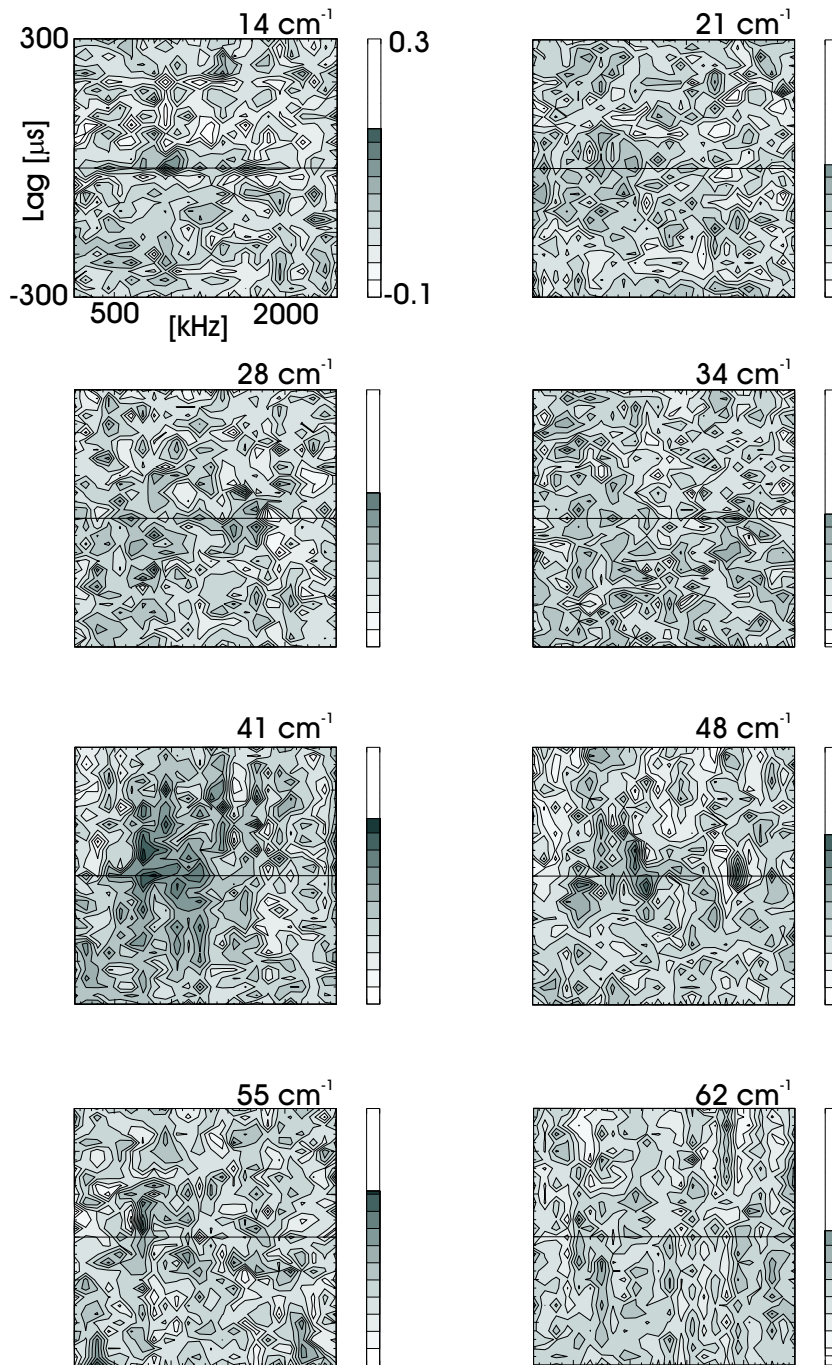


Figure 63. Crosscorrelation between Mirnov RMS signal and density fluctuation band autopower from collective scattering versus band central frequency and time lag for H-mode time windows (units of $20 \mu s$). The greyscale on the right-hand sides of the plots shows what range of the total scale is relevant for the particular wavenumber.

The small wavenumber power-law fit is quite close to the Kolmogorov value of $8/3$ [2], while the large wavenumber exponent is completely outside this range. The fact that an exponential can fit all wavenumbers could mean that the wavenumbers observed are entering the dissipation range [110]. To determine whether there is a 'hinge point' between two power-laws at a given scale or if the wavenumber

spectrum is exponentially decaying we would need more than the 8 datapoints used here. Converting the transition wavenumber for the power-law fits to a spatial scale gives $2\pi/k \sim 2$ mm. The only natural spatial scale in the plasma close to this value is the ion Larmor radius, which is 1 mm. Wavenumber scans in plasmas having different Hydrogen isotope ratios could clarify if the hinge point is connected to the ion Larmor radius. It is interesting to note that the found exponents apply to both L- and H-mode data, suggesting that the L-H transition does not change the relative weight of the fluctuation wavenumbers measured.

We have shown that high frequency density fluctuation bursts are strongly correlated with bursts in H_α -light and magnetic fluctuations on a sub ms time scale. In contrast, correlations are not observed at lower frequencies - this observation indicates that low and high frequency density fluctuations are two separate phenomena. Since the bursts associated with ELMy activity are known to originate a few centimeters inside the LCFS [72], it is likely that the high frequency density fluctuations are located here as well. The low frequency density fluctuations could be located somewhat outside the LCFS [132]. This would also be consistent with poloidal plasma rotation due to a large negative radial electric field E_r inside the LCFS and a small positive E_r outside. So, low frequency fluctuations (outside LCFS) are large in H-mode, while high frequency fluctuations (inside LCFS) are large in L-mode.

The separated L- and H-mode correlation analysis on a faster μs time scale showed that magnetic and density fluctuations are uncorrelated at low frequencies, but that L-mode high frequency density fluctuations are correlated to the magnetic fluctuations. H-mode fluctuations remain uncorrelated at high frequencies. We can think of two probable causes for the disappearance of high frequency correlations in going from L- to H-mode:

- A reduction of the radial correlation length \mathcal{L}_r at the L-H transition (as has been quantified in e.g. [35] using phase-contrast imaging)
- That the fluctuating zone moves radially inward

The first option would be in agreement with $\mathbf{E} \times \mathbf{B}$ shear suppression theory and has been experimentally verified in DIII-D.

The second option would help to explain why a significant density fluctuation level remains, even in H-mode. However, this would contradict the claim that the low frequency fluctuations are to be found outside the LCFS where E_r is small. Therefore it could be the case that the low frequency fluctuations are deep inside the plasma, where E_r becomes small again.

Comparison with DIII-D measurements We will here compare our results to those of the FIR scattering diagnostic installed on DIII-D [115]. In the cited paper initial L-H transition observations were published; they showed that low frequency turbulence (up to a few hundred kHz) was suppressed in both poloidal directions, and that a high frequency feature in the ion DD direction appeared and gradually (over tens of ms) broadened in frequency during the H-mode (observations for $k = 5 \text{ cm}^{-1}$). The broadening was attributed to an increase of toroidal rotation.

The L-H transition in DIII-D has subsequently been described as a two-step process, where an initial zone of turbulence suppression ('shear layer') having a radial extent of 3-5 cm just inside the separatrix is created within 1 ms [43]. A further transport reduction on a 10 ms time scale is observed extending deeper into the confined plasma. The interior relative fluctuation level decreases about 50 % during this period in comparison to the L-mode level.

A large positive E_r is observed in the core of DIII-D plasmas, attributed to toroidal rotation. The radial electric field decreases monotonically towards the

edge, where a small negative E_r is found (mainly due to poloidal rotation) [116]. The absolute value of E_r becomes larger after the L-H transition both inside and outside the LCFS, meaning that core/edge fluctuations increase their ion/electron DD direction. Assuming that $\mathbf{E} \times \mathbf{B}$ rotation dominates over turbulent mode frequencies, one can obtain localised information on the fluctuations [121]. This approach was used in [116] to conclude that the bulk of the fluctuations was localised at a normalised minor radius of 0.8.

The above paragraphs gave a brief overview of the L-H transition measurements from DIII-D. We will now relate these to the measurements from W7-AS. Let us begin by noting that our measurements deal with the fast initial suppression, since high NBI power is preventing the ELM-free H-mode. Therefore only features pertinent to the fast initial transition will be discussed.

The structure of E_r is quite different in DIII-D and W7-AS. We have already described that the radial electric field in W7-AS has a deep well/small hill just inside/outside the LCFS, respectively. In comparable discharges where the dithering frequency is lower, the H-mode is associated with a deeper well inside the LCFS, while no clear development is seen outside the LCFS (see section 8.3). This is in contrast to the DIII-D E_r -structure described above, where the field both inside and outside the LCFS increases in magnitude.

If the conjecture that $\mathbf{E} \times \mathbf{B}$ rotation dominates is correct, changes in the E_r of W7-AS are consistent with the changes observed in the density fluctuation autopower spectra: As the plasma goes from L- to H-mode, the high frequency component is suppressed due to the deeper well inside the LCFS that increases the E_r -shear. This agrees with the localisation of an edge transport barrier in W7-AS that is situated within the first 3-4 cm inside the separatrix [71]. The low frequency component remains unchanged or increases slightly, probably due to a minor flattening of the hill outside the LCFS. Apparently, this explanation means that we can reconcile our measurements with those made with the DIII-D FIR diagnostic. We note for completeness that there is a possible ambiguity in the radial localisation of the low frequency fluctuations, since a small E_r exists both outside the LCFS and deep in the confinement zone.

Comparing L- and H-mode autopower spectra [120] as we did in figure 19, a broadening of the spectrum was observed from L- to H-mode in DIII-D. This is interpreted as an indication of increased E_r -shear. Although the spectrum widens, the frequency integrated power decreases markedly. This observation is the opposite of what we found in W7-AS, where the autopower spectra narrowed at the L-H transition.

A possible source for systematic differences between DIII-D and W7-AS measurements could be that fluctuations are reacting in a different fashion on varying spatial scales (DIII-D range [2, 16] cm^{-1} , W7-AS range [14, 62] cm^{-1}). The validity of this idea is difficult to test, but there are indications that electron transport remains anomalously large, also in the majority of improved confinement regimes [122]. Turbulence in the ITB gradient region has been attributed to the possible occurrence of ETG turbulence or other short wavelength modes [44]. A distinction can be made between small wavenumber ion temperature gradient (ITG) turbulence and large wavenumber ETG turbulence [60]. This ordering is maintained in [123], where the increase of low frequency density fluctuations at the linear/saturated Ohmic confinement (LOC/SOC) transition is argued to be due to long wavelength ($k\rho_s \approx 0.2-0.5$) ITG turbulence. Since the majority of present fluctuation diagnostics have an upper wavenumber limit of about 15 cm^{-1} [115] [34] [42], a suppression of turbulence at these wavenumbers could still be consistent with turbulence remaining at larger wavenumbers. The usual observations are corroborated by reflectometry measurements at small wavenumbers in W7-AS [70]; these demonstrate a large reduction of edge turbulence entering the quiescent

H-mode in agreement with tokamak findings.

We briefly want to mention measurements of density fluctuations in DIII-D during negative central shear (NCS) operation [122]. A striking similarity between figure 3 in [122] (spectrogram of density fluctuation autopower versus time and frequency) and our figure 49 shows that the dithering signature in both cases consists of vertical lines in the plots (bursts of broadband frequency fluctuations). The transition from NCS L- to H-mode is accompanied by a fast drop in the low frequency edge fluctuations, while the high frequency core fluctuations are also reduced rather abruptly, but less pronounced in amplitude.

8.2.6 Conclusions

The autopower results first of all demonstrate that ELMy or dithering behaviour is seen in the density fluctuations at high frequencies, whereas the low frequency fluctuations do not display that connection. The overview figure 49 shows that the dithering activity manifests itself as high frequency bursts. We have further shown that the slope of the autopower spectra versus frequency can be described using an exponential function, and that the mean L-mode velocity is 1.6 times larger than the H-mode one. Low frequency turbulence remains present in H-mode plasmas, while high frequency structures are partially suppressed. From the assumption that the poloidal flow is dominated by the $\mathbf{E} \times \mathbf{B}$ Doppler shift we infer that low/high frequencies originate outside/inside the LCFS, respectively. The persistence of low frequency turbulence in H-mode could be an indication that small scale turbulence is responsible for the anomalous electron transport that is observed even in H-mode plasmas. L- and H-mode separated wavenumber spectra can either be fitted to power-laws or exponential functions, with almost identical exponents in both cases.

Our crosscorrelation analysis shows that the high frequency L-mode density fluctuations are correlated to the RMS magnetic fluctuations, while this connection is not found for the H-mode phases. This could be explained by a reduction of the radial correlation length. Further, we have proven that there is a definite answer to our 'Chinese boxes' question posed in the introduction: Bursts are correlated on a 100 μ s time scale, but not faster than that. The question remains whether the correlated structures are directly linked to global confinement.

The comparative analysis treating DIII-D and W7-AS measurements showed that density fluctuations behave disparately in the two machines; in DIII-D the fast suppression of turbulence was observed at low frequencies, while the high frequencies were reduced in W7-AS. The probable explanation is the differing E_r , in that there is a well/hill structure in W7-AS and a monotonic field in DIII-D. Alternatively, the reason could be the different spatial scales observed.

8.3 Confinement bifurcations

In section 8.2 we found that density fluctuations in dithering plasmas had distinct properties in the L- and H-mode phases. The remaining question is whether this behaviour is comparable to that of steady-state L- and H*-modes.

To answer this question we analyse density fluctuations in shot 47114, which was performed on the same day as the series treated in sections 8.1 and 8.2. This discharge developed from L-mode, through a dithering phase and finally made the transition to H*-mode. In this section we will compare fluctuations in these three confinement states.

The section is organised as follows: The first subsection (8.3.1) introduces the discharge analysed. Thereafter autopower spectra are treated in subsection 8.3.2 and correlations during dithering and steady-state conditions are reviewed in subsection 8.3.3. The phase separation technique is applied to dithering L- and H-mode plasmas in subsection 8.3.4 and finally conclusions are drawn in subsection 8.3.5.

8.3.1 Discharge description

Discharge 47114 had settings identical to those of shots 47133-47143, but two important parameters were different: The NBI power was reduced from 2.5 to 1 MW and the line density was ramped up throughout the shot, see figure 64. A reduction of the NBI power enables access to the H*-mode [72] while a density ramp under the given circumstances leads to a L-mode (100 to 400 ms) → dithering H-mode (400 to 550 ms) → H*-mode (550 to 600 ms) sequence. The improved confinement leads to impurity accumulation, causing a radiation collapse [57] at 600 ms.

Figure 64 shows waveforms of a few of the most important quantities; from top to bottom: Stored energy (note the disturbance in the signal from 400 to 550 ms, the dithering phase), line density (ramped up), H α -light (clearly marking the confinement progression), radial electric field E_r at five positions (two inner traces, solid and dotted, clearly displaying the dithering) and density fluctuations normalised by line density squared.

We measured density fluctuations having $k = 14 \text{ cm}^{-1}$ (as for shot 47133). Therefore the switching of E_r somewhat inside the LCFS at about 10^4 V/m corresponds to an $\mathbf{E} \times \mathbf{B}$ frequency of about 900 kHz (see equation 220). Unfortunately, causality between E_r and the density fluctuations can not be established due to the limited time resolution of E_r in this discharge (4 ms).

The development of the density fluctuation power closely reflects the confinement behaviour: Normalising by line density squared to obtain a quantity roughly describing the relative fluctuation level, we note that density fluctuations are significantly reduced in entering the H*-mode. The three analysis time windows that will be treated in the following subsections are indicated by grey rectangles in figure 64.

The behaviour of the magnetic fluctuations is shown in figure 65. The fluctuations in the dithering period (400 to 550 ms) exhibit a clear burst-like behaviour, more pronounced than that of shot 47133 (figure 39). Again, we caution that the spectrogram frequencies may be misleading due to aliasing effects (see discussion in section 8.1).

8.3.2 Autopower spectra

We begin our description of the density fluctuation autopower spectra by showing a spectrogram of shot 47114 (volume 1) in figure 66. Density fluctuations are shown

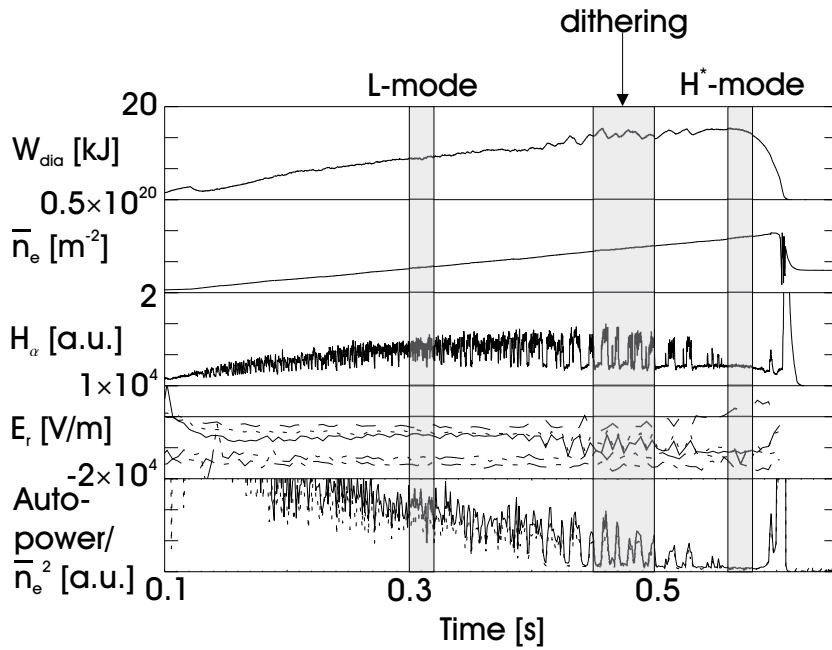


Figure 64. Discharge overview - time traces from 100 to 650 ms. From top to bottom: Diamagnetic energy [kJ], line density, H_α -light, radial electric field and frequency integrated density fluctuations (1 ms time windows) in volumes 1 (solid) and 2 (dotted) at $k = 14 \text{ cm}^{-1}$ normalised by line density squared. The radial electric field is shown for five radial positions corresponding to those in figure 40: Innermost to outermost position is represented by solid, dotted, dashed, dash dot and dash dot dot dot lines. The three analysis time windows are marked by grey semi-transparent rectangles.

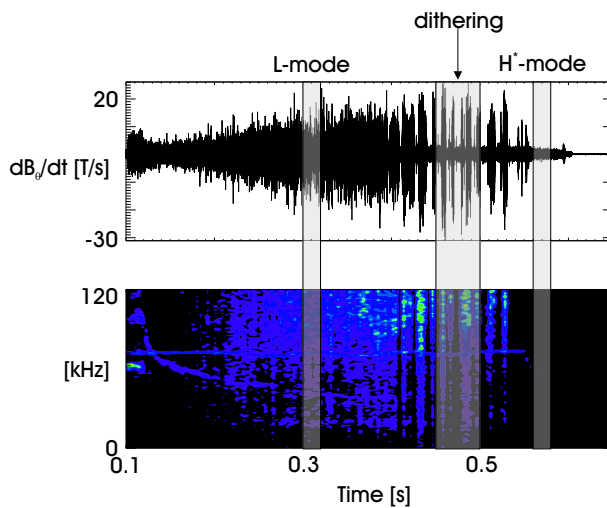


Figure 65. (Colour) Magnetic field derivative in T/s from the 'MIRTIM' monitor coil (top) and a spectrogram (bottom) covering 550 ms. The three analysis time windows are marked by grey semi-transparent rectangles.

up to $\pm 2 \text{ MHz}$ on a logarithmic colourscale; again, the confinement transition sequence is readily observable. ELM or dithering activity manifests itself as high frequency activity, while only low frequency fluctuations remain in H^* -mode (after

550 ms). Shortly after entering the H*-mode, a gradually chirping frequency mode develops spinning down as the radiation collapse is approached. It is not clear if these two phenomena are connected.

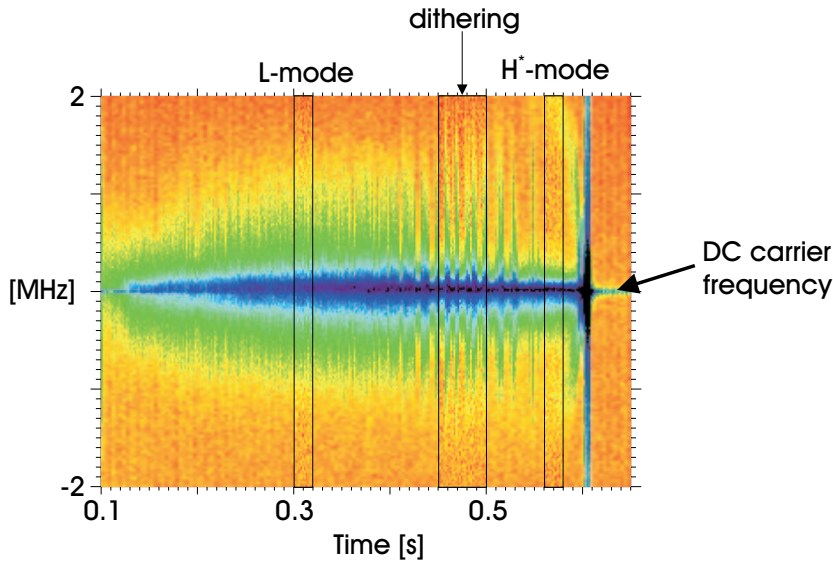


Figure 66. (Colour) Autopower versus time and frequency for discharge 47114, volume 1. The time resolution of the spectra is 1 ms and the colourscale is logarithmic.

In figure 67 we compare autopower spectra in the three analysis time windows. The left-hand plot shows spectra in the dithering phase separated using the technique described in section 8.2. The solid line spectrum is L-mode, the dotted line H-mode. As previously, the L-mode spectrum extends to higher frequencies than the H-mode spectrum. For positive L-mode frequencies two features seem to be present, above and below 500 kHz. Scaling of the H-mode frequencies by a factor 1.8 (see section 8.2) brings the low frequency spectra into agreement (for positive and negative frequencies), but can not account for the high frequency component. The right-hand plot shows spectra from steady-state L-mode (solid line) and H*-mode (dotted line). The L-mode spectrum is very similar to that during the dithering phase, while the H*-mode spectrum has an additional low amplitude feature at high positive frequencies; this is the chirping feature mentioned in connection with figure 66. Positive frequencies correspond to inward travelling fluctuations. If the chirping feature travels in the electron DD direction it is located towards the bottom of the plasma. Again, scaling by 1.8 accounts for the low frequency changes.

8.3.3 Correlations

In this subsection on correlations, we use the method explained in section 8.2 to correlate density fluctuations, H_α -light and the RMS Mirnov signal. First we compare dithering to steady-state L-mode and H*-mode on a 100 μ s time scale, thereafter we compare magnetic and density fluctuations on a 20 μ s time scale. Note that the correlations with the Mirnov coil system in this section are made using the MIRTIM coil instead of coil 8 in the MIR-1 system (see section 8.1 for a description of the Mirnov coil setup). This change is made for technical reasons.

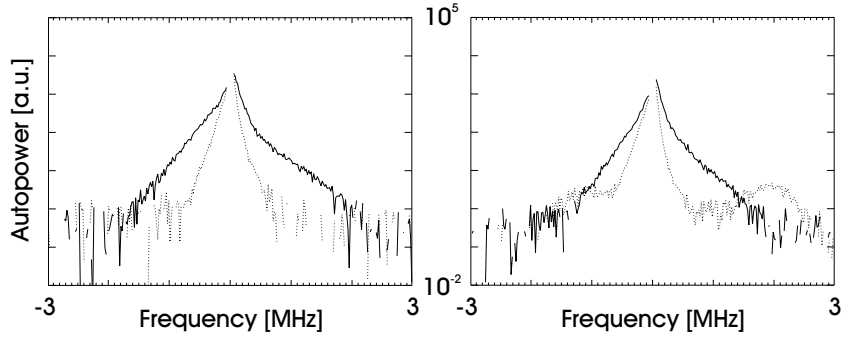


Figure 67. Autopower spectra. Left: L-mode part of dithering phase (solid line) and H-mode part of dithering phase (dotted line). Right: Steady-state L-mode (solid line) and H*-mode (dotted line).

Correlated changes in density fluctuations, limiter H_α -emission and magnetic fluctuation power

The comparison between dithering, steady-state L-mode and H*-mode on a $100 \mu\text{s}$ time scale is summarised in figure 68. The figure shows six contour plots, where the density fluctuation band autopower is correlated with H_α -light and the RMS Mirnov signal. The top row shows correlations for the dithering time interval, center row for steady-state L-mode and bottom row for H*-mode.

The top row plots can be compared to the plots showing data from shot 47133 (figures 58 and 59). The maximum H_α correlation is at zero time lag and largest for the smallest frequency, 150 kHz (about 80 %). For low frequencies, a measurable correlation exists beyond 1 ms, which is longer time than for shot 47133. This difference could be due to the fact that the dithering phase investigated for shot 47114 has a longer period (and longer H-mode phases) than 47133. At higher frequencies the long time correlation becomes reduced. The asymmetry for positive lags in the crosscorrelation due to the slow decay of the H_α -signal is found as it was for shot 47133. The crosscorrelation with the RMS Mirnov signal is similar to the H_α correlation, but is symmetric around a lag slightly shifted in the negative direction. This was also found in section 8.2, and means that the density fluctuations are delayed with respect to the magnetic fluctuations.

The center row shows crosscorrelations for the steady-state L-mode time window. In this case the correlation extends only up to a few hundred μs and up to 1.5 MHz. Again, the correlation with magnetic fluctuations shows that the density fluctuations are delayed. For both cases the maximum correlation is slightly above 60 % and has shifted to about 650 kHz.

Finally, the bottom row shows crosscorrelations for H*-mode. As is clear, no correlations exist, although density fluctuations remain at a significant level below 500 kHz. The correlation level is between $\pm 20 \%$, with no systematic behaviour.

Correlation between δn_e and $\partial_t B_\theta$ bursts As we did in section 8.2, we again turn to the fast crosscorrelation between density fluctuations and magnetic fluctuations.

The top row of figure 69 is an analysis of the crosscorrelation in the dithering phase, where the time windows have been separated using the H_α -signal. These plots are comparable to figure 60. The top row shows crosscorrelations between magnetic and density fluctuations for two frequencies, 150 kHz (left-hand plot) and 750 kHz (right-hand plot). The top subplots show L-mode results, bottom H-mode. The L-mode fluctuations are weakly correlated at low frequencies, but the H-mode fluctuations are not correlated. At higher frequencies, L-mode fluctuations

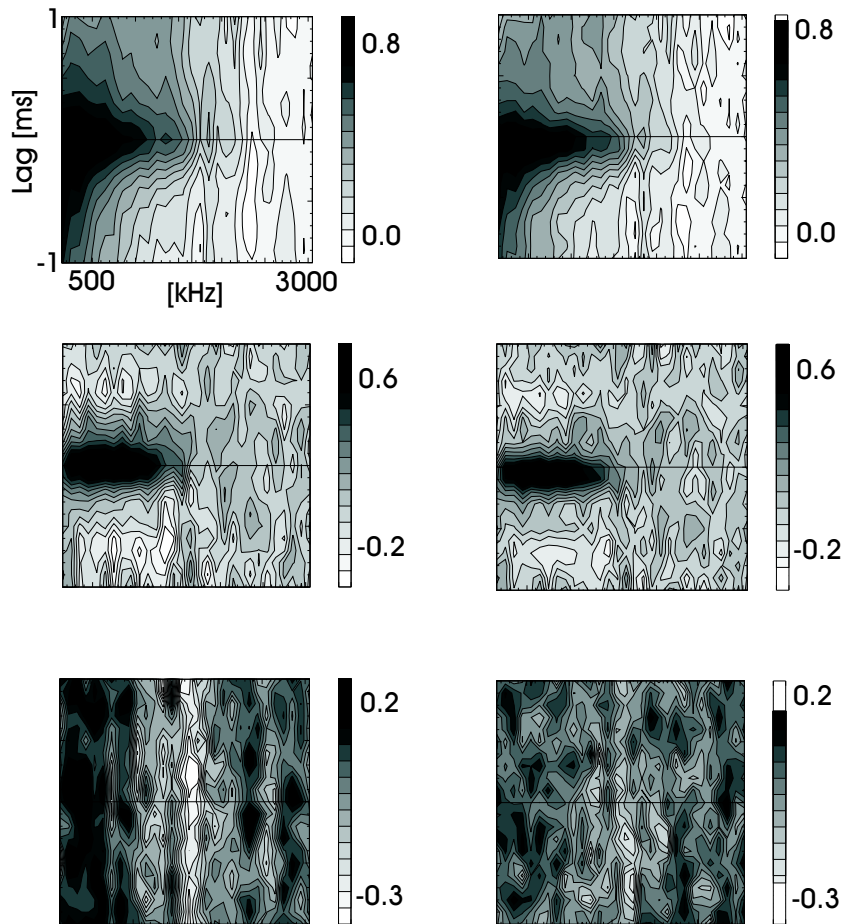


Figure 68. Left column: Crosscorrelation between H_α and density fluctuation band autopower from collective scattering versus band central frequency and time lag (units of $100 \mu\text{s}$). Right column: Crosscorrelation between RMS Mirnov signal and density fluctuation band autopower from collective scattering versus band central frequency and time lag (units of $100 \mu\text{s}$). Rows from top to bottom: Dithering, L-mode and H^* -mode. Note that the greyscale is different for each contour plot.

are clearly correlated. However, H-mode fluctuations remain uncorrelated. The L-mode high frequency toplag is slightly shifted towards negative lags, indicating that the magnetic fluctuations occur about $50 \mu\text{s}$ before the density fluctuations. This delay is somewhat longer than the delay observed for shot 47133; the FWHM of the correlation for shot 47114 is of the same order as that for shot 47133. The crosscorrelation in L-mode for high frequencies is seen to be just below 40 %.

The bottom row of figure 69 shows the analysis results for steady-state L-mode and H^* -mode, also at 150 and 750 kHz. There are no errorbars on these plots since the crosscorrelation is constructed from only one time interval. It is clear that the crosscorrelation found in the steady-state phases is almost identical to that found for the dithering plasma.

We have seen that the 2D slices of the crosscorrelation are close to identical for dithering L- and H-modes and steady-state modes. To verify this for all frequencies, we show contour plots of the crosscorrelation in figure 70. The top row shows the result for dithering states, left-hand L-mode and right-hand H-mode. These plots are comparable to figures 62 and 63, shot 47133. There are a few differences between this discharge and the present one, 47114: For 47114, the correlation exists also at quite low frequencies, and has a larger magnitude. Further,

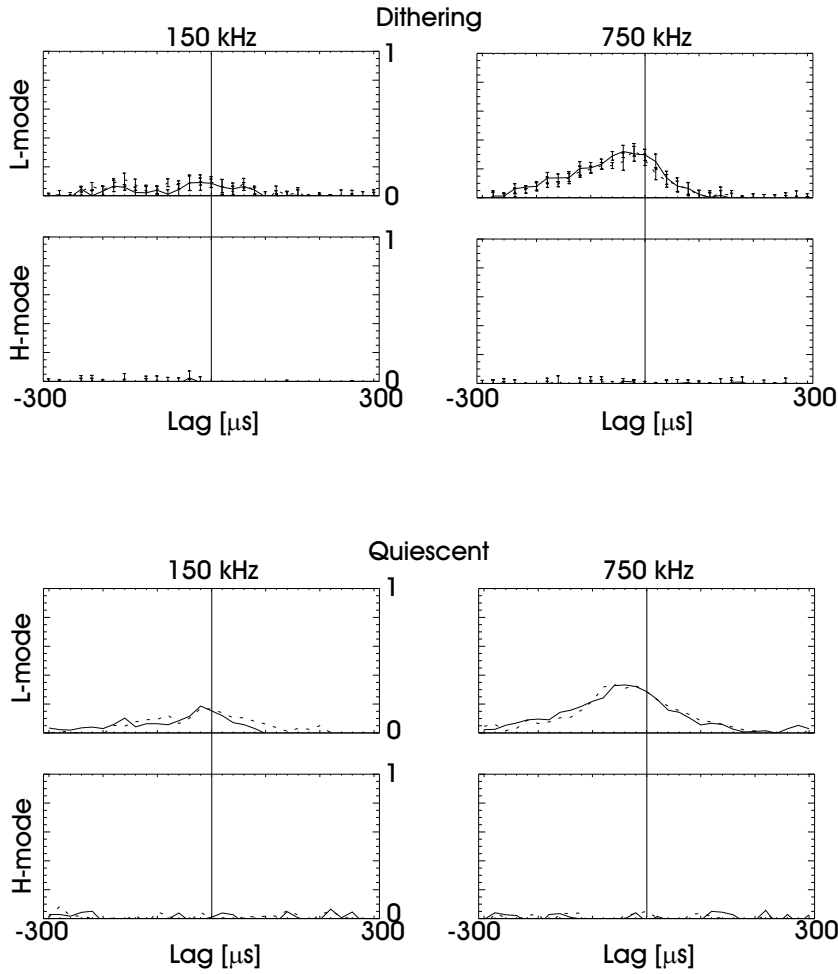


Figure 69. Crosscorrelation between magnetic and density fluctuations for L- and H-mode time windows versus time lag (units of $20 \mu\text{s}$). Top left: Crosscorrelation for 150 kHz dithering density fluctuations, top right: Crosscorrelation for 750 kHz dithering density fluctuations. Bottom left: Crosscorrelation for 150 kHz steady-state density fluctuations, bottom right: Crosscorrelation for 750 kHz steady-state density fluctuations. Solid line is volume 1, dotted line volume 2.

it is more clearly shifted towards negative lags, meaning that the density fluctuations occur after the magnetic fluctuations. The qualitative features are identical: A strong correlation during the dithering L-mode phase and no correlation during the dithering H-mode.

The steady-state analysis (bottom row of figure 70) is completely analogous to the results from separating the dithering phase into L- and H-mode. A strong steady-state L-mode correlation up to density fluctuation frequencies of 1.5 MHz and no detectable H*-mode correlation.

8.3.4 Phase separation

It would be interesting to inspect the raw density fluctuation signal itself to see if one can tell directly whether a given time interval is L- or H-mode. An ideal tool for this type of study is the derivative of the detected phase with respect to time, as has been mentioned in chapter 2.

Figure 71 shows the amplitude A (top) and phase derivative $\partial_t \Phi$ (bottom) versus

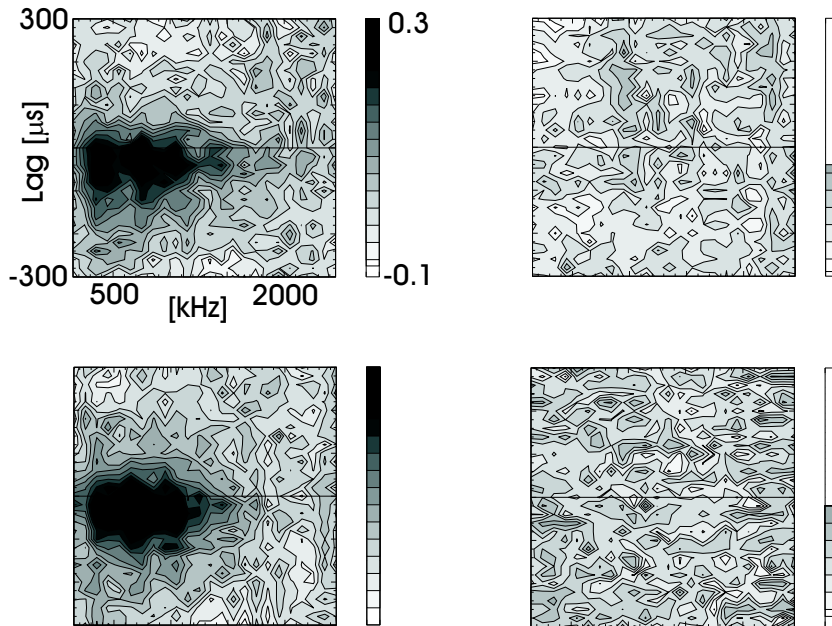


Figure 70. Crosscorrelation between Mirnov RMS signal and density fluctuation band autopower from collective scattering versus band central frequency and time lag (units of $20 \mu\text{s}$). Top left: Dithering L-mode, top right: Dithering H-mode. Bottom left: Steady-state L-mode, bottom right: H^* -mode. The greyscale on the right-hand sides of the plots shows what range of the total scale is relevant for the particular time window.

time for $100 \mu\text{s}$ of background (noise) data. The amplitude does not vary much on the scale shown (same scale as for figure 72), but the phase derivative varies enormously; this is understandable, since it is the derivative of a noisy signal.

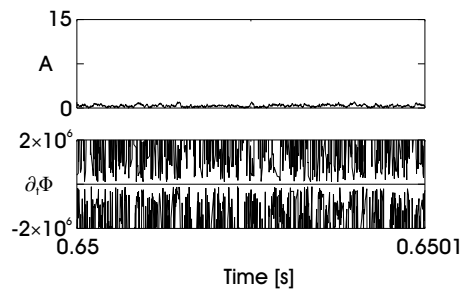


Figure 71. Representation of background data. Top: Signal amplitude versus time for $100 \mu\text{s}$, bottom: Time derivative of the phase for the same interval. The data has been band pass filtered between 1 kHz and 1 MHz .

In figure 72 we show two plots like the one shown for background data. The left-hand plots show $100 \mu\text{s}$ of dithering L-mode data, the right-hand plots show dithering H-mode data. The typical lifetime of an event is a few μs , compare to figure 2 in [3]. By visual inspection, the amplitudes are hard to tell apart; but the phase derivatives are distinct: The L-mode derivative seems to have a larger magnitude and to be more 'clean' than the 'grassy' H-mode derivative. The phase derivative has been shifted away from zero for clarity.

To elucidate the differences observed between the L- and H-mode phase derivatives, we show a plot of the phase derivative averaged over $100 \mu\text{s}$, $\langle \partial_t \Phi \rangle$, and a

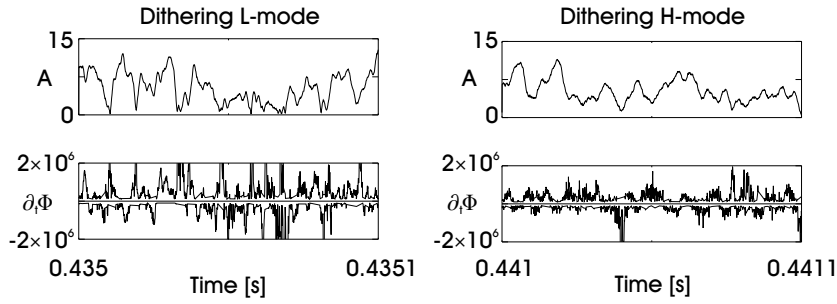


Figure 72. Representation of L-mode (left) and H-mode (right) data during dithering. Top: Signal amplitude versus time for 100 μ s, bottom: Derivative of the phase with respect to time for the same interval. The data has been band pass filtered between 1 kHz and 1 MHz.

plot of the average of the absolute value of the phase derivative, $\langle |\partial_t \Phi| \rangle$. The two different averages of the phase derivative are shown in the bottom row of figure 73, while the H_α -signal is shown for reference in the top row.

The averages tell us different things: The standard average includes the sign, i.e. direction, of the density fluctuations. If this average is different from zero, fluctuations travelling in one direction dominate over those in the opposite direction. The left-hand column of figure 73 shows that this is not the case. The average of the absolute value of the phase derivative contains information on the speed (size of velocity) of the fluctuations. The direction is here ignored; the right-hand column of figure 73 shows that this quantity is correlated with the H_α -light. The average is high in L-mode and low in H-mode, meaning that the speed of fluctuations is faster in L-mode than H-mode. Since $\langle |\partial_t \Phi| \rangle = kU$, where k is the measured wavenumber, a value of $7.5 \times 10^5 \text{ s}^{-1}$ at 14 cm^{-1} corresponds to a speed of 500 m/s. This is consistent with the results of section 8.2.

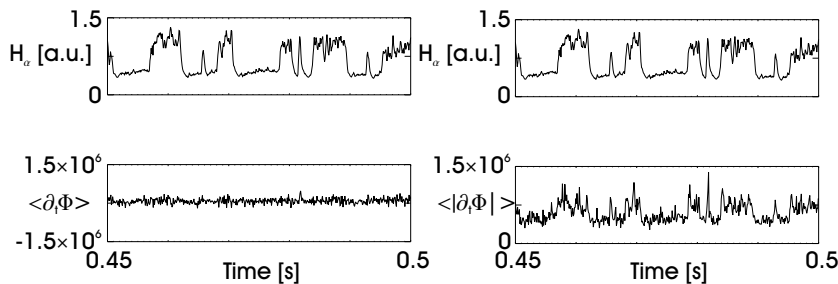


Figure 73. Left: H_α (top) and average of phase derivative (bottom) for 50 ms of a dithering plasma. Right: H_α (top) and average of the absolute value of the phase derivative (bottom) for the same time interval.

8.3.5 Conclusions

We have in this section treated a single discharge with the purpose of studying whether steady-state L-mode and H*-mode possess the same characteristics as those found by separating dithering phases into L- and H-mode time windows (see section 8.2).

Based on the analysis in the present section, it is clear that this indeed is the case. Apart from a couple of quantitative differences (e.g. the additional high

frequency feature in H*-mode), subsets of a dithering period and corresponding quiescent phases are qualitatively identical.

The remaining open question that we have not answered is whether L-mode dithers are collections of closely spaced ELMs or a distinguishable phenomenon. Unfortunately, we do not have sufficient measurements of discharges displaying single ELM activity to answer this question. If we were to speculate, our opinion would be that dithers are indeed collections of overlapping ELMs, where a single ELM has a lifetime of $\sim 100 \mu s$ - which is the correlation time we found, both in dithering and steady-state L-mode.

8.4 Slow confinement transitions

In sections 8.2 and 8.3 we have analysed how density fluctuations behave during fast confinement transitions, i.e. occurring on a μs time scale. In contrast, the present section deals with slow confinement transitions which are externally controllable. This allows us to study the interplay between turbulence and confinement in detail. Another advantage of this discharge type is that it is highly reproducible, giving us the opportunity to make scans, both in the wavenumber and the position of the fluctuations.

It is a well known fact that confinement in W7-AS is very sensitive to the boundary value t_a of the rotational transform. Optimum confinement is found in narrow t_a -windows close to (but not at) low-order rationals $t_a = 1/2, 1/3$ etc. [85] [21] [24]. The special significance of these windows is that they are free from the otherwise densely spaced higher-order rational t -values [161]. Therefore it has been assumed that perturbations arising at higher-order rational surfaces enhance the electron transport. These perturbations could be either static (due to the magnetic field) or dynamic (due to turbulence or MHD activity) [22] [26]. The investigation that follows is a study of the changes in density fluctuations associated with the varying confinement quality at different t_a .

The section is organised as follows: In subsection 8.4.1 we describe the discharge types analysed. Autopower and wavenumber spectra are treated in subsection 8.4.2 and the spatial distribution of turbulence is the topic of subsection 8.4.3. Localised measurements of slow confinement transitions are dealt with in subsection 8.4.4 and we discuss the found results in subsection 8.4.5.

8.4.1 Discharge description

The discharges in this section were all heated on-axis by 450 kW of ECRH power (1 gyrotron). The central density was $8 \times 10^{19} \text{ m}^{-3}$ and was kept constant by gas puffing. The toroidal magnetic field was 2.5 T and the vertical magnetic field (B_z) was 22 mT. In the early phase of the shots, the total plasma current (I_p) was set to zero.

Rotational transform effects Figure 74 illustrates the confinement degradation with increasing t_a above $t_a = 1/3$. The transition is shown for 3 different vertical magnetic fields and it is seen that an increase of this field shifts the 'iota-edge' towards larger t_a -values. This is at least in part due to the positive shear introduced by B_z at the plasma boundary [23]. We have analysed discharges where $B_z = 22$ mT, corresponding to the green squares in figure 74. The two vertical lines marked 'good' and 'bad' confinement correspond to initial t_a -settings in the plasmas considered. Due to the relatively low central plasma pressure ($\beta_0 = 0.5$ %), the contribution from the PS current to the t -profile can be neglected, see chapter 6.

We saw in chapter 6 that t_a can be dynamically varied by changing the Ohmic current. By doing this during a discharge, the confinement edge shown for fixed t_a in figure 74 can be scanned during a single discharge. That this is indeed possible can be seen in figure 75, where we show three of the experimental setups used. For each type, we show two quantities: The total plasma current and the stored energy (W_{dia}). The plasmas in the top left-hand plots are initially in the bad confinement state, $t_a = 0.362$. From 400 to 500 ms, the current is ramped up from 0 to 2 kA, leading to an increase of t_a to about 0.376 (see chapter 6). This does not alter the confinement, because the plasmas are already past the iota-edge at $t_a = 0.35$. From 500 to 600 ms, the plasma current is ramped down to 0 kA again. The plasmas on the top right-hand side are initially in the good confinement state,

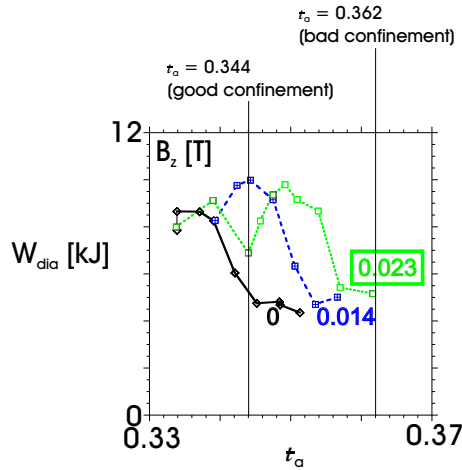


Figure 74. (Colour) Stored plasma energy versus edge rotational transform. Diamonds connected by solid black lines ($B_z = 0$ T), crossed squares connected by dashed blue lines ($B_z = 14$ mT) and squares connected by dotted green lines ($B_z = 23$ mT). The degradation of confinement with increasing rotational transform is clearly observed. The figure is adapted from [23].

$t_a = 0.344$. In this case, the current ramp has a large effect on the confinement: The 2 kA current increases t_a to about 0.358, leading to a pronounced drop of the stored energy. As the current is ramped down again, the plasma recovers, but has not fully recovered at 600 ms. The confinement lags somewhat behind the plasma current due to the finite current penetration time. Finally, the bottom plots show a transition like the one in the top right-hand plots, but with a current ramp-up lasting 700 ms instead of 100 ms. In this fashion we can prolong the transition from good to bad confinement. The slow current ramp minimises the lag of the confinement with respect to the plasma current.

Empirical model of electron energy transport Apart from the effect of t_a on confinement, an additional effect exists, namely that confinement improves with increased magnetic shear, ι' . These observations have been used as ingredients in an empirical model of the electron energy transport. This model was first presented in [23] [24]; particle transport is not considered, only energy transport [24]. Further, the electron-ion coupling is assumed to be small, meaning that the model would be valid for rather small densities. A refined version of the model can be found in [26]; here, we briefly recapitulate the main features of this model.

The model defines the electron heat conductivity χ_e using three terms:

$$\chi_e(r, t, t') = \chi_{\text{neo}}(r) + \chi_0(r) + \Sigma\chi_{nm}(t, t') \quad (237)$$

Here, χ_{neo} is the neoclassical heat conductivity, modelled as

$$\chi_{\text{neo}}(r) = \exp(\Sigma b_i(\rho)^i) \text{ m}^2/\text{s}, \quad (238)$$

where the b_i 's are constants. The heat conductivity due to anomalous transport (i.e. turbulence), χ_0 , is assumed to be

$$\chi_0(r) = c_1(n_e(r)/10^{20} \text{ m}^{-3})^{c_2}(P/\text{MW})^{c_3}, \quad (239)$$

where the c 's are constants [124]. This term is what is of interest from our point of view, since it is to account for the effect on the electron heat transport due to

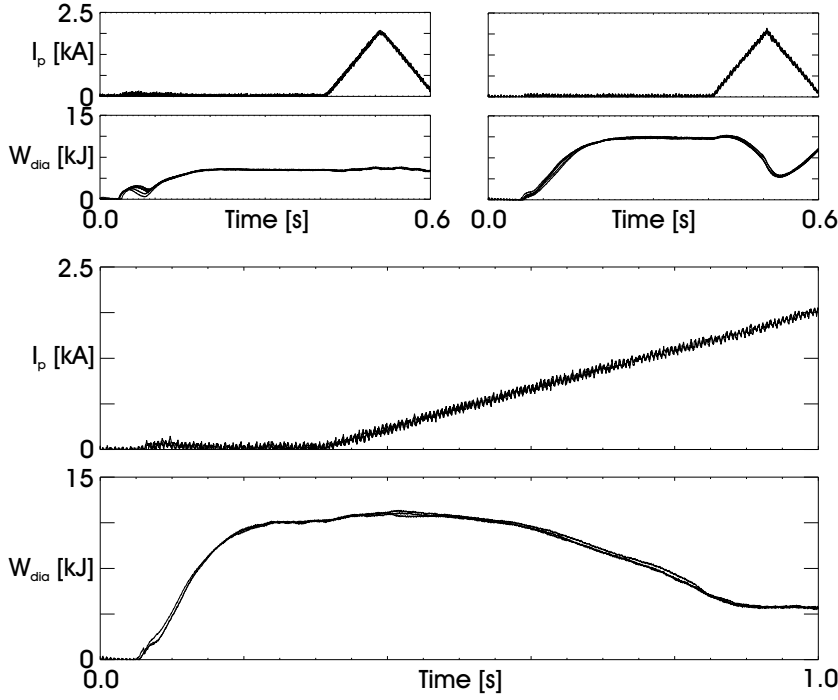


Figure 75. Total plasma current (I_p) and stored energy (W_{dia}) versus time for three cases. Top left: Initial edge rotational transform of 0.362 (bad confinement), top right: Initial edge rotational transform of 0.344 (good confinement) and bottom: Initial edge rotational transform of 0.344 (good confinement). In the top plots, six discharges are overlaid, in the bottom plot three discharges.

turbulence. The ansatz for the contribution to the conductivity close to a rational surface, χ_{nm} , is

$$\chi_{nm}(t, t') = \alpha_{nm} \exp(-|t - n/m|/\delta - \gamma|t'|) \quad (240)$$

The parameters $\alpha_{nm} = \alpha$, δ and γ are positive constants. The term including δ ensures that the conductivity decreases exponentially with $t - n/m$. The term including γ has the same effect with increasing shear. The maximum m -number, m_{max} , is set to 20.

To arrive at a more detailed understanding of how a ramp in the plasma current affects the ι -profile, we present an analysis of a slow current ramp discharge in figure 76 [25]. This discharge corresponds to those shown in the bottom part of figure 75. As the figure is rather complex, we describe it in some detail. The plot in the bottom right-hand side shows the plasma current (solid black line) versus time with coloured dots on top. These dots denote analysis time points for the calculation of the quantities shown in the other plots. The linestyles proceed in time as follows: Black (solid), red (solid), green (solid), dark blue (solid), light blue (solid), pink (solid), yellow (solid), black (dotted), red (dotted) and green (dotted). The plots show, from left to right, top to bottom: Electron temperature, bootstrap current density, total current density, electron density (assumed fixed), Ohmic current density, loop voltage, ι -profile, change in the ι -profile due to the Ohmic current and the total bootstrap and Ohmic current. Note that the loop voltage and total current plots are versus time, whereas the other plots are versus minor radius. Low-order rationals have been plotted on top of the ι -profile (solid lines, order up to 15, dotted lines, order up to 30) to indicate where these are dense or sparse.

We comment on each of the plots in turn, from left to right, top to bottom:

1. The top left plot shows the evolution of the electron temperature. It is clear that the confinement degradation is due to a collapse of the electron temperature, since the density is fixed at a constant value. The electron temperature profile first decreases in the core, and in the final phase drops at the edge as well. This could be interpreted as the initial breakdown of an internal transport barrier (steep gradient) positioned at $r = 4$ cm and a later additional destruction of the edge transport barrier at $r = 12$ cm.
2. The top center plot shows the development of the bootstrap current density; this current is basically proportional to the pressure gradient, meaning that it has two maxima (due to the shape of the electron temperature profile).
3. The top right plot shows the evolution of the total current density profile. It is made up by adding the bootstrap and Ohmic current density profiles. The current density increases with time, especially in the core region.
4. The middle left plot shows the density profile, which is kept unmodified for all time points.
5. The middle center plot shows the Ohmic current density due to the external transformer. In the early phase, it is negative to compensate for the positive bootstrap current. Later, it decreases in magnitude allowing the total current to rise to 2 kA.
6. The middle right plot shows the loop voltage from the calculations (black) compared to the measured one (dark blue).
7. The bottom left plot shows the ι -profile, the central result in this figure. The early profiles have two sections with large shear (the inner core A and inner edge C) and two sections with almost no shear (the outer core B and outer edge D). In response to the current ramp, the ι -profile increases, particularly in the inner core, but also in the outer core. As a consequence the shear decreases, and the profile moves towards rationals above $\iota = 1/3$. At about 750 ms into the discharge (pink profiles) the shear has almost completely disappeared and the profile is situated in the upper rationals.
8. The bottom center plot shows the change in the ι -profile due to the Ohmic current, i.e. the effect caused by the current ramp.
9. The bottom right plot shows the total current versus time (black) along with the contributions from bootstrap (red) and Ohmic (pink) current.

A cautionary statement: The analysis leading to the ι -profiles in figure 76 is not an exact one. This implies that the development of the profiles shows the correct trend, but the absolute values could be somewhat displaced with respect to the 'true' ones.

Auxiliary measurements After our exhaustive treatment of the rotational transform behaviour in response to the current ramp, it is time to take a look at what the different diagnostics can tell us.

Figure 77 shows electron cyclotron emission (ECE) temperature profiles and time traces for the slow good to bad confinement transition. The initial profiles (left-hand plot) are peaked due to the on-axis ECR heating. As the discharge progresses, the temperature decreases rapidly, fast in the core and slowly further outside. In the inboard time traces (right-hand plot, the shaded portion of the left-hand plot) it is clear that plateaus are formed at different times during the shot. The two central temperatures merge at 650 ms and are joined by the third

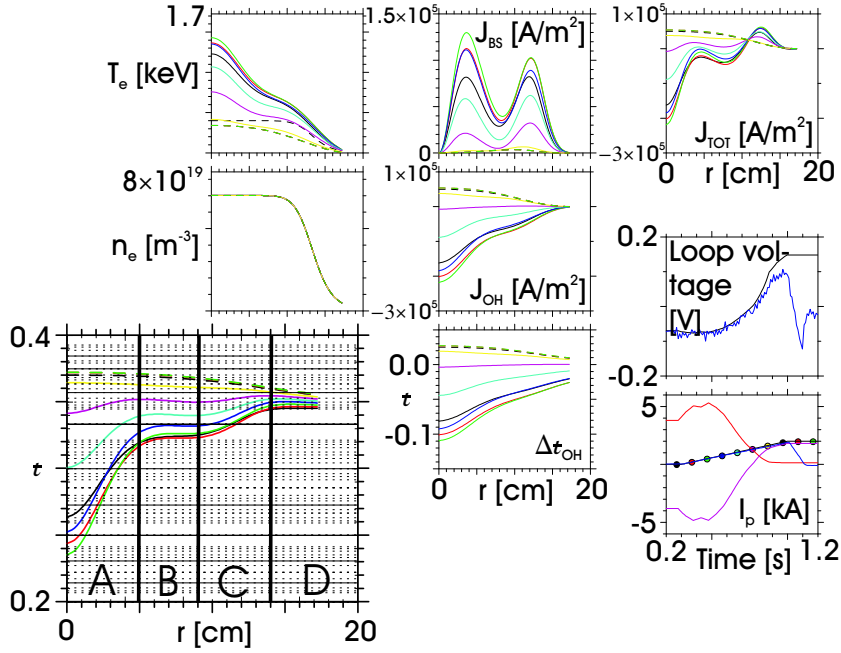


Figure 76. (Colour) Analysis of a slow current ramp discharge initially in the good confinement state. From left to right, top to bottom: Electron temperature, bootstrap current density, total current density, electron density (assumed fixed), Ohmic current density, loop voltage, edge rotational transform profile, change in the profile due to the Ohmic current and the total bootstrap and Ohmic current. The rotational transform profile has been expanded and low-order rationals have been superimposed onto the plot: Solid lines are rationals up to order 15, dotted lines are rationals up to order 30. The profile has been split up into four radial zones: Inner core (A), outer core (B), inner edge (C) and outer edge (D). The linestyles with increasing time are the following: Black (solid), red (solid), green (solid), dark blue (solid), light blue (solid), pink (solid), yellow (solid), black (dotted), red (dotted) and green (dotted).

trace at 700 ms. Two additional radial positions link up before 850 ms, so that the inner plateau consists of five traces. The innermost temperature drops more than a factor 4, whereas all the temperatures outside $r = 3$ cm drop approximately a factor 2.5. At 900 ms, the profile has reached the bad confinement state and does not evolve further, despite of the continuing increase of plasma current.

The edge radial electric field E_r was measured for some of the current ramp discharges using the Boron IV diagnostic (see section 8.1 for a description). In figure 78 we show E_r for two shot types, corresponding to the upper plots in figure 75. The traces in the left-hand plot show measurements from a discharge initially in the bad confinement state. The electric field is seen to be -1×10^4 V/m inside the LCFS and rising towards the edge. It is approximately zero for the outer trace. The current ramp from 400 to 600 ms does not lead to a development in E_r . In contrast to this, E_r in the discharge initially in the good confinement state (right-hand plot) is quite different. The two inner traces are almost identical and much larger in magnitude than the ones in the bad confinement discharge, namely -2×10^4 V/m. Further, the distance between these two traces and the two outer traces is larger, the outermost trace being slightly positive. This means that the shear in E_r is large compared to the bad confinement shot. In response to the initial confinement improvement due to the current ramp, the E_r -traces all

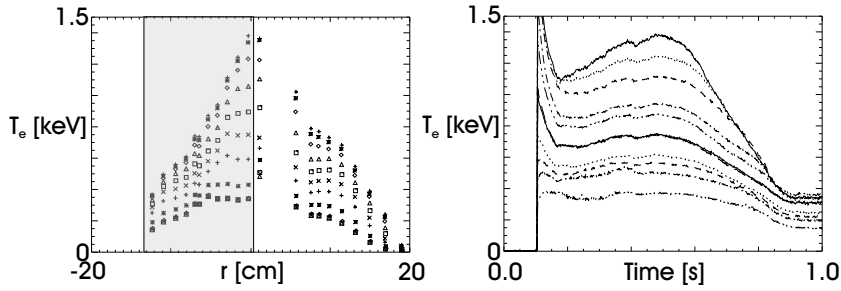


Figure 77. ECE measurements during the slow transition from good to bad confinement. Left: ECE profiles 50 ms apart, from 500 to 1000 ms. The symbols with increasing time are: Plusses, asterisks, diamonds, triangles, squares and crosses (cyclic permutation of symbols). Right: ECE traces from the high field side (shaded negative r section in the left-hand plot) versus time up to 1.0 s. Linestyle with increasing r : Solid, dotted, dashed, dash dot, dash dot dot dot, long dashed (cyclic permutation of linestyles).

move towards negative values. As the current increases further, the E_r -traces all move towards positive values and the radial electric field shear becomes smaller, particularly between the two inner traces and the third trace. This reduction in the size of E_r also means that the $\mathbf{E} \times \mathbf{B}$ velocity decreases, i.e. that the plasma spins down during the transition from good to bad confinement.

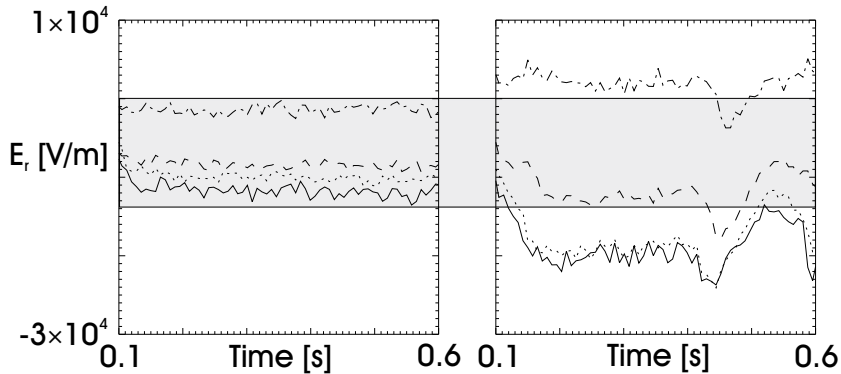


Figure 78. Measurements of the edge radial electric field E_r at four spatial positions for the fast current ramp experiments. Linestyle with increasing r : Solid, dotted, dashed, dash dot. Left: E_r from 100 to 600 ms in a bad confinement discharge, right: E_r in a good confinement discharge. The shading shows the E_r -range covered in the bad confinement discharge.

Figure 79 shows Mirnov coil measurements of magnetic fluctuations for a discharge experiencing a slow transition from good to bad confinement. The lines on the spectrogram are due to activity caused by low- m modes; typically, $m = 2-4$. It is interesting to compare this activity to the electron temperature time traces shown in figure 77. The frequencies present during good confinement (20, 40, 60 and 110 kHz) decrease, consistent with the results from the E_r -measurements. The two lowest frequencies in the spectrogram merge at 850 ms, seemingly linked to the final collapse of the central electron temperature. We also note that a similar process occurs for the 40 and 60 kHz modes at 600 ms.

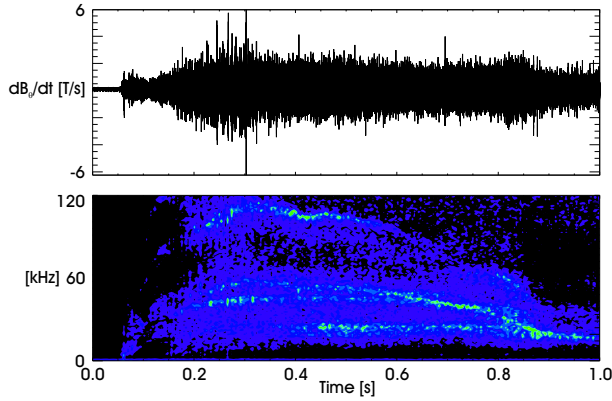


Figure 79. (Colour) Magnetic field derivative in T/s from the 'MIRTIM' monitor coil (top) and a spectrogram (bottom) covering 1.0 s.

8.4.2 Comparison between the density fluctuation autopower in good and bad confinement

Changes in the autopower spectrum A wavenumber scan was performed in the two discharge types shown at the top of figure 75, with wavenumbers ranging between 25 and 61 cm^{-1} .

To study whether the density fluctuations behave disparately at different wavenumbers, we show two sets of autopower spectra for discharges initially experiencing good confinement in figure 80. The top row shows autopower spectra at $k = 25 \text{ cm}^{-1}$ (left) and at 46 cm^{-1} (right). The good confinement ($I_p = 0 \text{ kA}$) phase spectra are shown using dotted lines, and the bad confinement ($I_p = 2 \text{ kA}$) spectra are solid lines. For the $k = 25 \text{ cm}^{-1}$ shot, the decrease of low frequency ($[-500, 500] \text{ kHz}$) fluctuations during the good to bad confinement transition is partly counteracted by an increase of turbulence at higher frequencies. This is clear to see in the bottom left-hand plot of figure 80, where the ratio bad/good confinement autopower spectra is plotted. A value above 1 means an increase in power, a value below 1 a decrease. In contrast, the high frequency increase at the transition no longer exists for $k = 46 \text{ cm}^{-1}$; only the drop of low frequency autopower remains. Note that in the initial good confinement phase of the high- k shot the autopower seems to contain two features: A broad high frequency low amplitude component and a larger amplitude low frequency element.

The spectra treated above can be compared to corresponding spectra from discharges initially in bad confinement, see figure 81. The development of the autopower spectra is quite modest, the main result being a slight decrease in power up to $\pm 1 \text{ MHz}$. Note that the spectra are similar to those in figure 80 for $I_p = 2 \text{ kA}$.

In figure 82 we show autopower spectra and their ratio for $k = 15 \text{ cm}^{-1}$. Here, the density fluctuation power increases strongly below $\pm 1 \text{ MHz}$; further, the high frequency feature present during good confinement decreases in frequency on top of the current ramp. Note that the frequency scale in figure 82 extends to $\pm 4 \text{ MHz}$ compared to $\pm 2 \text{ MHz}$ for figures 80 and 81.

To summarise our findings: Two phenomena are present, a low frequency ($< \pm 1 \text{ MHz}$) and a high frequency feature:

- The high frequency feature is symmetric in frequency and does not change at the confinement transition for $k = [25, 61] \text{ cm}^{-1}$. At $k = 15 \text{ cm}^{-1}$, however, the feature is highly asymmetric and decreases in frequency during the transition.
- The low frequency feature changes at all k , but only increases at the transition

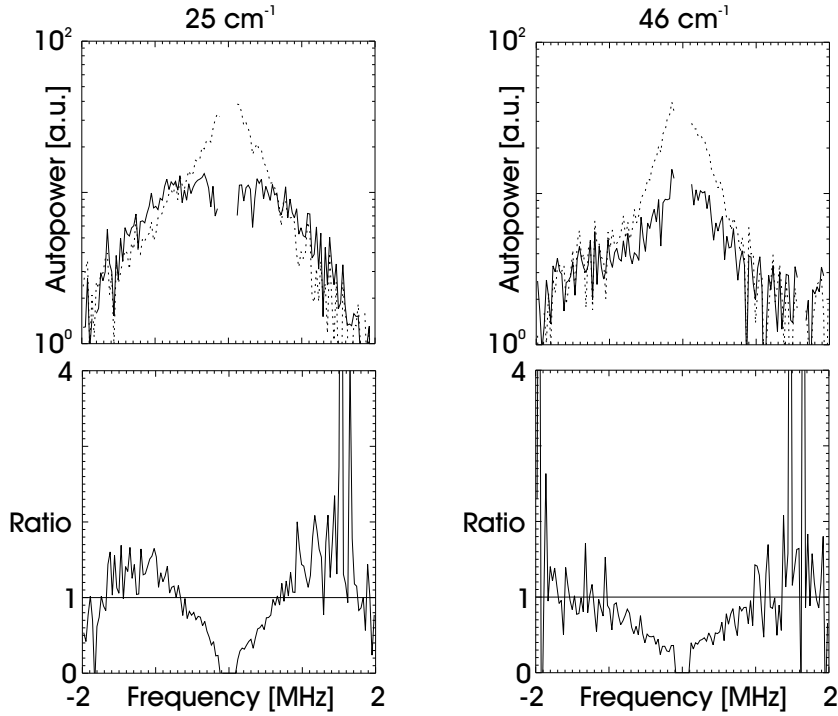


Figure 80. Top: Autopower spectra at $I_p = 0$ kA (dotted line) and on top of the current ramp ($I_p = 2$ kA, solid line) in good confinement discharges, bottom: The relative change in power. Left column: $k = 25$ cm^{-1} , right column: $k = 46$ cm^{-1} .

for 15 cm^{-1} . For higher wavenumbers, it drops and finally disappears at $k = 46$ cm^{-1} .

Changes in the wavenumber spectrum The observations made above can be condensed into wavenumber spectra, where fluctuations integrated over all frequencies are shown versus wavenumber. Four cases are plotted, two for discharges initially in good confinement and two for discharges in bad confinement. In each case, the wavenumber spectrum is calculated before and during the current ramp. The resulting spectra are fitted to power-laws ($P \propto k^{-m}$) as was done in sections 8.1 and 8.2. The wavenumber spectrum for the shots starting in good confinement becomes steeper with the confinement deterioration; the power drops especially for high wavenumbers. The spectrum for the shots initially in bad confinement only changes in amplitude (it decreases) at the transition.

The fitted power-law exponents m can also be studied versus time into the discharges, see figure 84. Here, the exponents for wavenumber spectra calculated in 10 ms time windows are shown versus time for both the good and bad confinement series. We observe that the exponent changes in a different manner for the two discharge types: For the bad confinement shots, the current ramp causes a gradual increase of the exponent. The behaviour in the good confinement case is more complex: The initial response to the current ramp is a decrease of the exponent, reflecting the initial further confinement enhancement. Later, as the confinement degrades, the exponent increases and transiently exceeds that of the bad confinement discharges slightly. Our conclusion would be that the size of the exponent corresponds to the confinement quality: A smaller exponent is associated with improved confinement.

The trend of the slope of the fits in figure 83 suggests that the fluctuation

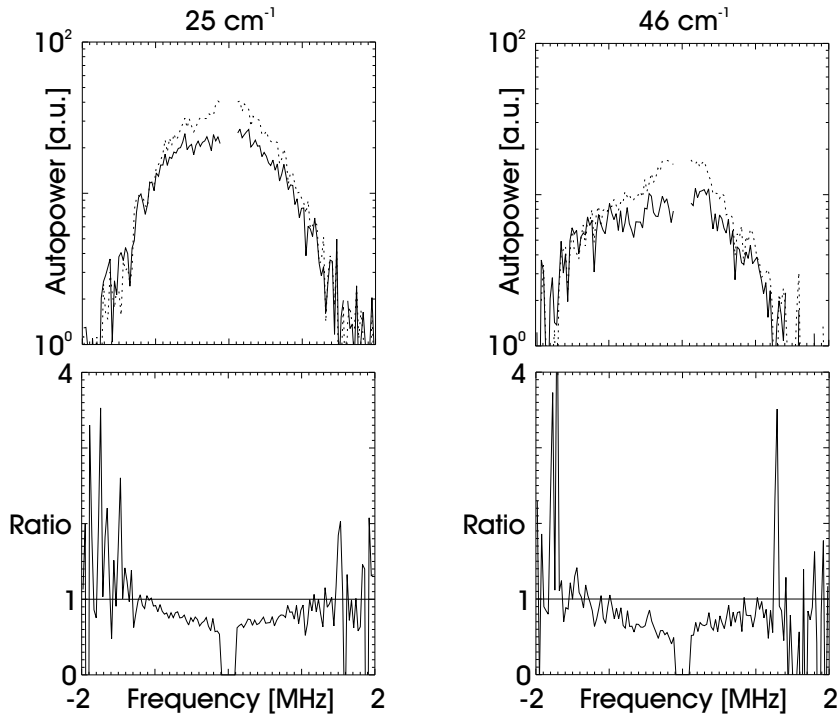


Figure 81. Top: Autopower spectra at $I_p = 0$ kA (dotted line) and on top of the current ramp ($I_p = 2$ kA, solid line) in bad confinement discharges, bottom: The relative change in power. Left column: $k = 25$ cm^{-1} , right column: $k = 46$ cm^{-1} .

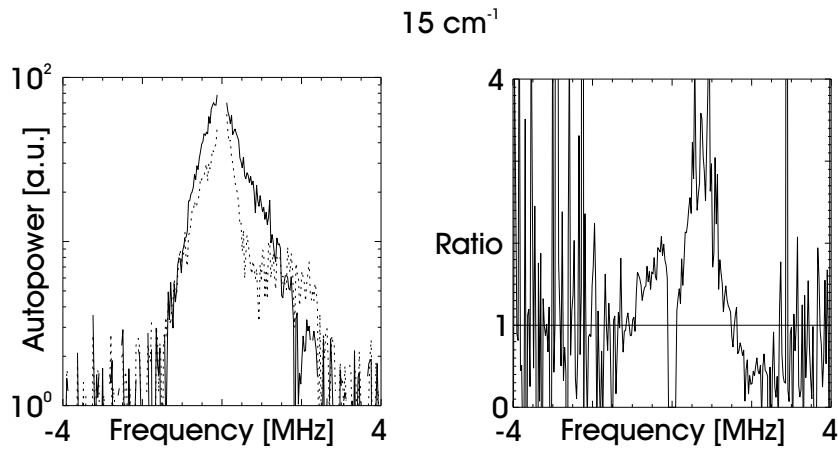


Figure 82. Left: Autopower spectra at $I_p = 0$ kA (dotted line) and on top of the current ramp ($I_p = 2$ kA, solid line) at $k = 15$ cm^{-1} in a good confinement discharge, right: The relative change in power.

power for $k < 25$ cm^{-1} could increase in bad confinement. That this is indeed the case is shown in figure 85, where the total fluctuation power in good confinement discharges measured at different wavenumbers is plotted. For $k = 32$ cm^{-1} , the total power drops as the confinement worsens, whereas for $k = 15$ cm^{-1} the total power increases significantly.

We have demonstrated that the wavenumber spectrum during the current ramp induced confinement degradation is very similar to the static bad confinement case.

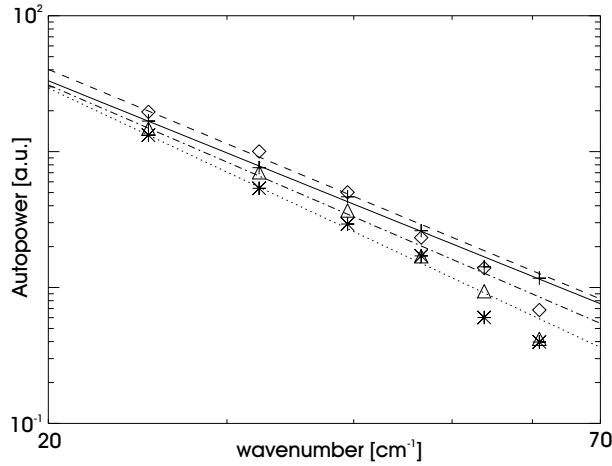


Figure 83. Wavenumber spectra in initially good and bad confinement discharges. Pluses fitted by a solid line (asterisks fitted by a dotted line): Good confinement discharge, $I_p = 0$ kA ($I_p = 2$ kA). Diamonds fitted by a dashed line (triangles fitted by a dot dashed line): Bad confinement discharge, $I_p = 0$ kA ($I_p = 2$ kA).

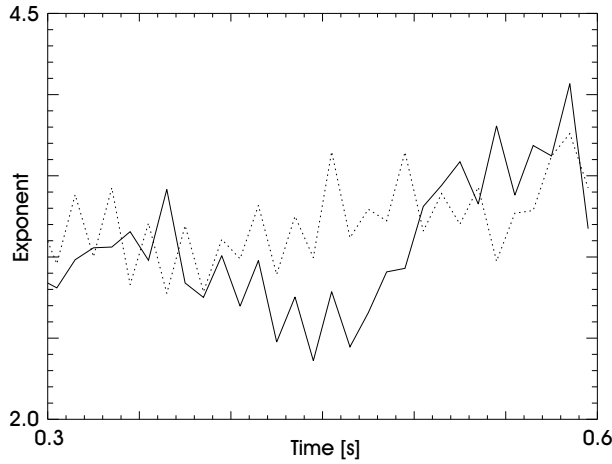


Figure 84. Power-law exponents versus time for bad (dotted) and good (solid) confinement discharges.

The results for $k = 15 \text{ cm}^{-1}$ (see figure 86) show the same tendency: The current induced bad confinement is very similar to the discharge at the bad confinement t_a -value. The power in the slow current ramp discharge initially in good confinement coincides with that of the bad confinement discharge at the time where the current ramp-up is completed.

8.4.3 Comparison between the radial profile of fluctuations in good and bad confinement

Up to this point we have exclusively presented measurements of density fluctuations line integrated along the measurement volumes. However, as we have described in chapter 3, some localisation is possible with one of two different techniques. In the following we describe results of both methods and thereafter compare the outcome. The density fluctuation profile is in both instances analysed for $k = 15 \text{ cm}^{-1}$, where the fluctuation amplitude increases for degraded

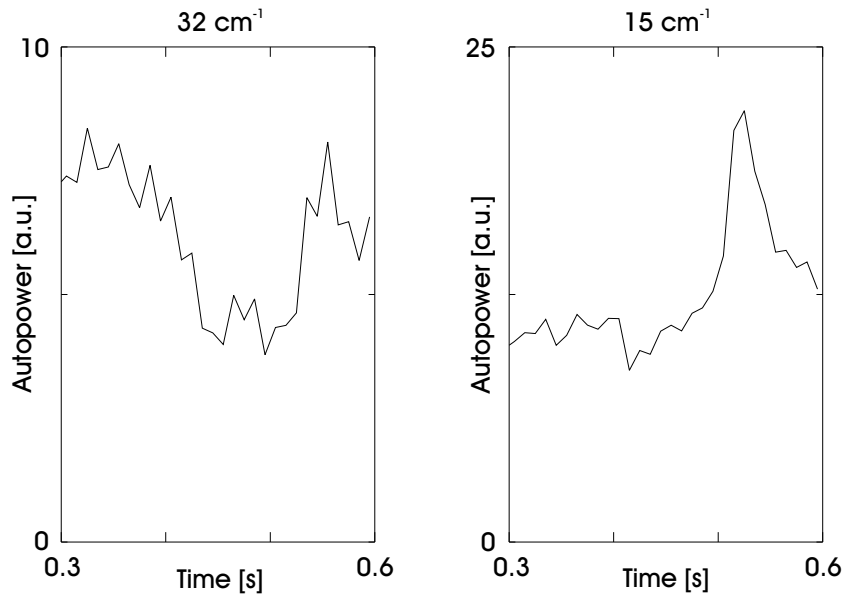


Figure 85. Total fluctuation power versus time in good confinement discharges. Left: $k = 32 \text{ cm}^{-1}$, right: $k = 15 \text{ cm}^{-1}$.

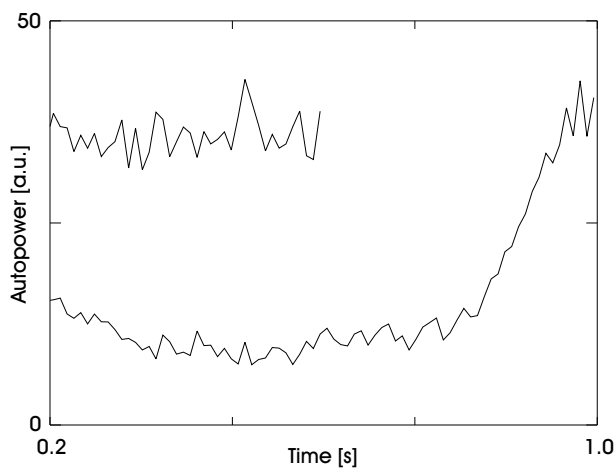


Figure 86. Total fluctuation power versus time. Top trace: A bad confinement discharge without a current ramp, bottom trace: A slow current ramp discharge initially in good confinement. Both traces are for $k = 15 \text{ cm}^{-1}$.

confinement. The measurement volumes were positioned as indicated in figure 35; therefore the total pitch angle variation $\Delta\theta_{p,\text{tot}}$ (see chapter 3) was about 16° .

Dual volume localisation The dual volume setup was as follows: The volume separation d was 29 mm and the beam waist $w = 4$ mm. Assuming a perpendicular correlation length $\mathcal{L}_\perp = 1$ cm, this means that $\frac{w+\mathcal{L}_\perp/2}{d} \times \frac{180}{\pi} = 18^\circ$. This situation signifies that the localisation criterion in equation 109 is not fulfilled. However, as we mentioned at the end of chapter 3, some localisation can still be realised by setting θ_R to values corresponding to the extreme top or bottom of the plasma.

Figure 87 shows crosspower amplitude spectra originating at the bottom (left-hand plot) and top (right-hand plot) of the measurement volumes. In both cases, spectra are shown during good (dotted lines) and bad (solid lines) confinement in

static discharges. Our initial observation is that negative and positive frequencies form two separable spectra. The low frequency feature exists for negative frequencies at the bottom and positive frequencies at the top, meaning that it rotates in the ion DD direction. Conversely, a higher frequency feature travelling in the electron DD direction is present. The low frequency ion feature has a larger amplitude than the high frequency electron mode. A strong up-down asymmetry is found for the electron feature by comparing the top and bottom measurements: The frequencies at the bottom are considerably higher (roughly a factor of two) than at the top, an effect probably due to the difference in flux compression between the bottom and top of the plasma [177]. There are two major differences between the spectra from good to bad confinement:

1. The amplitude of the ion feature increases, but the frequency does not change.
2. The frequency of the electron feature decreases, and the amplitude increases.

Further measurements of the crosspower amplitude during confinement transitions induced by slow current ramps are presented in subsection 8.4.4 describing the details of the confinement transition.

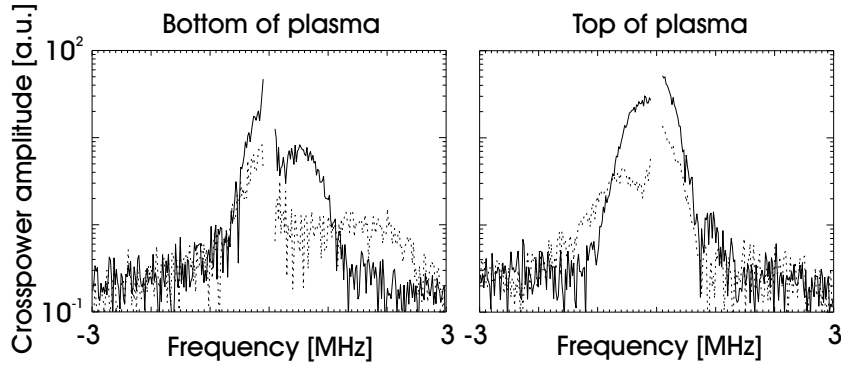


Figure 87. Crosspower amplitude spectra for $k = 15 \text{ cm}^{-1}$. Spectrum at good (dotted lines) and bad (solid lines) confinement in static discharges. Left: Signal due to fluctuations at the bottom of the plasma ($\theta_R = 10.5^\circ$), right: Signal due to fluctuations at the top of the plasma ($\theta_R = -9.5^\circ$).

Single volume localisation The single volume setup was as follows: The beam waist w was 33 mm, therefore the transverse relative wavenumber resolution $\Delta\alpha$ was $[2/(15 \times 3.3)] \times (180/\pi) = 2.3^\circ$. Since the total pitch angle variation is 16° , the single volume localisation criterion (equation 108) is applicable.

We made an α -scan (at $k = 15 \text{ cm}^{-1}$) of initially good confined plasmas with a fast current ramp at the end. Six shots were made, where α was set to 12° (bottom), 8° , 6° , 4° , 0° and -4° (top).

Figure 88 shows the autopower for the six angles at good (thin lines) and bad (thick lines) confinement. If we begin by commenting on the good confinement spectra, it is clear that for the outermost measurement volumes (upper left and lower right plots), two features are visible: The dominating one in amplitude is at low frequencies (a few hundred kHz) and slopes outward; the other feature at high frequencies has a broader shape and the frequency sign is opposite to that of the low frequency feature. We conclude that the high amplitude, low frequency fluctuations travel in the ion DD direction, while the low amplitude, high frequency feature travels in the electron DD direction. As one moves further into the plasma both features diminish and vanish almost completely in the core of the plasma.

The limited spatial resolution makes it impossible to determine whether the radial positions of the counter propagating features coincide or if they are separated.

Turning to the bad confinement spectra, we immediately observe that both the ion and electron feature increases in amplitude. Additionally, the electron feature decreases in frequency, i.e. it spins down. This is most clearly seen at the bottom of the plasma, compare to the dual volume localised measurements in figure 87.

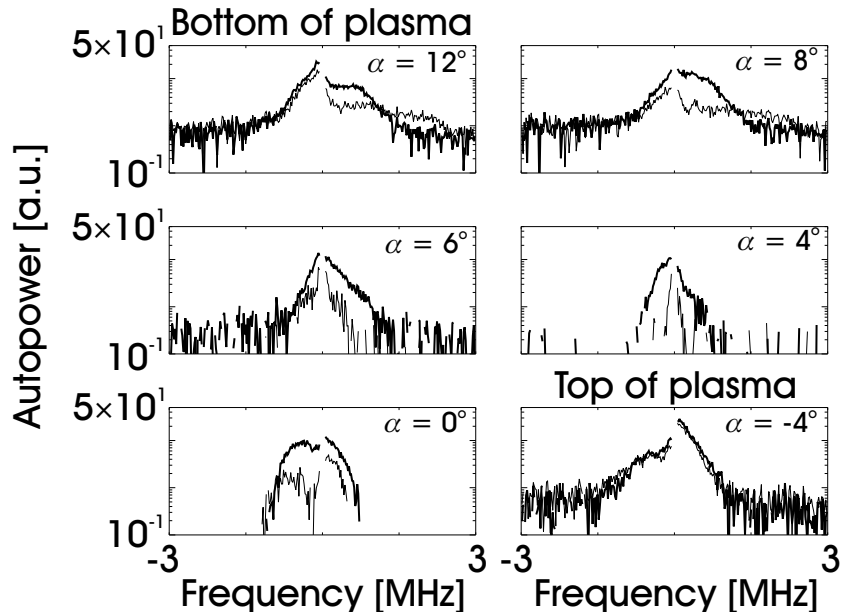


Figure 88. Autopower spectra for the α -scan in fast current ramp good confinement discharges. From top left to bottom right: $\alpha = 12^\circ$ (bottom), $\alpha = 8^\circ$, $\alpha = 6^\circ$, $\alpha = 4^\circ$, $\alpha = 0^\circ$ and $\alpha = -4^\circ$ (top). Thin lines are during good confinement, thick lines during bad confinement.

We have just discussed two snapshots of the fluctuations at good and bad confinement. In figure 89 we display the transition in a more dynamical fashion: We show contour plots of the low frequency density fluctuations versus spatial position and time. The traces above the contour plots show plasma current, particle fuelling and plasma energy. We again conclude that during the steady-state good confinement phase negative frequency fluctuations dominate at the bottom of the plasmas while positive frequencies dominate at the top, indicating movement in the ion DD direction. As the plasma enters the transient bad confinement phase, massive changes are observed in the profile: From being confined mostly to the edge plasma region, the fluctuations extend to the very core.

In figure 90 we show a contour plot like those shown in figure 89, but now displaying the autopower integrated over all frequencies. The same general behaviour is observed as for the low frequencies; note that the fluctuations at the bottom seem to reach deeper into the plasma than the top fluctuations. This is due to systematic errors in the calibration of the angle α , see the analysis below.

The final subject treated here is how the radial density fluctuation profile changes at the confinement transition. In chapter 3 we found that the measured autopower due to scattering in a single measurement volume is proportional to the integral along the measurement volume of the local spectral density multiplied by

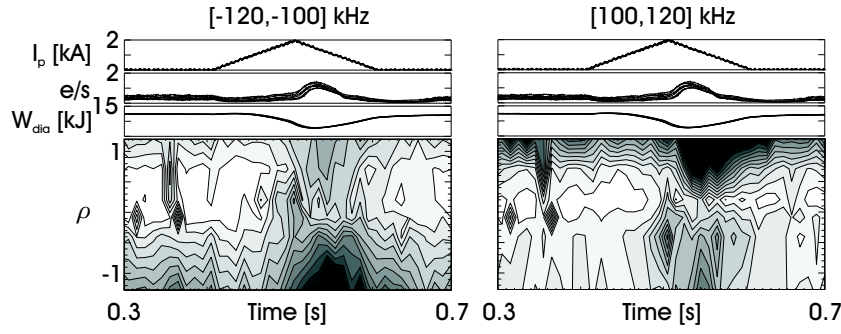


Figure 89. Traces of plasma quantities (net current I_p , gas fuelling in units of 10^{21} and stored energy) and contour plots of density fluctuations in the $[-120, -100]$ kHz (left) and $[100, 120]$ kHz (right) frequency bands. The contour plots are shown versus time and plasma position in normalised coordinates: $\rho = -1$ corresponds to the bottom position of the LCFS, 0 to the center and 1 to the top of the LCFS.

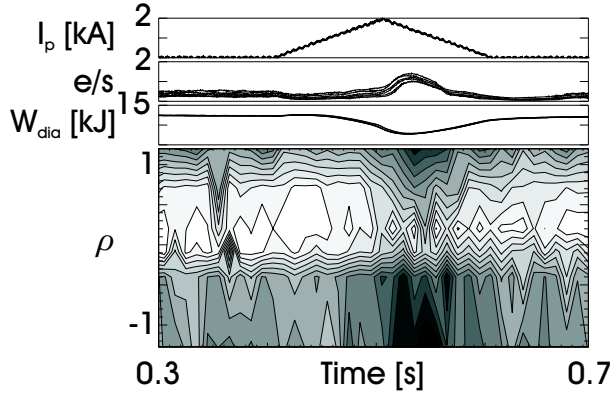


Figure 90. Traces (see figure 89) and contour plot of the density fluctuations integrated over all frequencies.

an instrumental selectivity function, see equation 103. Experimentally, both the autopower and the terms in the selectivity factor are known; the local spectral density is assumed to be a function of 3 free parameters (b , c and p), see equations 105 and 107:

$$f = \frac{\delta n(r)}{n(r)} = b + c |\rho|^p \quad (241)$$

Making an α -scan as described above, these 3 parameters can be determined by fitting to the measured autopower.

The measurement results are shown in figure 91. The curve connected by diamonds in the upper plot is frequency integrated scattered power during good confinement versus spatial position in normalised coordinates (-1 bottom LCFS, 0 center, 1 top LCFS of plasma). The triangle curve shows the profile during bad confinement. Finally, the asterisk curve in the lower plot shows the bad/good profile ratio. The measurements were averaged over 50 ms, the good confinement data from 300 to 350 ms and the bad confinement ones from 500 to 550 ms. We can make the following statements:

1. The turbulence level is generally low in the central plasma compared to the edge.

2. The turbulence level increases at all radial positions in going from good to bad confinement.
3. The increase of turbulence is largest in the central plasma.
4. The ratio between bad/good profiles is shifted somewhat with respect to $\rho = 0$. This indicates that our original α -calibration is somewhat off with respect to the 'real' calibration.

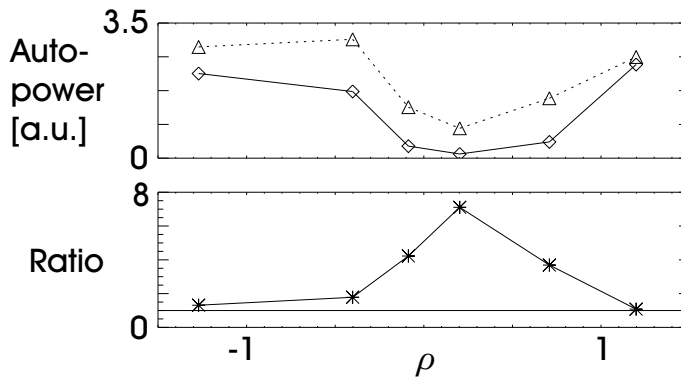


Figure 91. Measured turbulence profiles (top) and ratio between them (bottom). The symbols have the following meaning: Diamonds (connected by solid lines) are good confinement, triangles (connected by dotted lines) bad confinement and asterisks the bad/good ratio.

After modelling the $\delta n/n$ -profile, we need the density profile to calculate δn^2 , which is obtained from a fit to the profile measured by Ruby laser Thomson scattering. This fit is shown in figure 92 and is a density profile for the good confinement phase. Since the line density was kept constant with gas puffing, this profile is used for both the good and bad confinement profile fit.

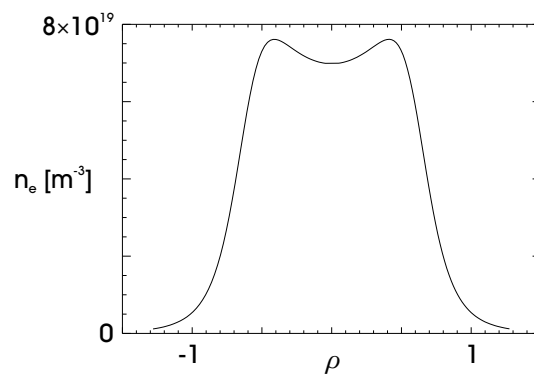


Figure 92. Density profile used in the fit procedure. The profile is a fit to Ruby laser Thomson scattering measurements.

The first step of the fit procedure was to re-calibrate α ; this was done by making α into a fourth fit parameter and performing the fit. In fitting to all six points for both the good and bad confinement data it was found that α increased for both cases, but not by the same amount. Excluding the spatial point 'pushed out' of the plasma in the direction indicated by the initial fits - and now only fitting to five points - the fitted α shifted by the same size in both cases, namely $1.65^\circ \pm$

0.03° (of 16° in total, a systematic error of 10 %). The resulting positional change can be observed by comparing figures 91 and 93. In the fits described below, α was set to the re-calibrated value.

Unfortunately, this means that the bottom point of the profile can no longer be used in the fit since it is outside the plasma. The very limited number of measurement points of course questions the validity of the following procedure, since we use 5 datapoints to arrive at 3 fit parameters. However, this was the only series of similar discharges where we have data using the setup presented, and performing a least squares fit is still the best way forward in the analysis of these discharges.

The result of the fits is shown in figure 93. The measured profile is displayed using the same symbols as in figure 91; squares are now the fit to good confinement and crosses the fit to bad confinement. No up-down asymmetries in the scattered power are present, but have been found previously in several devices, e.g. the Tore Supra tokamak [51] [56]. The errorbars on the measured data are set to 10 %, see chapter 7. The fitted parameters were: $(b, c, p)_{\text{good}} = (0.0067, 0.53, 8.0)$ and $(b, c, p)_{\text{bad}} = (0.019, 0.57, 6.2)$, where the subscripts refer to the confinement quality. Since we measure in arbitrary units, it is only the relative values $(c/b)_{\text{good}} = 79$ and $(c/b)_{\text{bad}} = 30$ that are important.

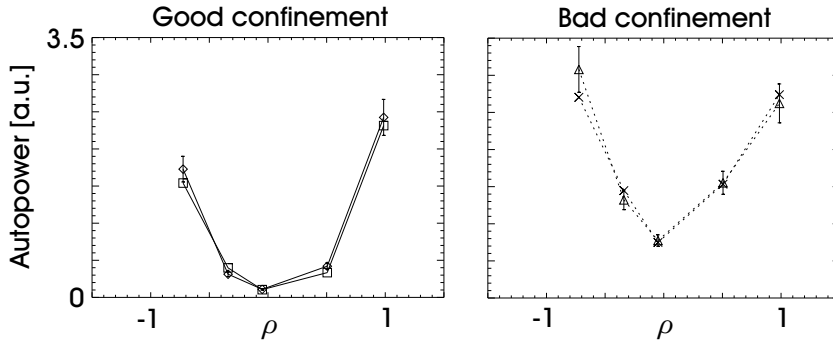


Figure 93. Measured and fitted profiles. Left: Good confinement (diamonds measurements, squares fit), right: Bad confinement (triangles measurements, crosses fit). The point beyond the bottom of the plasma is not included in the fits. The errorbars on the measured profiles are calculated assuming a 10 % error.

The relative $(\delta n/n)$ and absolute (δn^2) fluctuation profiles are shown in figure 94. Note that the relative profiles are shown on a logarithmic plot to elucidate the core behaviour. The errorbars on the relative profiles are found using the covariance matrix obtained when applying the Levenberg-Marquardt fit method [118]. The error Δf on the profile function f is given by

$$\begin{aligned}
 (\Delta f)^2 = & \left(\frac{\partial f}{\partial b}\right)^2 \sigma_{bb}^2 + 2 \left(\frac{\partial f}{\partial b}\right) \left(\frac{\partial f}{\partial c}\right) \sigma_{bc}^2 + \left(\frac{\partial f}{\partial c}\right)^2 \sigma_{cc}^2 + \\
 & 2 \left(\frac{\partial f}{\partial b}\right) \left(\frac{\partial f}{\partial p}\right) \sigma_{bp}^2 + 2 \left(\frac{\partial f}{\partial c}\right) \left(\frac{\partial f}{\partial p}\right) \sigma_{cp}^2 + \left(\frac{\partial f}{\partial p}\right)^2 \sigma_{pp}^2,
 \end{aligned} \tag{242}$$

where the σ^2 's are elements of the covariance matrix [8]. Note that it is important to retain the off-diagonal terms since they can act to reduce the error on the fit [17]. We conclude that the relative fluctuation level increases significantly in the core region of the plasma during degraded confinement. This is also the case for the absolute fluctuations, where the bad confinement profile furthermore develops

a 'hump' somewhat inside the LCFS [172]. The errorbars on the relative profiles show that the increased level of core turbulence during bad confinement is a real effect. Outside half-radius, the profiles are identical within errorbars. The errorbars on the absolute profiles are qualitatively identical to those on the relative profiles but are not shown.

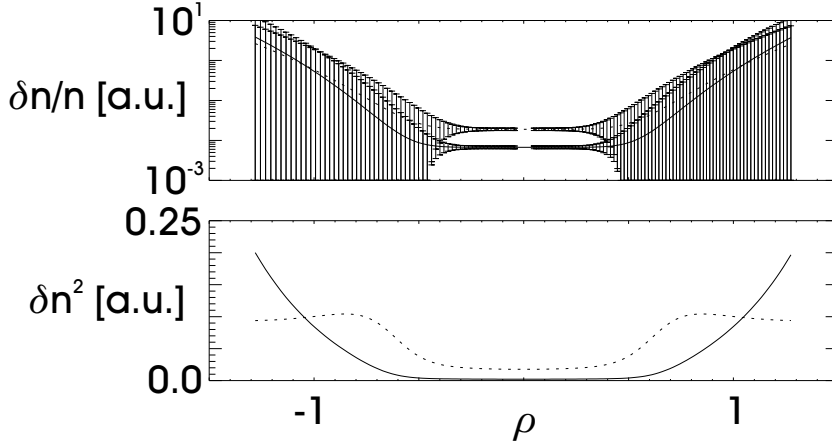


Figure 94. Fitted relative (top) and absolute (bottom) fluctuation profiles. Solid lines are good confinement, dotted lines are bad confinement profiles. Note that the data in the top plot are shown on a logarithmic scale. The errorbars on the relative profiles are calculated using a 10 % error on the measured data. We have left out the errorbars on the absolute profiles for clarity.

The procedure used above is identical to the one used by the ALTAIR team at the Tore Supra tokamak to study differences between L-mode and reversed shear (RS) discharges [4] [74].

We have seen that the same model can be used in Tore Supra and W7-AS to fit the measured data; however, this is not surprising in our case, since our number of datapoints is very small compared to the number of fit parameters. Nevertheless, a direct comparison of L-mode parameters stated in [4] and derived above yields:

- $(c/b)_{L\text{-mode}}^{\text{W7-AS}} = 79, p_{L\text{-mode}}^{\text{W7-AS}} = 8.0$
- $(c/b)_{L\text{-mode}}^{\text{Tore Supra}} = 14, p_{L\text{-mode}}^{\text{Tore Supra}} = 8$

From the above parameters it is quite difficult to make quantitative comparative remarks concerning the fluctuation profiles. Unfortunately, due to the installation of divertor modules in W7-AS (which severely limits the optical access), it is no longer possible to extend our measurement database.

A second point of some interest is that both the change from L-mode to RS confinement in Tore Supra and the sub-L [152] to L-mode transition in W7-AS is connected to a strong decrease of density fluctuations in the core plasma. A direct comparison of figure 6 in [4] and our figure 94 (top) shows that the transition from bad to good confinement is mainly associated with a reduction of core turbulence.

Further evidence of the connection between reduced core turbulence (measured using beam emission spectroscopy) and improved plasma performance has been found in the DIII-D tokamak for both internal transport barrier [60] and radiatively improved [105] discharges.

Summary of results from the two localisation techniques The results obtained using the two different methods of localisation fit together nicely. In both

cases two separate features are observed: A low frequency (± 500 kHz) feature propagating in the ion DD direction and a high frequency (± 2 MHz) feature propagating in the electron DD direction. Both components decrease in amplitude towards the plasma core. In the transition from good to bad confinement the electron feature spins down, i.e. its frequency drops, and the amplitude of both features increases. In the bad confinement state, fluctuations extend to the core and the increase in the derived turbulence profile is significant in the core.

8.4.4 The transition

We have seen that the confinement transition from good to bad confinement can be made to occur on a slow temporal scale by increasing the duration of the current ramp. The behaviour of several measured quantities during these slow ramps has been described in subsection 8.4.1. In figures 95 and 96 we show contour plots of the density fluctuation crosspower amplitude from two of these discharges. The fluctuations were localised at the top and bottom of the plasma using the dual volume localisation technique.

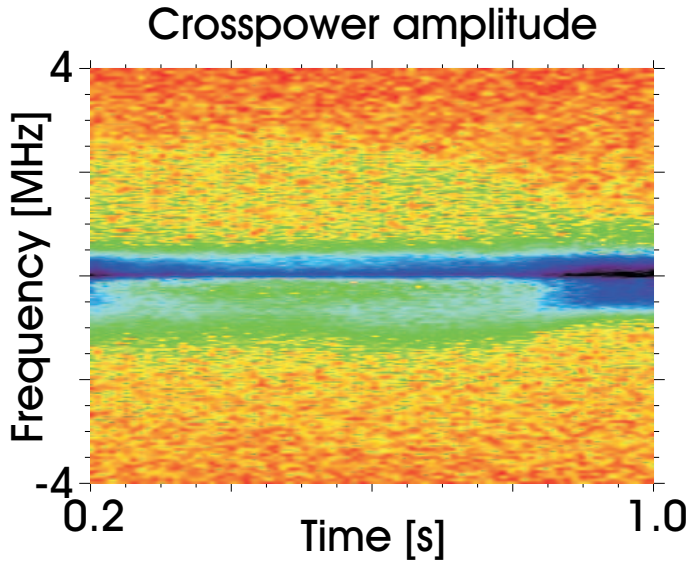


Figure 95. (Colour) Time evolution of the crosspower amplitude spectrum in a slow current ramp discharge. The signal originates at the top of the plasma ($\theta_R = -9.5^\circ$). The positive high frequency feature is crosstalk from the bottom of the plasma, see figure 96.

We have already found that two features are present, the low frequency ion DD and the high frequency electron DD feature. The temporal development of these features is clearly seen in both figures: The electron DD feature spins down and both components increase in amplitude. Two phases can be identified:

1. A gradual change of the features from 300 to 900 ms into the discharges.
2. Saturation of the fluctuations at 900 ms.

The electron feature spins down in frequency during the first phase, while both features increase their amplitude. We again note that the frequency of the electron feature is higher at the bottom of the plasma. Note that the early and late states can be compared to the plots in figure 87 where static good and bad confinement discharges were analysed.

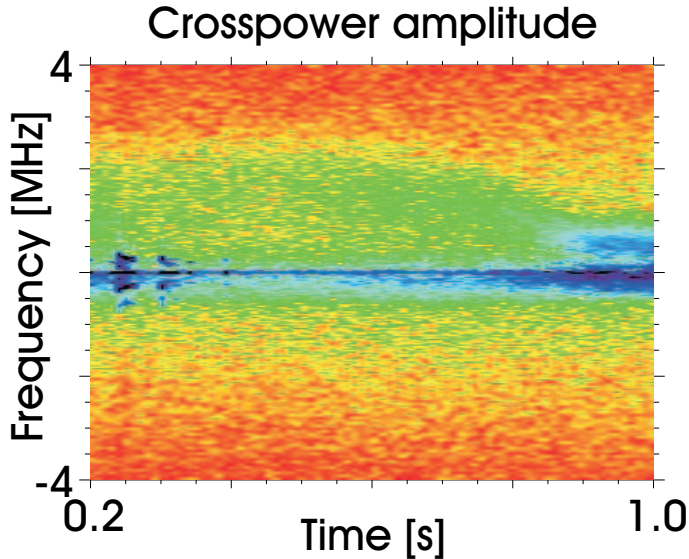


Figure 96. (Colour) Time evolution of the crosspower amplitude spectrum in a slow current ramp discharge. The signal originates at the bottom of the plasma ($\theta_R = 10.5^\circ$). The low frequency disturbance up to 350 ms is due to laser modes.

The existence of two phases is confirmed by the measurements presented in figures 75, 77 and 79: The saturation in bad confinement is seen as a fixed stored energy level, a constant (flat) electron temperature profile and the existence of a single strong magnetic mode at 20 kHz.

8.4.5 Conclusions

We have seen that the changes in confinement by static means (externally set t_a) can be mimicked by inducing a plasma current using the Ohmic transformer in W7-AS. This provides a tool to study confinement transitions lasting many energy confinement times.

The autpower increases in the transition from good to bad confinement for small wavenumbers and decreases for larger wavenumbers; so the weight of larger structures increases in bad confinement. This is also apparent in the development of the power-law exponents for initially bad or good confinement discharges. Two features separated in frequency range co-exist in the plasmas; their amplitudes both increase during bad confinement and the one rotating in the electron DD direction spins down. The analysis of the spatial distribution of the turbulence showed that the core fluctuation level more than doubles from good to bad confinement.

It is here appropriate to note that measurements of density fluctuations using reflectometry were made during several of the current ramp discharges [73]. Here, a frequency decrease of the electron feature in the transition to bad confinement was also found, along with an increase of the fluctuation amplitude.

Furthermore, density fluctuations in the plasma edge were measured using a Li-beam diagnostic and correlated with magnetic fluctuations [172]. We will not discuss the results in detail here, but note that the fluctuating fields are strongly correlated in the edge plasma (inside the LCFS) during degraded confinement.

An interesting discussion concerns the similarity of the observations in W7-AS to those from tokamaks; in the Rijnhuizen tokamak project (RTP) tokamak, local transport barriers near rational q ($= 1/t$) have been found [31] [6]. A thorough

comparative deliberation is given in [26]; the measurements and analysis we have presented above lends support to the conjecture that confinement transitions close to low-order rationals are correlated with the turbulence behaviour in these plasmas. If there are alternating radial zones of good and bad confinement in the initial good confinement plasma, these zones would gradually overlap due to the decrease of magnetic shear. The final transit to bad confinement could in this case be connected to interaction between the outermost bad confinement zones with the material surface of the machine, e.g. a limiter [52] [177].

8.5 High density H-mode

The installation of divertor modules in W7-AS has facilitated the discovery of a new operational regime [64] [104]. We will in this section call it the high density H-mode (HDH-mode); it occurs above a density threshold and exclusively in NBI heated discharges. Confinement below this threshold will be denoted the normal confinement mode (NC-mode).

The section is organised as follows: In subsection 8.5.1 we describe some changes to the LOTUS setup made after the measurements in the previous sections had been carried out. Thereafter, we outline characteristics of the discharges treated (subsection 8.5.2) and present autopower spectra in subsection 8.5.3. A series of shots is considered in subsection 8.5.4 and we investigate fast ($20 \mu\text{s}$) correlations in subsection 8.5.5. The results in the section are compared to a tokamak confinement regime (subsection 8.5.6) and finally conclusions are stated in subsection 8.5.7.

8.5.1 Hardware modifications

A number of changes took place between the measurements described here and in the previous sections.

First of all the centering of the volumes was shifted approximately 20 mm inward along the major radius R . This was due to the divertor installation, where a special hole in a divertor tile was constructed to enable the continued operation of LOTUS. The limited space through the hole meant that the volume separation was too small to achieve spatial localisation (see appendix A, table 7). Therefore the density fluctuations presented in this section are line integrated.

The second change was a reversal of the meaning of negative and positive frequencies. This means that after the change (i.e. for the measurements in the present section), positive frequency fluctuations propagate outward along R . The reason for the modification was purely technical.

The diffractive beam splitter angle θ_2 (see chapter 7) was changed from 25 to 10 mrad.

Finally, we installed notch filters (Eagle TNF411-7BF) to decrease the 40 MHz carrier signal. This was done in order to be able to increase the amplification in the acquisition card without experiencing saturation of the signals. The notch filters were set to damp 20 dB at 40 MHz. The response of the filters was calibrated using a signal generator and the resulting correction was built into the IDL analysis programs [176].

8.5.2 Discharge description

The discharges analysed below were heated by 2 MW of NBI power and had an edge rotational transform of 0.56 ($t_a = 5/9$ operation). At this input power level, the threshold line density \bar{n}_e is $1.8 \times 10^{20} \text{ m}^{-3}$ (vertical dashed line in figure 97). Below this density the discharges are in NC-mode, above in HDH-mode. In figure 97 we show the energy confinement time τ_E versus line density for a series of discharges. We analyse two discharges just below and above this density, 51883 ($\bar{n}_e = 1.75 \times 10^{20} \text{ m}^{-3}$) and 51885 ($\bar{n}_e = 2.39 \times 10^{20} \text{ m}^{-3}$).

The energy confinement time in NC-mode follows the ISS95 scaling law (equation 132), opposed to HDH-mode which is up to a factor of two above this scaling [64]. The increase in energy confinement time is accompanied by a favourable behaviour of the impurity confinement time τ_{imp} : Above the density threshold, τ_{imp} drops dramatically. The diffusion coefficients in NC- and HDH-mode are comparable, but the inward pinch velocity is reduced a factor of three in HDH-mode, leading to a reduction of impurity peaking [104]. The reduction of radiation en-

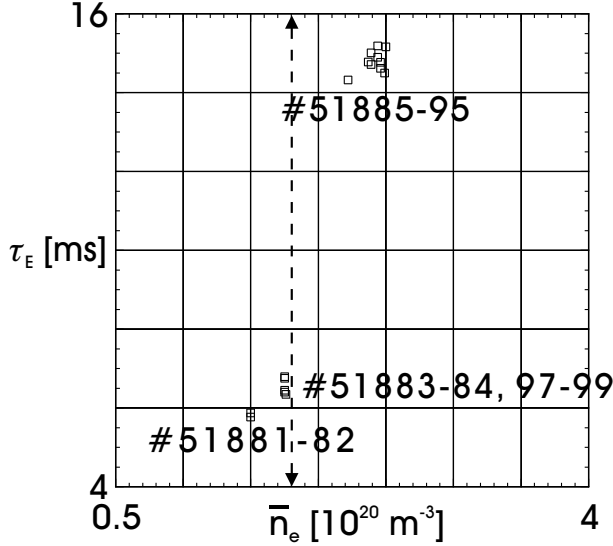


Figure 97. Energy confinement time versus line density [103]. The vertical dashed line marks the threshold density.

ables the attainment of steady-state plasmas in the HDH-mode. That is, high input power operation at high densities is feasible.

In figure 98 we show Mirnov coil measurements of fluctuations in the two discharges analysed. The left-hand column shows measurements in the NC-mode plasma; initial ELMy activity is seen from 150 to 250 ms, followed by a brief period of HDH-mode, where the magnetic activity is strongly reduced. The entrance into NC-mode (at 300 ms) is associated with strong magnetic fluctuations centered at 20 and 100 kHz. These fluctuations rotate in the electron DD direction. The discharge remains stationary until 800 ms where it is terminated. The right-hand column shows the HDH-mode discharge; initially, ELMs are observed from 150 to 250 ms. Thereafter, the fluctuations subside to a very low level and stay there in the remainder of the discharge.

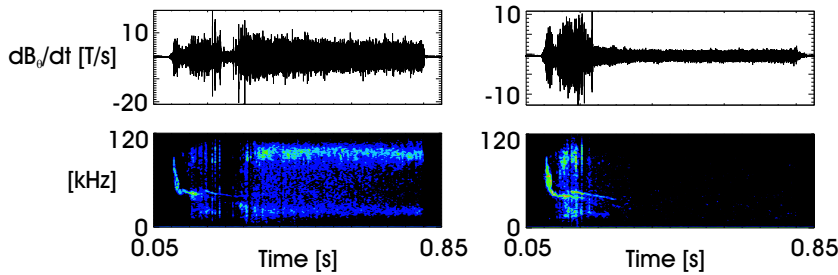


Figure 98. (Colour) Magnetic field derivative in T/s from the 'MIRTIM' monitor coil (top) and a spectrogram (bottom) covering 800 ms. Left: NC-mode (51883), right: HDH-mode (51885).

8.5.3 Autopower spectra

The density fluctuations measured had $k = 20 \text{ cm}^{-1}$ with identical diagnostic settings for all shots in the series. We will show results from only one of the volumes (2). In figure 99 we show spectrograms of shots 51883 (left, NC-mode)

and 51885 (right, HDH-mode). In the early phase of both discharges, ELM bursts are visible as vertical lines extending to high frequencies (see figure 66). Comparing the steady-state phases, we can conclude that low frequency fluctuations ($< \pm 1$ MHz) are larger in HDH-mode than in NC-mode. The situation is reversed for high negative frequencies: Here, the fluctuation amplitude decreases in going from NC- to HDH-mode.

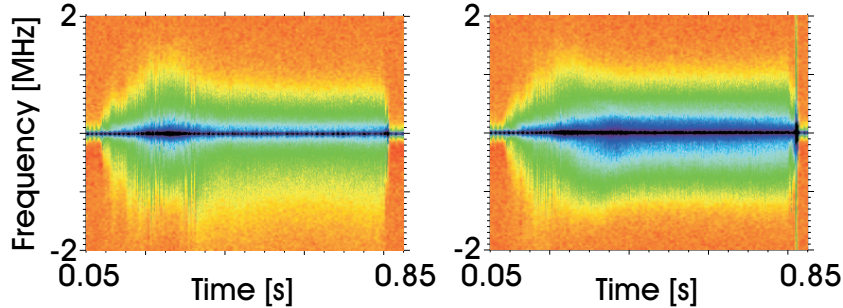


Figure 99. (Colour) Autopower versus time and frequency for discharges 51883 (left) and 51885 (right), volume 2. The time resolution of the spectra is 1 ms and the colourscales are identical and logarithmic.

To elucidate the differences observed in the spectrograms, 2D autopower spectra are shown in figure 100. The spectra are integrated over 100 ms, from 500 to 600 ms into the discharges. This confirms that low fluctuations up to ± 1 MHz increase and high negative frequencies decrease from NC- to HDH-mode confinement. Assuming that these high frequency fluctuations travel in the electron DD direction, they are localised at the top of the plasma.

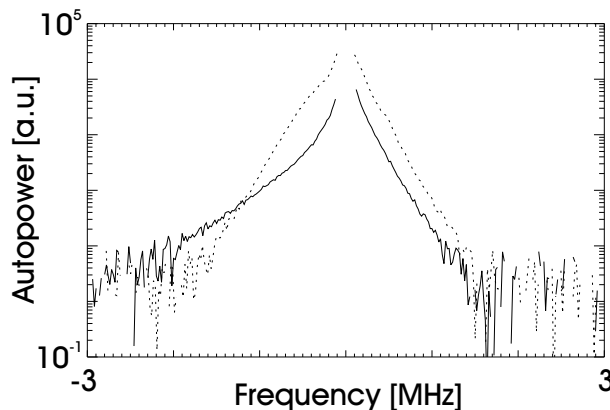


Figure 100. Overlaid autopower spectra. The solid line is NC-mode, the dotted line is HDH-mode.

To enable a visual inspection of the correlation between various fluctuating fields, we show Mirnov coil, H_α -light and density fluctuations in figure 101. The left-hand column shows traces for NC-mode, the right-hand column for HDH-mode. The difference in stored energy (top traces) is more than a factor two for a density increase only a factor 1.4. The ELMs in the early phases are clearly correlated for all fluctuations. The NC-mode is characterised by large fluctuation amplitudes detected by the Mirnov coil and the H_α -light. In contrast, these fluctuations are significantly reduced in HDH-mode. The density fluctuations are quiescent in

both steady-state modes, but the amplitude in HDH-mode is 5-10 times higher than for the NC-mode. This dramatic increase could not be accounted for by a density squared scaling of the density fluctuations, since this would only amount to a factor 2 increase.

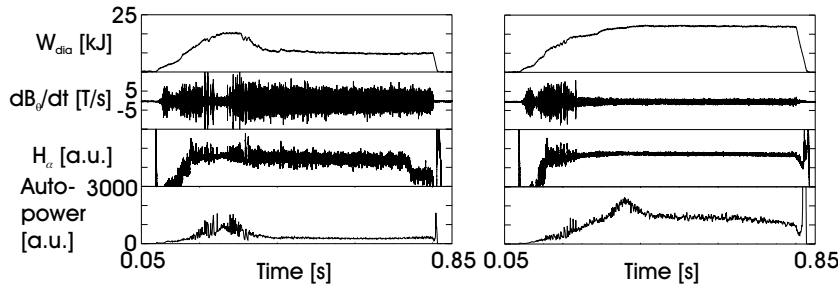


Figure 101. Discharge overview - time traces from 50 to 850 ms. From top to bottom: Diamagnetic energy [kJ], magnetic fluctuations [T/s], H_α -light and frequency integrated density fluctuations (1 ms time windows) in volume 2 at $k = 20 \text{ cm}^{-1}$. Left column: NC-mode, right column: HDH-mode.

8.5.4 Discharge series

As we stated above, the two discharges singled out for the comparative analysis were part of a series. Here, we present results pertaining to the entire series. All discharges had the same auxiliary settings, the only difference being the line density value. The series consisted of 16 discharges; the first 4 (51881-51884) and last 3 (51897-51899) were in NC-mode, the others in HDH-mode. In figure 102 we show the density fluctuation power and stored energy versus shot number (left) and density fluctuation power versus line density (right). The left-hand plots show the difference between NC- and HDH-mode clearly: A marked increase in stored energy and an increased density fluctuation level; this effect is completely reproducible. The right-hand plot shows the density fluctuation power versus line density. Two groups at low densities have almost the same magnitude despite some difference in density; the high density group exhibits a significantly increased fluctuation level with a large scatter of the datapoints.

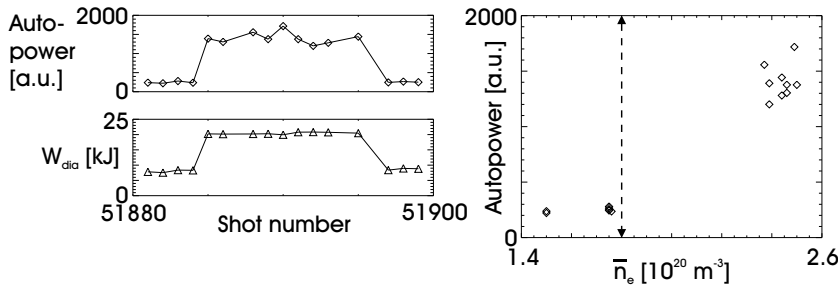


Figure 102. Left: Frequency integrated density fluctuations (top) and stored energy (bottom) versus shot number, right: Frequency integrated density fluctuations versus line density. The threshold density is marked by a vertical dashed line.

Although the total density fluctuation level increases, we have found (see for instance figure 100) that the amplitude drops at high negative frequencies. Restricting the frequency integration to this range and performing the analysis on

the series again, we verify a factor 2 drop in the amplitude, see figure 103. The scatter at low densities is somewhat larger than that in figure 102, probably due to the reduced SNR at high frequencies.

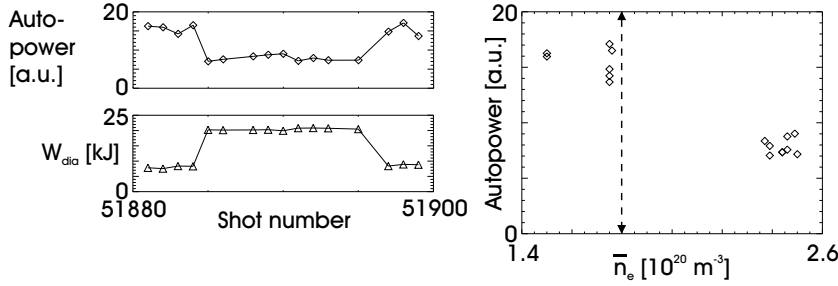


Figure 103. Left: Density fluctuations integrated over high negative frequencies ($[-3, -1.3]$ MHz, top) and stored energy (bottom) versus shot number, right: Density fluctuations integrated over high negative frequencies ($[-3, -1.3]$ MHz) versus line density. The threshold density is marked by a vertical dashed line.

To sum up, we can conclude that:

- The total density fluctuation level is a factor 5-10 higher in HDH-mode compared to NC-mode.
- The high negative frequency fluctuation level is a factor 2 lower in HDH-mode than in NC-mode.

8.5.5 Correlations

It would be interesting to correlate the density fluctuations in NC- and HDH-mode to the Mirnov coil signal on a fast $20 \mu\text{s}$ timescale as we did for the discharges in sections 8.2 and 8.3. The question we address is the following: Are the (NC- & L-mode) and (HDH- & H*-mode) pairs equivalent?

Comparison between NC- and HDH-mode We continue to analyse shot 51883 (NC-mode) and shot 51885 (HDH-mode). By performing a correlation procedure like the one described in section 8.2, we arrive at figure 104. The left-hand contour plot shows the NC-mode crosscorrelation versus density fluctuation frequency and time lag. A correlation up to just below 30 % is present, in accordance with the L-mode results in section 8.3. However, the lifetime of the correlation is somewhat shorter than that found for L-mode. The right-hand contour plot showing the HDH-mode crosscorrelation displays no systematic correlation, analogous to the outcome of the H*-mode analysis.

Comparison between HDH- and H*-mode We have just found that the differences in correlation between L- and H*-mode correspond to those between NC- and HDH-mode. From this point onward we assume that NC- and L-mode are identical states. Here, we want to resolve what distinctions exist between HDH- and H*-mode. For this purpose we analyse a discharge (51887) that evolved from HDH- through L- to H*-mode, see figure 105. Again, bursts signify ELMs; the initial ELM phase is followed by a HDH-mode (250 to 450 ms). Thereafter confinement worsens and a dithering period commences; this lasts until about 700 ms into the discharge where an H*-mode is entered. The discharge thereafter rapidly accumulates impurities and collapses around 750 ms.

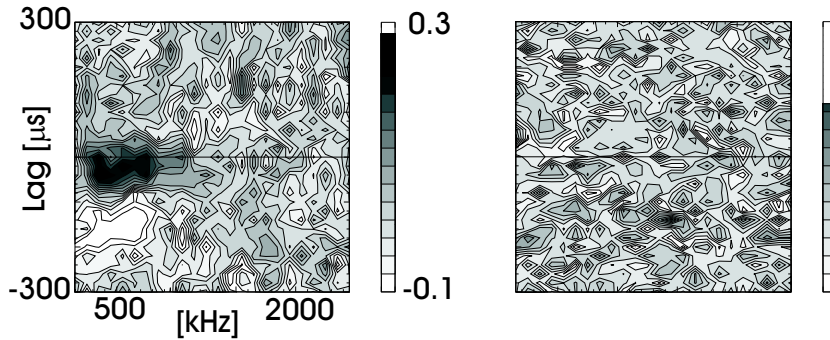


Figure 104. Crosscorrelation between Mirnov RMS signal and density fluctuation band autopower from collective scattering versus band central frequency and time lag (units of $20 \mu\text{s}$). Left: NC-mode, right: HDH-mode. The greyscale on the right-hand sides of the plots shows what range of the total scale is relevant for the particular time window.

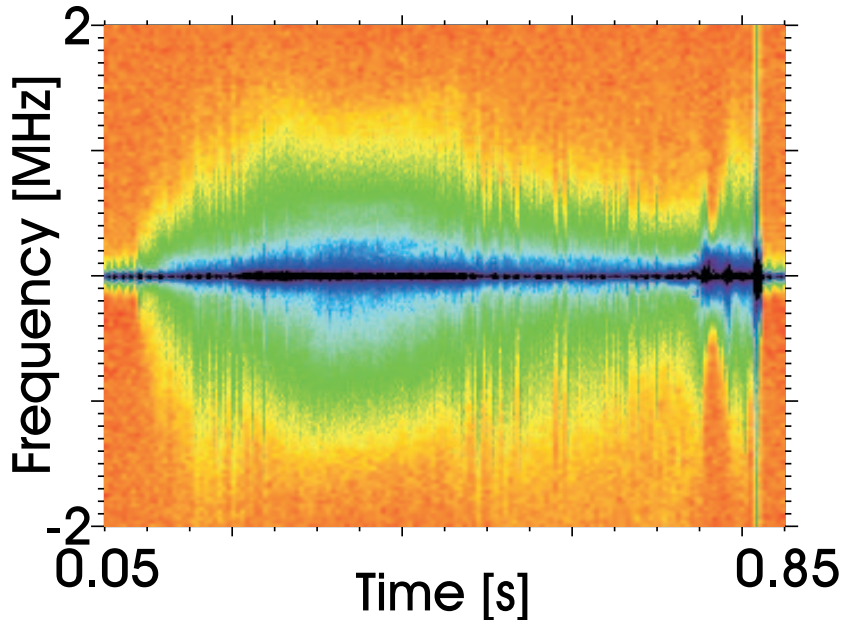


Figure 105. (Colour) Autopower versus time and frequency for discharge 51887, volume 2. The time resolution of the spectra is 1 ms and the colourscale is logarithmic.

In figure 106 (top) we show traces of Mirnov coil, H_α -light and density fluctuations as we did for the steady-state discharges in figure 101. The dynamical behaviour of the different fluctuating quantities is marked; so is the effect on the stored energy in the uppermost trace. The contour plots below the traces show crosscorrelations for three time intervals indicated by semi-transparent rectangles above. The left-hand plot is for HDH-mode, the center plot for L-mode and the right-hand plot for H^* -mode.

If one compares the magnetic fluctuations in HDH- and H^* -mode it is observed that the amplitude in HDH-mode is reduced compared to L-mode, but not to the extremely low level measured in H^* -mode. In contrast, the H_α -signal is nearly identical in the two confinement states. The most pronounced development is in the density fluctuations: As we found previously, the amplitude is very large in

HDH-mode compared to L-mode. Additionally, it is evident from figure 106 that the density fluctuation amplitude in H*-mode is much smaller than the HDH-mode level. It is interesting to note that the density fluctuation power never becomes stationary in this plasma.

The remaining question concerns the behaviour of correlated fluctuations. The 3 contour plots at the bottom of figure 106 display the answer: No correlations between Mirnov coil and density fluctuation measurements are observed during either HDH- or H*-mode. In that sense the two improved modes are identical. As we have found previously, clear correlations exist in the L-mode phase.

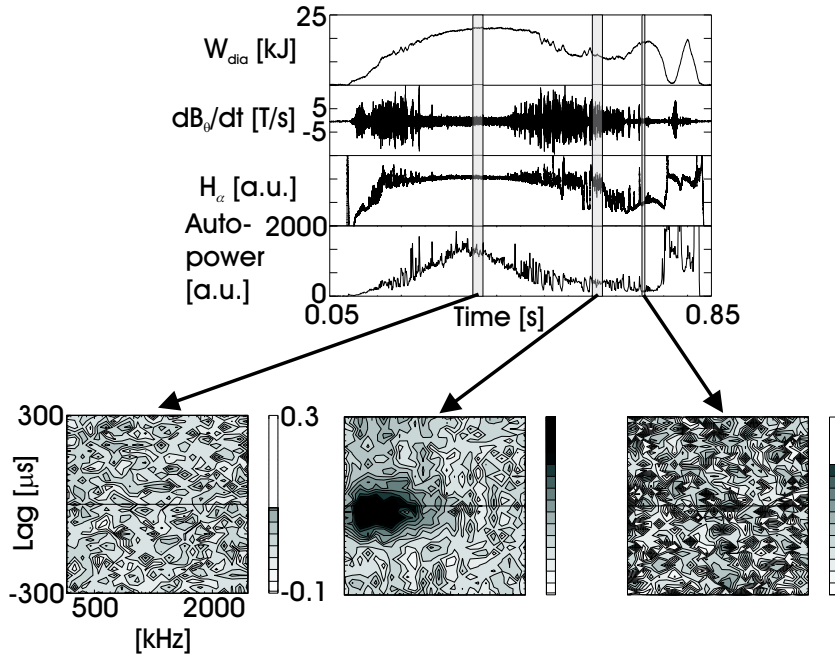


Figure 106. Top: Discharge overview - time traces from 50 to 850 ms. From top to bottom: Diamagnetic energy [kJ], magnetic fluctuations [T/s], H_α -light and frequency integrated density fluctuations (1 ms time windows) in volume 2 at $k = 20 \text{ cm}^{-1}$. Bottom: Crosscorrelation between Mirnov RMS signal and density fluctuation band autopower from collective scattering versus band central frequency and time lag (units of 20 μs). Left: HDH-mode, center: L-mode and right: H*-mode. The greyscale on the right-hand sides of the plots shows what range of the total scale is relevant for the particular time window.

8.5.6 Discussion

We now turn to a discussion of the analysis performed in this section. However, before we discuss the W7-AS measurements, we present a brief review of an enhanced confinement regime discovered in the Alto Campo Torus C-Mod (Alcator C-Mod) tokamak [83].

Enhanced D_α H-mode in Alcator C-Mod The confinement state found in Alcator C-Mod is called the enhanced D_α (EDA) H-mode because of the increased D_α -light activity compared to the H*-mode [145]. Further, the EDA H-mode is characterised by [145] [62]:

- Short particle confinement time τ_p compared to H*-mode.

- ELMs are either small in amplitude or totally absent.
- High density ($\bar{n}_e \sim 4 \times 10^{20} \text{ m}^{-3}$).
- Good energy confinement.
- No accumulation of impurities (small τ_{imp}).
- Steady-state operation.

These features are remarkably similar to those displayed by the HDH-mode in W7-AS; therefore it would be reasonable to investigate what the turbulence behaviour is like in EDA H-mode and compare that to what we have found.

* * *

In the EDA H-mode, high density fluctuation levels have been observed compared to those in H*-mode [62]. The reflectometry system measures broadband fluctuations with a quasi coherent (QC) feature superposed. The phase-contrast imaging system sees only the QC peak. The range of wavenumbers covered is $k = [1, 5] \text{ cm}^{-1}$.

In continued investigations, the QC feature was also observed with fast scanning Langmuir probes and Mirnov coils in the 100-150 kHz range [136]. It is not present in either L- or H*-mode. Rotation in the electron DD direction was measured. The QC mode seems to drive a substantial particle flux at the edge of the same order as the total fuelling rate.

The position of the fluctuations associated with the QC mode has been determined to be in the region where the density gradient is very steep, close to the LCFS [81].

W7-AS measurements After our recapitulation of the EDA H-mode properties, we discuss these along with the findings in the HDH-mode. The purpose of this deliberation is to find out whether the EDA H-mode and the HDH-mode are manifestations of a single mechanism.

The fact that the density fluctuation level in EDA H-mode exceeds that of H*-mode is compatible with the measurements of density fluctuations we have shown above. The main difference is that only broadband fluctuations are observed with LOTUS, no QC feature seems to exist. The QC component could still exist at smaller wavenumbers; we measured at 20 cm^{-1} whereas the density fluctuation measurements in Alcator C-Mod were made in the range $[1, 5] \text{ cm}^{-1}$.

In contrast to the magnetic fluctuation measurements in EDA H-mode, the Mirnov coils in W7-AS show a reduced fluctuation level in HDH-mode.

In W7-AS, the NC- \rightarrow HDH-mode transition is associated with a slight increase of the temperature, but without a change of the gradient. The situation is opposite for the density profile: In going from NC- to HDH-mode, the profile becomes very steep at the edge and almost flat in the center compared to the almost constant gradient in NC-mode over most of the plasma cross section [104]. For EDA H-mode, the gradients of both temperature and density are almost identical to those in H*-mode [108], but still considerable with respect to L-mode [62]. This is compatible with the W7-AS measurements.

8.5.7 Conclusions

In this section we have characterised the density fluctuations measured by LOTUS in the new confinement regime discovered in W7-AS, the HDH-mode.

The fluctuation amplitude in the HDH-mode is substantially above that of the NC-mode, except for high negative frequencies where the trend is opposite. Magnetic and density fluctuations are correlated in NC- but not in HDH-mode, corresponding to the L- and H*-mode correlations.

To sum up our discussion, we can state that most of the global features in EDA H-mode and HDH-mode are similar, but that the behaviour of fluctuations is not identical.

9 Conclusions

In this thesis we have investigated turbulence in fusion plasmas measured by the collective scattering of infrared light. The experimental results have been obtained using the LOTUS diagnostic, which is a system capable of measuring fluctuations in the electron density.

The conclusions are split into three parts: Section 9.1 concerns the theoretical work presented in the thesis and section 9.2 treats measurements of density fluctuations in the W7-AS stellarator. Finally, in section 9.3, we discuss how the diagnostic and analysis tools could be improved upon.

9.1 Theoretical results

In chapter 2 a complete derivation of an expression for the detected photocurrent has been presented. A multitude of sources was used for the construction of this chapter and have here been collected to form one coherent derivation.

The measurement volume is treated in detail in chapter 3 and the different methods of spatial localisation are explained. Analytical expressions for the autopower are derived and simulations illustrate the components entering the formulae.

Spectral analysis is an essential part of the analysis tools used in this thesis. Therefore the quantities used for interpretation are presented in chapter 4 and are visualised by simulations.

9.2 Experimental results

We introduce important quantities related to confinement and transport in chapter 5. Simplified equations describing transport and quasilinear fluxes due to correlated fluctuating fields are summarised. Simple instabilities, concepts from turbulence studies and a short review of fluctuation measurements in fusion devices are also covered. The chapter is ended by a section on turbulence suppression due to sheared flows.

The W7-AS stellarator is introduced in chapter 6. First, the main engineering parameters, thereafter the plasma current and finally the magnetic field topology.

The actual implementation of the LOTUS diagnostic is reviewed in chapter 7. A stepwise explanation of the components is given and the chapter is ended by a section on the acquisition system.

The most important chapter of the thesis is chapter 8, where the measurements are described and analysed. Below, we give an overview of the main findings from each section:

9.2.1 Quasi steady-state

A wavenumber scan (14 to 62 cm⁻¹) of quasi steady-state plasmas was presented in section 8.1. A statistical analysis of the raw data showed that it is roughly Gaussian. The density fluctuations observed extend to 2-3 MHz, which is consistent with the $\mathbf{E} \times \mathbf{B}$ velocity calculated from the measured radial electric field. The autopower spectra decrease monotonically with frequency and wavenumber. The wavenumber spectrum can be fitted using either power-laws or an exponential fit.

9.2.2 Fast confinement transitions

Section 8.2 describes the density fluctuation behaviour in dithering plasmas. The confinement state switches fast between L- and H-mode. This switching is observed as activity in the high frequency fluctuations. The slopes of the autopower spectra versus frequency can be fitted by exponential functions. The L-mode velocity is a factor 1.6 times larger than the H-mode one. We deduce that low/high frequencies originate outside/inside the LCFS, respectively. The L- and H-mode wavenumber spectra are almost identical and can both be fitted to power-laws or exponential functions, with almost identical exponents in both cases. Cross correlation calculations between magnetic and density fluctuations show that the L-mode fluctuations are correlated, but that the H-mode fluctuations are uncorrelated. The turbulence during L-mode bursts is correlated on a $100 \mu\text{s}$ time scale.

9.2.3 Confinement bifurcations

Analysis of a single discharge having both L- and H*-mode phases is contained in section 8.3. The purpose of this section was to clarify whether our separation procedure described in section 8.2 was a valid approach to study L- and H-mode fluctuations. The answer to that question is 'yes': Steady-state L-mode and H*-mode possess the same characteristics as those found by separating dithering plasmas into L- and H-mode phases. Further, the phase separation technique was applied to the discharge, indicating that events during L- and H-mode have disparate behaviour and confirming the velocity difference found earlier between the two states.

9.2.4 Slow confinement transitions

Slow reproducible confinement transitions can be made using externally controllable means. Density fluctuations during such transitions (from 'good' to 'bad' confinement) is the topic of section 8.4. Wavenumber spectra fitted to power-laws during such transitions are steeper for bad confinement than for good confinement. Spatially localised measurements were made at 15 cm^{-1} using both the dual and single volume localisation techniques. Here, it was found that two features separated in frequency co-exist in the plasmas: One in the ion and one in the electron DD direction. The amplitude of each feature increases in bad confinement and the electron feature spins down, i.e. its frequency decreases. The core fluctuation level more than doubles from good to bad confinement.

9.2.5 High density H-mode

In 2001 a new operational regime with improved confinement properties, the high density H-mode (HDH-mode), was discovered in W7-AS. The occurrence of this regime was associated with the installation of divertor modules. Density fluctuations during the HDH-mode are analysed in section 8.5 and compared to normal confinement mode (NC-mode) plasmas. The fluctuation amplitude in HDH-mode is much larger than that of the NC-mode, except for high negative frequencies where the situation is reversed. Magnetic and density fluctuations are correlated in NC- but not in HDH-mode, corresponding to the L- and H*-mode correlations.

9.3 Roads not taken

It is always the case that both the diagnostic and analysis methods could be improved upon. Due to the limited amount of time and manpower available, a

number of ideas had to be omitted from the thesis (reason for the Frostian section title).

Concerning diagnostic capabilities, new cooled detectors would be very beneficial. It has been shown that cooled detectors improve the SNR an order of magnitude [131], enabling the following enhancements to LOTUS:

- Measure at larger wavenumbers
- Measure at lower densities
- Measure at higher frequencies

Regarding data analysis, a full simulation of turbulent events - including the realistic geometry of W7-AS and the measurement volumes - would be of great interest. The investigation of phase separation in chapter 4 will be made systematic elsewhere. A substantial amount of measurements have not been presented due to restrictions in the size of the thesis, for example treating fluctuations in plasmas heated by co- and counter-NBI [9], extended H*-modes [10] and high- β plasmas [13]. Parameters scans have been made in high- β plasmas (not yet published).

*ich dreh mich um dich
ich dreh mich um dich
stell mich vor den bösen blick
deine tränen werde ich übernehmen
alle qualen und alle folter überstehen
auch wenn du greinst, du dich kasteist
auch wenn du haderst, du dich zerreisst
wenn sich alles verdunkelt
bring ich dich durch die nacht*

Herbert Grönemeyer

References

- [1] Observation des petites échelles de la turbulence développée par diffusion collective de la lumière, G.Antar, Ph.D. thesis (1996)
- [2] Statistical study of density fluctuations in the Tore Supra tokamak, G.Antar et al., Plasma Phys. Control. Fusion **40** (1998) 947
- [3] Temporal separation of the density fluctuation signal measured by light scattering, G.Antar et al., Plasma Phys. Control. Fusion **41** (1999) 733
- [4] Turbulence reduction and poloidal shear steepening in reversed shear plasmas investigated by light scattering on Tore Supra, G.Antar et al., Phys. Plasmas **8** (2001) 186
- [5] Analysis of W7-AS Mirnov data using SVD and correlation techniques, M.Anton et al., 24th EPS, ECA **21A** (1997) 1645
- [6] Tokamak plasmas with dominant electron cyclotron heating; evidence for electron thermal transport barriers, M.R.de Baar et al., Phys. Plasmas **6** (1999) 4645
- [7] Measurement and calculation of the radial electric field in the stellarator W7-AS, J.Baldzuhn et al., Plasma Phys. Control. Fusion **40** (1998) 967
- [8] Modelling of neutron emissivities at JET using charge exchange spectroscopic data, N.P.Basse, M.Sc. thesis (1998)
- [9] Relationship between confinement and core plasma fluctuations in the W7-AS stellarator, N.P.Basse et al., 12th International Stellarator Workshop, Madison (1999)
- [10] Density fluctuations during confinement changes in the Wendelstein 7-AS stellarator, N.P.Basse et al., 27th EPS, ECA **24B** (2000) 940
- [11] Separation of L- and H-mode density fluctuations in dithering Wendelstein 7-AS plasmas, N.P.Basse et al., 28th EPS, ECA **25A** (2001) 1941
- [12] Spatial distribution of turbulence in the Wendelstein 7-AS stellarator, N.P.Basse et al., 25th ICPIG **4** (2001) 335
- [13] Interplay between magnetic topology, density fluctuations and confinement in high- β Wendelstein 7-AS plasmas, N.P.Basse et al., 13th International Stellarator Workshop, Canberra (2002)
- [14] Low- and high-mode separation of short wavelength turbulence in dithering Wendelstein 7-AS plasmas, N.P.Basse et al., Phys. Plasmas **9** (2002) 3035
- [15] Spatial distribution of turbulence in the Wendelstein 7-AS stellarator, N.P.Basse et al., Plasma Sources Sci. Technol. **11** (2002) A138
- [16] Random data: Analysis and measurement procedures, J.S.Bendat and A.G.Piersol, John Wiley and Sons (2000)
- [17] Data reduction and error analysis for the physical sciences, P.R.Bevington and D.K.Robinson, McGraw-Hill (1992)
- [18] Influence of sheared poloidal rotation on edge turbulence, H.Biglari et al., Phys. Fluids B **2** (1990) 1
- [19] Density fluctuations dispersion measurement in the Tokamak de Varennes, A.Boileau and J.-L.Lachambre, Phys. Lett. A **148** (1990) 341

- [20] Principles of optics, M.Born and E.Wolf, Cambridge University Press (1999)
- [21] Confinement in W7-AS and the role of radial electric field and magnetic shear, R.Brakel et al., Plasma Phys. Control. Fusion **39** (1997) B273
- [22] The role of magnetic shear in the confinement of W7-AS plasmas, R.Brakel et al., J. Plasma Fusion Res. SERIES **1** (1998) 80
- [23] On the influence of rotational transform and magnetic shear on confinement in the W7-AS stellarator, R.Brakel et al., 25th EPS, ECA **22C** (1998) 423
- [24] An empirical model of electron energy transport in the presence of rational surfaces in W7-AS, R.Brakel et al., 12th International Stellarator Workshop, Madison (1999)
- [25] R.Brakel, private communication (2001, 2002)
- [26] Electron energy transport in the presence of rational surfaces in the Wendelstein 7-AS stellarator, R.Brakel, Nucl. Fusion **42** (2002) 903
- [27] The spectrum, spatial distribution and scaling of microturbulence in the TEXT tokamak, D.L.Brower et al., Nucl Fusion **27** (1987) 2055
- [28] A study of low-frequency microturbulence by CO₂-laser collective scattering in the FT-2 tokamak, V.V.Bulanin et al., Plasma Phys. Rep. **24** (1998) 191
- [29] Physics of the L-mode to H-mode transition in tokamaks, K.H.Burrell et al., Plasma Phys. Control. Fusion **34** (1992) 1859
- [30] Tests of causality: Experimental evidence that sheared $\mathbf{E} \times \mathbf{B}$ flow alters turbulence and transport in tokamaks, K.H.Burrell et al., Phys. Plasmas **6** (1999) 4418
- [31] Electron thermal transport in RTP: Filaments, barriers and bifurcations, N.J.Lopes Cardozo et al., Plasma Phys. Control. Fusion **39** (1997) B303
- [32] Progress in anomalous transport research in toroidal magnetic confinement devices, B.A.Carreras, IEEE Trans. on Plasma Science **25** (1997) 1281
- [33] Chinese boxes; defined in Merriam-Webster's dictionary (<http://www.m-w.com>) as:
 Function: *noun plural*
 Date: 1829
 1: a set of boxes graduated in size so that each fits into the next larger one
 2: something that resembles a set of Chinese boxes especially in complexity
- [34] A phase contrast interferometer on DIII-D, S.Coda et al., Rev. Sci. Instrum. **63** (1992) 4974
- [35] Decorrelation of edge plasma turbulence at the transition from low- to high-confinement mode in the DIII-D tokamak, S.Coda et al., Phys. Lett. A **273** (2000) 125
- [36] Characterization of density fluctuations during ELMs in the DIII-D tokamak, S.Coda et al., Nucl. Fusion **41** (2001) 1885
- [37] Edge-localized modes - physics and theory, J.W.Connor, Plasma Phys. Control. Fusion **40** (1998) 531
- [38] A review of theories of the L-H transition, J.W.Connor and H.R.Wilson, Plasma Phys. Control. Fusion **42** (2000) R1
- [39] A review of the dimensionless parameter scaling studies, J.G.Cordey et al., Plasma Phys. Control. Fusion **38** (1996) A67

- [40] Plasma physics, an introductory course, ed. R.Dendy, Cambridge University Press (1996)
- [41] Infrared detectors and systems, E.L.Dereniak and G.D.Boreman, John Wiley and Sons (1996)
- [42] Localized measurements of turbulence in the Tore Supra tokamak, P.Devynck et al., Plasma Phys. Control. Fusion **35** (1993) 63
- [43] Modifications in turbulence and edge electric fields at the L-H transition in the DIII-D tokamak, E.J.Doyle et al., Phys. Fluids B **3** (1991) 2300
- [44] Observation of simultaneous internal transport barriers in all four transport channels and correlation with turbulence behaviour in NCS discharges in DIII-D, E.J.Doyle et al., Plasma Phys. Control. Fusion **42** (2000) A237
- [45] Observation of a localized transition from edge to core density turbulence in the TFTR tokamak, R.D.Durst et al., Phys. Rev. Lett. **71** (1993) 3135
- [46] Elektromagnetisme, B.Elbek, Niels Bohr Institutet (1994)
- [47] Experimentelle untersuchung und modellierung elektrostatischer fluktuation in den abschälsschichten des tokamak ASDEX und des stellarators Wendelstein 7-AS, M.Endler, Ph.D. thesis (1994)
- [48] Measurements and modelling of electrostatic fluctuations in the scrape-off layer of ASDEX, M.Endler et al., Nucl. Fusion **35** (1995) 1307
- [49] H mode of the W7-AS stellarator, V.Erckmann et al., Phys. Rev. Lett. **70** (1993) 2086
- [50] Electron cyclotron resonance heating and EC-current drive experiments at W7-AS, status at W7-X, V.Erckmann et al., Fusion Eng. Design **53** (2001) 365
- [51] Up-down asymmetries of density fluctuations in Tore Supra, C.Fenzi et al., Plasma Phys. Control. Fusion **41** (1999) 1043
- [52] Interplay between edge and outer core fluctuations in the tokamak Tore Supra, C.Fenzi et al., Nucl. Fusion **40** (2000) 1621
- [53] Long-wavelength density turbulence in the TFTR tokamak, R.J.Fonck et al., Phys. Rev. Lett. **70** (1993) 3736
- [54] Turbulence, U.Frisch, Cambridge University Press (1996)
- [55] Turbulence and energy confinement in Tore Supra Ohmic discharges, X.Garbet et al., Nucl. Fusion **32** (1992) 2147
- [56] Kelvin-Helmholtz instabilities in tokamak edge plasmas, X.Garbet et al., Phys. Plasmas **6** (1999) 3955
- [57] Physics of the density limit in the W7-AS stellarator, L.Giannone et al., Plasma Phys. Control. Fusion **42** (2000) 603
- [58] Introduction to plasma physics, R.J.Goldston and P.H.Rutherford, Institute of Physics Publishing (1995)
- [59] Introduction to Fourier optics, J.W.Goodman, McGraw-Hill (1968)
- [60] Behaviour of electron and ion transport in discharges with an internal transport barrier in the DIII-D tokamak, C.M.Greenfield et al., Nucl. Fusion **39** (1999) 1723

- [61] Quiescent double barrier regime in the DIII-D tokamak, C.M.Greenfield et al., Phys. Rev. Lett. **86** (2001) 4544
- [62] Characterization of enhanced D_α high-confinement modes in Alcator C-mod, M.Greenwald et al., Phys. Plasmas **6** (1999) 1943
- [63] Density fluctuation measurement by far infrared light scattering, D.Grésillon et al., Physica Scripta **T2/2** (1982) 459
- [64] First island divertor experiments on the W7-AS stellarator, P.Grigull et al., Plasma Phys. Control. Fusion **43** (2001) A175
- [65] Flow shear induced fluctuation suppression in finite aspect ratio shaped tokamak plasma, T.S.Hahm and K.H.Burrell, Phys. Plasmas **2** (1995) 1648
- [66] Flow speed measurement using two-point collective light scattering, N.P.Heinemeier, Risø-R-1064(EN) (1998)
- [67] P.Hennequin, private communication (2001)
- [68] Untersuchung der plasmarandschicht am stellarator Wendelstein 7-AS, G.Herre, Ph.D. thesis (1998)
- [69] Theory of plasma transport, F.L.Hinton and R.D.Hazeltine, Reviews of Modern Physics **48** (1976) 239
- [70] Edge transport barrier and edge turbulence during H-mode operation in the W7-AS stellarator, M.Hirsch et al., Proc. 16th IAEA Conf. (Montreal) **2** (1996) 315
- [71] Operational range and transport barrier of the H-mode in the stellarator W7-AS, M.Hirsch et al., Plasma Phys. Control. Fusion **40** (1998) 631
- [72] Operational conditions and characteristics of ELM-events during H-mode plasmas in the stellarator W7-AS, M.Hirsch et al., Plasma Phys. Control. Fusion **42** (2000) A231
- [73] Doppler reflectometry for the investigation of propagating density perturbations, M.Hirsch et al., Plasma Phys. Control. Fusion **43** (2001) 1641
- [74] Internal transport barrier with ion-cyclotron-resonance minority heating on Tore Supra, G.T.Hoang et al., Phys. Rev. Lett. **84** (2000) 4593
- [75] Stellarator optimization studies in W7-AS, J.V.Hofmann et al., Plasma Phys. Control. Fusion **38** (1996) A193
- [76] An analysis of optical mixing in plasma scattering experiments, E.Holzhauser and J.H.Massig, Plasma Physics **20** (1978) 867
- [77] Collective laser light scattering from electron density fluctuations in fusion research plasmas, E.Holzhauser et al., Rev. Sci. Instrum. **61** (1990) 2817
- [78] The H-mode in the ASDEX tokamak, E.Holzhauser et al., Plasma. Phys. Control. Fusion **36** (1994) A3
- [79] Le signal complexe de la diffusion collective de la lumière et les écoulements turbulents, C.Honoré, Ph.D. thesis (1996)
- [80] Small scale density fluctuations in Tore Supra: Rupture in the scaling law, C.Honoré et al., 25th EPS, ECA **22C** (1998) 647
- [81] Pedestal profiles and fluctuations in C-Mod enhanced D-alpha H-modes, A.E.Hubbard et al., Phys. Plasmas **8** (2001) 2033

- [82] Principles of plasma diagnostics, I.H.Hutchinson, Cambridge University Press (1987)
- [83] First results from Alcator C-Mod, I.H.Hutchinson et al., Phys. Plasmas **1** (1994) 1511
- [84] Classical electrodynamics, J.D.Jackson, John Wiley and Sons (1962)
- [85] Detailed investigation of the vacuum magnetic surfaces on the W7-AS stellarator, R.Jaenicke et al., Nucl. Fusion **33** (1993) 687
- [86] High power heating experiments on Wendelstein 7-AS stellarator, R.Jaenicke et al., Plasma Phys. Control. Fusion **37** (1995) A163
- [87] Operational boundaries on the stellarator W7-AS at the beginning of the divertor experiments, R.Jaenicke et al., Proc. 18th IAEA Conf. (Sorrento) (2000)
- [88] Electron temperature gradient driven turbulence, F.Jenko et al., Phys. Plasmas **7** (2000) 1904
- [89] A practical introduction to electronic circuits, M.H.Jones, Cambridge University Press (1993)
- [90] Density fluctuations in Heliotron E measured using CO₂ laser phase contrast method, S.Kado et al., Fusion Eng. and Design **34-35** (1997) 415
- [91] An introduction to mechanics, D.Kleppner and R.J.Kolenkow, McGraw-Hill (1978)
- [92] Doppler model for adiabatic toroidal compressor driftwave frequency profiles, R.A.Koch and W.M.Tang, Phys. Fluids **21** (1978) 1236
- [93] Report on CO₂ laser scattering system test, G.Kocsis (1999)
- [94] Two-dimensional turbulence, R.H.Kraichnan and D.Montgomery, Rep. Prog. Phys. **43** (1980) 547
- [95] User manual, quadrature demodulator PCI2577, H.Larsen (1997)
- [96] Resonant and nonresonant electron cyclotron heating at densities above the plasma cutoff by O-X-B mode conversion at the W7-AS stellarator, H.P.Laqua et al., Phys. Rev. Lett. **78** (1997) 3467
- [97] Improved confinement with reversed magnetic shear in TFTR, F.M.Levinton et al., Phys. Rev. Lett. **75** (1995) 4417
- [98] Measurements of microturbulence in tokamaks and comparisons with theories of turbulence and anomalous transport, P.C.Liewer, Nucl. Fusion **25** (1985) 543
- [99] Effects of collisional zonal flow damping on turbulent transport, Z.Lin et al., Phys. Rev. Lett. **83** (1999) 3645
- [100] Stimulated optical radiation in Ruby, T.H.Maiman, Nature **187** (1960) 493
- [101] Turbulent fluctuations in TFTR configurations with reversed magnetic shear, E.Mazzucato et al., Phys. Rev. Lett. **77** (1996) 3145
- [102] Core-edge studies with boundary island configurations on the W7-AS stellarator, K.McCormick et al., Plasma Phys. Control. Fusion **41** (1999) B285
- [103] K.McCormick, private communication (2001)

- [104] New advanced operational regime on the W7-AS stellarator, K.McCormick et al., Phys. Rev. Lett. **89** (2002) 015001-1
- [105] Impurity-induced turbulence suppression and reduced transport in the DIII-D tokamak, G.R.McKee et al., Phys. Plasmas **7** (2000) 1870
- [106] Etude des fluctuations de densité dans les plasmas de tokamak: Application à l'interspectre du signal turbulent, O. Menicot (1994)
- [107] High confinement and high density with stationary plasma energy and strong edge radiation in the TEXTOR-94 tokamak, A.M.Messiaen et al., Phys. Rev. Lett. **77** (1996) 2487
- [108] H-mode pedestal characteristics and MHD stability of the edge plasma in Alcator C-Mod, D.A.Mossessian et al., Plasma Phys. Control. Fusion **44** (2002) 423
- [109] Beyond paradigm: Turbulence, transport, and the origin of the radial electric field in low to high confinement mode transitions in the DIII-D tokamak, R.A.Moyer et al., Phys. Plasmas **2** (1995) 2397
- [110] Collected works **VI**: Theory of games, astrophysics, hydrodynamics and meteorology, J. von Neumann, ed. A.H.Taub, Pergamon Press (1963) 437
- [111] Chaos in dynamical systems, E.Ott, Cambridge University Press (2000)
- [112] Turbulence during ergodic divertor experiments in Tore Supra, J.Payan et al., Nucl. Fusion **35** (1995) 1357
- [113] Low frequency waves in magnetized plasmas, H.L.Pécsele (2001)
- [114] The bootstrap current and its consequences, A.G.Peeters, Plasma Phys. Control. Fusion **42** (2000) B231
- [115] Far-infrared heterodyne scattering to study density fluctuations on the DIII-D tokamak, R.Philipona et al., Rev. Sci. Instrum. **61** (1990) 3007
- [116] Two-stage turbulence suppression and $\mathbf{E} \times \mathbf{B}$ velocity shear measured at the L-H transition, R.Philipona et al., Phys. Fluids B **5** (1993) 87
- [117] Spectral techniques for experimental investigation of plasma diffusion due to polychromatic fluctuations, E.J.Powers, Nucl. Fusion **14** (1974) 749
- [118] Numerical recipes in Fortran, W.H.Press et al., Cambridge University Press (1994)
- [119] Initial operation of the Wendelstein 7-AS advanced stellarator, H.Renner et al., Plasma Phys. Control. Fusion, **31** (1989) 1579
- [120] Edge turbulence reduction at the L-H transition in DIII-D, C.L.Rettig et al., Nucl. Fusion **33** (1993) 643
- [121] Enhanced spatial localization of collective scattering measurements in the DIII-D tokamak, C.L.Rettig et al., Rev. Sci. Instrum. **66** (1995) 848
- [122] Microturbulence reduction during negative central shear tokamak discharges, C.L.Rettig et al., Phys. Plasmas **4** (1997) 4009
- [123] Search for the ion temperature gradient mode in a tokamak plasma and comparison with theoretical predictions, C.L.Rettig et al., Phys. Plasmas **8** (2001) 2232
- [124] Confinement studies on the Wendelstein 7-AS stellarator, H.Ringler et al., Plasma Phys. Control. Fusion **32** (1990) 933

- [125] Fluctuation-induced energy flux in the tokamak edge, C.P.Ritz et al., Phys. Rev. Lett. **62** (1989) 1844
- [126] On standard forms for transport equations and fluxes, D.W.Ross, Comm. Plasma Phys. Control. Fusion **12** (1989) 155
- [127] On standard forms for transport equations and quasilinear fluxes, D.W.Ross, Plasma Phys. Control. Fusion **34** (1992) 137
- [128] Extended technical description, M.Saffman (1995)
- [129] Signal level estimates, M.Saffman (1995)
- [130] Operating procedures, CO₂ laser collective scattering diagnostic at W7-AS, M.Saffman (2000)
- [131] Analysis of cooled dual detector for the LOTUS diagnostic, M.Saffman (2001)
- [132] CO₂ laser based two-volume collective scattering instrument for spatially localized turbulence measurements, M.Saffman et al., Rev. Sci. Instrum. **72** (2001) 2579
- [133] Electron density fluctuations in a plasma, E.E.Salpeter, Phys. Rev. **120** (1960) 1528
- [134] Lasers, A.E.Siegman, University Science Books (1986)
- [135] Study of density fluctuations in plasmas by small-angle CO₂ laser scattering, R.E.Slusher and C.M.Surko, Phys. Fluids **23** (1980) 472
- [136] The quasi-coherent signature of enhanced D_α H-mode in Alcator C-Mod, J.A.Snipes et al., Plasma Phys. Control. Fusion **43** (2001) L23
- [137] Mathematical handbook, M.R.Spiegel, McGraw-Hill (1991)
- [138] Waves in plasmas, T.H.Stix, Springer-Verlag (1992)
- [139] Energy confinement scaling from the international stellarator database, U.Stroth et al., Nucl. Fusion **36** (1996) 1063
- [140] Study of the density fluctuations in the Adiabatic Toroidal Compressor scattering tokamak using CO₂ laser, C.M.Surko and R.E.Slusher, Phys. Rev. Lett. **37** (1976) 1747
- [141] Study of plasma density fluctuations by the correlation of crossed CO₂ laser beams, C.M.Surko and R.E.Slusher, Phys. Fluids **23** (1980) 2425
- [142] Roles of electric field shear and Shafranov shift in sustaining high confinement in enhanced reversed shear plasmas on the TFTR tokamak, E.J.Synakowski et al., Phys. Rev. Lett. **78** (1997) 2972
- [143] Formation and structure of internal and edge transport barriers, E.J.Synakowski, Plasma Phys. Control. Fusion **40** (1998) 581
- [144] Comparative studies of core and edge transport barrier dynamics of DIII-D and TFTR tokamak plasmas, E.J.Synakowski et al., Nucl. Fusion **39** (1999) 1733
- [145] Radiofrequency-heated enhanced confinement modes in the Alcator C-Mod tokamak, Y.Takase et al., Phys. Plasmas **4** (1997) 1647
- [146] A first course in turbulence, H.Tennekes and J.L.Lumley, MIT Press (1990)

- [147] Correlation between low frequency turbulence and energy confinement in TFR, A.Truc et al., Nucl. Fusion **26** (1986) 1303
- [148] ALTAIR: An infrared laser scattering diagnostic on the Tore Supra tokamak, A.Truc et al., Rev. Sci. Instrum. **63** (1992) 3716
- [149] Regime of improved confinement and high beta in neutral-beam-heated divertor discharges of the ASDEX tokamak, F.Wagner et al., Phys. Rev. Lett. **49** (1982) 1408
- [150] Importance of the divertor configuration for attaining the H-regime in ASDEX, F.Wagner et al., Journal of Nucl. Mater. **121** (1984) 103
- [151] H-mode of W7-AS stellarator, F.Wagner et al., Plasma Phys. Control. Fusion **36** (1994) A61
- [152] Overview on W7-AS results with relevance for Wendelstein 7-X and the low-shear stellarator line, F.Wagner et al., Proc. 17th IAEA Conf. (Yokohama) (1998)
- [153] Stellarator and heliotron devices, M.Wakatani, Oxford University Press (1998)
- [154] Low-frequency density fluctuations in a tokamak plasma, R.L.Watterson et al., Phys. Fluids **28** (1985) 2857
- [155] Collective modes in inhomogeneous plasma, J.Weiland, Institute of Physics Publishing (2000)
- [156] Optimum confinement in the Wendelstein 7-AS stellarator, A.Weller et al., Plasma Phys. Control. Fusion **33** (1991) 1559
- [157] Survey of magnetohydrodynamic instabilities in the advanced stellarator Wendelstein 7-AS, A.Weller et al., Phys. Plasmas **8** (2001) 931
- [158] A.Weller, private communication (2001)
- [159] A.Werner, private communication (2001)
- [160] Tokamaks, J.Wesson, Oxford University Press (1997)
- [161] Plasma confinement in the Wendelstein 7-A stellarator, H.Wobig et al., Proc. 11th IAEA Conf. (Kyoto) **2** (1986) 369
- [162] Viscous damping of rotation in Wendelstein 7-AS, H.Wobig and J.Kisslinger, Plasma Phys. Control. Fusion **42** (2000) 823
- [163] Fluctuations and anomalous transport in tokamaks, A.J.Wootton et al., Phys. Fluids B **2** (1990) 2879
- [164] Comparison of the density fluctuation spectrum and amplitude in TEXT with expectations for electron drift waves, C.X.Yu et al., Phys. Fluids B **4** (1992) 381
- [165] Correlation analysis of 110 GHz ECH modulation experiments on the DIII-D tokamak, M.Zerbini et al., Plasma Phys. Control. Fusion **41** (1999) 931
- [166] Report on CO₂ laser scattering data processing, S.Zoletnik (1999)
- [167] IDL programs for the CO₂ laser scattering diagnostic at W7-AS, S.Zoletnik (1999)
- [168] The data acquisition system of the W7-AS CO₂ scattering diagnostic, S.Zoletnik (1999)

- [169] Relationship between confinement and core plasma fluctuations in the W7-AS stellarator, S.Zoletnik et al., 26th EPS, ECA **23J** (1999) 1493
- [170] Report on CO₂ laser scattering data processing, S.Zoletnik (1999)
- [171] Calculation of different correlation functions used in the CO₂ scattering experiment, S.Zoletnik (1999)
- [172] Density fluctuation phenomena in the scrape-off layer and edge plasma of the Wendelstein 7-AS stellarator, S.Zoletnik et al., Phys. Plasmas **6** (1999) 4239
- [173] Comparison of different ways of correlation calculation for the CO₂ scattering diagnostic, S.Zoletnik (2001)
- [174] Correlation between the two signals of the W7-AS CO₂ scattering diagnostic as a function of volume alignment angle, S.Zoletnik (2001)
- [175] Note on wide 100 kHz peak in scattering signals during the confinement transition at $\nu = 0.35$, S.Zoletnik (2001)
- [176] 40 MHz leakage and calibration of notch filter performance in the CO₂ scattering diagnostics, S.Zoletnik (2001)
- [177] Changes in density fluctuations associated with confinement transitions close to a rational edge rotational transform in the W7-AS stellarator, S.Zoletnik et al., Plasma Phys. Control. Fusion **44** (2002) 1581
- [178] Edge plasma transport experiments in the Caltech tokamak, S.Zweben et al., Journal of Nucl. Mater. **111-112** (1982) 39

A LOTUS setups, 1999-2000

The wavenumber of the density fluctuations in terms of calibrated factors is:

$$\text{kplasma} = \text{factor} \times [\text{sm1pos} \times \text{slope} + \text{sepooffset}] \quad (\text{A.243})$$

Here, $\text{factor} = \text{kplasma}/\text{beamsep}$ and $\text{beamsep} = [\text{sm1pos} \times \text{slope} + \text{sepooffset}]$. These quantities are given in table 5 for the four setups that we had in 1999. Further, we show w_p , w_d and d_{vol} , which is the beam waist in the plasma, on the detectors and the volume separation in the plasma, respectively.

Date	17/1/99	27/3/99	16/5/99	28/7/99
sm1pos [mm]	7	15	2	12
beamsep [mm]	11	28	10	29
sepooffset [mm]	-3	-2	6	5
slope [-]	2	2	2	2
kplasma [cm^{-1}]	39.41	48.15	17.20	15.59
factor [cm^{-1}/mm]	3.58	1.72	1.72	0.537
$2 w_p$ [mm]	3.97	8.27	8.27	66.16
$2 w_d$ [mm]	1.05	0.65	0.87	0.89
d_{vol} [mm]	13.8	28.8	28.8	-

Table 5. Experimental setups in the 1999 campaign - calibration factors.

The corresponding lenses used for these setups are shown in table 6.

Date	17/1/99	27/3/99	16/5/99	28/7/99
L1 [mm]	400	400	400	400
L2 [mm]	200	200	200	200
L3 [mm]	300	300	300	300
L4 [mm]	750	750	750	300
L5 [mm]	300	300	300	300
L6 [mm]	100	100	100	100
L7 [mm]	200	500	500	600
L8 [mm]	500	600	600	225
L9 [mm]	800	800	800	800
L10 [mm]	800	800	800	800
L11 [mm]	1380	1380	1380	1380
L12 [mm]	1080	1080	1080	1080
L13 [mm]	600	300	300	500
L14 [mm]	400	500	500	500
L15 [mm]	335	335	335	85
L16 [mm]	150	200	150	500
L17 [mm]	85	85	85	85

Table 6. Experimental setups in the 1999 campaign - lenses.

We now turn to the 2000 setup. Changes in the acquisition software were made during mid-1999, where the measured wavenumber and other instrumental data was written into the data file preamble. This meant that it was no longer necessary to keep the old calibration factors. Only the present factors need to be kept; these are stored in a configuration file. Therefore, we combine the calibration and lens table for the 2000 setups, see table 7.

Date	1/7/00	19/11/00
$2 w_p$ [mm]	6.9	6.9
$2 w_d$ [mm]	0.80	0.54
d_{vol} [mm]	19.2	19.2
$L1$ [mm]	400	400
$L2$ [mm]	200	200
$L3$ [mm]	300	300
$L4$ [mm]	750	750
$L5$ [mm]	300	300
$L6$ [mm]	200	200
$L7$ [mm]	600	600
$L8$ [mm]	431	431
$L9$ [mm]	800	800
$L10$ [mm]	800	800
$L11$ [mm]	1380	1380
$L12$ [mm]	1080	1080
$L13$ [mm]	500	500
$L14$ [mm]	500	500
$L15$ [mm]	335	335
$L16$ [mm]	400	400
$L17$ [mm]	150	101.6

Table 7. Experimental setups in the 2000 campaign.

B Dedicated experimental programs

1. We have measured correlations with toroidally and poloidally displaced measurement volumes in high density ECRH discharges with both good and bad confinement around $t_a = 0.35$, see table 8.
2. Scans with dual volume localisation, see table 9.
3. A follow-up series of shots to those in table 9, see table 10.
4. Series of NBI shots to test influence of toroidal flow reversal, see table 11.
5. Scan with single volume localisation, see table 12.
6. Slow current ramp discharges, low density, see table 13.
7. Slow current ramp discharges, higher density, see table 14.

Reference shots 48338-43:

One ECRH gyrotron (400 kW), D₂, $t_a = 0.344$, current ramp up from 400 to 500 ms (max 2 kA), ramp down from 500 to 600 ms. Line density about 3×10^{19} m⁻². $W_{\text{dia}} \sim 11$ kJ in the good confinement phase.

Shot types:

1. 'Fast' current ramp shots as 48338-43 ($t_a = 0.344$).
2. 'Slow' (300-1000 ms) current ramp shots ($t_a = 0.344$).
3. Good confinement shots ($t_a = 0.344$) without current ramp.
4. Bad confinement shots ($t_a = 0.362$) with 'fast' current ramp.
5. Good confinement shots with one co-NBI (E4) source instead of ECRH.
6. Good confinement shots with one counter-NBI (W3) source instead of ECRH.
7. Bad confinement shots ($t_a = 0.362$) without current ramp.
8. 'Slow' current ramp, low density.
9. 'Slow' current ramp, higher density.

Shotno.	Angle (deg.)	k (cm ⁻¹)	Gains (dB)	Shot type	Exp. notes
45230	90.0	39.44	6/6	1	Ok
45231	90.0	46.61	6/6	1	Ok
45232	90.0	53.78	6/6	1	Ok
45233	90.0	60.95	6/6	1	Ok, failed pulse
45234	90.0	60.95	6/6	1	Ok, failed pulse
45235	90.0	60.95	6/6	1	Ok, failed pulse
45236	90.0	60.95	6/6	1	Ok
45237	90.0	68.12	6/6	1	Ok
45238	90.0	32.27	6/6	1	Ok
45239	90.0	32.27	6/6	4	Ok
45240	90.0	39.44	6/6	4	Ok
45241	90.0	46.61	6/6	4	Ok
45242	90.0	53.78	6/6	4	Ok
45243	90.0	60.95	6/6	4	Ok
45244	90.0	68.12	6/6	4	Ok
45275	0.0	25.1	10/10	1	Laser trouble
45276	0.0	32.27	10/10	1	Laser trouble
45277	0.0	39.44	10/10	1	Ok
45278	0.0	46.61	10/10	1	Ok
45279	0.0	53.78	10/10	1	Ok
45280	0.0	60.95	10/10	1	Ok
45281	0.0	32.27	10/10	1	Ok
45282	0.0	25.1	10/10	1	Ok
45283	0.0	25.1	10/10	4	Ok
45284	0.0	32.27	10/10	4	Ok
45285	0.0	39.44	10/10	4	Ok
45286	0.0	46.61	10/10	4	Ok
45287	0.0	53.78	10/10	4	Ok
45288	0.0	60.95	10/10	4	Ok

Table 8. Experiments performed on 27th and 29th of January 1999. Note: Shots 45230-44 had 4 mA detector current, shots 45275-88 had 7 mA detector current.

Shotno.	Angle (deg.)	k (cm ⁻¹)	Gains (dB)	Shot type	Exp. notes
47189	-4.5	20	7/7	1, rad.	Ch.1 sat.
47190	0.5	20	5/5	1	Ok
47191	5.5	20	5/5	1	Ok
47192	10.5	20	7/7	1	Ok
47193	-9.5	20	7/7	1	Ch.1 sat.
47194	15.6	20	7/7	1	Ch.1 sat.
47195	-14.6	20	7/7	1	Ok
47196	20.9	20	5/5	1	Ok
47197	26.3	20	5/5	1	Ok
47198	32.0	20	5/5	1	Ok
47199	5.5	40	12/12	1	Ch.1 sat.
47200	5.5	30	7/7	1	Ch.1 sat.
47201	0.5	30	7/7	1	Ch.1 sat.
47202	0.5	30	4/4	1	Ok
47203	15.6	30	4/4	1	Ok
47204	-4.5	30	7/7	1	Ok
47205	10.5	30	7/7	1	Ok
47206	-9.5	30	5/5	1	Ok
47207	20.9	30	5/5	1	Ok
47208	-14.6	30	5/5	1	Ok
47209	-19.9	30	5/5	1	Ok
47210	15.6	15	3/3	1	Ok

Table 9. Experiments performed on 17th of May 1999. NOTE: ECRH deposition change between shot 47192 (HF launch, good) and shot 47193 (LF launch, bad).

Shotno.	Angle (deg.)	k (cm ⁻¹)	Gains (dB)	Shot type	Exp. notes
47932	0.5	11	4/5	1	Ch.1 sat.
47933	0.5	15	3/10	1	Ok
47934	0.5	20	4/10	1	Ok
47935	0.5	25	4/10	1	Ch.1 sat.
47936	0.5	30	0/10	1	Ok
47937	-9.5	15	0/10	2	Ok
47938	0.5	15	0/10	2	Failed pulse
47939	0.5	15	0/10	2	Ok
47940	10.5	15	0/10	2	Modes to 300 ms
47941	-9.5	15	0/10	3	Ok
47942	0.5	15	0/10	3	Ok
47943	10.5	15	0/10	3	Ok
47944	-9.5	15	0/10	7	Ok
47945	0.5	15	0/10	7	Ok
47946	10.5	15	0/10	7	Ok
47974	20.0	15	0/10	2	Ld. low
47975	20.0	15	0/10	2	Ok
47976	-20.0	15	0/10	2	Ok

Table 10. Experiments performed on 14th and 16th of July 1999. Note: For shots 47932-46 laser exciter was on 9.5 mA, for shots 47974-76 on 6 mA.

Shotno.	Angle (deg.)	k (cm ⁻¹)	Gains (dB)	Shot type	Exp. notes
48091	180	15	0/0	1	Ok
48094	-9.5	15	0/10	5	Ok
48095	10.5	15	0/10	5	Ok
48096	-9.5	15	0/10	6	Ok
48098	10.5	15	0/10	6	Ok

Table 11. Experiments performed on 26th of July 1999.

Shotno.	Angle (deg.)	k (cm ⁻¹)	Gains (dB)	Shot type	Exp. notes
48338	90	15	3/3	1	Ok
48339	94	15	3/3	1	Ok
48340	98	15	3/3	1	Ok
48341	102	15	3/3	1	Ok
48342	106	15	3/3	1	Ok
48343	96	15	3/3	1	Ok

Table 12. Experiments performed on 11th of August 1999.

Shotno.	Angle (deg.)	k (cm ⁻¹)	Gains (dB)	Shot type	Exp. notes
49723	5	20	8/8	-	Ok
49724	5	20	8/8	-	Ok
49725	5	20	8/8	-	Ok
49726	5	25	8/8	-	Ok
49727	0	35	8/8	-	Ok
49728	0	45	8/8	8	Ok
49729	7	20	12/12	8	Ok
49730	9	20	12/12	8	Ok
49731	11	20	12/12	8	Ok
49732	-	-	-	8	LOST(IDL)
49733	-	-	-	8	LOST(IDL)
49734	-	-	-	8	OVERRAN
49735	15	20	12/12	8	Ok
49736	0	25	12/12	8	Ok

Table 13. Experiments performed on 13th of November 2000.

Shotno.	Angle (deg.)	k (cm ⁻¹)	Gains (dB)	Shot type	Exp. notes
50028	0	20	7/7	-	Ok
50029	0	20	7/7	-	Ok
50030	0	20	7/7	-	Ok
50031	4	20	7/7	9	Ok
50032	0	20	7/7	9	Ok
50033	-4	20	7/7	9	Ok
50034	-8	20	7/7	9	Ok
50035	8	20	7/7	9	Ok
50036	12	20	7/7	9	Ok
50037	-12	20	7/7	9	Ok

Table 14. Experiments performed on 4th of December 2000.

 Title and author(s)

Turbulence in Wendelstein 7-AS plasmas measured by collective light scattering

Nils Plesner Basse

 ISBN

87-550-3092-0; 87-550-3093-9 (internet)

ISSN

0106-2840

 Dept. or group

Optics and Fluid Dynamics

Date

August 2002

 Groups own reg. number(s)

Project/contract No.

 Sponsorship

 Pages

168

Tables

14

Illustrations

106

References

178

 Abstract (Max. 2000 char.)

This Ph.D. thesis contains theoretical and experimental work on plasma turbulence measurements using collective light scattering.

The motivation for measuring turbulence in hot fusion plasmas is, along with the method used and results obtained, the subject of chapter 1.

The theoretical part is divided into three chapters. Chapter 2 contains a full analytical derivation of the expected dependency of the detected signal on plasma parameters. Thereafter, spatial resolution of the measurements using different methods is treated in chapter 3. Finally, the spectral analysis tools used later in the thesis are described and illustrated in chapter 4.

The experimental part is divided into four chapters. In chapter 5 transport concepts relevant to the thesis are outlined. Main parameters of the Wendelstein 7-AS (W7-AS) stellarator in which measurements were made are collected in chapter 6. The setup used to study fluctuations in the electron density of W7-AS plasmas is covered in chapter 7. This localised turbulence scattering (LOTUS) diagnostic is based on a CO₂ laser radiating at a wavelength of 10.59 μm . Fast, heterodyne, dual volume detection at variable wavenumbers between 14 and 62 cm^{-1} is performed. The central chapter of the thesis, chapter 8, contains an analysis of the measured density fluctuations before, during and after several confinement transition types. The aim was to achieve a better understanding of the connection between turbulence and the confinement quality of the plasma.

Conclusions and suggestions for further work are summarised in chapter 9.

 Descriptors

Electron density; hot plasma; light scattering; magnetic confinement; plasma confinement; turbulence; Wendelstein-7 stellarator
